Mechanochemical synthesis of amorphous inorganic carbonates

Mainz, Oktober 2021

Dissertation
zur Erlangung des akademischen Grades
„Doktor der Naturwissenschaften“

am Fachbereich Chemie, Pharmazie, Geographie und Geowissenschaften
der Johannes Gutenberg – Universität Mainz
im Promotionsfach Chemie

vorgelegt von:
Phil Kypros Opitz

geboren in Berlin-Wilmersdorf

Dekan:

Erster Berichterstatter:

Zweiter Berichterstatter:

Tag der mündlichen Prüfung:

Erklärung:

Die vorliegende Arbeit wurde in der Zeit 07/2018 bis 10/2021 unter der Betreuung von Herrn Prof. Dr. Wolfgang Tremel am Department Chemie der Johannes Gutenberg – Universität Mainz durchgeführt.

Hiermit erkläre ich, dass die vorliegende Arbeit selbstständig verfasst und keine anderen als die angegebenen Quellen und Hilfsmittel verwendet wurden. Alle Stellen, die wörtlich oder sinngemäß aus anderen Quellen übernommen wurden, sind als solche gekennzeichnet.

Mainz, Oktober 2021

Phil Opitz

Für meine Eltern

Abstract

In this dissertation, the mechanochemical amorphization of earth alkali metal carbonates, especially calcite, is studied using different “impurities”, in particular monetite ($CaHPO_4$), sodium hydrogen sulfate ($NaHSO_4$) and basic magnesia carbonate. Amorphous alkaline earth metal carbonates are general transient and often metastable species that pose a particular synthetic challenge. Utilizing a high-energy ball mill, a wide variety of amorphous alkaline earth metal carbonates, phosphates and sulfates were synthesized. These new amorphous phases represent an interesting class of solid solutions of very well-known groups of compounds and were covered in three projects: i) amorphous earth alkali metal carbonate calcium hydrogen phosphate (aMCP), ii) amorphous magnesian calcium carbonate (aMCC) and amorphous calcium carbonate sodium hydrogen sulfate (aCCSHS). A particular challenge for the investigation of the formation mechanism and the structure of these phases is the lack of a long-range order, which makes conventional x-ray powder diffraction analyses not suitable. Therefore, the amorphous phases were mainly investigated by Fourier transformed infrared spectroscopy (FTIR), solid-state nucleus magnetic resonance spectroscopy (ssNMR) and total scattering analysis. This work contributes not only to a deeper understanding of crystallization and ball milling reactions but also shows routes for the targeted control of crystallization pathways in order to synthesize new materials.

In the first project, calcium, strontium and barium carbonates were amorphized mechanochemically using monetite. This reaction leads to an inert amorphous phase which cannot be crystallized in water. One focus of this project is the formation mechanism which was investigated *ex situ* by NMR and FTIR spectroscopy. An acid-base reaction of basic carbonate and acidic hydrogen phosphate ion was identified as the driving force of the reaction. The surprising feature is that the acid-base reaction takes place in the absence of water. Furthermore, the transferred echo double resonance (TEDOR) and heterogeneous correlation (HETCOR) NMR methods were applied to detect calcium hydrogen carbonate species, which were not reported in the literature so far. Further, long-term grinding leads to the formation of pyrophosphates in the amorphous mixture.

In the second project, amorphous calcium magnesium carbonate was synthesized. The focus was on the crystallization of the amorphous phase depending on the magnesium content. Thus, aMCC with about 3:1 Ca^{2+} to Mg^{2+} ratio was identified as a potential bone regeneration material: The magnesium content is high enough to stabilize the amorphous

material and low enough that the crystallization path does not change from Mg-rich Calcite to Aragonite ($CaCO_3$) via Monohydrocalcite ($CaCO_3 \cdot H_2O$). Furthermore, it was shown that aMCC 30% incubated in simulated body fluid forms a carbonate-rich apatite species and could therefore be a promising material for bone regeneration.

By recognizing that an acid-base reaction is feasible in the ball mill, in the third project, calcium carbonate was mechanochemically treated with sodium hydrogen sulfate. Therefore, amorphous calcium carbonate sodium hydrogen sulfate (aCCSHS) could be synthesized and characterized. In contrast to aMCP, aCCSHS is a transient phase that crystallizes fast. During amorphization, the acid base reaction was confirmed by the detection of sodium sulfate. In the further progress of the amorphization, which lasts up to 18 h, a rare mineral omongwaite was detected, which appears as an intermediate just before the mixture becomes a solid solution. A new mineral, $Ca_2Na_4(SO_4)_3(CO_3) \cdot 3H_2O$ (*mainzite*) was discovered during the crystallization of bassanite ($CaSO_4 \cdot ½H_2O$), gypsum ($CaSO_4 \cdot 2H_2O$) and glauberite, depending on the solvent concentration.

Zusammenfassung

In dieser Dissertation wird die mechanochemische Amorphisierung von Erdalkalicarbonaten, insbesondere von Calcit, unter Verwendung verschiedener Verbindungen, insbesondere von Monetit ($CaHPO_4$), Natriumhydrogensulfat ($NaHSO_4$) und basischem Magensiumcarbonat, untersucht. Amorphe Erdalkalicarbonate sind allgemein kurzlebige und oft metastabile Spezies, die daher eine besondere synthetische Herausforderung darstellen. Unter Verwendung einer Hochenergie-Kugelmühle wurde eine Vielzahl von unterschiedlichen amorphen Erdalkali-carbonaten, -phosphaten und -sulfaten synthetisiert. Diese neuen amorphen Phasen stellen eine interessante Klasse von Mischkristallen sehr bekannter Verbindungsgruppen dar und wurden in drei Projekten behandelt: i) amorphes Erdalkalicarbonat-Calciumhydrogenphosphat (aMCP), ii) amorphes Magnesiumcarbonat (aMCC) und amorphes Calciumcarbonat-Natriumhydrogensulfat (aCCSHS). Eine besondere Herausforderung für die Untersuchung des Bildungsmechanismus und der Struktur dieser Phasen ist das Fehlen einer Fern-Ordnung, was die konventionelle Röntgenpulverdiffraktionsanalyse ungeeignet macht. Daher wurden die amorphen Phasen hauptsächlich mittels Fourier-transformierter Infrarot-Spektroskopie (FTIR), Festkörper-Kernspinresonanzspektroskopie (ssNMR) und der Totalstreuungsanalyse untersucht. Diese Arbeiten tragen nicht nur zu einem tieferen Verständnis von Kristallisations- und Kugelmahlreaktionen bei, sondern zeigen auch Wege zur gezielten Steuerung von Kristallisationswegen auf, um somit neue Materialien zu synthetisieren.

Im ersten Projekt wurden Calcium-, Strontium- und Bariumcarbonate mechanochemisch mit Monetit amorphisiert. Diese Reaktion führt zu einer relativ inerten amorphen Phase, die in Wasser nicht kristallisierbar ist. Ein Schwerpunkt dieses Projekts ist der Bildungsmechanismus, der *ex situ* mittels NMR- und FTIR-Spektroskopie untersucht wurde. Eine Säure-Base-Reaktion von basischem Carbonat und saurem Hydrogenphosphat-Ion wurde als treibende Kraft der Reaktion identifiziert. Das Überraschende dabei ist, dass die Säure-Base-Reaktion in Abwesenheit von Wasser abläuft. Darüber hinaus wurden die 2D NMR-Methoden transfer Echo-Doppelresonanz (TEDOR) und die heterogene Korrelation (HETCOR) angewandt, um Calciumhydrogencarbonat-Spezies nachzuweisen, über die in der Literatur bisher nicht berichtet wurde. Weiterhin führt das Langzeitmahlen zur Bildung von Pyrophosphaten in der amorphen Mischung.

Im zweiten Projekt wurde amorphes Calcium-Magnesium-Carbonat synthetisiert. Der Fokus lag dabei auf der Kristallisation der amorphen Phase in Abhängigkeit vom Magnesiumgehalt. So wurde aMCC mit einem Verhältnis von etwa 3:1 Ca^{2+} zu Mg^{2+} als potenzielles Knochenregenerationsmaterial identifiziert: Der Magnesiumgehalt ist hoch genug, um das amorphe Material zu stabilisieren und niedrig genug, dass der Kristallisationsweg nicht von Mg-reichem Calcit über Monohydrocalcit ($CaCO_3 \cdot H_2O$) zu Aragonit ($CaCO_3$) wechselt. Weiterhin wurde gezeigt, dass aMCC 30% in simulierter Körperflüssigkeit inkubiert eine Spezies bildet, die einem carbonatreichen Apatit ähnlich ist und daher ein vielversprechendes System für die Knochenregeneration sein kann.

Da erkannt wurde, dass eine Säure-Base-Reaktion in der Kugelmühle möglich ist, wurde im dritten Projekt Calciumcarbonat mit Natriumhydrogensulfat mechanochemisch behandelt. So konnte amorphes Calciumcarbonat-Natriumhydrogensulfat (aCCSHS) synthetisiert und charakterisiert werden. Im Gegensatz zu aMCP handelt es sich bei aCCSHS um eine sehr kurzlebige Phase, die kristallisieren kann. Während des Amorphisierungsprozesses wurde die Säure-Base-Reaktion durch den Nachweis von Natriumsulfat bestätigt. Im weiteren Verlauf der Amorphisierung, die bis zu 18 h dauert, wurde das seltene Mineral Omongwait nachgewiesen, das als Zwischenprodukt auftritt, kurz bevor das Gemisch zu einer festen Lösung wird. Es konnte ein neues Mineral $Ca_2Na_4(SO_4)_3(CO_3) \cdot 3H_2O$ (*mainzite*), während der Kristallisation von Bassanite ($CaSO_4 \cdot ½H_2O$), Gips ($CaSO_4 \cdot 2H_2O$) und Glauberite abhängig von der Lösungsmittelkonzentration, entdeckt werden.

Acknowledgements

Contents

1 Theory

1.1 Mechanochemistry

Humankind uses grinding since millenia to *e.g.* ignite fires, grind seeds or process building materials.[1–4] A tool that appears consistently in the history of chemistry and alchemy is the mortar and pestle, which can be found in almost every modern laboratory. It is evident that grinding is one of the most important processing methods in chemistry[5–7], pharmacy[8–10], physics[11,12], and food/construction[4,13] industry to reduce the size of materials or to achieve homogenous mixtures of solid materials. In the 19th century, the focus of chemistry was on wet chemical synthesis routes. The main reason for the rediscovery of mechanochemistry is the growing interest in green chemistry.[1–4,14] In order to develop clean sustainable synthesis routes, solvents must be drastically reduced - in laboratories but also on an industrial scale. Mechanochemical methods are promising in this respect, as they offer a solvent-free or drastically reduced (liquid-assisted grinding) synthesis route.[15–17]

Mechanical energy can be introduced into a system through impact, compression, shearing *etc.*, causing the reduction of the particle size, creating active sites for chemical reactions or form new active surfaces for particle growth or coalescence.[4] Modern ball mill devices are not always required to achieve mechanochemical syntheses of novel materials. Askew *et al.*[18] reported the synthesis of a spin cross over complex by simple grinding of the starting materials with a mortar and pestle. The mechanical energy causes the starting materials to be dissolved in its own crystal water *i.e.* an elegant variation of liquid-assisted grinding (released due to mechanical impact) and then to react. In contrast, with the help of a planetary ball mill, high mechanical stress intensities can be achieved due to the high number of rotations on a planetary similar trajectory resulting in high centrifugal forces (Figure 1). This enables complex novel syntheses for organic,[19–23] organometallic[24–26] and inorganic compounds[27–31] besides amorphization[5,32,33] and alloying.[34,35] The exact physical and chemical processes during high-energy ball milling have not yet been finally clarified and is highly dependent upon the systems under consideration. Two prominent theories are the magma-plasma model[36] and the hot-spot theory.[12] The models propose a local temperature rise of over 1000 K for a short time depending on a mechanical event *e.g.* impact or shearing. The hot spot theory describes the reactivity of high-melting-point inorganic substances through regions of local temporal high diffusion caused by a mechanical event. The magma-plasma model addresses covalent solids or polymers. A mechanical event leads to plastic deformation, cracking and rapture which produce radicals, dislocations etc. However, other authors propose mechanisms that do not necessarily require models which depends on local high-energies.[37]

Recently, mechanochemical reactions were monitored *in situ* via X-ray diffraction[15], Raman spectroscopy[38], thermography[38] and imaging by high-speed video cameras.[39] The initial mechanical treatment leads to particle size reduction of the reactants coupled with a rapid increase in temperature. The following processes are highly dependent on the nature of the system – showing the diversity of mechanochemical reactions. Temperature changes can be detected caused by chemical reactions, solvent release and phase transformations of any kind. Therefore, there is no general guideline for the selection of the optimal parameters. In addition, studies utilizing the discrete-element method (DEM)[40–45] show strong dependencies of the milling process on the material of the grinding equipment, the size of the balls, ratio of the balls to starting materials and rotation speed.

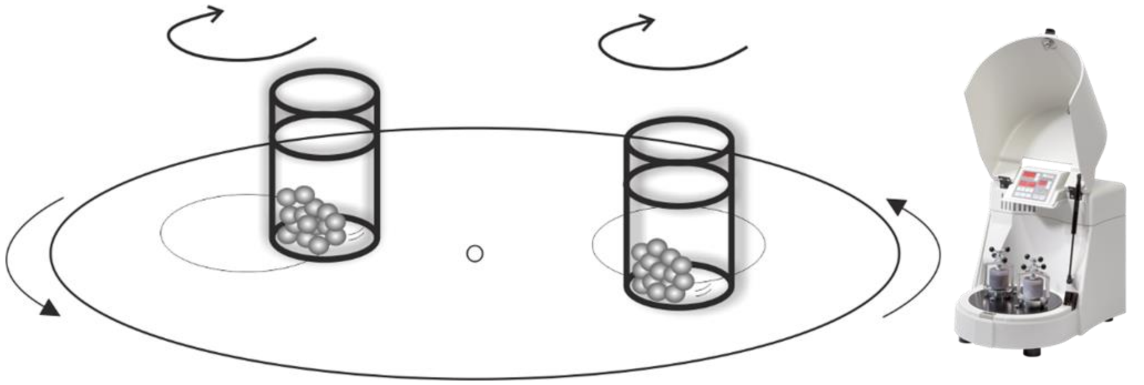

Figure 1. Principle of the planetary ball mill and the planetary ball mill from the manufacturer Fritsch Pulverisette 7 classic line.

1.2 Total scattering

In standard crystallographic X-ray powder diffraction analysis, Bragg peaks and diffuse scattering are treated separately.[46,47] The structure is determined by the position and intensity of the Bragg peaks. In addition, the deviations from the perfect lattice are obtained through the analysis of the diffuse scattering. However, if the structure is strongly disordered, the conventional method fails, especially for amorphous systems.[48–52] In diffraction methods, diffracted intensity is measured as a function of momentum transfer of the scattering particle $\boldsymbol{Q}$ (vectors in bold). The momentum transfer is defined as the $\boldsymbol{Q} = \boldsymbol{k}_{\mathbf{init}} - \boldsymbol{k}_{\mathbf{final}}$, where $\boldsymbol{k}_{\mathbf{init}}$ is the incident wave vector and $\boldsymbol{k}_{\mathbf{final}}$ is the scattered wave vector. $\boldsymbol{Q}$ has the magnitude of

$$|\boldsymbol{Q}| = \frac{4\pi \sin\theta}{\lambda} \tag{1}$$

, where λ is the wavelength of the scattered particle and θ is the angle between the incident and diffracted beam.[46]

Total scattering includes the intensity coming from Bragg peaks (the global structure), elastic diffuse scattering (static local structure) and inelastic diffuse scattering from moving atoms (dynamics). This “total scattering” intensity is measured over a wide range of $\boldsymbol{Q}$ that nearly all information of the coherent scattering is collected.[53,54]

Investigating the local structure implies the study of the total scattering intensity, $S(\boldsymbol{Q})$. The fundamental is the scattering amplitude $\psi(\boldsymbol{Q})$[47]

$$\psi(\boldsymbol{Q}) = \frac{1}{\langle b \rangle} \sum_{\nu} b_{\nu} \mathrm{e}^{\mathbf{iQ \cdot R_{\nu}}} \tag{2}$$

, where $\boldsymbol{R}_{\mathbf{v}}$ defines the position of the atom v, b_{v} is the scattering amplitude of the atom v and $\langle b \rangle$ represents a compositional average. However, it is not possible to measure the scattering amplitude directly but only the intensity of the diffracted beam, which is proportional to the square of the magnitude of the scattering amplitude, $|\psi(\boldsymbol{Q})|^2$.[46] As a consequence, the phase information is lost and only the phase difference remains between scattering events from different atoms. In practice, for total scattering measurements the background intensity must be determined exactly with the help of measurements without the sample. From this, the experimentally coherent intensity I_{C} can be determined correctly[47]

$$I_{\mathrm{C}} = APC \, \frac{\mathrm{d}\sigma_{\mathrm{C}}}{\mathrm{d}\Omega} \tag{3}$$

, where A is the absorption factor, P is the electric polarization factor for X-rays and C is the normalization factor. $\frac{\mathrm{d}\sigma_{\mathrm{C}}}{\mathrm{d}\Omega}$ is the scattering cross section (probability of a particle being scattered related to the counts of a detector and therefore directly proportional to the measured intensity of the total scattering experiment) which is related to the scattering amplitude as follows

$$\frac{\mathrm{d}\sigma_{\mathrm{C}}}{\mathrm{d}\Omega} = \frac{\langle b\rangle^2}{N}|\psi(\boldsymbol{Q})|^2 = \frac{1}{N}\sum_{\nu,\mu} b_\nu b_\mu \mathrm{e}^{\mathrm{i}\mathbf{Q}\cdot(\mathbf{R}_\nu - \mathbf{R}_\mu)} \tag{4}$$

, where *N* is the number of atoms in the sample.[47]

Therefore, the definition of S(***Q***) is[47]

$$I(\boldsymbol{Q}) = \frac{\mathrm{d}\sigma_{\mathrm{C}}}{\mathrm{d}\Omega}\langle b\rangle^2 - \langle b^2\rangle, \tag{5}$$

$$S(\boldsymbol{Q}) = \frac{I(\boldsymbol{Q})}{\langle b\rangle^2}. \tag{6}$$

In many systems, such as amorphous systems, the scattering is isotropic. Therefore, ***Q*** depends only on its magnitude and not on its direction. The Fourier transform the total scattering function intensity is the reduced pair distribution function (PDF) G(*r*), as[47,55]

$$\mathrm{G}(r) = \left(\frac{2}{\pi}\right)\int_{Q_{min}}^{\mathrm{Q}_{max}} Q[\mathrm{S}(Q) - 1]\sin(Qr)\,\mathrm{d}Q. \tag{7}$$

Figure 2a shows a simulated PDF of crystalline gold.[56] The PDF can be interpreted as a kind of distance histogram of atomic pairs. The corresponding first four distances are highlighted in the unit cell of Gold in Figure 2b. This easily accessible information reflects the strength of the total scattering method. By comparing the experimental data with simulated or reference data, a lot of chemical information such as disorder can be obtained from the PDF without much modelling effort. For further reading, the following monograph is highly recommended.[47]

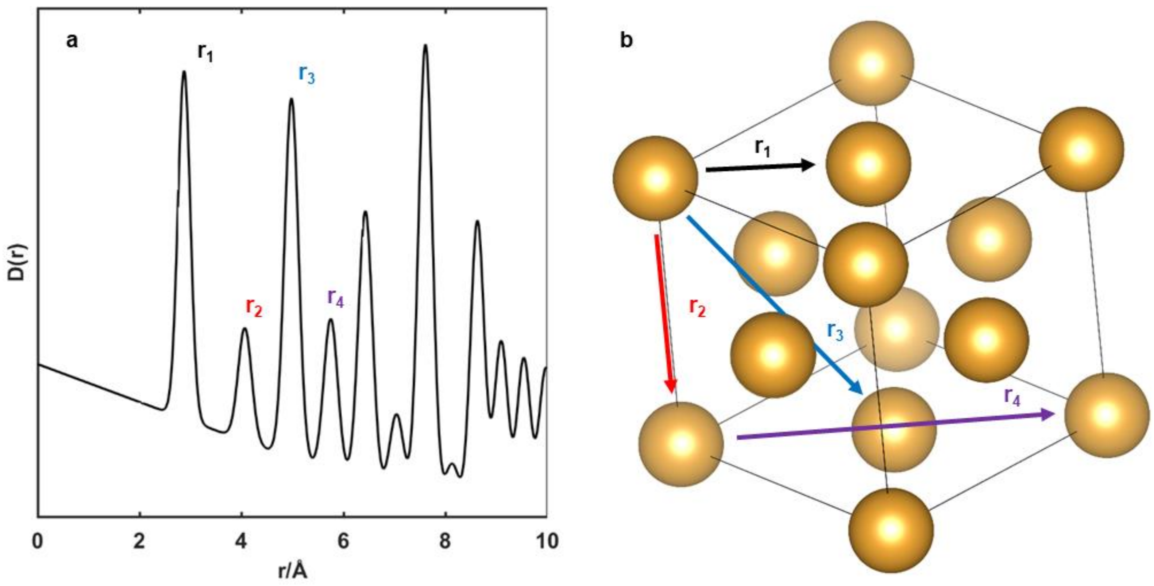

Figure 2. (a) Simulated pair distribution function of crystalline gold. (b) Corresponding unit cell of gold which was used for simulation, space group $Fm\overline{3}m$. The first four distances are highlighted.

1.3 Local order

The aim of material science is to optimize and discover new functional materials.[57] A basic requirement is the understanding of the relationship of the material properties, chemistry and atomic scale structural arrangement. The structural arrangement of the nearest atomic neighbors are mainly dependent on bond strengths, atom sizes, oxidation states, etc. Therefore, this close atomic arrangements are very robust towards external synthesis conditions and other factors.[58] These primary building blocks are fairly unaffected by changes in the crystal structure.[59–61] Figure 3 shows the experimental PDF of amorphous calcium carbonate and a simulated PDF of crystalline calcite. Clearly, the first two peaks are assigned to the primary building blocks of calcium carbonate (highlighted in blue), in particular the C-O and Ca-O distances. These bond distances are expected to be nearly the same for all calcium carbonate polymorphs.[62,63] Beyond these two peaks, there is an extreme difference in the PDF caused by the different nature of the materials. Therefore, information about the physical and chemical properties of amorphous materials is mainly found in this “short-range” to “medium-range” region (highlighted in orange).

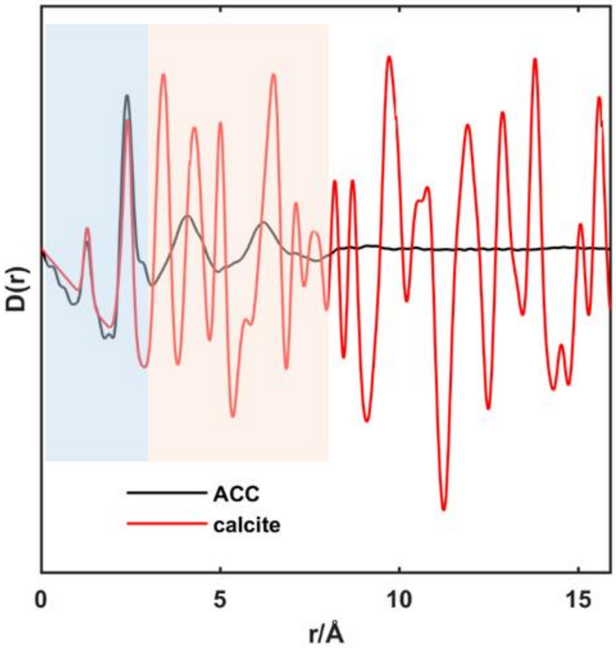

Figure 3. (a) Simulated pair distribution function of crystalline calcite (red). Experimental pair distribution function of amorphous calcium carbonate (black).

The local order is not only of interest for amorphous materials but for most materials in nature, there are high deviations from the long-range to the short-range order.[59,64] These structural disordered materials are designed to achieve enhanced functional materials for catalysis[65], electronically devices[66,67] etc. In general, the structural models and, thus the common means of understanding of the materials are mainly obtained by PDF with the Reversed Monte Carlo (RMC) method.[68] Although very powerful, this method needs a chemical meaningful starting model. In addition, the obtained structures have to be verified with complementary analytical methods.

1.4 Classical nucleation theory

A supersaturated homogeneous phase leads to a phase separation, which results in a mixture of two heterogeneous phases. This process is called nucleation and is a first order phase transition. A thermodynamically metastable phase is transformed into two new phases, *e.g.* during the condensation of a gas or the crystallization of a solid from dissolved ions. The classical nucleation theory describes the change of the free enthalpy, which determines if the process of phase transformation may occur.[69–72] The free enthalpy of nucleation ΔG_{N} is a sum of the volume term ΔG_{V} and the surface term ΔG_{S}

$$\Delta G_{\mathrm{N}} = \Delta G_{\mathrm{V}} + \Delta G_{\mathrm{S}} \tag{8}$$

, where the volume term represents the amount of energy released by the nucleation of the nucleus. Further, the surface term refers to the energy required to form the surface of the nucleus.

The volume term can be described by the following equations

$$\begin{gathered}\Delta G_{\mathrm{V}} = -N \cdot \phi \\ \phi = -\frac{\Delta G}{\Delta N} = \mu_1 - \mu_2\end{gathered} \tag{9}$$

, where ϕ is the affinity describing the change of the chemical potential during a phase transition from a phase 1 with the potential μ_1 to a phase 2 with the potential μ_2. In case the affinity ϕ is greater than zero, the contribution of the volume term for each atom N results in an energy increase. The process of phase transition decreases the total energy of the system when the free energy ΔG for ΔN atoms undergo a change. Since the chemical potential is difficult to access, the affinity is described by the supersaturation S.

$$\phi = \mathrm{k_B} T \cdot \ln(S)\,;\; S = \frac{c'}{c_0}\,, S = \frac{p'}{p_0}\,, S = \frac{a'}{a_0} \tag{10}$$

Supersaturation allows the change in chemical potential which is represented by an accessible parameter, such as concentration, pressure or activity. An increase in the difference between the instantaneous concentration c' and the equilibrium concentration c_0 results in an increase in supersaturation and thus in affinity. Thus, in the case of dissolved ions with the concentration c' one can conclude that $S<1$ is a undersaturated solution, $S=1$ is a solution in equilibrium, and $S>1$ is a supersaturated solution. The free nucleation enthalpy is described by the following expression, assuming that spherical nuclei with radius r are formed.

$$\Delta G_{\mathrm{N}} = -\frac{4}{3}\pi r^3 \frac{\phi}{V_{\mathrm{M}}} + 4\pi r^2 \sigma \tag{11}$$

Based on the volume of an atom V_{M}, the expression $\frac{4}{3}\pi r^3 \frac{\phi}{V_{\mathrm{M}}}$ describes the number of atoms of a spherical nucleus. Thus, the volume term has a cubic dependence and the surface term a quadratic dependence. At radii smaller than r^* the surface term with the surface tension σ dominates and nucleation does not occur. However, once a critical radius r^* is passed, the volume term dominates the surface term and thus the total energy of the system is reduced by the nucleation process (Figure 4).[71]

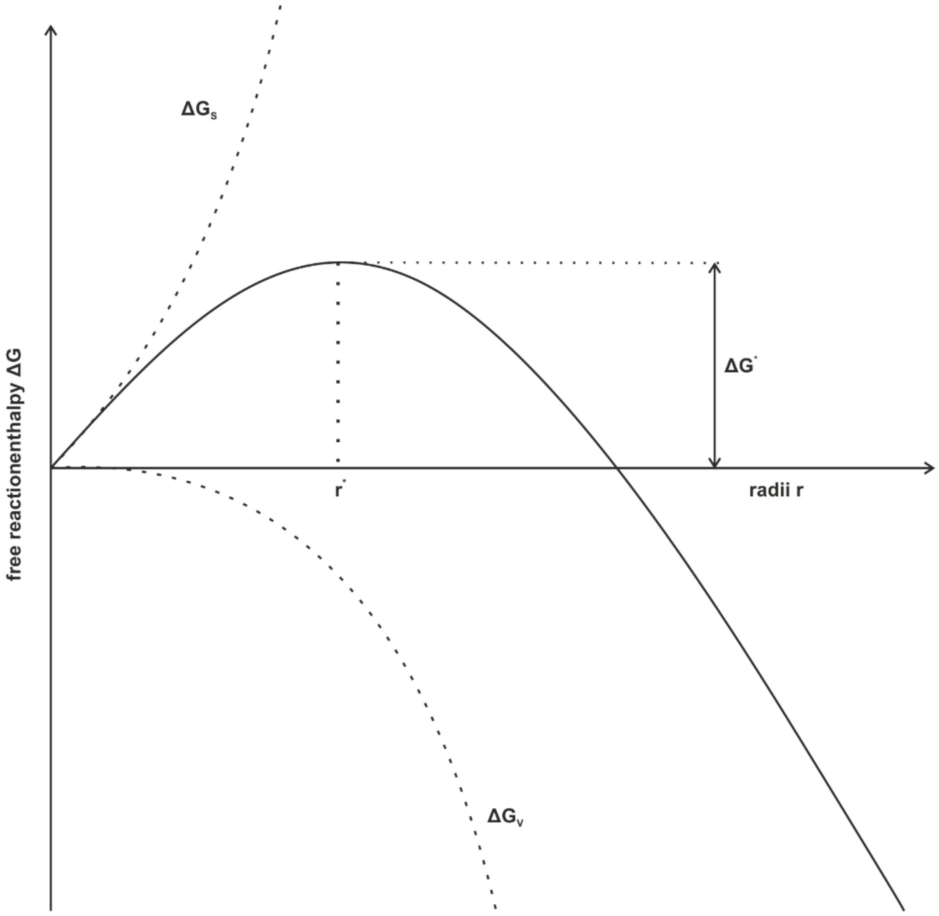

Figure 4. Homogeneous nucleation according to the classical nucleation theory.

1.5 Classical heterogeneous nucleation theory

Mainly, nucleation takes place at interfaces in real systems.[73] The energy barrier can be reduced to such an extent that heterogeneous nucleation takes place even at very low supersaturation, since the required surface energy is significantly reduced. The free enthalpy of heterogeneous nucleation ΔG_N is described by the following equation

$$\Delta G_\mathrm{N} = -\frac{2}{3}\pi r^3 \frac{\phi}{V_M} + 4\pi r^2 \sigma_\mathrm{c} \quad ; \quad \sigma_\mathrm{c} = \sigma_\mathrm{ln}\left[1 - \frac{(\sigma_\mathrm{ls} - \sigma_\mathrm{sn})}{2\sigma_\mathrm{ln}}\right] \tag{12}$$

, where σ_ln is the surface energy between the liquid and the nuclei, σ_ls between the liquid and the substrate and σ_sn between the substrate and the nuclei. The volume term is divided by two, since the seed is formed as a hemisphere on a substrate. Depending on the surface energy of the material, the heterogeneous nucleation is favored. By using a Teflon coating, heterogeneous nucleation can be suppressed as far as possible and almost exclusively homogeneous crystallization can be observed.

1.6 Johnson-Mehl-Avrami-Kolmogorov equation

Nucleation occurs when nuclei with critical radius r^* are formed, thus reducing the energy of the whole system. The driving force of this phase separation is represented by supersaturation. Then, the slowest growing process determines the growth rate of the crystalline phase. The growth rate depends on the rate of mass flow via the phase boundary J_i in case of solutions in which far-reaching diffusion does not have to be considered. Both diffusion-limited and interface-limited growth is strongly dependent on temperature. An Arrhenius approach can be used to describe both processes, in which the growth rate becomes very slow at low temperatures. By using the Johnson-Mehl-Avrami-Kolmogorov equation (JMAK equation), an isothermal phase transition, like crystallization, can be described in kinetic manner.[74–77]

It is assumed that there is an isothermal phase transition. For the nucleus radius r applies approximately

$$r(t) = r^* + vt \approx vt \tag{13}$$

, where v is radial velocity of crystal growth.

Thus, at the time t=0 nuclei with the critical nucleus radius r^* are present and the new phase is formed. The radius r of a growing nucleus at time t is described by the following equations.

$$r = vt \;\; ; \;\; \mathrm{d}r = v\mathrm{d}t \tag{14}$$

For the nucleus density n at time t the following applies

$$n(t) = n[1 - x(t)] \tag{15}$$

, where the volume fraction $x(t)$ represents the proportion of crystalline phase formed at time t from the homogeneous phase by phase separation.

For spherical nuclei, the volume fraction as a function of time is

$$\mathrm{d}x(t) = 4\pi r^2 \mathrm{d}rn[1 - x(\mathrm{t})] \tag{16}$$

Using the expressions $r=vt$ and $\mathrm{d}r=v\mathrm{d}t$ the function of the volume fraction can be transformed as follows:

$$\mathrm{d}x(t) = 4\pi nv^3t^2\mathrm{d}t[1 - x(t)] \tag{17}$$

After transformation and integration of the function over time *t*, follows the JMAK equation for spherical crystallization:

$$\frac{\mathrm{d}x(\mathrm{t})}{1 - x(t)} = 4\pi nv^3t^2\mathrm{d}t \tag{18}$$

$$-\ln[1 - x(t)] = \frac{4\pi nv^3t^3}{3} \tag{19}$$

$$x(t) = 1 - \mathrm{e}^{\left(-\frac{4\pi \mathrm{n}\mathrm{v}^3\mathrm{t}^3}{3}\right)} = 1 - \mathrm{e}^{\left(-\left(\frac{\mathrm{t}}{\tau}\right)^3\right)};\ \tau = \left[\frac{3}{4\pi n}\right]^{\frac{1}{3}}\frac{1}{v} \tag{20}$$

, where τ is the kinetic constant of the process.

For the general case of crystal growth the following applies

$$x(t) = 1 - e^{\left(-\left(\frac{\mathrm{t}}{\tau}\right)^{\mathrm{n}}\right)} \tag{21}$$

, where n is the Avrami-exponent, which is often interpreted as a dimension of the new growing phase. In order to be able to relate the Avrami-exponent obtained from experimental data to the dimension of the growing phase, several factors have to be considered. The Avrami-exponent n consists of two parts, the nucleation and the growth mechanism.

$$n = n_{\mathrm{nucleation}} + n_{\mathrm{growth}} \tag{22}$$

In a three-dimensional process, the Avrami-exponent of the nucleation mechanism $n_{\mathrm{nucleation}}$ can have a value of 1 in the case of a constant nucleation rate, or if nuclei are already present, a value of 0 is assumed. The Avrami exponent of the 3D growth mechanism n_{growth} has a value of 3 in case of a constant growth rate, or a value of 1.5 in case of a parabolic growth mechanism or diffusion controlled growth.

Depending on the complexity of the nucleation and growth mechanism, the Avrami exponent varies. The Avrami-exponent can be assigned to a homogeneous, heterogeneous or limited to specific sites nucleation mechanism with constant or varying growth rates. Furthermore, different growth mechanisms are possible, in particular: one, two or three dimensional, where the speed-determining step is diffusion or mass transfer across the phase boundary. It should be noted that the same Avrami-exponent can describe different processes.

1.7 Calcium carbonate

Calcium carbonate is one of the most abundant compounds on earth, occurs mainly as sedimentary rock[78], and in biomaterials like mollusks[79], shells[80] and corals.[81] Furthermore, it has a wide range of applications such as supplement for building materials[82], filler material for paper[83] and pharmaceutical industry[84] or for agriculture use.[85] Calcium carbonate minerals are also part of the global carbon cycle.[86] The acidification of the ocean is of particular interest, whereby carbon dioxide bound as carbonate is emitted gradually into the atmosphere, due to climate change. The crystallization path and kinetics of calcium carbonate is one of the most studied systems and therefore is considered as a model system although it is still under active research. The manifold polymorphism of calcium carbonateis remarkable.[87] The high solubility range of the different modifications, the possibility of reversible hydration of the calcium ion and the pH dependence of the system which allows different reaction pathways, enables the various modifications to occur. The diverse modifications are described in the following:

Amorphous calcium carbonate. Amorphous calcium carbonate (ACC) is the thermodynamically most unstable phase which transforms in solution rapidly into calcite or aragonite *via* ordering, dehydration and crystallization processes.[88,89] Usually, it is the first modification formed according to Ostwald's step rule. ACC can be found in many biological materials like nacre.[90] In biomineralization, nature utilizes ACC as a calcium carbonate reservoir for targeted re-/crystallization.[91,92] Proteins or templates provide an organic matrix dictating the shape and phase of the bioinorganic material forcing nucleation and crystallization of the inorganic compound in a distinct manner.[93] In this way, more complex bioinorganic materials such as bones and teeth are formed. ACC can appear in various morphologies and modifications depending on the way it is formed *e.g.* stabilized *via* surfactants, peptides, proteins and ions (like Mg^{2+}), quenched in different solvents, prepared by freeze-drying, hydrolysis of carbonic esters and ball-milling.

Ikaite. Ikaite is a metastable, crystalline, hydrated modification of calcium carbonate with the formula of $CaCO_3{\cdot}6H_2O$. The name derives from the Ika Fjord in Greenland, where it was first discovered. Ikaite is a very rare mineral that is formed naturally in the sea at temperatures near freezing point in an anaerobic environment. The mineral is not stable at temperatures above 8 °C transforming into calcite.[94]

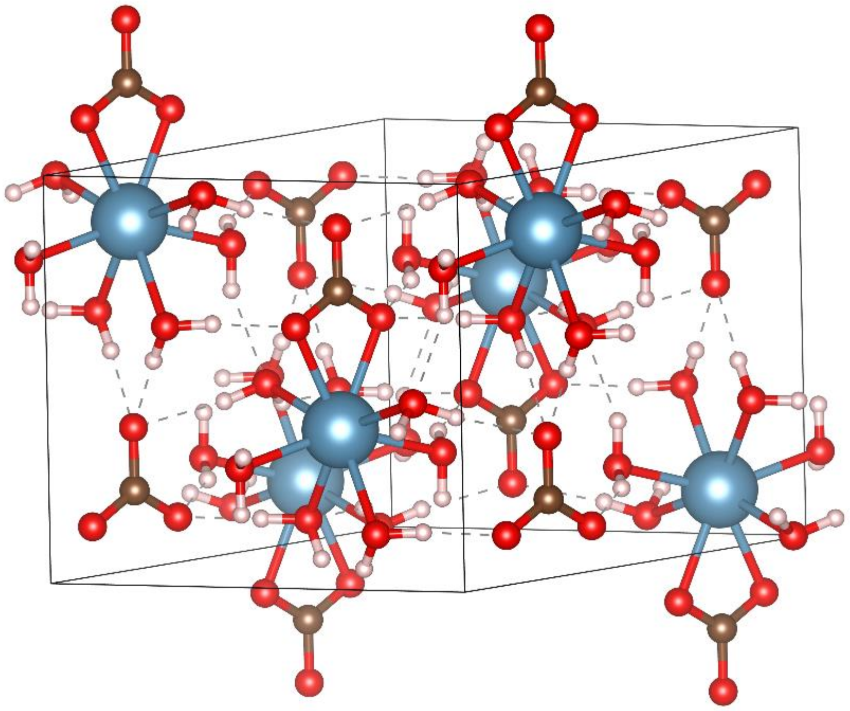

Figure 5. Unit cell of ikaite. Calcium: blue, Carbon: brown, Oxygen: red, Hydrogen: white.

Monohydrocalcite. Monohydrocalcite (MHC) is a hydrated phase of calcium carbonate with the composition $CaCO_3{\cdot}H_2O$. The crystal system of MHC is trigonal, where the calcium atoms are surrounded by eight oxygen atoms, where two originate from water. MHC occurs as a mineral in nature including basaltic caves, saline spring waters, marine polar systems, humid mine galleries and lacustrine deposits.[95] MHC is found in nature in association with other carbonate minerals like dolomite, aragonite, Mg-calcite, etc. Further, MHC occurs in various biological life forms and is therefore of interest for biomineralization *e.g.* molluscs, flatworms, algae, etc. MHC is thermodynamically unstable under normal conditions on the earth's surface and slowly transforms into calcite or aragonite. Although MHC is described as a pure calcium carbonate phase, magnesium ions are often present as foreign ions in natural MHC. Therefore, it is discussed whether the mechanism for the formation of MHC takes place via magnesium-rich ACC. However, MHC has also been reported in silica-rich alkaline solution and in the formation of portland cement.[95,96]

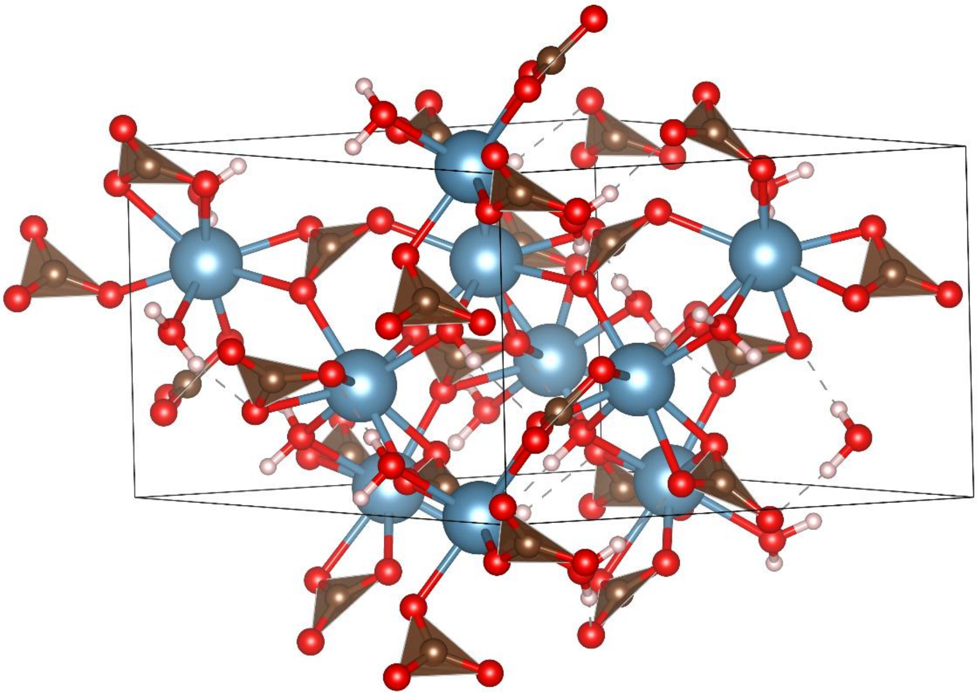

Figure 6. Unit cell of Monohydrocalcite. Calcium: blue, Carbon: brown, Oxygen: red, Hydrogen: white.

Calcium carbonate hemihydrate. Calcium carbonate hemihydrate was recently found by Zou *et al.*[97] It forms in solution in the presence of Mg^{2+} with Mg/Ca molar ratios of circa 5/1.

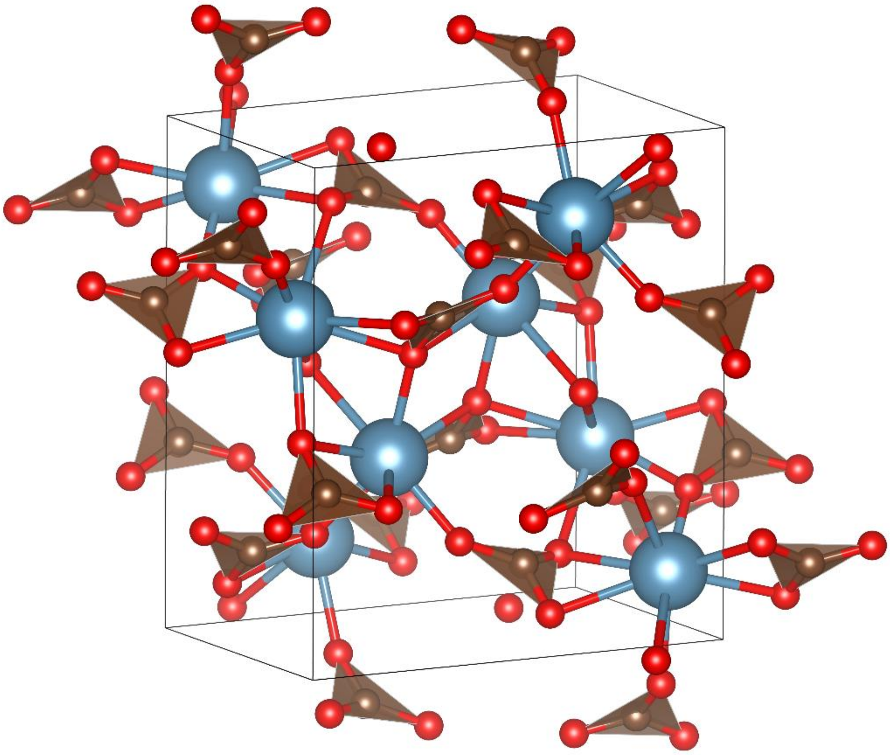

Figure 7. Unit cell of Calcium carbonate hemihydrate. Calcium: blue, Carbon: brown, Oxygen: red.

Monoclinic Aragonite. Recently, Monoclinic Aragonite (mAra) has been discovered in a cold cave decorated by aragonite speleothems at Obstanser Eishöhle, which is located 3 km south of Kartitsch close to the Austrian-Italian border. This nanocrystalline calcium carbonate modification forms from Mg-rich drip water with a Mg^{2+} to Ca^{2+} ratio of >1.5. mAra seems to be apparent as a precursor of conventional orthorhombic aragonite.[98]

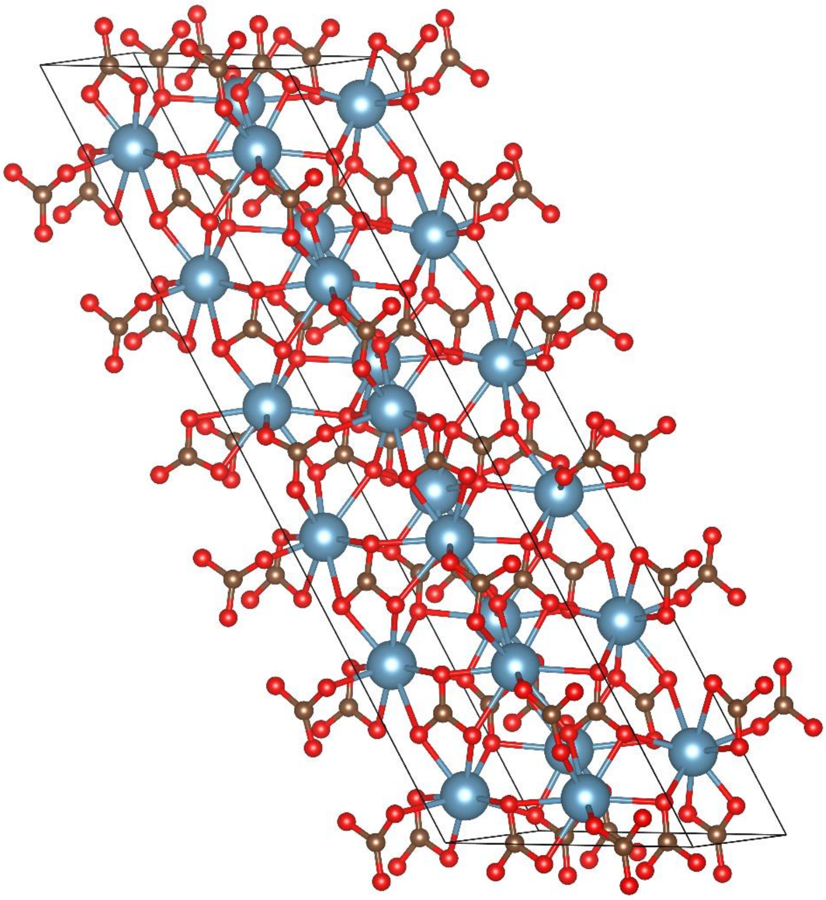

Figure 8. Unit cell of monoclinic Aragonite. Calcium: blue, Carbon: brown, Oxygen: red.

Aragonite. Aragonite is the high pressure polymorph of calcium carbonate. Calcite and aragonite are by far the most abundant calcium carbonate modification. Since magnesium ions favor the formation of aragonite, marine systems mainly precipitate aragonite. In contrast to calcite, magnesium cations cannot be incorporated into the crystal lattice because the cation with its small size does not fit into a lattice site with such a high coordination number. Therefore, in magnesium-rich systems, aragonite is more likely to form than calcite. The solubility product of magnesium-rich calcite is greater and it thus dissolves in favor of aragonite.[99–101]

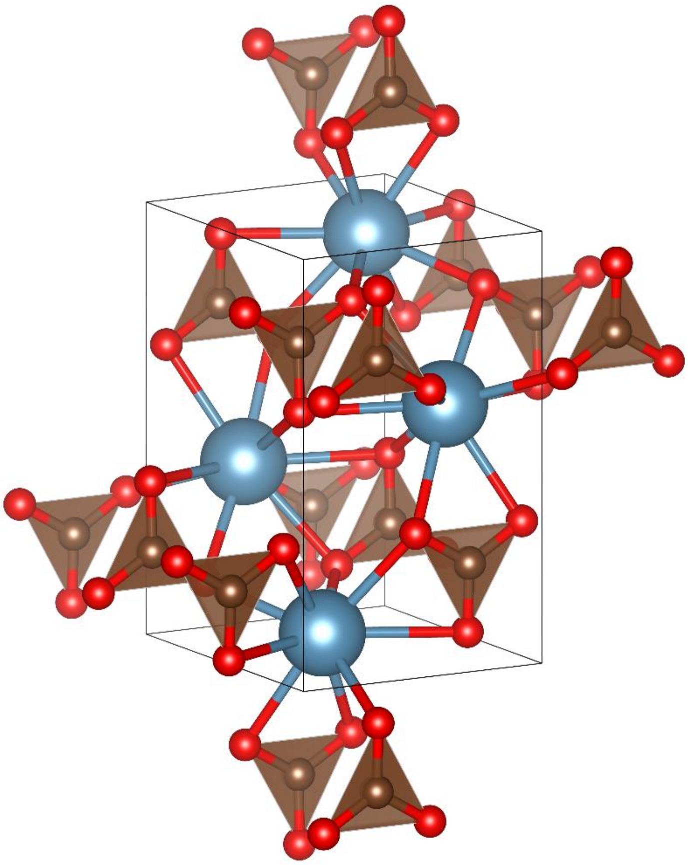

Figure 9. Unit cell of Aragonite. Calcium: blue, Carbon: brown, Oxygen: red.

Calcite. Calcite is the thermodynamic stable polymorph at ambient conditions. The term calcite is derived from the Latin word for lime, calx (gen. calcis) with the suffix -ite. Vast deposits of chalk and limestone, therefore, consist mainly of calcite. Sedimentary rock exhibits approximately 10% limestone. Calcite is known as "Doppelspat", because of its optical properties. Light passing through a calcite single crystal results in double refraction. The phenomenon is described by birefringence which is the property of a material with a refractive index dependent on the polarization and propagation direction of light. Further, calcite is often the major constituent of the shells of marine organisms, e.g., the shells of bivalves, sponges, coccoliths.[102]

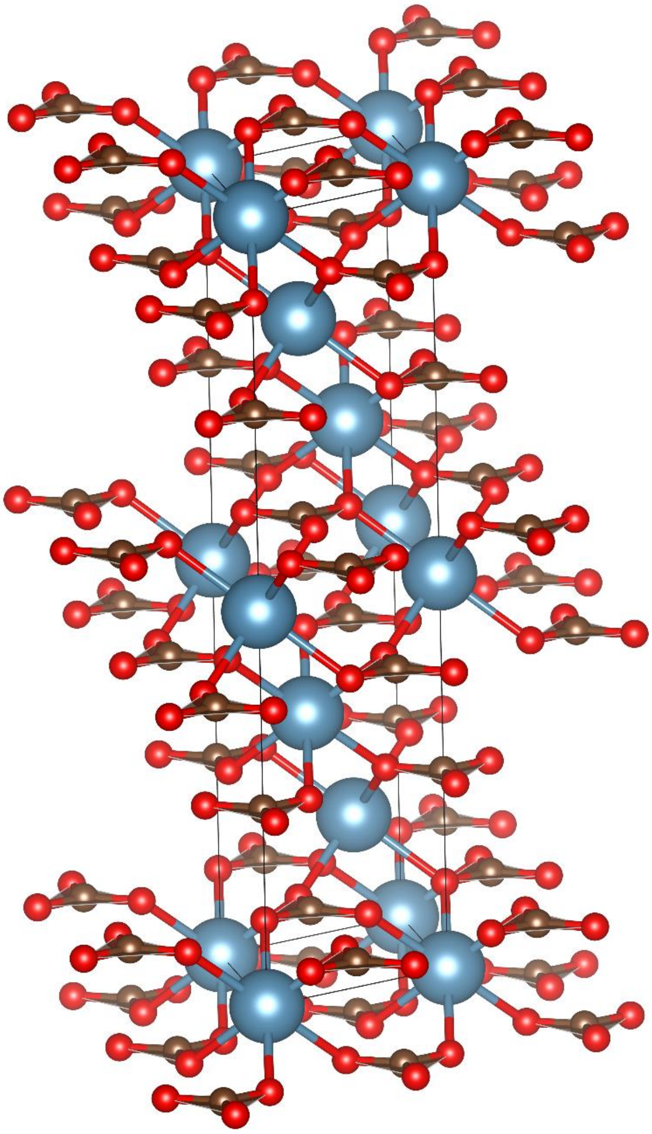

Figure 10. Unit cell of Calcite. Calcium: blue, Carbon: brown, Oxygen: red.

1.8 Calcium sulfate

For centuries calcium sulfate is essential as a building material and is now one of the most produced inorganic compounds in the world. It occurs in three modifications, in particular the anhydrous polymorph anhydrite, the hemihydrate bassanite and the dihydrate gypsum.[103] Calcium sulfates are found mostly in evaporites in multiple locations around the world as gypsum and anhydrite. These can be quarried by open pit or deep mining. World production of naturally occurring gypsum is about 127 million tons per year.[104] Further, calcium sulfate was even detected on mars.[105,106]

Anhydrite. Anhydrite is the anhydrous modification of calcium sulfate. Above 60 °C it is the most thermodynamic stable phase. Even in geological periods, anhydrite does not react with water. However, hydration can take place, if it is present as a powder.[107,108]

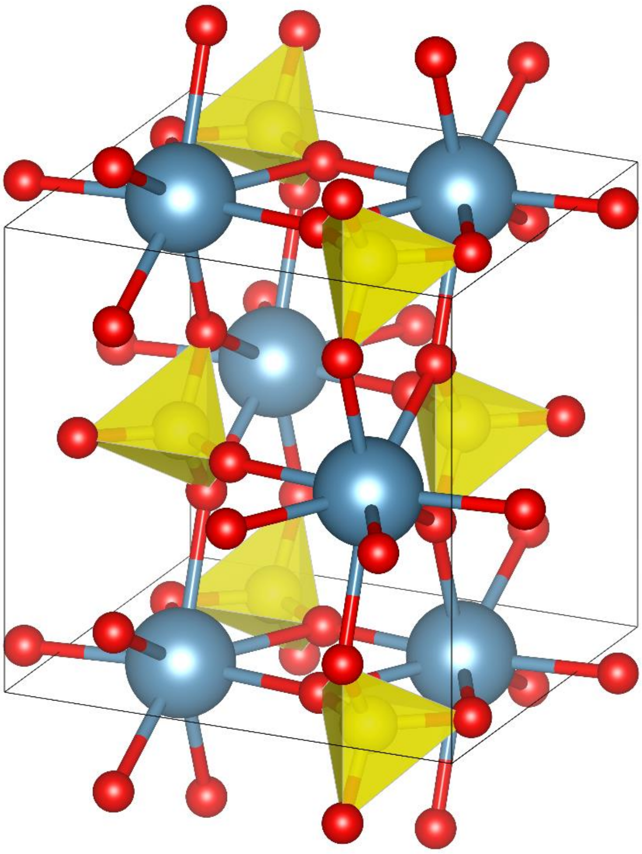

Figure 11. Unit cell of Anhydrite. Calcium: blue, Sulfur: yellow, Oxygen: red.

Bassanite. Bassanite or “plaster of Paris” is one of the most-produced inorganic compounds.[103] It is obtained via thermal dehydration of gypsum at 120-180 °C. This reaction is reversible; therefore, plaster of Paris solidifies by treating with water. It has various applications, *e.g.* toys, fire-proofing materials, in medicine for stetting fractured bones in position.[109]

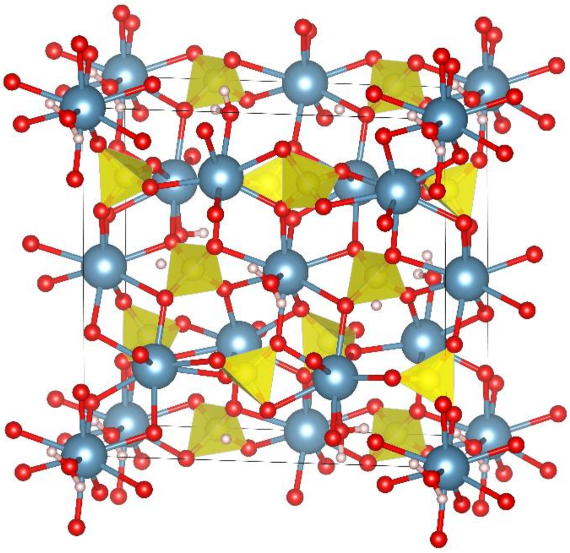

Figure 12. Unit cell of Bassanite. Calcium: blue, Sulfur: yellow, Oxygen: red, Hydrogen: white.

Gypsum. Gypsum is the thermodynamically stable phase at ambient conditions. It is widely used in construction, as a cement additive and fertilizer.[103]

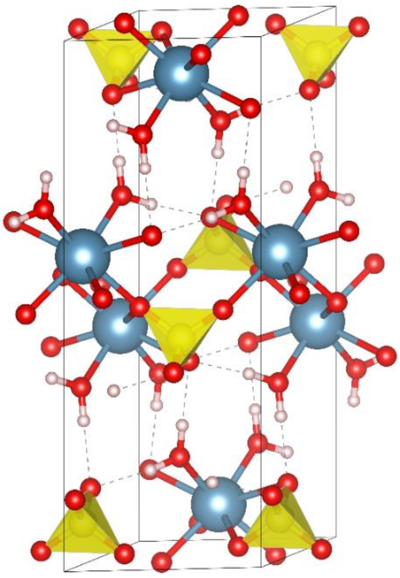

Figure 13. Unit cell of Gypsum. Calcium: blue, Sulfur: yellow, Oxygen: red, Hydrogen: white.

In the following, sulfate-containing phases important for this thesis are described:

Rapidcreekite. Rapidcreekite is a rare mineral with formula of $Ca_2(SO_4)(CO_3)\cdot 4H_2O$. It was discovered in the Rapid Creek - Big Fish area of the northern Yukon Territory, Canada, and has been described in 1986 by Roberts *et al.* The structure is very similar to gypsum. Removal of the sulfate groups in the gypsum structure by carbonate groups coupled with twinning by a twofold rotation about the [100] axis essentially leads to a doubling of the unit cell along the [010] direction. Recently, a sodium-containing precursor was discussed in the crystallization of rapidcreekite.[110,111]

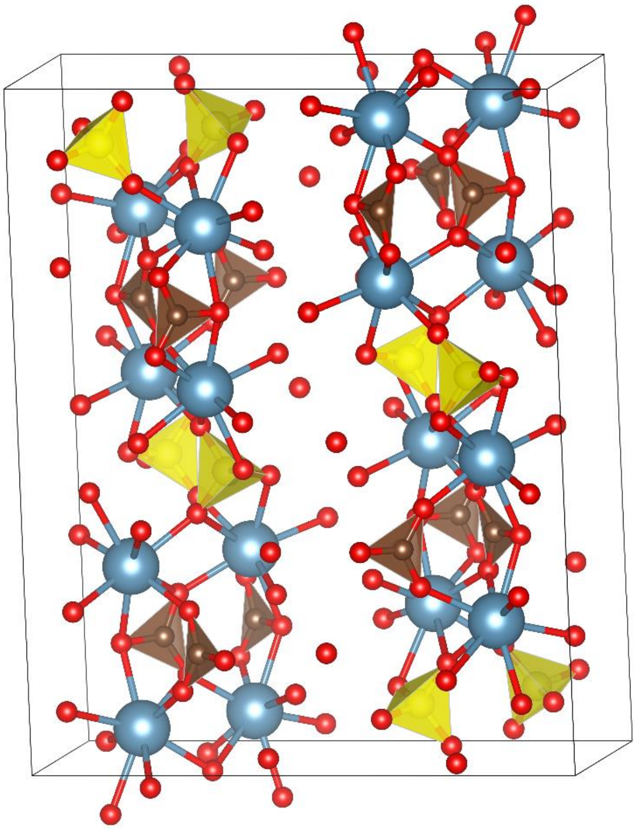

Figure 14. Unit cell of Rapidcreekite. Calcium: blue, Sulfur: yellow, Carbon: brown, Oxygen: red.

Sodium hydrogen sulfate. Sodium hydrogen sulfate is an acidic sodium salt of the sulfuric acid. It can be synthesized by the reaction of sulfuric acid and 1) sodium chloride, 2) sodium hydroxide or a mixture of sodium and sodium hydrogen carbonate. Sodium hydrogen sulfate has various applications like supplement for pH regulation of swimming pools, component of cleaning agents or as additive in food industry. Heating the acidic sodium hydrogen sulfate leads to its dehydration and thus it reacts to sodium disulfate.[112]

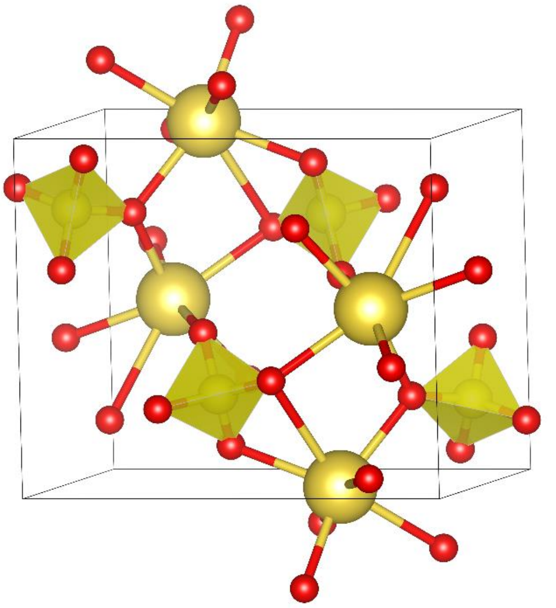

Figure 15. Unit cell of Sodium hydrogen sulfate. Sodium: yellow, Sulfur: yellow, Oxygen: red.

1.9 Calcium orthophosphates

Calcium orthophosphates are the main mineral components of bones and teeth.[113] Phosphorite is sedimentary rock containing orthophosphate phases, in particular mostly hydroxyapatite. In industry, phosphorite is mainly processed into phosphoric acid. Almost 90% of phosphoric acid is used for the production of fertilizer and is therefore essential for global agriculture. Phosphorite is a finite, limited and indispensable resource on earth for the production of fertilizers.[114,115] However, phosphorite deposits will deplete in the future, requiring the use of other phosphate sources to produce sufficient amounts of inorganic fertilizers. Further applications are in *e.g.* food industry, water treatment, toothpastes. The orthophosphates dissolve sparingly in water but can be dissolved in mineral acids.[116]

Hydroxyapatite. Hydroxyapatite is a mineral of the formula $Ca_{10}(PO_4)_6(OH)_2$. It is a member of the apatite group whose general formula of the most common compound is $Ca_{10}(PO_4)_6(F,Cl,OH)_2$. The least soluble orthophosphate Hydroxyapatite is formed preferentially under neutral or basic conditions.[117] However, in minerals even in basic conditions non-stoichiometric compounds are present, indicating calcium deficient hydroxyapatite. In acidic conditions, minerals like brushite $CaHPO_4{\cdot}H_2O$ or octacalcium phosphate $Ca_8H_2(PO_4)_6{\cdot}5H_2O$ are often encountered.[118] Additionally, a carbonate substituted apatite similar to dahllite $Ca_5(PO_4,CO_3)_3(OH)$ is suggested as a potential component for bone regeneration.[119,120]

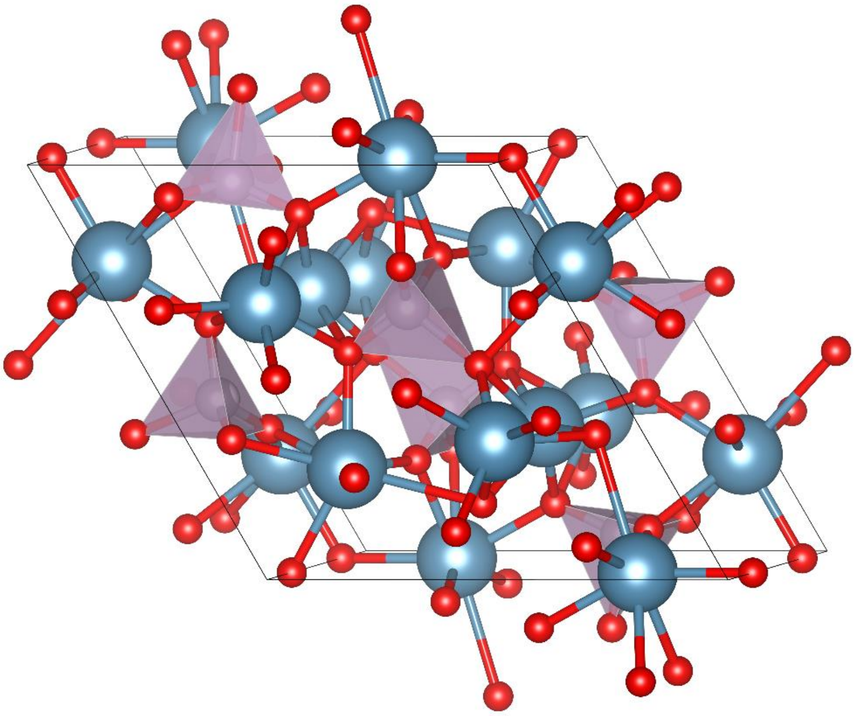

Figure 16. Unit cell of Hydroxyapatite. Calcium: blue, Phosphor: purple, Oxygen: red.

Tricalciumphosphate. Tricalciumphosphate is not soluble in water. Therefore, it is produced commercially by the reaction with phosphoric acid and slaked lime following annealing. There are three known polymorphs of tricalciumphosphate, in particular the rhombohedral β- and two high temperature forms monoclinic α- and hexagonal α'-.[121,122]

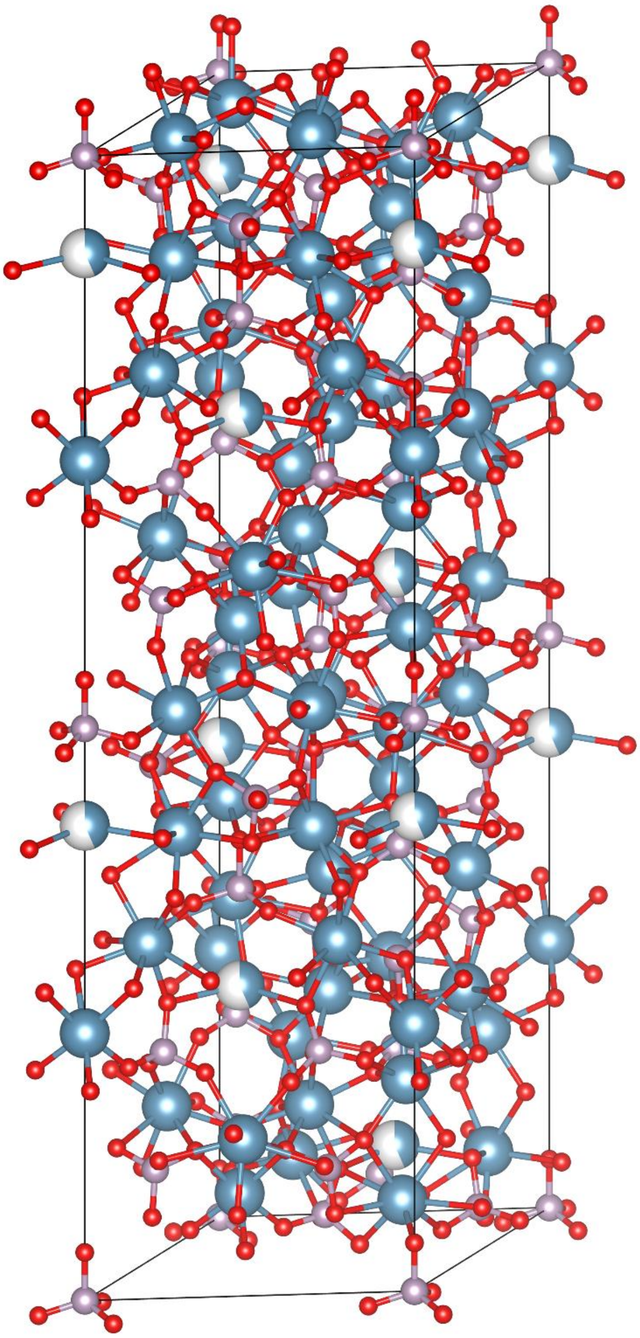

Figure 17. Unit cell of β-Tricalciumphosphate. Calcium: blue, Phosphor: purple, Oxygen: red, Vacancies: white.

Calciumhydrogenphosphate. Calcium hydrogen phosphate occurs naturally as the mineral Brushite $CaHPO_4 \cdot 2H_2O$ and the anhydrous Monetite. Technically, it can be synthesized by reacting phosphoric acid with portlandite $Ca(OH)_2$.[116]

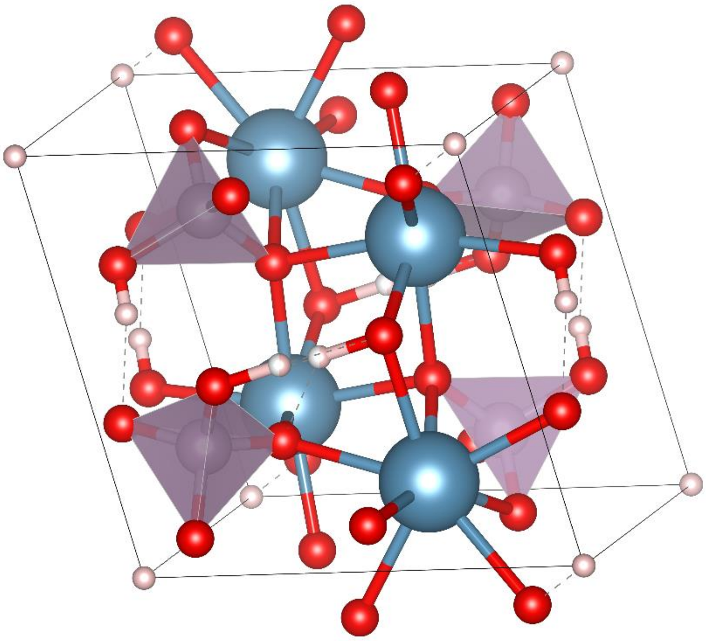

Figure 18. Unit cell of Monetite. Calcium: blue, Phosphor: purple, Oxygen: red, Hydrogen: white.

1.10 References

(1) Baláž, P.; Achimovičová, M.; Baláž, M.; Billik, P.; Cherkezova-Zheleva, Z.; Criado, J. M.; Delogu, F.; Dutková, E.; Gaffet, E.; Gotor, F. J.; Kumar, R.; Mitov, I.; Rojac, T.; Senna, M.; Streletskii, A.; Wieczorek-Ciurowa, K. Hallmarks of Mechanochemistry: From Nanoparticles to Technology. *Chem. Soc. Rev.* **2013**, *42* (18), 7571. https://doi.org/10.1039/c3cs35468g.

(2) Boldyreva, E. Mechanochemistry of Inorganic and Organic Systems: What Is Similar, What Is Different? *Chem. Soc. Rev.* **2013**, *42* (18), 7719. https://doi.org/10.1039/c3cs60052a.

(3) James, S. L.; Adams, C. J.; Bolm, C.; Braga, D.; Collier, P.; Friščić, T.; Grepioni, F.; Harris, K. D. M.; Hyett, G.; Jones, W.; Krebs, A.; Mack, J.; Maini, L.; Orpen, A. G.; Parkin, I. P.; Shearouse, W. C.; Steed, J. W.; Waddell, D. C. Mechanochemistry: Opportunities for New and Cleaner Synthesis. *Chem. Soc. Rev.* **2012**, *41* (1), 413–447. https://doi.org/10.1039/C1CS15171A.

(4) Tan, D.; García, F. Main Group Mechanochemistry: From Curiosity to Established Protocols. *Chem. Soc. Rev.* **2019**, *48* (8), 2274–2292. https://doi.org/10.1039/C7CS00813A.

(5) Leukel, S.; Panthöfer, M.; Mondeshki, M.; Kieslich, G.; Wu, Y.; Krautwurst, N.; Tremel, W. Mechanochemical Access to Defect-Stabilized Amorphous Calcium Carbonate. *Chem. Mater.* **2018**, *30* (17), 6040–6052. https://doi.org/10.1021/acs.chemmater.8b02339.

(6) Protesescu, L.; Yakunin, S.; Nazarenko, O.; Dirin, D. N.; Kovalenko, M. V. Low-Cost Synthesis of Highly Luminescent Colloidal Lead Halide Perovskite Nanocrystals by Wet Ball Milling. *ACS Appl. Nano Mater.* **2018**, *1* (3), 1300–1308. https://doi.org/10.1021/acsanm.8b00038.

(7) Bach, S.; Visnow, E.; Panthöfer, M.; Gorelik, T.; Buzanich, A. G.; Gurlo, A.; Kolb, U.; Emmerling, F.; Lind, C.; Tremel, W. Hydrate Networks under Mechanical Stress - A Case Study for $Co_3(PO_4)_2\cdot 8H_2O$. *Eur. J. Inorg. Chem.* **2016**, *2016* (13–14), 2072–2081. https://doi.org/10.1002/ejic.201501481.

(8) Hüttenrauch, R.; Fricke, S.; Zielke, P. Mechanical Activation of Pharmaceutical Systems. *Pharmaceutical Research* **1985**, *02* (6), 302–306. https://doi.org/10.1023/A:1016397719020.

(9) Stolar, T.; Lukin, S.; Tireli, M.; Sović, I.; Karadeniz, B.; Kereković, I.; Matijašić, G.; Gretić, M.; Katančić, Z.; Dejanović, I.; Michiel, M. di; Halasz, I.; Užarević, K. Control of Pharmaceutical Cocrystal Polymorphism on Various Scales by Mechanochemistry: Transfer from the Laboratory Batch to the Large-Scale Extrusion Processing. *ACS Sustainable Chem. Eng.* **2019**, *7* (7), 7102–7110. https://doi.org/10.1021/acssuschemeng.9b00043.

(10) Kamali, N.; Gniado, K.; McArdle, P.; Erxleben, A. Application of Ball Milling for Highly Selective Mechanochemical Polymorph Transformations. *Org. Process Res. Dev.* **2018**, *22* (7), 796–802. https://doi.org/10.1021/acs.oprd.8b00073.

(11) Bowden, F. P.; Tabor, D. *The Friction and Lubrication of Solids*; Oxford classic texts in the physical sciences; Clarendon Press ; Oxford University Press: Oxford : New York, 2001.

(12) Jost, W. Fast Reactions in Solids, vonF. P. Bowden undA. D. Yoffe. Butterworths Scientific Publications, London 1958. 1. Aufl., IX, 164 S., 82 Abb., 32 Tab., £ 2.0.0. geb. *Angew. Chem.* **1959**, *71* (23), 752–752. https://doi.org/10.1002/ange.19590712309.

(13) Singh', N.; Eckhoff, S. R. Wet Milling of Corn-A Review of Laboratory-Scale and Pilot Plant-Scale Procedures. **1991**, 9.

(14) *Ball Milling Towards Green Synthesis: Applications, Projects, Challenges*; Stolle, A., Ranu, B., Eds.; Green Chemistry Series; Royal Society of Chemistry: Cambridge, 2014. https://doi.org/10.1039/9781782621980.

(15) Friščić, T.; Reid, D. G.; Halasz, I.; Stein, R. S.; Dinnebier, R. E.; Duer, M. J. Ion- and Liquid-Assisted Grinding: Improved Mechanochemical Synthesis of Metal-Organic

Frameworks Reveals Salt Inclusion and Anion Templating. *Angewandte Chemie International Edition* **2010**, *49* (4), 712–715. https://doi.org/10.1002/anie.200906583.

(16) Gower, L. B.; Odom, D. J. Deposition of Calcium Carbonate Films by a Polymer-Induced Liquid-Precursor (PILP) Process. *Journal of Crystal Growth* **2000**, *210* (4), 719–734. https://doi.org/10.1016/S0022-0248(99)00749-6.

(17) Hasa, D.; Schneider Rauber, G.; Voinovich, D.; Jones, W. Cocrystal Formation through Mechanochemistry: From Neat and Liquid-Assisted Grinding to Polymer-Assisted Grinding. *Angew. Chem. Int. Ed.* **2015**, *54* (25), 7371–7375. https://doi.org/10.1002/anie.201501638.

(18) Askew, J. H.; Shepherd, H. J. Mechanochemical Synthesis of Cooperative Spin Crossover Materials. *Chem. Commun.* **2018**, *54* (2), 180–183. https://doi.org/10.1039/C7CC06651A.

(19) Egorov, I. N.; Santra, S.; Kopchuk, D. S.; Kovalev, I. S.; Zyryanov, G. V.; Majee, A.; Ranu, B. C.; Rusinov, V. L.; Chupakhin, O. N. Ball Milling: An Efficient and Green Approach for Asymmetric Organic Syntheses. *Green Chem.* **2020**, *22* (2), 302–315. https://doi.org/10.1039/C9GC03414E.

(20) El-Sayed, T.; Aboelnaga, A.; El-Atawy, M.; Hagar, M. Ball Milling Promoted N-Heterocycles Synthesis. *Molecules* **2018**, *23* (6), 1348. https://doi.org/10.3390/molecules23061348.

(21) Wang, G.-W. Mechanochemical Organic Synthesis. *Chem. Soc. Rev.* **2013**, *42* (18), 7668. https://doi.org/10.1039/c3cs35526h.

(22) Mallick, S.; Pattnaik, S.; Swain, K.; De, P. K.; Saha, A.; Ghoshal, G.; Mondal, A. Formation of Physically Stable Amorphous Phase of Ibuprofen by Solid State Milling with Kaolin. *European Journal of Pharmaceutics and Biopharmaceutics* **2008**, *68* (2), 346–351. https://doi.org/10.1016/j.ejpb.2007.06.003.

(23) Bordet, P.; Bytchkov, A.; Descamps, M.; Dudognon, E.; Elkaïm, E.; Martinetto, P.; Pagnoux, W.; Poulain, A.; Willart, J.-F. Solid State Amorphization of β-Trehalose: A Structural Investigation Using Synchrotron Powder Diffraction and PDF Analysis. *Crystal Growth & Design* **2016**, *16* (8), 4547–4558. https://doi.org/10.1021/acs.cgd.6b00660.

(24) Baxter, E. F.; Bennett, T. D.; Cairns, A. B.; Brownbill, N. J.; Goodwin, A. L.; Keen, D. A.; Chater, P. A.; Blanc, F.; Cheetham, A. K. A Comparison of the Amorphization of Zeolitic Imidazolate Frameworks (ZIFs) and Aluminosilicate Zeolites by Ball-Milling. *Dalton Trans.* **2016**, *45* (10), 4258–4268. https://doi.org/10.1039/C5DT03477A.

(25) Bennett, T. D.; Saines, P. J.; Keen, D. A.; Tan, J.-C.; Cheetham, A. K. Ball-Milling-Induced Amorphization of Zeolitic Imidazolate Frameworks (ZIFs) for the Irreversible Trapping of Iodine. *Chem. Eur. J.* **2013**, *19* (22), 7049–7055. https://doi.org/10.1002/chem.201300216.

(26) Cao, S.; Bennett, T. D.; Keen, D. A.; Goodwin, A. L.; Cheetham, A. K. Amorphization of the Prototypical Zeolitic Imidazolate Framework ZIF-8 by Ball-Milling. *Chem. Commun.* **2012**, *48* (63), 7805. https://doi.org/10.1039/c2cc33773h.

(27) All-Inorganic CsPbBr3 Nanocrystals: Gram-Scale Mechanochemical Synthesis and Selective Photocatalytic CO2 Reduction to Methane | ACS Applied Energy Materials https://pubs.acs.org/doi/abs/10.1021/acsaem.0c00195 (accessed 2020 -12 -01).

(28) Palazon, F.; Ajjouri, Y. E.; Sebastia-Luna, P.; Lauciello, S.; Manna, L.; Bolink, H. J. Mechanochemical Synthesis of Inorganic Halide Perovskites: Evolution of Phase-Purity, Morphology, and Photoluminescence. *J. Mater. Chem. C* **2019**, *7* (37), 11406–11410. https://doi.org/10.1039/C9TC03778K.

(29) Ajjouri, Y. E.; Chirvony, V. S.; Vassilyeva, N.; Sessolo, M.; Palazon, F.; Bolink, H. J. Low-Dimensional Non-Toxic A3Bi2X9 Compounds Synthesized by a Dry Mechanochemical Route with Tunable Visible Photoluminescence at Room Temperature. *J. Mater. Chem. C* **2019**, *7* (21), 6236–6240. https://doi.org/10.1039/C9TC01765H.

(30) Fang, S.; Wang, Y.; Li, H.; Fang, F.; Jiang, K.; Liu, Z.; Li, H.; Shi, Y. Rapid Synthesis and Mechanochemical Reactions of Cesium Copper Halides for Convenient Chromaticity Tuning and Efficient White Light Emission. *J. Mater. Chem. C* **2020**, *8* (14), 4895–4901. https://doi.org/10.1039/D0TC00015A.

(31) Oliveira, P. F. M. de; M. Torresi, R.; Emmerling, F.; C. Camargo, P. H. Challenges and Opportunities in the Bottom-up Mechanochemical Synthesis of Noble Metal Nanoparticles. *Journal of Materials Chemistry A* **2020**, *8* (32), 16114–16141. https://doi.org/10.1039/D0TA05183G.

(32) Gaffet, E. Phase Transition Induced by Ball Milling in Germanium. *Materials Science and Engineering: A* **1991**, *136*, 161–169. https://doi.org/10.1016/0921-5093(91)90451-R.

(33) Weeber, A. W.; Bakker, H. Amorphization by Ball Milling. A Review. *Physica B: Condensed Matter* **1988**, *153* (1–3), 93–135. https://doi.org/10.1016/0921-4526(88)90038-5.

(34) Schwarz, R. B.; Koch, C. C. Formation of Amorphous Alloys by the Mechanical Alloying of Crystalline Powders of Pure Metals and Powders of Intermetallics. *Appl. Phys. Lett.* **1986**, *49* (3), 146–148. https://doi.org/10.1063/1.97206.

(35) Adelfar, R.; Mirzadeh, H.; Ataie, A.; Malekan, M. Amorphization and Mechano-Crystallization of High-Energy Ball Milled Fe Ti Alloys. *Journal of Non-Crystalline Solids* **2019**, *520*, 119466. https://doi.org/10.1016/j.jnoncrysol.2019.119466.

(36) Fink, M. Grundlagen Der Tribochemie. P. A. Thiessen, K. Meyer Und G. Heinicke, 194 S., 157 Abb., 23 Tab., DIN A 4, 1967 Akademie Verlag, Berlin-Ost, 33,— DM. *Materials and Corrosion* **1968**, *19* (2), 188–189. https://doi.org/10.1002/maco.19680190219.

(37) Kaupp, G. Solid-State Molecular Syntheses: Complete Reactions without Auxiliaries Based on the New Solid-State Mechanism. *CrystEngComm* **2003**, *5* (23), 117–133. https://doi.org/10.1039/B303432A.

(38) Kulla, H.; Haferkamp, S.; Akhmetova, I.; Röllig, M.; Maierhofer, C.; Rademann, K.; Emmerling, F. In Situ Investigations of Mechanochemical One-Pot Syntheses. *Angew. Chem. Int. Ed.* **2018**, *57* (20), 5930–5933. https://doi.org/10.1002/anie.201800147.

(39) Deidda, C.; Delogu, F.; Cocco, G. In Situ Characterisation of Mechanically-Induced Self-Propagating Reactions. *Journal of Materials Science* **2004**, *39* (16/17), 5315–5318. https://doi.org/10.1023/B:JMSC.0000039236.48464.8f.

(40) Rodriguez, V. A.; de Carvalho, R. M.; Tavares, L. M. Insights into Advanced Ball Mill Modelling through Discrete Element Simulations. *Minerals Engineering* **2018**, *127*, 48–60. https://doi.org/10.1016/j.mineng.2018.07.018.

(41) Hlungwani, O.; Rikhotso, J.; Dong, H.; Moys, M. H. Further Validation of DEM Modeling of Milling: Effects of Liner Profile and Mill Speed. *Minerals Engineering* **2003**, *16* (10), 993–998. https://doi.org/10.1016/j.mineng.2003.07.003.

(42) Kwan, C. C.; Mio, H.; Qi Chen, Y.; Long Ding, Y.; Saito, F.; Papadopoulos, D. G.; Craig Bentham, A.; Ghadiri, M. Analysis of the Milling Rate of Pharmaceutical Powders Using the Distinct Element Method (DEM). *Chemical Engineering Science* **2005**, *60* (5), 1441–1448. https://doi.org/10.1016/j.ces.2004.10.002.

(43) Mori, H.; Mio, H.; Kano, J.; Saito, F. Ball Mill Simulation in Wet Grinding Using a Tumbling Mill and Its Correlation to Grinding Rate. *Powder Technology* **2004**, *143–144*, 230–239. https://doi.org/10.1016/j.powtec.2004.04.029.

(44) Sato, A.; Kano, J.; Saito, F. Analysis of Abrasion Mechanism of Grinding Media in a Planetary Mill with DEM Simulation. *Advanced Powder Technology* **2010**, *21* (2), 212–216. https://doi.org/10.1016/j.apt.2010.01.005.

(45) Mio, H.; Kano, J.; Saito, F.; Kaneko, K. Optimum Revolution and Rotational Directions and Their Speeds in Planetary Ball Milling. *International Journal of Mineral Processing* **2004**, *74*, S85–S92. https://doi.org/10.1016/j.minpro.2004.07.002.

(46) Giacovazzo, C.; Monaco, H. L.; Viterbo, D.; Scordari, F.; Gilli, G.; Zanotti, G.; Catti, M. Fundamentals of Crystallography; 1992.

(47) Egami, T.; Billinge, S. J. L. *Underneath the Bragg Peaks: Structural Analysis of Complex Materials*; 2012.

(48) Egami, T. Atomic Correlations in Non-Periodic Matter. *Mater. Trans., JIM* **1990**, *31* (3), 163–176. https://doi.org/10.2320/matertrans1989.31.163.

(49) Billinge, S. J. L.; Levin, I. The Problem with Determining Atomic Structure at the Nanoscale. *Science* **2007**, *316* (5824), 561–565. https://doi.org/10.1126/science.1135080.

(50) Andrievskii, A. I.; Nabitovich, I. D.; Voloshchuk, Y. V. Electron Diffraction Study of the Structure of Thin Layers of Amorphous Selenium. *Kristallografiya* **1960**, *5*, 369.

(51) Kaplow, R.; Rowe, T. A.; Averbach, B. L. Atomic Arrangement in Vitreous Selenium. *Physical Review* **1968**, *168* (3), 1068.

(52) Borie, B. X-Ray Diffraction Effects of Atomic Size in Alloys. *Acta Cryst* **1957**, *10* (2), 89–96. https://doi.org/10.1107/S0365110X57000274.

(53) Petkov, V.; Billinge, S. J. L.; Shastri, S. D.; Himmel, B. Polyhedral Units and Network Connectivity in Calcium Aluminosilicate Glasses from High-Energy X-Ray Diffraction. *Phys. Rev. Lett.* **2000**, *85* (16), 3436–3439. https://doi.org/10.1103/PhysRevLett.85.3436.

(54) Petkov, V.; Billinge, S. J. L.; Heising, J.; Kanatzidis, M. G. Application of Atomic Pair Distribution Function Analysis to Materials with Intrinsic Disorder. Three-Dimensional Structure of Exfoliated-Restacked WS2: Not Just a Random Turbostratic Assembly of Layers. *J. Am. Chem. Soc.* **2000**, *122* (47), 11571–11576. https://doi.org/10.1021/ja002048i.

(55) Billinge, S. J. L.; Kanatzidis, M. G. Beyond Crystallography: The Study of Disorder, Nanocrystallinity and Crystallographically Challenged Materials with Pair Distribution Functions. *Chem. Commun.* **2004**, No. 7, 749. https://doi.org/10.1039/b309577k.

(56) Coelho, A. A.; Chater, P. A.; Kern, A. Fast Synthesis and Refinement of the Atomic Pair Distribution Function. *J Appl Crystallogr* **2015**, *48* (3), 869–875. https://doi.org/10.1107/S1600576715007487.

(57) Ashby, M. F.; Shercliff, H.; Cebon, D. *Materials: Engineering, Science, Processing and Design*, 1st ed.; Butterworth-Heinemann: Amsterdam ; Boston, 2007.

(58) Shyam, B.; Stone, K. H.; Bassiri, R.; Fejer, M. M.; Toney, M. F.; Mehta, A. Measurement and Modeling of Short and Medium Range Order in Amorphous Ta 2 O 5 Thin Films. *Scientific Reports* **2016**, *6* (1), 32170. https://doi.org/10.1038/srep32170.

(59) O'Quinn, E. C.; Sickafus, K. E.; Ewing, R. C.; Baldinozzi, G.; Neuefeind, J. C.; Tucker, M. G.; Fuentes, A. F.; Drey, D.; Lang, M. K. Predicting Short-Range Order and Correlated Phenomena in Disordered Crystalline Materials. *Sci. Adv.* **2020**, *6* (35), eabc2758. https://doi.org/10.1126/sciadv.abc2758.

(60) Wei, D.; Yang, J.; Jiang, M.-Q.; Dai, L.-H.; Wang, Y.-J.; Dyre, J. C.; Douglass, I.; Harrowell, P. Assessing the Utility of Structure in Amorphous Materials. *J. Chem. Phys.* **2019**, *150* (11), 114502. https://doi.org/10.1063/1.5064531.

(61) Keen, D. A.; Goodwin, A. L. The Crystallography of Correlated Disorder. *Nature* **2015**, *521* (7552), 303–309. https://doi.org/10.1038/nature14453.

(62) Morandeau, A. E.; White, C. E. Role of Magnesium-Stabilized Amorphous Calcium Carbonate in Mitigating the Extent of Carbonation in Alkali-Activated Slag. *Chem. Mater.* **2015**, *27* (19), 6625–6634. https://doi.org/10.1021/acs.chemmater.5b02382.

(63) Albéric, M.; Bertinetti, L.; Zou, Z.; Fratzl, P.; Habraken, W.; Politi, Y. The Crystallization of Amorphous Calcium Carbonate Is Kinetically Governed by Ion Impurities and Water. *Adv. Sci.* **2018**, *5* (5), 1701000. https://doi.org/10.1002/advs.201701000.

(64) Wełnic, W.; Pamungkas, A.; Detemple, R.; Steimer, C.; Blügel, S.; Wuttig, M. Unravelling the Interplay of Local Structure and Physical Properties in Phase-Change Materials. *Nature Materials* **2006**, *5* (1), 56–62. https://doi.org/10.1038/nmat1539.

(65) Du, P.; Kokhan, O.; Chapman, K. W.; Chupas, P. J.; Tiede, D. M. Elucidating the Domain Structure of the Cobalt Oxide Water Splitting Catalyst by X-Ray Pair Distribution Function Analysis. *J. Am. Chem. Soc.* **2012**, *134* (27), 11096–11099. https://doi.org/10.1021/ja303826a.

(66) Schubert, E. F.; Miller, D. L. Doping in III–V Semiconductors. *Physics Today* **2008**, *47* (10), 71. https://doi.org/10.1063/1.2808673.

(67) Izyumskaya, N.; Alivov, Y.-I.; Cho, S.-J.; Morkoç, H.; Lee, H.; Kang, Y.-S. Processing, Structure, Properties, and Applications of PZT Thin Films. *Critical Reviews in Solid State and Materials Sciences* **2007**, *32* (3–4), 111–202. https://doi.org/10.1080/10408430701707347.

(68) Eremenko, M.; Krayzman, V.; Gagin, A.; Levin, I. Advancing Reverse Monte Carlo Structure Refinements to the Nanoscale. *J Appl Cryst* **2017**, *50* (6), 1561–1570. https://doi.org/10.1107/S1600576717013140.

(69) Volmer, M.; Flood, H. Tröpfchenbildung in Dämpfen. *Zeitschrift für Physikalische Chemie* **1934**, *170* (1), 273–285.

(70) Becker, R.; Döring, W. Kinetische Behandlung Der Keimbildung in Übersättigten Dämpfen. *Annalen der Physik* **1935**, *416* (8), 719–752. https://doi.org/10.1002/andp.19354160806.

(71) Kashchiev, D. *Nucleation: Basic Theory with Applications*; Butterworth Heinemann: Oxford ; Boston, 2000.

(72) Sear, R. P. Nucleation: Theory and Applications to Protein Solutions and Colloidal Suspensions. *J. Phys.: Condens. Matter* **2007**, *19* (3), 033101. https://doi.org/10.1088/0953-8984/19/3/033101.

(73) Liu, X. Y. Heterogeneous Nucleation or Homogeneous Nucleation? *The Journal of Chemical Physics* **2000**, *112* (22), 9949–9955. https://doi.org/10.1063/1.481644.

(74) Shiryayev, A. N. On The Statistical Theory of Metal Crystallization. In *Selected Works of A. N. Kolmogorov: Volume II Probability Theory and Mathematical Statistics*; Shiryayev, A. N., Ed.; Mathematics and Its Applications (Soviet Series); Springer Netherlands: Dordrecht, 1992; pp 188–192. https://doi.org/10.1007/978-94-011-2260-3_22.

(75) Barmak, K. A Commentary on: "Reaction Kinetics in Processes of Nucleation and Growth"*. *Metall and Mat Trans A* **2010**, *41* (11), 2711–2775. https://doi.org/10.1007/s11661-010-0421-1.

(76) Avrami, M. Kinetics of Phase Change. I General Theory. *The Journal of Chemical Physics* **1939**, *7* (12), 1103–1112. https://doi.org/10.1063/1.1750380.

(77) Avrami, M. Kinetics of Phase Change. II Transformation-Time Relations for Random Distribution of Nuclei. *The Journal of Chemical Physics* **1940**, *8* (2), 212–224. https://doi.org/10.1063/1.1750631.

(78) Nebel, H. Kontrollierte Fällung von CaCO3 in einem modular aufgebauten Kristallisationsreaktor. **2008**.

(79) Meldrum, F. C.; Cölfen, H. Controlling Mineral Morphologies and Structures in Biological and Synthetic Systems. *Chem. Rev.* **2008**, *108* (11), 4332–4432. https://doi.org/10.1021/cr8002856.

(80) Gbadeyan, O. J.; Adali, S.; Bright, G.; Sithole, B.; Onwubu, S. Optimization of Milling Procedures for Synthesizing Nano-CaCO $_3$ from *Achatina Fulica* Shell through Mechanochemical Techniques. *Journal of Nanomaterials* **2020**, *2020*, 1–9. https://doi.org/10.1155/2020/4370172.

(81) Gattuso, J.-P.; Frankignoulle, M.; Bourge, I.; Romaine, S.; Buddemeier, R. W. Effect of Calcium Carbonate Saturation of Seawater on Coral Calcification. *Global and Planetary Change* **1998**, *18* (1–2), 10. https://doi.org/10.1016/S0921-8181(98)00035-6.

(82) Matschei, T.; Lothenbach, B.; Glasser, F. P. The Role of Calcium Carbonate in Cement Hydration. *Cement Concrete Res.* **2007**, *37* (4), 551–558. https://doi.org/10.1016/j.cemconres.2006.10.013.

(83) Gamelas, J. A. F.; Lourenço, A. F.; Xavier, M.; Ferreira, P. J. Modification of Precipitated Calcium Carbonate with Cellulose Esters and Use as Filler in Papermaking. *Chemical Engineering Research and Design* **2014**, *92* (11), 2425–2430. https://doi.org/10.1016/j.cherd.2014.02.003.

(84) Alvarez, V.; Paulis, M. Effect of Acrylic Binder Type and Calcium Carbonate Filler Amount on the Properties of Paint-like Blends. *Progress in Organic Coatings* **2017**, *112*, 210–218. https://doi.org/10.1016/j.porgcoat.2017.07.023.

(85) Rowell, D. L. *Bodenkunde: Untersuchungsmethoden und ihre Anwendungen*; 1997.

(86) Janzen, H. H. Carbon Cycling in Earth Systems—a Soil Science Perspective. *Agriculture, Ecosystems & Environment* **2004**, *104* (3), 399–417. https://doi.org/10.1016/j.agee.2004.01.040.

(87) Morse, J. W.; Arvidson, R. S.; Lüttge, A. Calcium Carbonate Formation and Dissolution. *Chem. Rev.* **2007**, *107* (2), 342–381. https://doi.org/10.1021/cr050358j.

(88) Leukel, S.; Mondeshki, M.; Tremel, W. Hydrogen Bonding in Amorphous Alkaline Earth Carbonates. *Inorganic Chemistry* **2018**, *57* (17), 11289–11298. https://doi.org/10.1021/acs.inorgchem.8b02170.

(89) Leukel, S.; Panthöfer, M.; Mondeshki, M.; Kieslich, G.; Wu, Y.; Krautwurst, N.; Tremel, W. Trapping Amorphous Intermediates of Carbonates – A Combined Total Scattering and NMR Study. *Journal of the American Chemical Society* **2018**, *140* (44), 14638–14646. https://doi.org/10.1021/jacs.8b06703.

(90) Finnemore, A.; Cunha, P.; Shean, T.; Vignolini, S.; Guldin, S.; Oyen, M.; Steiner, U. Biomimetic Layer-by-Layer Assembly of Artificial Nacre. *Nature Communications* **2012**, *3* (1). https://doi.org/10.1038/ncomms1970.

(91) Gower, L. B. Biomimetic Model Systems for Investigating the Amorphous Precursor Pathway and Its Role in Biomineralization. *Chemical Reviews* **2008**, *108* (11), 4551–4627. https://doi.org/10.1021/cr800443h.

(92) Addadi, L.; Raz, S.; Weiner, S. Taking Advantage of Disorder: Amorphous Calcium Carbonate and Its Roles in Biomineralization. *Adv. Mater.* **2003**, *15* (12), 959–970. https://doi.org/10.1002/adma.200300381.

(93) Raz, S.; Hamilton, P. C.; Wilt, F. H.; Weiner, S.; Addadi, L. The Transient Phase of Amorphous Calcium Carbonate in Sea Urchin Larval Spicules: The Involvement of Proteins and Magnesium Ions in Its Formation and Stabilization. *Advanced Functional Materials* **2003**, *13* (6), 480–486. https://doi.org/10.1002/adfm.200304285.

(94) Marland, G. The Stability of CaCO3·6H2O (Ikaite). *Geochimica et Cosmochimica Acta* **1975**, *39* (1), 83–91. https://doi.org/10.1016/0016-7037(75)90186-6.

(95) Rodriguez-Blanco, J. D.; Shaw, S.; Bots, P.; Roncal-Herrero, T.; Benning, L. G. The Role of Mg in the Crystallization of Monohydrocalcite. *Geochimica et Cosmochimica Acta* **2014**, *127*, 204–220. https://doi.org/10.1016/j.gca.2013.11.034.

(96) Rodriguez-Blanco, J. D.; Shaw, S.; Bots, P.; Roncal-Herrero, T.; Benning, L. G. The Role of PH and Mg on the Stability and Crystallization of Amorphous Calcium Carbonate. *Journal of Alloys and Compounds* **2012**, *536*, S477–S479. https://doi.org/10.1016/j.jallcom.2011.11.057.

(97) Zou, Z.; Habraken, W. J. E. M.; Matveeva, G.; Jensen, A. C. S.; Bertinetti, L.; Hood, M. A.; Sun, C.; Gilbert, P. U. P. A.; Polishchuk, I.; Pokroy, B.; Mahamid, J.; Politi, Y.; Weiner, S.; Werner, P.; Bette, S.; Dinnebier, R.; Kolb, U.; Zolotoyabko, E.; Fratzl, P. A Hydrated Crystalline Calcium Carbonate Phase: Calcium Carbonate Hemihydrate. *Science* **2019**, *363* (6425), 396–400. https://doi.org/10.1126/science.aav0210.

(98) Németh, P.; Mugnaioli, E.; Gemmi, M.; Czuppon, G.; Demény, A.; Spötl, C. A Nanocrystalline Monoclinic CaCO $_3$ Precursor of Metastable Aragonite. *Sci. Adv.* **2018**, *4* (12), eaau6178. https://doi.org/10.1126/sciadv.aau6178.

(99) Beruto, D.; Giordani, M. Calcite and Aragonite Formation from Aqueous Calcium Hydrogencarbonate Solutions: Effect of Induced Electromagnetic Field on the Activity of CaCO3 Nuclei Precursors. *Faraday Trans.* **1993**, *89* (14), 2457. https://doi.org/10.1039/ft9938902457.

(100) Wray, J. L.; Daniels, F. Precipitation of Calcite and Aragonite. *J. Am. Chem. Soc.* **1957**, *79* (9), 2031–2034. https://doi.org/10.1021/ja01566a001.

(101) Zhang, Z.; Xie, Y.; Xu, X.; Pan, H.; Tang, R. Transformation of Amorphous Calcium Carbonate into Aragonite. *Journal of Crystal Growth* **2012**, *343* (1), 62–67. https://doi.org/10.1016/j.jcrysgro.2012.01.025.

(102) *Calciumcarbonat: Von der Kreidezeit ins 21. Jahrhundert.*; Birkhäuser Basel, 2013.

(103) Wang, Y.-W.; Kim, Y.-Y.; Christenson, H. K.; Meldrum, F. C. A New Precipitation Pathway for Calcium Sulfate Dihydrate (Gypsum) via Amorphous and Hemihydrate Intermediates. *Chem. Commun.* **2012**, *48* (4), 504–506. https://doi.org/10.1039/C1CC14210K.

(104) Ropp, R. C. *Encyclopedia of the Alkaline Earth Compounds*; Amsterdam : Elsevier, 2013.

(105) Wray, J. J.; Squyres, S. W.; Roach, L. H.; Bishop, J. L.; Mustard, J. F.; Noe Dobrea, E. Z. Identification of the Ca-Sulfate Bassanite in Mawrth Vallis, Mars. *Icarus* **2010**, *209* (2), 416–421. https://doi.org/10.1016/j.icarus.2010.06.001.

(106) Stawski, T. M.; Besselink, R.; Chatzipanagis, K.; Hövelmann, J.; Benning, L. G.; Van Driessche, A. E. S. Nucleation Pathway of Calcium Sulfate Hemihydrate (Bassanite) from Solution: Implications for Calcium Sulfates on Mars. *J. Phys. Chem. C* **2020**, *124* (15), 8411–8422. https://doi.org/10.1021/acs.jpcc.0c01041.

(107) Bishop, J. L.; Lane, M. D.; Dyar, M. D.; King, S. J.; Brown, A. J.; Swayze, G. A. Spectral Properties of Ca-Sulfates: Gypsum, Bassanite, and Anhydrite. *American Mineralogist* **2014**, *99* (10), 2105–2115. https://doi.org/10.2138/am-2014-4756.

(108) Blounot, C. W.; Dickson, F. W. The Solubility of Anhydrite (CaSO4) in NaCl-H2O from 100 to 450°C and 1 to 1000 Bars. *Geochimica et Cosmochimica Acta* **1969**, *33* (2), 227–245. https://doi.org/10.1016/0016-7037(69)90140-9.

(109) Driessche, A. E. S. V.; Benning, L. G.; Rodriguez-Blanco, J. D.; Ossorio, M.; Bots, P.; García-Ruiz, J. M. The Role and Implications of Bassanite as a Stable Precursor Phase to Gypsum Precipitation. *Science* **2012**, *336* (6077), 69–72. https://doi.org/10.1126/science.1215648.

(110) Cooper, M.; Hawthorne, F. The Crystal Structure of Rapidcreekite, Ca 2 (SO 4)(CO 3)(H 2 O) 4 , and Its Relation to the Structure of Gypsum. *The Canadian Mineralogist* **1996**, *34*.

(111) Onac, B. P.; Effenberger, H. S.; Wynn, J. G.; Povara, I. Rapidcreekite in the Sulfuric Acid Weathering Environment of Diana Cave, Romania. *American Mineralogist* **2013**, *98* (7), 1302–1309. https://doi.org/10.2138/am.2013.4452.

(112) von Plessen, H. Sodium Sulfates. In *Ullmann's Encyclopedia of Industrial Chemistry*; Wiley-VCH Verlag GmbH & Co. KGaA, Ed.; Wiley-VCH Verlag GmbH & Co. KGaA: Weinheim, Germany, 2000; p a24_355. https://doi.org/10.1002/14356007.a24_355.

(113) Dorozhkin, S. V. Calcium Orthophosphates. *Biomatter* **2011**, *1* (2), 121–164. https://doi.org/10.4161/biom.18790.

(114) Walan, P.; Davidsson, S.; Johansson, S.; Höök, M. Phosphate Rock Production and Depletion: Regional Disaggregated Modeling and Global Implications. *Resources, Conservation and Recycling* **2014**, *93*, 178–187. https://doi.org/10.1016/j.resconrec.2014.10.011.

(115) Edixhoven, J. D.; Gupta, J.; Savenije, H. H. G. Recent Revisions of Phosphate Rock Reserves and Resources: A Critique. *Earth Syst. Dynam.* **2014**, *5* (2), 491–507. https://doi.org/10.5194/esd-5-491-2014.

(116) Holleman, A. F.; Wiberg, E.; Wiberg, N. *Lehrbuch der anorganischen Chemie*, 91.-100., verb. u. stark erw. Aufl.; de Gruyter: Berlin, 1985.

(117) Wang, L.; Nancollas, G. H. Calcium Orthophosphates: Crystallization and Dissolution. *Chem. Rev.* **2008**, *108* (11), 4628–4669. https://doi.org/10.1021/cr0782574.

(118) Tseng, Y.-H.; Mou, C.-Y.; Chan, J. C. C. Solid-State NMR Study of the Transformation of Octacalcium Phosphate to Hydroxyapatite: A Mechanistic Model for Central Dark Line Formation. *Journal of the American Chemical Society* **2006**, *128* (21), 6909–6918. https://doi.org/10.1021/ja060336u.

(119) Wopenka, B.; Pasteris, J. D. A Mineralogical Perspective on the Apatite in Bone. *Materials Science and Engineering: C* **2005**, *25* (2), 131–143. https://doi.org/10.1016/j.msec.2005.01.008.

(120) Habraken, W.; Habibovic, P.; Epple, M.; Bohner, M. Calcium Phosphates in Biomedical Applications: Materials for the Future? *Materials Today* **2016**, *19* (2), 69–87. https://doi.org/10.1016/j.mattod.2015.10.008.

(121) Carrodeguas, R. G.; De Aza, S. α-Tricalcium Phosphate: Synthesis, Properties and Biomedical Applications. *Acta Biomaterialia* **2011**, *7* (10), 3536–3546. https://doi.org/10.1016/j.actbio.2011.06.019.

(122) Salinas, A. J.; Vallet-Regí, M. Bioactive Ceramics: From Bone Grafts to Tissue Engineering. *RSC Adv.* **2013**, *3* (28), 11116. https://doi.org/10.1039/c3ra00166k.

2 Chapter 1

The contents of the following chapter are taken and partially adapted from Cryst. Growth Des. 2020, 20, 10, 6831–6846.

2.1 Monitoring a Mechanochemical Reaction Reveals the Formation of a New ACC Defect Variant Containing the HCO3– Anion Encapsulated by an Amorphous Matrix

2.1.1 ABSTRACT

“Amorphous calcium carbonate (ACC) is an important precursor in the biomineralization of crystalline $CaCO_3$. In nature it serves as a storage material or as permanent structural element, whose lifetime is regulated by an organic matrix. The relevance of ACC in materials science is primarily related to our understanding of $CaCO_3$ crystallization pathways and $CaCO_3$/(bio)polymer nanocomposites. ACC can be synthesized by liquid-liquid phase separation, and it is typically stabilized with macromolecules. We have prepared ACC by milling calcite in a planetary ball mill. Ball-milled amorphous calcium carbonate (BM-ACC) was stabilized with monetite ($CaHPO_4$). The addition of phosphate ions from $CaHPO_4$ generates a strained network that hinders recrystallization kinetically. In comparison to wet-chemically prepared ACC, ball-milling forms anhydrous BM-ACC. The amorphization process and the structure of BM-ACC were studied by quantitative Fourier transform infrared spectroscopy and solid state ^{31}P, ^{13}C, and ^{1}H magic angle spinning nuclear magnetic resonance spectroscopy, which are highly sensitive to symmetry changes of the local environment. In the first - and fast - reaction step, the CO_3^{2-} anions are protonated by the HPO_4^{2-} groups. The formation of unprecedented hydrogen carbonate (HCO_3^-) and orthophosphate anions appears to be the driving force of the reaction, because the phosphate group has a higher Coulomb energy and the tetrahedral PO_4^{3-} unit can fill space more efficiently. In a competing second - and slow - reaction step, pyrophosphate anions are formed in a condensation reaction. No pyrophosphates are formed at higher carbonate contents. High strain leads to such a large energy barrier that any reaction is suppressed. Our findings aid in the understanding of the mechanochemical amorphization of calcium carbonate and emphasize the effect of impurities for the stabilization of the amorphous phase. This allowed the synthesis of a new ACC defect variant containing the unique HCO_3^- anion. Our approach outlines a general strategy to obtain new amorphous solids for a variety of carbonate/phosphate systems that offer promise as biomaterials for bone regeneration.

2.1.2 INTRODUCTION

Mechanochemistry has become a tool for the synthesis of new inorganic,[1] organic,[2] and metal–organic compounds.[3] The product range can be extended by using small amounts of solvents or dispersants (liquid-assisted grinding),[4] ionic compounds (ion- and liquid-assisted grinding),[5] or polymers (polymer-assisted grinding) during grinding.[6] Ball-milling is an established strategy for producing out-of-equilibrium structures, and it can be employed for breaking down bulk materials to nano-size.[7,8] Defect formation on a large scale leads to an amorphization of crystalline solids.[9] Elemental germanium[10] or zeolites[11,12] show a loss of crystallinity during ball-milling, and changes of extended hydrate networks have been reported for $Co_3(PO_4)_2 \times 8\ H_2O$.[13] Ball milling can induce an alloying of metals[14] or polymorph changes (e.g., a transformation from the anatase to the rutile phase of TiO_2).[15] Similarly, organic compounds mixtures of organic and inorganic compounds[16] undergo structural changes during mechanochemical treatment. This is of particular interest for pharmaceuticals as the higher solubility of amorphous phases enhances the uptake of drugs with poor water solubility.[17] Mechanochemistry is of particular interest for large applications due to its scalability and the reduced use of solvents, which make it a “green chemistry” technique.[18]

Continuous mechanical stress during ball milling was proposed to trigger unusual reactivity and lead to the formation of transient phases that are different from those accessible in conventional solid state reactions.[19] There is limited evidence for or against this hypothesis. *Ex situ* studies,[20,21] where the reactants are converted and analyzed after the reaction, provide little information about intermediates, kinetics and dynamics during the mechanochemical reaction itself. *In situ* measurements, on the other hand, can provide real-time insight into a ball milling environment.[22–24] Time-resolved X-ray diffraction with synchrotron radiation (PXRD) is the method of choice for elucidating chemical reaction pathways by the structure determination of intermediates whose existence might be deduced only indirectly otherwise. Diffraction, however, provides meaningful information only for crystalline materials. Non-crystalline solids elude structural analysis with diffraction methods. Only local probes, such as vibrational (IR, Raman) and nuclear magnetic resonance (NMR) spectroscopy or total scattering[12,16] can aid in the structural analysis. Since solid state transformations are typically diffusion limited and therefore comparatively slow, a step by step analysis can be used to identify transient phases, where "snapshots" are taken at different stages of the reaction.[25,26] We demonstrate the utility of this approach by unravelling the structure of non-crystalline intermediates from the mechanochemical reaction of calcium carbonate ($CaCO_3$) and calcium hydrogenphosphate (monetite, $CaHPO_4$).

Calcium carbonate is an important biomineral in ascidians and molluscs, and calcium phosphate is an essential constituent of vertebrate hard tissues (bone, dentine, enamel).[27–29] The corresponding amorphous polymorphs play a prominent role in biomineralization.[28,30–33] The transition from amorphous to crystalline phases allows Nature to exert control through ion concentrations (with ion pumps) and organic matrices or molecules.[34] Many research groups have invested substantial efforts to achieve a deep understanding of the mechanism of biomineralization.[35] An application-oriented result of the crystallization mechanisms is the use of amorphous calcium carbonate and phosphate for bone grafting materials or nanocomposites.[36–40] There is a growing interest on the effect of impurities in the local structure of amorphous calcium carbonate (ACC)[41,42] and amorphous calcium phosphate (ACP).[43] Organisms control the metastability of ACC by incorporating additives (like Mg^{2+}, PO_4^{3-} or water).[43] These impurities have strong effects on the local structure of ACC and ACP, and several studies have been carried out to investigate the effect of additives such as magnesium and phosphate ions on ACC.[40–43]

The local structure in ACC is a matter of debate.[44] A "protostructuring" of ACC with respect to different crystalline $CaCO_3$ polymorphs has been proposed,[45,46] and the concept of "polyamorphism" has been considered for biogenic ACC.[44] Although the short-range order in ACC is pH dependent[47] and OH^- groups were found to be incorporated in ACC,[48] there are no indications for the presence of hydrogen carbonate (HCO_3^-) ions in ACC or any hydrated $CaCO_3$ polymorph.[49–52] The synthesis and stabilization of ACC have been pursued by freeze-drying,[53] with polymers[54] and proteins,[55] or foreign ions like Mg^{2+} [56] and phosphate.[43] These approaches start from the Ca^{2+} and CO_3^{2-} ion constituents in aqueous solution, and the crystallization process is stopped at the ACC stage by stabilizing the product kinetically.

Mechanochemical treatment of calcium carbonate has been a topic of previous research.[57–60] The transformation of calcite to its high-pressure polymorph aragonite has been reported in a mechanically operated mortar.[61] The reverse transformation from aragonite to calcite, the thermodynamically stable polymorph, was described later.[62] Likewise, vaterite can be transformed to calcite mechanochemically.[63,64] In an earlier study we have shown that amorphous $CaCO_3$ could be prepared by ball milling only, when Na_2CO_3 (minimum 7.5

mol %) was added to stabilize the metastable ball-milled amorphous calcium carbonate phase (BM-ACC) by cationic defects.[65] It was, however, not possible to obtain other amorphous alkaline earth metal carbonates for metals other than Ca (e.g. Sr and Ba) by cation "doping" with Sr and Ba. Here we show that amorphous alkaline earth carbonates, in particular amorphous calcium carbonate/calcium hydrogen phosphate (aCCP), amorphous strontium carbonate/calcium hydrogen phosphate (aSCP) and amorphous barium carbonate/calcium hydrogen phosphate (aBCP) can be stabilized by mechanical treatment of crystalline alkaline earth metal carbonates (M = Ca, Sr, Ba, Scheme 1) with $CaHPO_4$.

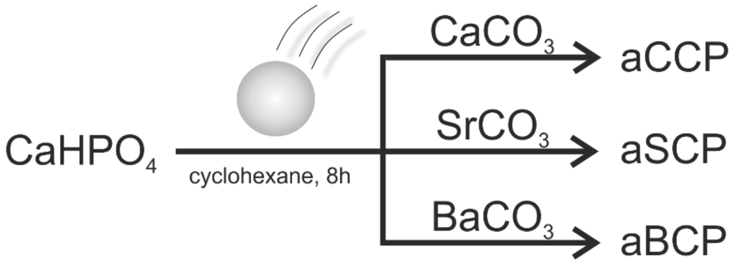

Scheme 1. Summary of the ball-milling experiment

Different compositions of the starting materials were ground in a high-energy planetary ball mill. The amount of monetite was kept constant (1 mmol) and mixed with different amounts of earth alkali carbonates. The composition of the product is expressed in terms of the mole fraction x(carbonate) = $n(CaCO_3)/(n(CaCO_3)+n(CaHPO_4))$ (*e.g.* aCCP (0.2): 1 mmol $CaHPO_4$ and 0.25 mmol $CaCO_3$, i.e. x(carbonate)=0.2). Static spin echo delay NMR measurements revealed that even small mole fractions (x = 0.05) cause large structural changes.

The process of amorphization was studied *ex situ* using solid-state nuclear magnetic resonance (ssNMR) spectroscopy and Fourier transform infrared (FTIR) spectroscopy. The local structure of the amorphous compounds was probed by ssNMR spectroscopy. Complementary structural information about the local structure motifs revealing the coordination sphere for the alkaline earth cations was derived from the analysis of total scattering data using synchrotron radiation. The molecular dynamics was derived from X-ray photon correlation spectroscopy (XPCS). An outstanding feature of the amorphous phases is their extraordinary stability and slow crystallization (up to several months). This is very unexpected as ACC and BM-ACC crystallize within minutes in contact with humidity.[37,66,67] The evaluation of the XPCS data indicates the presence of a highly-strained system in BM-aCCP.

In the first - and fast - reaction step the carbonate anions are protonated by the hydrogen phosphates groups. The formation of hydrogen carbonates (HCO_3^-) and orthophosphates (*i.e.* higher Coulomb energy, the tetrahedral unit can fill space more efficiently) appears to be the driving force of the reaction. This rearrangement reaches mechanochemical equilibrium quickly. In a second reaction step, pyrophosphate anions are formed in a condensation reaction, which competes with proton transfer. Although the energy balance of pyrophosphate formation from two equivalents of hydrogen phosphate ($2HPO_4^{2-}$ -> $P_2O_7^{4-} + H_2O$) may not be strongly disfavored, the kinetics is slow. No pyrophosphates are formed at higher carbonate contents. Strain due to hydrogen-bonded HCO_3^- groups leads to a large energy barrier that suppresses any reaction.

2.1.3 RESULTS AND DISCUSSION

Ball Milling Reaction

The milling process was monitored *ex situ* using ^{1}H- and ^{31}P- single pulse excitation (SPE) magic angle spinning solid-state nuclear magnetic resonance spectroscopy (^{31}P-MAS-ssNMR) at 10 kHz and FTIR spectroscopy. The full width at half maximum (fwhm) of the NMR signals in crystalline solids is a sensitive measure of the uniformity of the local field[68] and thus suitable to follow the changes during the amorphization process.

The milling process of amorphous calcium carbonate/calcium hydrogen phosphate (aCCP 0.2) was stopped after 10 min, 30 min, 60 min, 240 min and 480 min.

Figure19a shows the ^{31}P-MAS-ssNMR spectra of aCCP 0.2 as a function of milling time. During the first 30 minutes of milling the two phosphorous resonances at -1.62 and -0.34 ppm are broad but can still be detected. These singals are associated with two different crystallographic environments of the phosphate ion in crystalline $CaHPO_4$. For longer milling times, signal broadening increases due to a loss of crystalline order. The two individual resonances merge indicating complete amorphization. During the milling process the signal shifts to lower field. After 8 h of milling the resonance becomes asymmetric with a maximum at ~ 3 ppm and a broad shoulder at ~ –10 ppm. The appearance of this shoulder indicates the existence of another process besides amorphization.

The same trend was observed in the ^{1}H-MAS-ssNMR spectra (Figure 19b). The ^{1}H spectrum of crystalline monetite displays three ^{1}H resonances at 12.55, 13.22 and 15.60 ppm associated with different environments of the hydrogen phosphate proton. After 10 min of milling time four additional “solvent” signals can be detected in the ^{1}H spectrum: The signal (i) at 1.22 ppm can be assigned to the presence of the cyclohexane as dispersion medium, (ii) the signal at 4.8 ppm

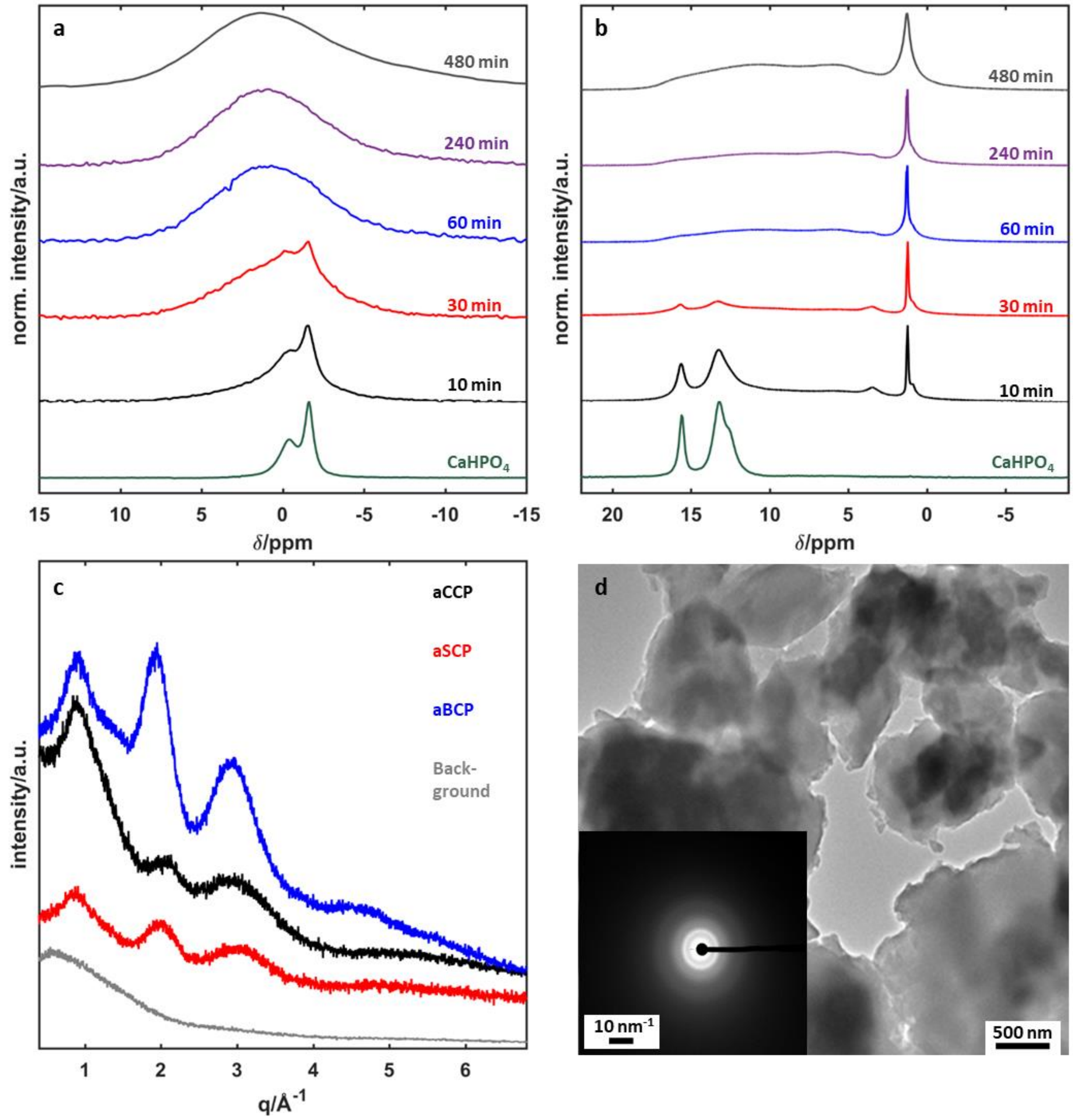

Figure 19. (a) ^{31}P-MAS-ssNMR spectra of aCCP 0.2 as a function of milling time in comparison to crystalline $CaHPO_4$. (b) ^{1}H-MAS-ssNMR spectra of aCCP 0.2 as a function of milling time in comparison to crystalline $CaHPO_4$. The ^{1}H spectrum of crystalline $CaHPO_4$ contains three ^{1}H resonances at 12.55, 13.22 and 15.60 ppm related with different environments of the hydrogen phosphate group. After 10 min of milling solvent signals (1.22 ppm: cyclohexane, 4.8 ppm: water, 0.88 and 3.52 ppm: ethanol) appear. The signals broaden with milling time. The broad resonance at 11 ppm (8 h) corresponds to a chemical reaction. (c) X-ray powder diffractograms (XRPD) of aCCP 0.5 (black), aSCP 0.5 (red), aBCP 0.5 (blue) after 480 min of milling time.

Background measurement is presented in grey. (d) TEM image of aCCP 0.5 and the associated diffraction pattern after 480 min of milling show complete amorphization.

shows the presence of residual water and (iii) the signals at 0.88 and 3.52 ppm are related to ethanol used in the washing step. These resonances remained unaffected even after drying the sample for 8 h at 40 °C in a vacuum oven (Figure S1, Supporting Information). This indicates that the solvent molecules are encapsulated in nanocavities of the amorphous structure. Increasing the milling time leads to broadening of all signals, related with a loss of order and/or mobility. The appearance of a broad resonance at 11 ppm after 8 h of milling is attributed to changes in the ^1H environment leading to higher shielding of the phosphate proton or to a chemical reaction.

Figure 19c shows the X-ray powder diffractograms (XRPD) of the amorphous alkaline earth metal carbonate phosphates (x(carbonate)= 0.5) after 480 min of milling. The loss of all reflections associated with the starting crystalline components and the simultaneous appearance of modulations characteristic for amorphous materials reveal all samples to be “X-ray amorphous”. However, the pure starting materials, MCO_3 (M = Ca, Sr, Ba) and $CaHPO_4$, cannot be amorphisized completely by ball milling (exemplary for $CaCO_3$ Figure S2a, Supporting Information as well as the Quantification of the remaining crystalline proportion: Table S1). Transmission electron microscopy (TEM) images and the associated diffraction patterns for aCCP 0.5 confirm the complete lack of long-range order. The morphology of the particles (Figure 19d) is very different compared to amorphous carbonates precipitated from solution,[69] and the particles have much larger diameters (up to 1 μm, TEM images of aSCP and aBCP 0.5: Figure S3, Supporting Information.

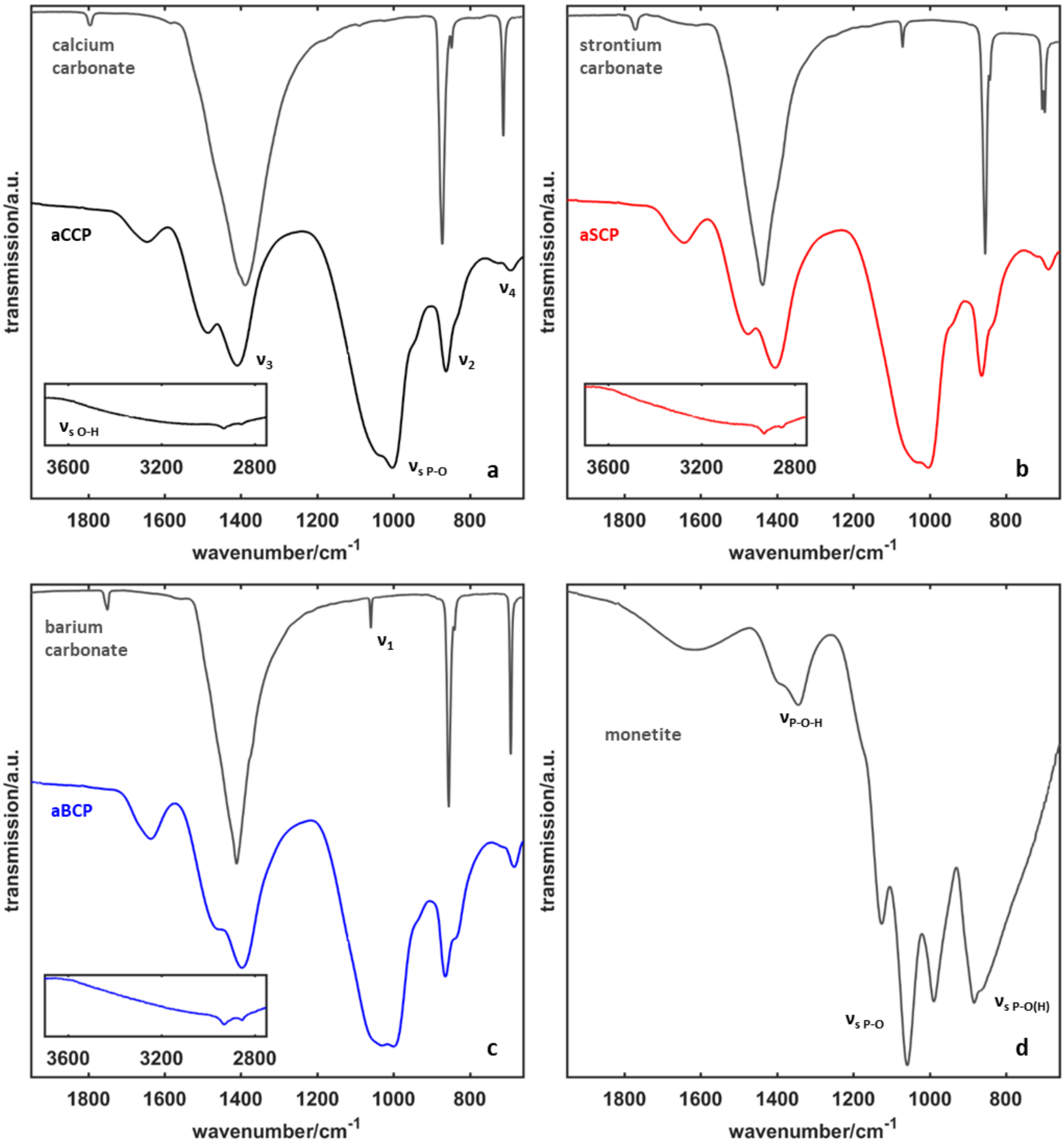

Figure 20. IR spectra of crystalline alkaline earth carbonates and ball-milled amorphous alkaline earth carbonate phosphates ($x_{\text{Carbonate}} = 0.5$) after 480 min of milling time. (a) M = Ca, (b) M = Sr, (c) M = Ba. (d) IR reference spectrum of $CaHPO_4$ (monetite).

Crystalline starting compounds and amorphous products

Figure 20 shows FTIR spectra of amorphous alkaline earth metal carbonate phosphates ($x_{Carbonate} = 0.5$) with their respective crystalline precursors. All samples show the characteristic vibration modes of the carbonate ion in amorphous solids,[70,71] in particular for aCCP 0.5: $\nu_2 \approx 862$ and 836 cm^{-1}, $\nu_3 \approx 1410$ and 1493 cm^{-1}, $\nu_4 \approx 693$ and 728 cm^{-1} (Figure 20a). The expected ν_1 mode of the carbonate ion overlaps with the P-O stretch ($\nu_{s\ P\text{-}O} \approx 1010$

cm^{-1}). Overall, the FTIR spectra of the samples are similar (Figure 20a-c). Therefore, we expect that the mechanism leading to amorphization is independent of the cation. However, the different Pearson hardness[72] of the alkaline earth cations (absolute values for Mg^{2+}: η=32.5; Ca^{2+}: η=19.7; Ba^{2+}:η=12.8) leads to slight shifts in the ν_2 vibration mode to higher wavenumbers and to lower wavenumbers for the ν_3 and ν_4 vibration modes, which is consistent with the size of the cations. Therefore, the different charge density of the cations leads to different ionic bond strengths, and bands appear at different positions (*i.e.* vibrational energies, Table S1, Supporting Information).

For crystalline monetite the bands of the $\nu_{s\text{-}POH}$ vibrational in-plane bending mode at 1348 and 1401 cm^{-1} overlap with the ν_3 carbonate band (Figure 20d).[73] Surprisingly, the pronounced band of the $\nu_{s\ P\text{-}O(H)}$ stretch at 884.2 cm^{-1} in crystalline monetite cannot be detected in any of the amorphous products. Possible explanations are (i) strong shifts of the absorption maxima, (ii) strong signal broadening, or (iii) loss of intensity due to chemical transformation. Furthermore, the $\nu_{s\text{-}PO}$ stretch remained broadened in all samples, which is well known for amorphous phosphates.[43,74] The broad bands at about 3500 cm^{-1} are assigned to $\nu_{s\ O\text{-}H}$ stretching modes. All spectral bands show a significant broadening due to the loss of long-range order compared to those of the crystalline compounds. The bands at 2931 and 2853 cm^{-1} indicate that the dispersant medium cyclohexane is occluded in the amorphous product. The bands are characteristic for the asymmetric and symmetric C-H stretch of the CH_2 groups in cyclohexane.[75]

Phosphate Environment: ^{31}P NMR Spectroscopy

The ratio between the starting materials $CaCO_3$ and $CaHPO_4$ has a great effect on the structure of the amorphous products (Figure 21a). The increase of the carbonate content for a milling time of 480 min results in a shift of the ^{31}P signal of the amorphous product to lower field. For carbonate mole fractions $x > 0.3$ the maximum of the ^{31}P signal at 1.6 ppm remains unchanged (Figure 21b). Thus, the average phosphorus environment depends on the milling time (Figure 19b) and the carbonate:hydrogen phosphate ratio, especially for low carbonate concentrations. For low carbonate contents a shoulder appears at ~ -9 ppm which decreases with increasing carbonate content and disappears almost completely for $x = 0.66$, i.e. the ^{31}P resonance becomes symmetric.

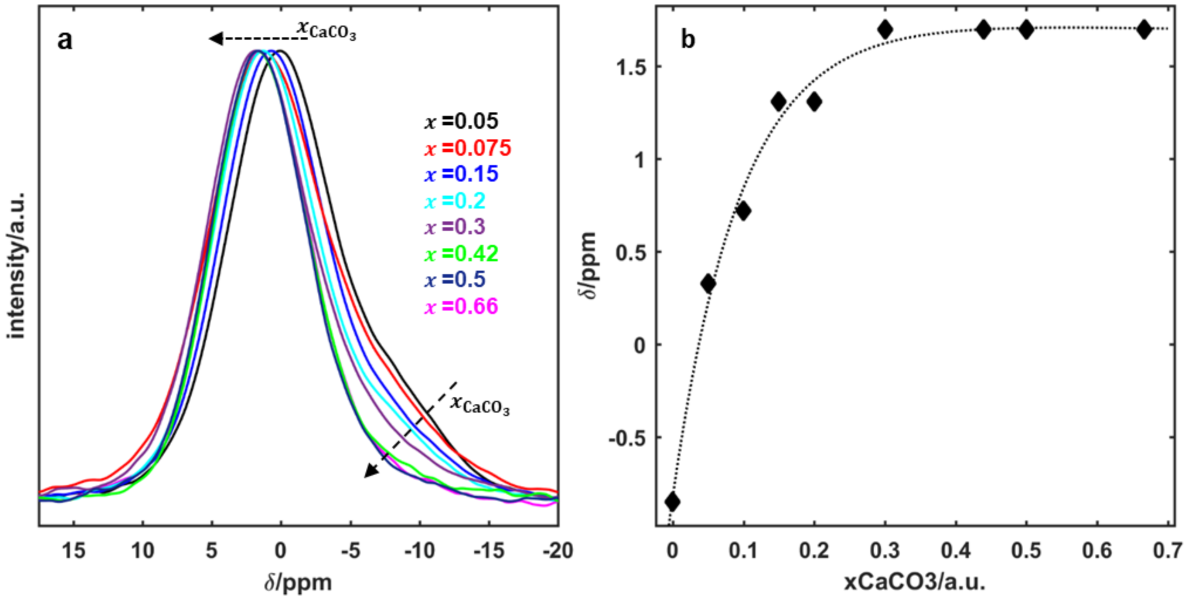

Figure 21. (a) ^{31}P signals of ball-milled amorphous calcium carbonate phosphates after 480 min of milling time. (b) Signal maxima of ball-milled amorphous calcium carbonate phosphates as a function of the carbonate mole fraction $x_{Carbonate}$. The ball-milled $CaHPO_4$ after 480 min of ball milling is included additionally. The dashed line represents a trend line.

To further investigate the results of the amorphization process as a function of the carbonate: hydrogen phosphate ratio a TEDOR (Transferred Echo DOuble Resonance) recoupling experiment at 25 kHz MAS was used.[76] The fast magic angle spinning averages the heteronuclear ^{1}H-^{31}P dipole-dipole couplings; this leads to a loss of the associated information. To reintroduce the heteronuclear coupling interaction in the TEDOR experiment, 180° pulses are applied in the middle of the rotor period. The spectra are recorded as a function of the recoupling time (rotor period). Those recorded with short recoupling times provide information about the strongly coupled heteronuclear pairs and those with longer recoupling times reveal information about long range dipolar couplings or about mobile systems where the dipolar interaction is influenced by the motion.

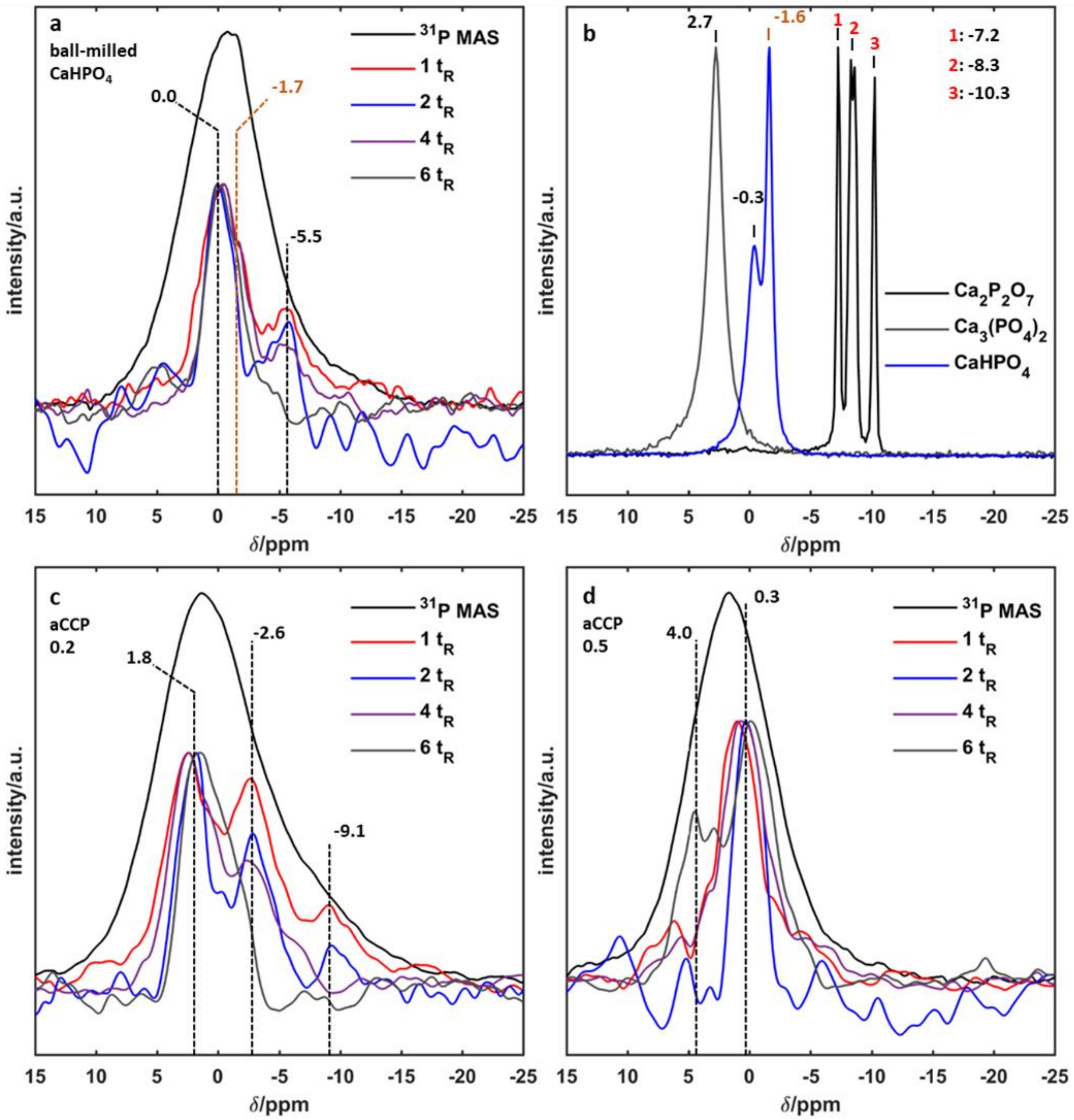

Figure 22. (a) ^{1}H-^{13}P TEDOR spectrum of ball-milled calcium hydrogen phosphate, recorded at 1, 2, 4, and 6 rotor periods (40, 80, 160 and 240 µs recoupling time respectively) after 480 min of ball milling. (b) ^{31}P single pulse excitation (SPE) reference spectra of crystalline $CaHPO_4$, $Ca_3(PO_4)_2$ and $Ca_2P_2O_7$. (c) TEDOR spectra of amorphous aCCP ($x_{Carbonate}$ = 0.2) after 480 min of ball milling and (d) amorphous aCCP ($x_{Carbonate}$ = 0.5) after 480 min of ball milling as a function of the rotor period, with the respective ^{31}P single pulse excitation (SPE) spectra.

Neutron diffraction studies on crystalline calcium hydrogen carbonate revealed the presence of two crystallographically distinct phosphate groups.[73] At ambient conditions one half of the phosphate groups exist as HPO_4^{2-} with one O-H group covalently bound to the central P atom while the other half has one proton in a symmetrically bridging hydrogen bond and one proton statistically distributed between two centrosymmetric positions.[73,77,78] The existence of two phases – an ordered low temperature and a disordered high temperature phase with a phase transition at about 280 K was suggested.[78] Furthermore, the increased ^{1}H linewidth in low-temperature NMR spectra was assumed to result from a reduced proton mobility.[77] The increased temperature for longer milling times would induce disorder and enhance proton transfer, i.e. destabilize the hydrogen bonds. The applied mechanical force would most probably facilitate the transfer of the protons participating in destabilized hydrogen bonds (orange marked signals at -1.7 and -1.6 ppm, Figure 22a and b) to different from the original environments (Figure 22a, signal at -5.5 ppm). This would lead to different phosphorus environments and ^{31}P resonances as observed in the TEDOR spectra (Figure 22) of the ball-milled calcium hydrogen carbonate phosphate. The ^{31}P signal appearing at ~ -0.3 ppm in the crystalline compound is significantly broadened, but its chemical shift is hardly influenced. On the other hand, the sharp ^{31}P resonance at -1.6 ppm in crystalline $CaHPO_4$ disappears almost completely, and a new signal appears at -5.5 ppm. It may be related with the new environment of the mobile protons and thus lead to different ^{31}P shifts.

Figure 4a shows a typical ^{1}H-^{31}P TEDOR spectrum of ball-milled calcium hydrogen phosphate, recorded at 1, 2, 4, and 6 rotor periods (40, 80, 160 and 240 μs recoupling time respectively). Reference spectra of crystalline $CaHPO_4$, $Ca_3(PO_4)_2$ and $Ca_2P_2O_7$ are presented in Figure 22b for comparison. Surprisingly, well defined resonances rather than one broad (amorphous) signal appear in all TEDOR spectra, which implies local order. The ^{31}P SPE reference spectrum is broadened inhomogeneously. In addition, the ^{31}P resonances in the TEDOR spectra (depending on the recoupling time) are shifted by up to 7.5 ppm up- and downfield with respect to the signals for crystalline $CaHPO_4$. These differences - not typical for a simple amorphization - are associated with changes in the chemical (and electronic) environment of the phosphorus atoms when new bonds are formed.

In the TEDOR spectra of the aCCP sample ($x_{Carbonate} = 0.2$) (Figure 22c) three resonances appear at 1.8, -2.6 and -9.1 ppm together with a shoulder at ~ -5.5 ppm. The broadened ^{31}P signal at -9.3 ppm and the shoulder at -5.5 ppm are in harmony with the shift range typical for crystalline $Ca_2P_2O_7$.[79] Thus, it is likely that pyrophosphate was formed as an intermediate in a condensation reaction during the ball milling process. The other ^{31}P shifts are compatible with hydrogen phosphate or orthophosphate units from the reference spectra. A higher calcium carbonate content (aCCP = $x_{Carbonate} = 0.5$) (Figure 22d) results in a loss of the signal at -9.1 ppm. All other resonances in the TEDOR spectra are shifted to lower field (i.e. at 0.3, ~2 and 4.0 ppm). By "diluting" the phosphate starting compound with carbonate the mean P–P distance increases, and a condensation reaction is less likely.

In addition, new signals appear at low field, in agreement with the results of the ^{31}P-MAS ssNMR experiments (Figure 21b). Figure S4-8 (Supporting Information) summarize the results of the ^{31}P NMR and TEDOR experiments for x = 0.2 and 0.5 for different alkaline earth metals.

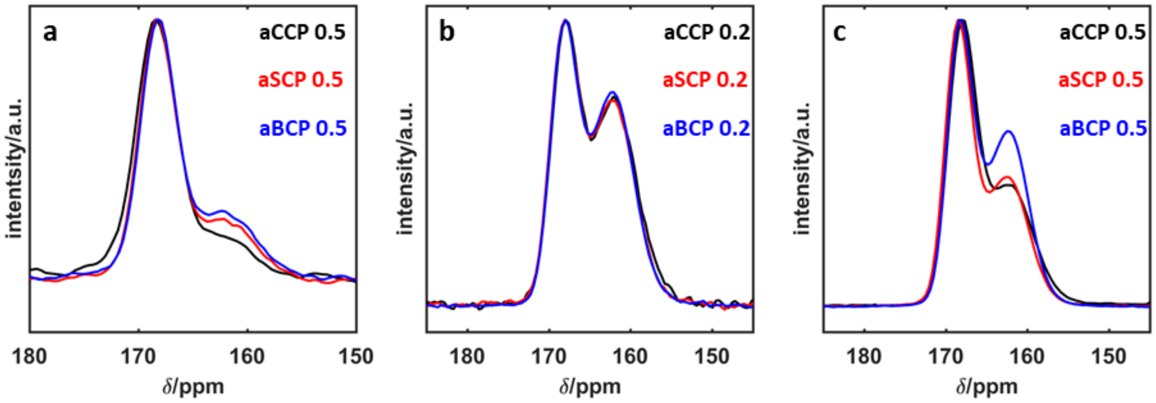

Figure 23. (a) SPE ^{13}C NMR spectra and (b) ^{13}C CP NMR spectra of aMCP (M = Ca, Sr, Ba) ($x_{Carbonate}$ = 0.2,
t_{cp}= 2ms) and (c) ^{13}C CP NMR spectra (($x_{Carbonate}$ = 0.5, t_{cp}= 2ms) (all spectra: 480 min of ball milling).

Carbonate Environment: ^{13}C NMR Spectroscopy

Ball milling leads to pronounced changes in the ^{31}P environments. The ^{13}C environment was probed as a function of the carbonate content and the alkaline earth metal using ^{13}C SPE, cross-polarization (CP) and heteronuclear correlation (HETCOR) NMR experiments, where two different types of nuclei are correlated *via* through-space dipole-dipole couplings. Figure 23a shows the SPE ^{13}C NMR spectra for aCCP, aSCP and aBCP ($x_{Carbonate}$ = 0.2)). Figure 23b presents the corresponding ^{13}C CP NMR spectra and Figure 23c the ^{13}C CP NMR spectra ($x_{Carbonate}$ = 0.5 content). Two broad resonances appear in all spectra. The first signal at ~168 ppm (full width at half maximum (fwhm): 436 Hz) is typical for amorphous carbonates. The width at half maximum decreases for strontium (aSCP: 390 Hz) and barium ion (aBCP: 379 Hz). This reflects the least ordered local environment in the case of aCCP with decreasing order in the order Ba > Sr > Ca.

The second broad resonance appears at ~162 ppm. Such chemical shifts have been reported by Nebel *et al.*[70] for sodium and potassium hydrogen carbonate. Although the existence of alkaline earth metal hydrogen carbonates is well known in solution,[80–82] there are no reports about alkaline earth metal hydrogen carbonate in the solid state. This is assessed from this resonance which is associated with the hydrogen carbonate chemical environment. Therefore, in line with the data of the ^{31}P NMR, it can be envisioned that (i) the carbonate group is protonated in an acid/base reaction by the hydrogen phosphate group or (ii) that this specific "hydrogen carbonate" (bicarbonate) environment is formed by reorganization during the milling process. The ^{13}C SPE spectra show a 7:1 ratio between the signals of amorphous calcium carbonate and the hydrogen carbonate. The hydrogen carbonate content in the samples increases drastically for the heavier group homologues $SrCO_3$ (2.6:1) and $BaCO_3$ (2.4:1). The fwhm for the resonance at ~162 ppm is 549 Hz for aCCP, 690 Hz for aSCP, and 703 Hz for aBCP. This correlates well with the increasing ionic radii of the alkaline earth metals ($r(Ca^{2+})$ = 99 pm; $r(Sr^{2+}$ = 113 pm; $r(Ba^{2+})$ = 135 pm).[83]

The fraction of the hydrogen carbonate signal is significantly higher for samples with low mole fractions of calcium carbonate. To obtain more information about the distances between the protons and the carbonate group in the different samples, 2D HETCOR NMR spectra were recorded.

Figure 24 shows prototypical ^{1}H-^{13}C HETCOR spectra of aCCP 0.5 recorded with contact times of 50 and 2000 μs. The spectra of aSCP and aBCP are displayed in Figure S9 and S10 (Supporting Information). The HETCOR spectrum recorded with a contact time of 50 μs (short range contacts) reveals correlations between the proton signal at 12.2 ppm (bicarbonate) and the signal at 162 ppm (Figure 24c). Long range contacts due to the heteronuclear dipole-dipole couplings are displayed in the HETCOR experiment recorded with 2000 μs contact time. Correlation between the ^{13}C resonances and protons with a shift in the range of the entrapped solvents (especially cyclohexane) appear additionally in the spectrum (4 ppm).

The spectra with short contact times allow different proton environments around the ^{13}C nuclei and thus the carbonate ions to be resolved. The signal of the amorphous carbonate species at 168 ppm correlates strongly with a proton signal of 15.6 ppm (Figure 24b). This signal can be assigned to protons of hydrogen phosphates. In contrast, the signal of the hydrogen carbonate species at 162 ppm correlates weaker with the hydrogen phosphate signal. Furthermore, an additional proton signal at 12.4 ppm appears, which can be assigned to the hydrogen carbonate species. This is an indication that unreacted hydrogen phosphates enclose carbonate ions and hydrogen carbonate ions are surrounded by orthophosphate ions. This assumption becomes even more evident in the HETCOR spectra of aSCP and aBCP due to the higher hydrogen carbonate content (see Supporting Information).

The spectra with long contact times additionally reveal ^{1}H signals in the range of the entrapped solvents (especially cyclohexane). Therefore, the heteronuclear dipole-dipole coupling reaches to ^{1}H atoms of entrapped solvents in the grain boundaries.

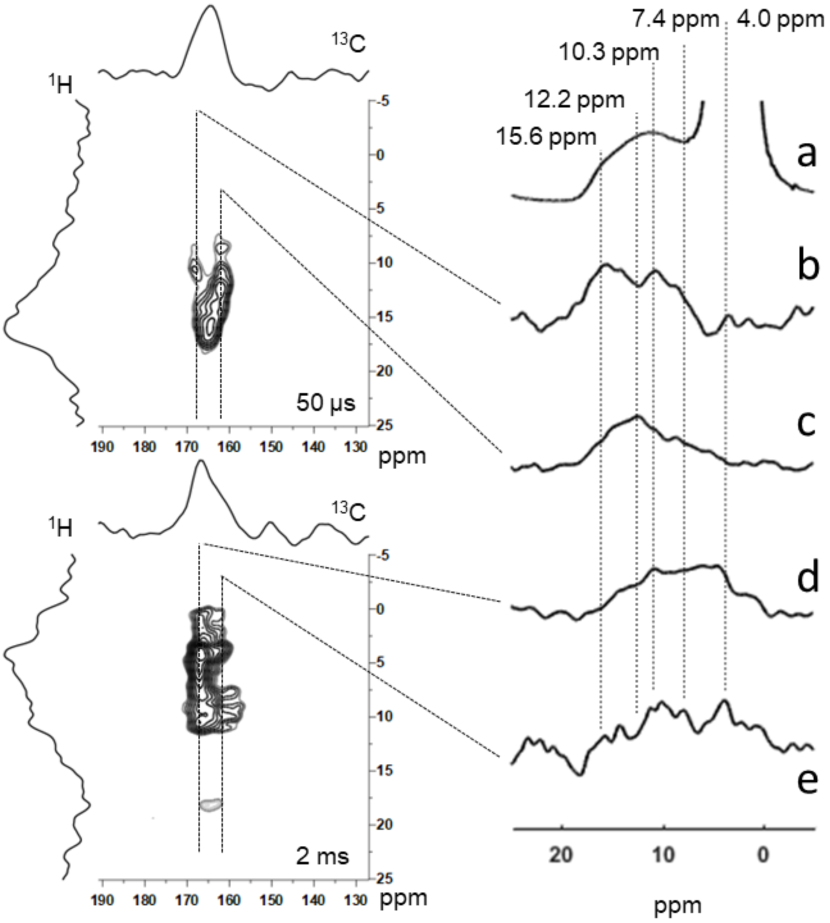

Figure 24. ^1H-^{13}C HETCOR spectra of aCCP ($x_{Carbonate}$ = 0.5) recorded with contact times of 50 and 2000 µs and respective projections, in particular (a) ^1H SPE spectra, (b) projection at 168 ppm with contact times of 50 µs, (c) projection at 162 ppm with contact times of 50 µs, (d) projection at 168 ppm with contact times of 2 ms, (e) projection at 162 ppm with contact times of 2 ms.

Chemical Transformations during Ball-Milling: FTIR Spectroscopy

FTIR spectroscopy provides complementary information to solid state NMR spectroscopy on the chemical transformations of MCO_3/$CaHPO_4$ (M = Ca, Sr, Ba) during ball-milling. ^{13}C enriched samples of aMCP (M = Ca, Sr, Ba) were used to facilitate the assignment of the carbonate or phosphate bands in the FTIR spectra. The higher mass of the ^{13}C isotope shifts the carbonate bands to lower wavenumbers.[84] The difference between samples containing carbon in natural abundance and enriched with ^{13}C is displayed for aCCP for milling time of 480 min in Figure 25. The difference spectrum shows the bands assigned to (or affected by) the carbonate vibration modes. Particularly relevant are the bands at ~1640 and 850 cm^{-1}. The first is related to the $(HO)CO_2$ stretch.[85,86] Since the ν_2 (out of plane) mode of the carbonate ion is not degenerate, the associated band splits in two subbands. One of them at 862.7 cm^{-1} can be assigned to the amorphous calcium carbonate environment, the one at 828.2 cm^{-1} is associated with calcium hydrogen carbonate. Fitting the FTIR spectra for aCCP 0.5 revealed a ratio of 7:1 for the amorphous and hydrogen carbonate species (see Figure S11, Supporting Information) which perfectly matches the results from ssNMR. Unfortunately, a similar comparison was not possible for aCCP ($x_{Carbonate}$ = 0.2) due to the overlap with the $\nu_{s\ P\text{-}O(H)}$ stretch at 884.2 cm^{-1}.

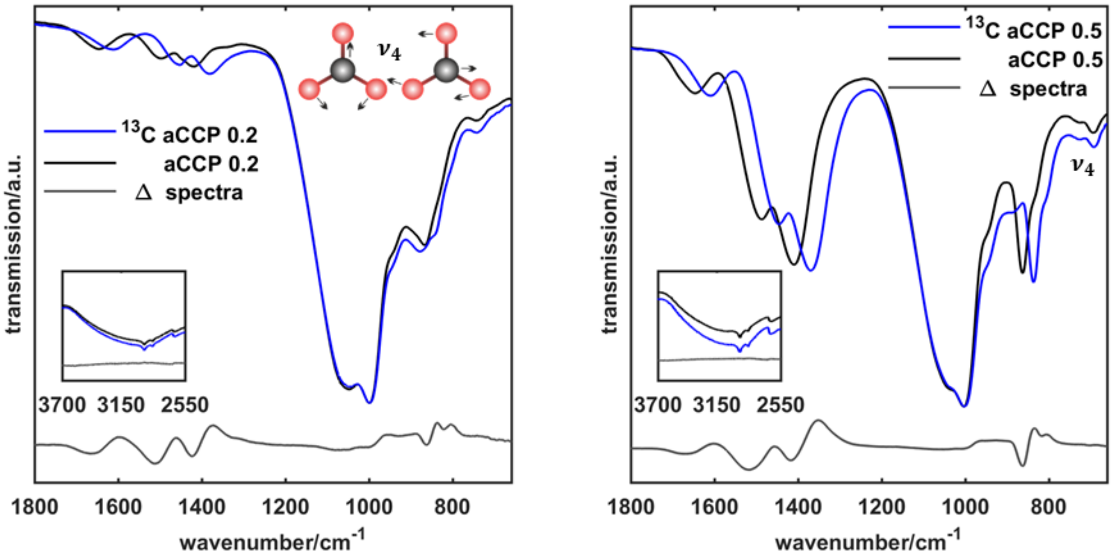

Figure 25. Difference spectra of aCCP (a) with $x_{Carbonate}$ = 0.2 and (b) with $x_{Carbonate}$ = 0.5 enriched with ^{13}C and with C in natural abundance for aCCP. The spectra show the essential bands at ~1640 and 850 cm^{-1} assigned to (or influenced by) the carbonate vibrations. The visualized ν_4 vibration mode shows that the carbon atom has only a small influence on the position of these bands.

The FTIR spectra confirm a proton transfer reaction associated with the formation of a chemical bond (HCO_3^-) during ball-milling according to:

$$CaCO_3 + CaHPO_4 \rightarrow (HCO_3)^- + (CaPO_4)^- + Ca^{2+}.$$

Replacement monetite by tricalcium phosphate did not lead to complete amorphization (Supporting Information S2b). Thus, *proton transfer is crucial for the amorphization.* Remarkably, alkaline earth hydrogen carbonates in solid-state have not been reported so far although they are quite common in solution. Pyrophosphates were detected for aCCP ($x_{Carbonate}$ = 0.2) based on the band at 750 cm^{-1}. This band disappears for higher carbonate contents, in agreement with the NMR results (*vide supra*). Finally, the ν_4 band at 683 and 727 cm^{-1} in aCCP ($x_{Carbonate}$ = 0.5) shows no ^{13}C-related shift, although it can be clearly assigned to the carbonate ion. An explanation is that the ν_4 mode is associated with displacements of the oxygen atoms. Therefore it is nearly independent from the mass of the carbon atom.[84]

Structure: ^{31}P - static spin echo experiments

^{31}P - static spin echo experiments were performed for different compositions x of calcium hydrogen phosphate and alkaline earth carbonates. The Hahn spin echo intensity was measured as a function of evolution time to deduce the homonuclear dipole-dipole interaction. At short evolution times (2τ) the normalized intensities ($\frac{I}{I_o}$) were fitted with a Gaussian function to obtain the second moment $M_{P\text{-}P}$ (Figure S12, Supporting Information):[87–89]

$$\frac{I(2\tau)}{I_o} = \exp - \left[\left(\frac{M_{\mathrm{P-P}}}{2}\right)(2\tau)^2\right] \qquad (1)$$

The NMR second moment reflects the strength of the nuclear magnetic dipole–dipole interaction in solids. The second moment is inversely proportional to the sum of all distances between the nuclei of the same kind and can be calculated on the basis of Van Vleck formula:[90]

$$M_{\mathrm{P-P}} = P\left(\frac{\mu_0}{4\pi}\right)^2 \gamma^4 S(S+1)\hbar^2 \sum_j \frac{1}{r_{ij}^6} \qquad (2)$$

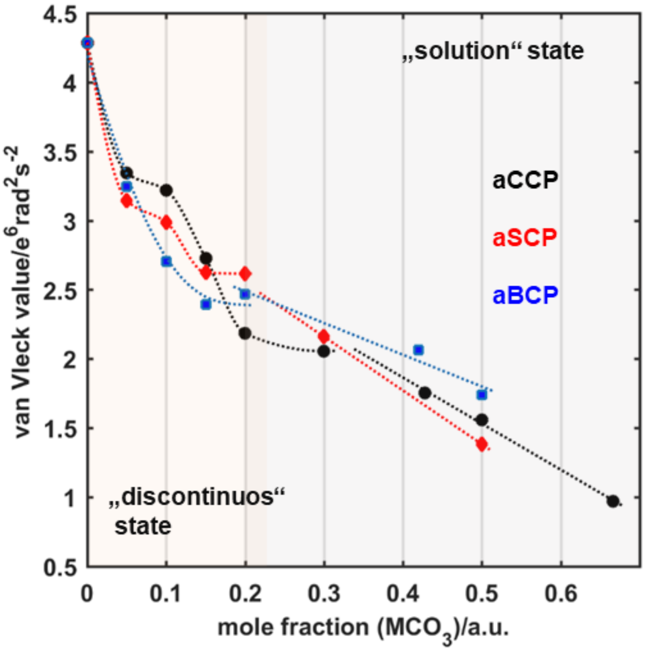

Figure 26. Second moment of aMCP (M = Ca, Sr, Ba) as a function of composition ($x_{\mathrm{Carbonate}}$). ($CaHPO_4$, $x_{\mathrm{Carbonate}} = 0$) has the highest second moment because it is not completely amorphous in the absence of $CaCO_3$. The second moment of crystalline monetite is (for comparison) $4.6 \cdot 10^6\, rad^2 s^{-2}$. The addition small amounts of alkaline earth carbonates lead to a significant decrease of the second moment. The curve is discontinuous, with two steps for calcium and strontium carbonates. This may be rationalized by a chemical reaction (rather than by a physical mixture of the components) for compositions of $x_{\mathrm{Carbonate}} < 0.3$. The curve suggests four different processes to occur: (i) Dilution of the phosphates, (ii) condensation reaction to pyrophosphates, (iii) protonation of carbonate and formation of orthophosphates and (iv) increase of the disorder.

Here, γ is the gyromagnetic ratio of the nuclei studied, S the nuclear spin, r_{ij} the internuclear distance, μ_0 the Bohr magneton, and $\hbar$ the Planck constant divided by 2π. Due to the r^{-6} dependence, 90-95 % of the first two coordination spheres contribute to the second moment.[91]

In systems containing abundant magnetically active nuclei of different kind both homo- as well as heteronuclear dipole-dipole couplings are present. Both interactions have an influence on the Hahn echo intensity, however, esp. for amorphous systems containing solvent molecules (in this case water and cyclohexane) these contributions are difficult to evaluate. Thus, our aim is to follow the trend in the Hahn echo signal intensity and relate it with the composition of the mixture of $CaHPO_4$ and earth-alkali carbonates rather than investigating in detail the coupling contributions. Figure 26 illustrates the dependence of the second moment on the composition of the amorphous alkaline earth carbonate hydrogen phosphate. Monetite shows the highest value of the second moment after mechanochemical treatment because it is not completely amorphous. The second moment of crystalline monetite is (for comparison) with $4.6 \cdot 10^6\ \mathrm{rad}^2\mathrm{s}^{-2}$ only slightly higher. The addition of only 5 mmol of alkaline earth carbonate lead to a significant decrease of the second moment, *i.e.* to a higher average phosphorus-phosphorus distance. The curve has a discontinuous shape with two steps for calcium and strontium carbonates, which can only be explained by a chemical reaction (and not merely by a physical mixture of the components) for compositions up to $x_{\mathrm{Carbonate}} = 0.3$. For compositions with $x_{\mathrm{Carbonate}} > 0.3$ the behavior is linear, compatible with a solid solution. The shape of the curve suggests four different processes to occur: (i) Dilution of the phosphates, (ii) condensation reaction to pyrophosphates, (iii) protonation of carbonate and formation of orthophosphates and finally (iv) increase of disorder. The curves in Figure 8 are in good agreement with the results of the ^{31}P MAS and ^{1}H-^{31}P TEDOR NMR experiments. We assume that due to the reaction of hydrogen phosphate to pyro- and orthophosphates the amorphization becomes more favorable.

X-ray total-scattering experiments were performed to probe the local structure of the amorphous products. *GudrunX4* was used to calculate the pair distribution function (PDF) from this data. Figure 27a shows the PDFs of aCCP 0.5, aSCP 0.5 and aBCP 0.5 with seven significant peaks. The first can be assigned mainly to the phosphorus-oxygen (phosphate ion) distance at 1.52 Å (Figure 27b: Peak 1). We assume that carbon-oxygen (carbonate ion) distances contribute to this peak as well. This can be explained by the shift of the peak to lower distance values depending on the amount of the starting material calcite and thus a higher ratio of carbonate (aCCP 0.1: 1.54 Å, aCCP 0.2: 1.54 Å, aCCP 0.5: 1.52 Å, aCCP 0.6: 1.50 Å). Further, the decrease of the height of the peak with increasing carbonate amount can be explained by the higher amount of the carbonate due to its less neighbor atoms compared to phosphate. However, the effective shift is small as the peak is a superposition of both, the P-O as well as the C-O distances, the latter contributing far less (in comparison to synthetic hydrous ACC: 1.25 Å, Figure S13, Supporting Information) because of the small atomic form factor of both carbon and oxygen which keep the contribution of the C-O pair small. Hoeher et al.[92] reported a C-O distance of 1.3 Å which could also be an explanation for the merged peak. The peak height is not only a measure of the coordination number, but also the total number and product of the atomic form factors.

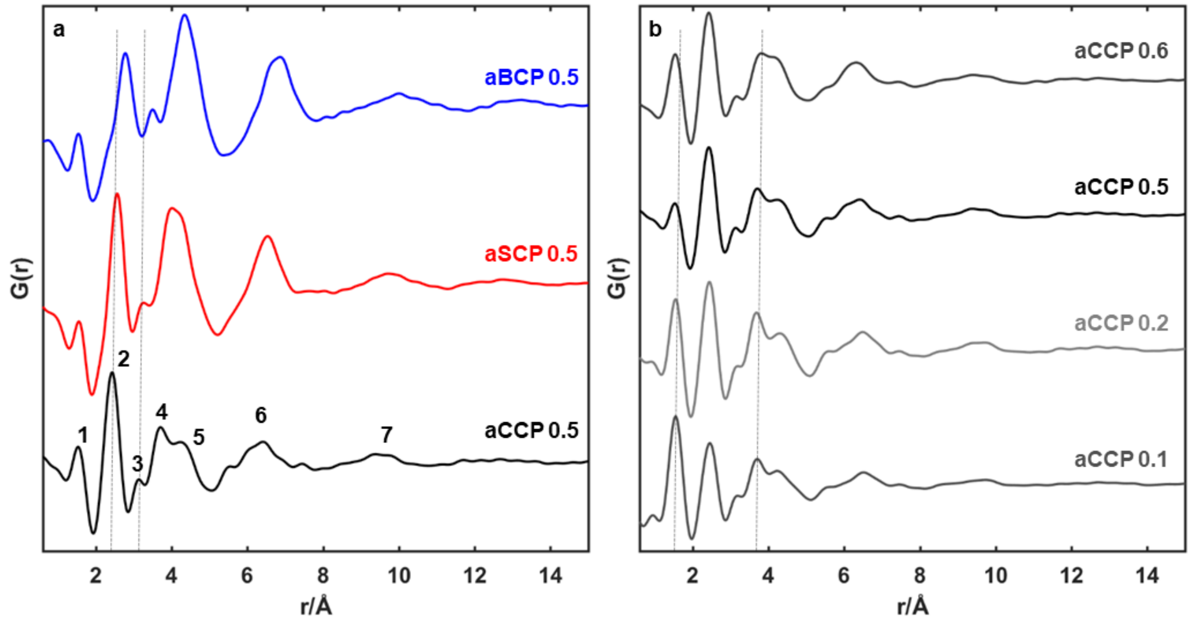

Figure 27. Pair distribution function of amorphous products after 480 min of milling: a) Comparison of the PDF data for aCCP (black), aSCP (red), aBCP (blue) x (carbonate) = 0.5. b) Comparison of the PDF data for aCCP with different x(carbonate) = 0.1-0.6. The grey dotted lines highlights the shifts of the peaks.

The most pronounced peak at 2.42 Å for aCCP 0.5 is assigned to the metal-oxygen bonds of the phosphate and carbonate ions. As expected, this peak shifts to higher distances with the larger strontium and barium ions (aSCP 0.5: 2.56 Å and aBCP: 2.78 Å) (Figure 27a: Peak 2). Note, that this peak, again, is a superposition. The contribution of the molecular O-O pairs of the phosphate ions is low (as above). Further, only for the PDF of aBCP the peaks split due to the Ba-O and Ca-O pairs (due to the mixture of $BaCO_3$ and $CaHPO_4$). The peak at 3.12 Å for aCCP 0.5 can be assigned most probably to the metal-phosphorus distance (Figure 9a: Peak 3). Since the peak shifts depending on metal cations, a metal is involved in these pairs (aSCP 0.5: 3.26 Å aBCP 0.5: 3.50 Å). In the next peak at 3.66 Å for aCCP 0.5, phosphorus-metal, phosphorus-phosphorus and metal-metal distances are expected to have a large contribution (in comparison to crystalline monetite, Figure 27a: Peak 4).[78] The shift to lower P-P distances compared to crystalline monetite (3.91 Å) indicates changes in the phosphorous coordination sphere and most probably a stressed and distorted system. Furthermore, a variety of different interatomic distances contribute to the higher peaks (4.3 Å, 6.3 Å and 9.42 Å, Figure 9a: Peak 5,6,7), mainly metal-metal distances. The PDF fade out early and become virtually flat at ~10 Å indicating a total lack of translational coherence. The PDF of aSCP and aBCP are in Figure S14 (supporting information).

Dynamics of the Amorphous Alkaline Earth Carbonate Hydrogen Phosphates: X-ray photon correlation spectroscopy

X-ray photon correlation spectroscopy (XPCS) is a powerful tool to probe the dynamics of disordered systems, giving information about the rate of structural rearrangements per unit of time (see Supporting Information for further details about data analysis). XPCS experiments yield relaxation curves from which structural relaxation times and shape factors related to the nature of the dynamics (Figure 28) can be extracted. XPCS confirms the extraordinarily low dynamics in this system, *i.e.* the rate of rearrangements per unit of time is very slow. Values for the structural relaxation time are one to two orders of magnitude higher than those of synthetic hydrous ACC precipitated from solution (see Table 1).[41] Furthermore, and similar to synthetic hydrous ACC, the shape factor β shows extremely high values. In comparison, Brownian molecular motion has a value of one. This is a strong indication for a dynamically highly strained system.[93]

Table 1. Fitted parameters (τ, β) obtained from the intensity auto-correlation functions measured at the start of the experiment, i.e., minimizing the effect of vacuum and related water loss. Relaxation times for the aCCP 0.2 sample cannot be determined precisely, only lower boundary can be established.

Sample	τ (s)	β
aCCP 0.2	>7000	-
aCCP 0.5	756 ± 27	1.69 ± 0.067
aSCP 0.5	1707 ± 133	1.91 ± 0.096
ACC	572 ± 11	1.64 ± 0.041

As discussed by Koishi *et al.*,[41] ACC shows physical aging, *i.e.* τ evolves over time. The same behavior was observed for ball-milled ACC (Figure 28). This can be explained for ACC by the loss of small amounts (few weight %) of water during the measurement due to an active vacuum. These minor changes in the mass of water cannot be detected by the static structure factor S(q), but they can have a large impact on the dynamics. DTA/TG measurements (Figure S15, Supporting Information) showed that ball-milled ACC is almost anhydrous, with water mass losses (temperature range from RT to ~200°C) of <1 % (as opposed to 15-20 % in synthetic hydrous ACC). *Ex situ* measurements for aCCP ($x_{\text{Carbonate}}$ = 0.2) and aCCP ($x_{\text{Carbonate}}$ = 0.5) with and without these vacuum conditions showed a decrease in the mass loss after exposing the samples to vacuum, confirming the hypothesis for the observed aging of the dynamics under active vacuum (Figure S16, Supporting Information). The relatively broad band at about 3000 cm^{-1} in the FTIR spectra can be assigned to the O—H stretch of the hydrogen carbonates and hydrogen phosphates ions (with the exception of CH_2-CH_3 stretching bands between 3000-2800 cm^{-1}). The FTIR spectra of the same samples before and after exposure to vacuum show a lower stability to vacuum of the sample aCCP ($x_{\text{Carbonate}}$ = 0.2), the spectra of the aCCP ($x_{\text{Carbonate}}$ = 0.5) remaining unchanged (Figure S17, Supporting Information). These complementary observations confirm the observed aging response of each of the samples, with a more pronounced aging for the aCCP ($x_{\text{Carbonate}}$ = 0.2) sample (Figure 10).

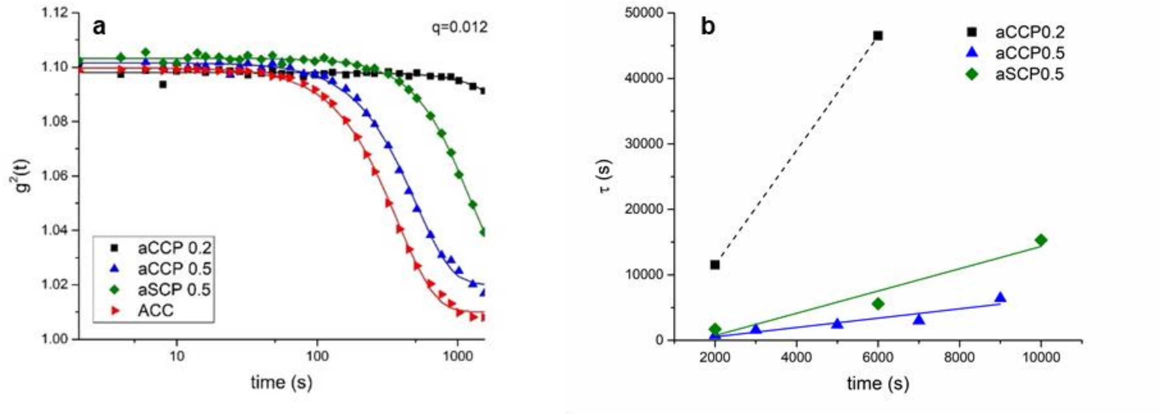

Figure 28. (a) Intensity auto-correlation functions at initial experimental time for synthetic ACC prepared from solution (red triangles), aCCP for $x_{\text{Carbonate}}$ = 0.2 and 0.5 and for aSCP for $x_{\text{Carbonate}}$ = 0.5 at q = 0.012 Å^{-1} (d ≈ 50 nm). (b) Evolution of the relaxation times τ as a function of the experimental time for aCCP for $x_{\text{Carbonate}}$ = 0.2 and 0.5 and for aSCP for $x_{\text{Carbonate}}$ = 0.5.

2.1.4 DISCUSSION

Reactions and Mechanisms

The ^{1}H-^{13}P TEDOR spectrum (see Figure 22a) reveals that only the environment of one phosphorous atom in pure $CaHPO_4$ is significantly affected (loss of the ^{31}P resonance at -1.6 ppm) during the ball milling process, whereas the other resonance signal is only broadened. As a result of a condensation reaction, a signal at -5.5 ppm (typical for pyrophosphates) appears in the ^{1}H-^{31}P TEDOR spectrum. Based on the structural and spectroscopy data the following scenario may be derived for the sequence of events in the ball-milling reaction between $CaHPO_4$ and MCO_3 (M = Ca, Sr, Ba) for different ratios $x_{Carbonate}$ (Figure 29).

The first - and fast - reaction is a proton transfer resulting in a local charge disorder. This forces the system to reorganize. The carbonate anions act in this step as proton acceptors (bases), the hydrogen phosphates act as proton donors (acids). The formation of hydrogen carbonates and orthophosphates (*i.e.* higher Coulomb energy, the tetrahedral unit can fill space more efficiently) appears to be the driving force of the reaction.

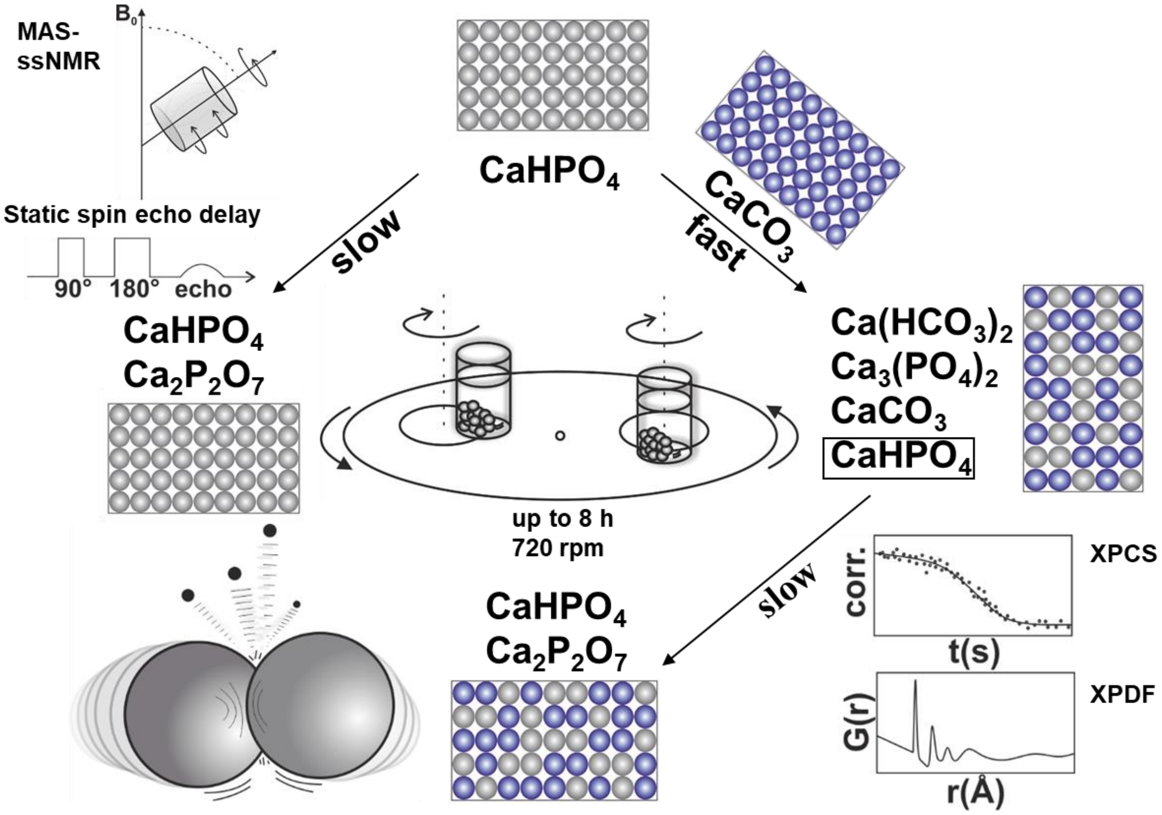

Figure 29. Summary of solid state reactions induced by ball-milling of $CaCO_3$ and $CaHPO_4$.

This rearrangement quickly reaches mechanochemical equilibrium. There are two possible reasons for the observed incomplete reaction to hydrogen carbonate. (a) Only the disordered protons statistically distributed between the two positions of the phosphate unit are involved in the reaction, whereas those protons bound covalently to one phosphate group do not react (activation barrier too high). (b) The newly formed structures may be stabilized by strong hydrogen bonds. The proton transfer reaction leads to local charge disbalances which can be compensated by cation motion. The strong hydrogen-bonded network hinders cation motion (the energy of the ball mill is not sufficient to induce cation "jumps"). The result is a highly strained system.

Additionally, a second -and slow - condensation reaction to pyrophosphates occurs, which competes with proton transfer. Although the energy balance of pyrophosphate formation from two equivalents of hydrogen phosphate ($2HPO_4^{2-} \rightarrow P_2O_7^{4-} + H_2O$) may not be strongly disfavored, the kinetics is slow.[94]

It has been suggested that crystalline monetite has an ordered low temperature phase (space group $P1$) and a disordered high temperature phase (space group $P\overline{1)}$.[78] A second order phase transition (order/disorder transformation) occurs between 273 and 287 K, where only H positions are significantly affected. Therefore, the disordered phase is present at room temperature with small amounts of the ordered phase. We speculate that in aCCP ($x_{Carbonate} = 0.2$) H atoms undergo an order/disorder transformation under vacuum conditions. Since this phase transition only affects protons, no difference can be detected in the structure factor. Furthermore, the proportion of monetite in the aCCP ($x_{Carbonate} = 0.2$) sample is significantly higher.

No pyrophosphates are formed at higher carbonate contents (x(carbonate) > 0.2). Possible reasons are: (i) At higher dilution the mean distance between two HPO_4^{2-} groups (and therefore contact probability and time) decreases. Therefore, it is much less likely that two hydrogen phosphate ions will be able to stay in contact long enough and react. (ii) The formation of orthophosphates (PO_4^{3-}) in the acid-base reaction between CO_3^{2-} and HPO_4^{2-} preceding pyrophosphate condensation leads to an even stronger dilution effect. (iii) The highly-strained system leads to such a large energy barrier that any reaction is suppressed.

2.1.5 Conclusions

In conclusion, we have explored the formation of amorphous anhydrous alkaline earth carbonates in a planetary ball mill. In essence, the phosphate anions stabilize the metastable product through the formation of a highly strained network that hinders recrystallization kinetically. The minimum concentration of phosphate “impurities” for the successful amorphization of calcite was determined by PXRD, ^{31}P and ^{1}H MAS-NMR and electron microcopy. Since diffraction is not suited for studying amorphous solids, the intermediates of the ball-milling reaction were studied by local probes using vibrational spectroscopy, double resonance ^{1}H-^{31}P TEDOR and ^{1}H-^{13}C HETCOR spectroscopy, which are highly sensitive to symmetry changes of the local environment. Mechanistically, CO_3^{2-} anions are protonated *via* an acid-base process by hydrogen phosphate groups in the first - and fast - reaction step of the ball-milling reaction. The concomitant formation of unprecedented hydrogen carbonate (HCO_3^-) anions and orthophosphate groups are the driving force of the reaction, because the phosphate group has a higher Coulomb energy and the tetrahedral PO_4^{3-} unit can fill space more efficiently. In a competing second - and slow - reaction step, pyrophosphate anions are formed in a condensation reaction. No pyrophosphates are formed at higher carbonate contents. The structure and dynamics of the amorphous ball-milled products were studied by vibrational spectroscopy, ^{31}P - static spin echo experiments, pair distribution analysis and X-ray photon correlation spectroscopy, which show the evolution of the phosphorus environment and the strength of the hydrogen bonded network.

Our findings aid not only in the in the understanding of the mechanochemical amorphization of calcium carbonate and the effect of impurities for the stabilization of the amorphous phase. They shed light on elementary reaction steps during ball-milling reactions which are ubiquitous in pharmaceutical or chemical industry, although a mechanistic understanding required for their development is still lacking. Finally, the ball-milling process allowed the synthesis of a new ACC defect variant containing the unique hydrogen carbonate anions.

2.1.6 METHODS

Materials. Calcite (98%, Socal 31, Solvay), monetite ($CaHPO_4$) (>98.5%, anhydrous, Sigma-Aldrich), $SrCO_3$ (99+%, chempur), $BaCO_3$ (99+%, Sigma-Aldrich), β-Tricalcium phosphate (96+%, Sigma-Aldrich), Strontium chloride (anhydrous, 99.5%, Alfa Aesar), Calcium carbonate-^{13}C (99 atom % ^{13}C, isotec), Sodium carbonate (13C 99%, deutero), Barium carbonate (13C 98%, deutero) , cyclohexane (Analytical reagent grade, Fisher Chemicals), ethanol (absolute 99.8+%, Fisher Chemicals) and milliQ deionized water.

Synthesis of Calcium Pyrophosphate. Loaded in a corundum jar, monetite (7.35 mmol) was heated to 800 °C in a horizontal tube furnace oven for 8 h (5 °C/min). Afterward, the resulting product was grinded.

Synthesis of ^{13}C Enriched $SrCO_3$. $SrCl_2$ (2.1 mmol) was dissolved in 50 mL of deionized water. The solution was degassed with an argon stream for 30 minutes. Under argon atmosphere and vigorous stirring ^{13}C enriched Na_2CO_3 (2 mmol) was added to the solution. The reaction solution was stirred for one hour. Afterward, the precipitate was separated by centrifugation and washed with water and ethanol. The product was dried in vacuo.

Synthesis of Amorphous Earth Alkaline Metal Carbonate Hydrogenphosphates. Monetite (0.136 g, 1 mmol) was treated with different amounts of earth alkali metal carbonates (*e.g.* aCCP 0.5: 0.100 g, 1 mmol) in a planetary ball mill (Pulverisette 7 Classic, Fritsch). The starting materials and 10 mL of cyclohexane were transferred together with 3.65 grams of grinding balls (about 1100 balls, 1 mm diameter, ZrO_2) into ZrO_2 grinding jars. The mixture was milled for certain times at 720 rpm. To avoid overheating, alternate 10 minutes of grinding and then a 10 minute rest phase was used. Therefore, 480 min of ball milling results in 950 minutes of reaction time. Afterward, the cyclohexane was removed with a pipette. The product was dispersed in ethanol and separated from the grinding balls by decanting. The product was isolated by centrifugation and dried in vacuo.

2.1.7 Characterization

X-ray Powder Diffraction. X-ray diffractograms were recorded with a STOE Stadi P equipped with a Mythen 1k detector using Mo $K\alpha_1$ radiation (λ=0.7093 Å). The dry samples were prepared between polyvinyl acetate foils in perfluoroether (Fomblin Y, Aldrich). The measurements were performed in the 2θ range from 2° to 45° with a step size of 0.015° (continuous scan, 150 s/deg). Crystalline phases were identified according to the PDF-2 database using Bruker AXS.

ATR-FTIR Spectroscopy. The attenuated total reflection (ATR) FTIR spectra were recorded on a Nicolet iS10 spectrometer (Thermo scientific) using a frequency range from 650 to 4000 cm^{-1} with a resolution of 1.4 cm^{-1} per data point.

Solid-State NMR Spectroscopy. All solid state NMR spectra were recorded on a Bruker Advance 400 DSX NMR spectrometer (Bruker BioSpin GmbH, Rheinstteten, Germany operated by Topspin 1.3, 2007, patchlevel 8) at a ^{1}H frequency of 399.87 MHz, ^{13}C frequency of 100.55 MHz and ^{31}P frequency of 161.87 MHz. A commercial 3 channel 4 mm Bruker probe head at 10 kHz magic angle spinning (MAS) was used for all experiments. The ^{1}H NMR spectra and ^{1}H background corrected spectra were recorded averaging 32 transients with 8 s recycle delay. For all solid-state ^{13}C cross-polarization (CP) magic angle spinning (MAS) NMR experiments, an initial 90° pulse with 4.0 μs length and 5 s recycle delay were used. A ramped CP pulse (from 64 to 100%) with duration of 20 μs, 50 μs, 100 μs, 200 μs, 500 μs, 1 ms, 2 ms, 3 ms, 5 ms and 7 ms was used for recording the CP build-up curves. Two pulse phase modulation (TPPM) ^{1}H decoupling scheme was used while acquiring the ^{13}C signal. 512 transients were averaged for the CP experiments. The spectra were baseline-corrected and a broadening of 30 Hz was applied. Quantitative ^{13}C single pulse excitation experiments allowing full relaxation have been recorded averaging 16 transients with a recycle delay of 2200 s and TPPM heteronuclear decoupling. The spectrum was background corrected and a broadening of 30 Hz was applied. The ^{1}H-^{13}C heteronuclear correlation (HETCOR) 2D NMR spectra were acquired using ^{1}H-^{13}C magnetization transfer with contact times of 50 and 2000 μs and 256 transients/t1. The data points recorded were 1 k (t1) and 96 or 128 (t2) and zero-filled to 4 k (t1) and 256 (t2) before the 2D Fourier transformation. The other parameters were identical to those for the 1D CP NMR experiments. Single pulse excitation ^{31}P experiments were recorded using 60 s recycle delay averaging 16 scans under TPPM heteronuclear decoupling while acquiring the NMR signal. For all ^{31}P cross-polarization (CP) magic angle spinning (MAS) NMR experiments, an initial 90° pulse with 4.0 μs length and 5 s recycle delay were used. A ramped CP pulse (from 64 to 100%) with duration of 20 μs, 50 μs, 100 μs, 250 μs, 500 μs, 1 ms, 2 ms, 3 ms, 4 ms and 5 ms was used for recording the CP build-up curves. Two pulse phase modulation (TPPM) ^{1}H decoupling scheme was used while acquiring the ^{31}P signal. Transients of 64 were averaged for the CP experiments. The spectra were baseline-corrected and a broadening of 30 Hz was applied. The ^{1}H-^{31}P heteronuclear correlation (HETCOR) 2D NMR spectra were acquired using ^{1}H-^{31}P magnetization transfer with contact times of 20 and 2000 μs and 64 transients/t1. The data points recorded were 2 k (t1) and 128 (t2) and zero-filled to 4 k (t1) and 256 (t2) before the 2D Fourier transformation. The other experimental parameters were identical to those for the 1D CP NMR experiments. All ^{1}H-^{31}P transferred echo double resonance (TEDOR) experiments were recorded averaging 512 scans using TPPM heteronuclear decoupling while acquiring the NMR signal. 1, 2, 4, 6, 8 and 10 full rotor periods (□$_{R}$) were used for recoupling the heteronuclear dipolar couplings corresponding resp. to 40 μs, 80 μs, 160 μs, 240 μs, 320 μs and 400 μs recoupling time. A broadening of 30 Hz and background correction were applied. All static ^{31}P Hahn echo experiments were recorded with echo delays of 30, 40, 50, 60, 70, 80, 90 and 100 µs.[95,96] A broadening of 150 Hz and background correction were applied. The spectra were referenced to external adamantine at 1.63 ppm (^{1}H) and 38.5 ppm (^{13}C) and to external NH_4HPO_3 at 0.9 ppm (^{31}P). Spectral deconvolution and fitting the intensity decrease in the spin-echo experiments were performed using self-written MatLab scripts (version 2017b).

Thermal Analysis. Coupled thermogravimetry-differential thermal analysis (TG-DTA) was carried out at a Netzsch STA 449 F3 Jupiter device. About 10 mg of the sample was heated in an alumina cup in argon atmosphere from 50 to 900 °C at a heating rate of 10 K/min.

Transmission Electron Microscopy (TEM). Samples were prepared by drop-casting 20 µL of the respective sample dispersion on 400 mesh carbon copper grids (Plano GmbH, Wetzlar, Germany) and measured with a Technai Spirit G2 at 120 kV acceleration voltage, equipped with a standard 4K CCD camera.

Total Scattering. Total scattering measurements of amorphous earth alkali metal carbonate hy-drogen phosphates were performed at beamline P02.1 at Petra III, DESY, Germany using an X-ray energy of 60 keV ($\lambda = 0.20724$ Å).[97] All samples were prepared in a 0.5 mm borosilicate capillary and measured in transmission mode with a 2D Perkin Elmer area detector with 2048 x 2048 pixels. The exposure time for each sample was 15 min. The resulted 2D images were integrated by using the program DAWNscience.[98] The analysis of the atomic pair distribution function (PDF) was performed utilizing the Gudrun X software using an empty capillary (0.5 mm) for background subtraction with Qmax = 24 Å-1.[99]

X-ray Photon Correlation Spectroscopy. XPCS experiments were performed at the beam line P10 of PETRA III at DESY synchrotron radiation source at Hamburg (Germany), using an incident energy of Xrays of 15 keV. Samples were prepared by loading the powders into 1 mm diameter holes drilled in ~100 µm thickness Al foils. The hydrated, plastic texture of the sample results in a homogeneous filling of all the space. The ~100 µm thickness ensure a transmission of ~9% at 15 keV. Measurements were performed under active vacuum (of $\sim 10^{-3}$ mbar), covering a 0.007-0.013 Å^{-1} q range (small-angle configuration) and with a beam size of 15×15 µm. Series of speckles patterns were collected in transmission geometry by a CCD detector (Andor, 13 µm pixel size). In order to avoid radiation damage of the sample, a delay time (waiting time between two consecutive frames) of 1.9 s was set after each 0.1 s acquisition. Series of acquisitions were taken for at least 2000 frames, covering relaxation times of several hours. These series of measurements were taken by moving the sample by at least twice the beamsize to avoid exposing the same spot for long time, preventing radiation damage and beam induced dynamics. All measurements were carried out at T = 25°C. Details about the XPCS data analysis are given in the Supporting Information."

2.1.8 References

(1) Šepelák, V.; Düvel, A.; Wilkening, M.; Becker, K.-D.; Heitjans, P. Mechanochemical Reactions and Syntheses of Oxides. *Chem. Soc. Rev.* **2013**, *42* (18), 7507. https://doi.org/10.1039/c2cs35462d.

(2) Boldyreva, E. Mechanochemistry of Inorganic and Organic Systems: What Is Similar, What Is Different? *Chem. Soc. Rev.* **2013**, *42* (18), 7719. https://doi.org/10.1039/c3cs60052a.

(3) Garay, A. L.; Pichon, A.; James, S. L. Solvent-Free Synthesis of Metal Complexes. *Chem. Soc. Rev.* **2007**, *36* (6), 846. https://doi.org/10.1039/b600363j.

(4) Bowmaker, G. A. Solvent-Assisted Mechanochemistry. *Chem. Commun.* **2013**, *49* (4), 334–348. https://doi.org/10.1039/C2CC35694E.

(5) Friščić, T.; Reid, D. G.; Halasz, I.; Stein, R. S.; Dinnebier, R. E.; Duer, M. J. Ion- and Liquid-Assisted Grinding: Improved Mechanochemical Synthesis of Metal-Organic Frameworks Reveals Salt Inclusion and Anion Templating. *Angew. Chem. Int. Ed.* **2010**, *49* (4), 712–715. https://doi.org/10.1002/anie.200906583.

(6) Hasa, D.; Schneider Rauber, G.; Voinovich, D.; Jones, W. Cocrystal Formation through Mechanochemistry: From Neat and Liquid-Assisted Grinding to Polymer-Assisted Grinding. *Angew. Chem. Int. Ed.* **2015**, *54* (25), 7371–7375. https://doi.org/10.1002/anie.201501638.

(7) Fecht, H. J.; Hellstern, E.; Fu, Z.; Johnson, W. L. Nanocrystalline Metals Prepared by High-Energy Ball Milling. *Metall. Trans. A* **1990**, *21* (9), 2333–2337. https://doi.org/10.1007/BF02646980.

(8) Annenkov, M.; Blank, V.; Kulnitskiy, B.; Larionov, K.; Ovsyannikov, D.; Perezhogin, I.; Popov, M.; Sorokin, P. Boron Carbide Nanoparticles for High-Hardness Ceramics: Crystal Lattice Defects after Treatment in a Planetary Ball Mill. *J. Eur. Ceram. Soc.* **2017**, *37* (4), 1349–1353. https://doi.org/10.1016/j.jeurceramsoc.2016.12.001.

(9) Weeber, A. W.; Bakker, H. Amorphization by Ball Milling. A Review. *Phys. B Condens. Matter* **1988**, *153* (1–3), 93–135. https://doi.org/10.1016/0921-4526(88)90038-5.

(10) Gaffet, E. Phase Transition Induced by Ball Milling in Germanium. *Mater. Sci. Eng. A* **1991**, *136*, 161–169. https://doi.org/10.1016/0921-5093(91)90451-R.

(11) Cao, S.; Bennett, T. D.; Keen, D. A.; Goodwin, A. L.; Cheetham, A. K. Amorphization of the Prototypical Zeolitic Imidazolate Framework ZIF-8 by Ball-Milling. *Chem. Commun.* **2012**, *48* (63), 7805. https://doi.org/10.1039/c2cc33773h.

(12) Baxter, E. F.; Bennett, T. D.; Cairns, A. B.; Brownbill, N. J.; Goodwin, A. L.; Keen, D. A.; Chater, P. A.; Blanc, F.; Cheetham, A. K. A Comparison of the Amorphization of Zeolitic Imidazolate Frameworks (ZIFs) and Aluminosilicate Zeolites by Ball-Milling. *Dalton Trans.* **2016**, *45* (10), 4258–4268. https://doi.org/10.1039/C5DT03477A.

(13) Bach, S.; Visnow, E.; Panthöfer, M.; Gorelik, T.; Buzanich, A. G.; Gurlo, A.; Kolb, U.; Emmerling, F.; Lind, C.; Tremel, W. Hydrate Networks under Mechanical Stress - A Case Study for $Co_3(PO_4)_2\cdot 8H_2O$. *Eur. J. Inorg. Chem.* **2016**, *2016* (13–14), 2072–2081. https://doi.org/10.1002/ejic.201501481.

(14) Schwarz, R. B.; Koch, C. C. Formation of Amorphous Alloys by the Mechanical Alloying of Crystalline Powders of Pure Metals and Powders of Intermetallics. *Appl. Phys. Lett.* **1986**, *49* (3), 146–148. https://doi.org/10.1063/1.97206.

(15) Šepelák, V.; Bégin-Colin, S.; Le Caër, G. Transformations in Oxides Induced by High-Energy Ball-Milling. *Dalton Trans.* **2012**, *41* (39), 11927. https://doi.org/10.1039/c2dt30349c.

(16) Bordet, P.; Bytchkov, A.; Descamps, M.; Dudognon, E.; Elkaïm, E.; Martinetto, P.; Pagnoux, W.; Poulain, A.; Willart, J.-F. Solid State Amorphization of β-Trehalose: A Structural Investigation Using Synchrotron Powder Diffraction and PDF Analysis. *Cryst. Growth Des.* **2016**, *16* (8), 4547–4558. https://doi.org/10.1021/acs.cgd.6b00660.

(17) Kobayashi, M.; Hattori, Y.; Sasaki, T.; Otsuka, M. Effect of Ball Milling on the Physicochemical Properties of Atorvastatin Calcium Sesquihydrate: The Dissolution Kinetic Behaviours of Milled Amorphous Solids. *J. Pharm. Pharmacol.* **2017**, *69* (1), 15–22. https://doi.org/10.1111/jphp.12636.

(18) *Ball Milling Towards Green Synthesis: Applications, Projects, Challenges*; Stolle, A., Ranu, B., Eds.; Green Chemistry Series; Royal Society of Chemistry: Cambridge, 2014. https://doi.org/10.1039/9781782621980.

(19) Gilman, J. J. Mechanochemistry. *Science* **1996**, *274* (5284), 65–65. https://doi.org/10.1126/science.274.5284.65.

(20) Bellosta von Colbe, J. M.; Felderhoff, M.; Bogdanović, B.; Schüth, F.; Weidenthaler, C. One-Step Direct Synthesis of a Ti-Doped Sodium Alanate Hydrogen Storage Material. *Chem. Commun.* **2005**, No. 37, 4732. https://doi.org/10.1039/b506502j.

(21) Zevalkink, A.; Zeier, W. G.; Pomrehn, G.; Schechtel, E.; Tremel, W.; Snyder, G. J. Thermoelectric Properties of Sr3GaSb3 – a Chain-Forming Zintl Compound. *Energy Environ. Sci.* **2012**, *5* (10), 9121. https://doi.org/10.1039/c2ee22378c.

(22) Halasz, I.; Kimber, S. A. J.; Beldon, P. J.; Belenguer, A. M.; Adams, F.; Honkimäki, V.; Nightingale, R. C.; Dinnebier, R. E.; Friščić, T. In Situ and Real-Time Monitoring of Mechanochemical Milling Reactions Using Synchrotron X-Ray Diffraction. *Nat. Protoc.* **2013**, *8* (9), 1718–1729. https://doi.org/10.1038/nprot.2013.100.

(23) Katsenis, A. D.; Puškarić, A.; Štrukil, V.; Mottillo, C.; Julien, P. A.; Užarević, K.; Pham, M.-H.; Do, T.-O.; Kimber, S. A. J.; Lazić, P.; Magdysyuk, O.; Dinnebier, R. E.; Halasz, I.; Friščić, T. In Situ X-Ray Diffraction Monitoring of a Mechanochemical Reaction Reveals a Unique Topology Metal-Organic Framework. *Nat. Commun.* **2015**, *6* (1), 6662. https://doi.org/10.1038/ncomms7662.

(24) Fischer, F.; Wenzel, K.-J.; Rademann, K.; Emmerling, F. Quantitative Determination of Activation Energies in Mechanochemical Reactions. *Phys. Chem. Chem. Phys.* **2016**, *18* (33), 23320–23325. https://doi.org/10.1039/C6CP04280E.

(25) Leukel, S.; Panthöfer, M.; Mondeshki, M.; Kieslich, G.; Wu, Y.; Krautwurst, N.; Tremel, W. Trapping Amorphous Intermediates of Carbonates – A Combined Total Scattering and NMR Study. *J. Am. Chem. Soc.* **2018**, *140* (44), 14638–14646. https://doi.org/10.1021/jacs.8b06703.

(26) Stawski, T. M.; Roncal-Herrero, T.; Fernandez-Martinez, A.; Matamoros-Veloza, A.; Kröger, R.; Benning, L. G. "On Demand" Triggered Crystallization of $CaCO_3$ from Solute Precursor Species Stabilized by the Water-in-Oil Microemulsion. *Phys. Chem. Chem. Phys.* **2018**, *20* (20), 13825–13835. https://doi.org/10.1039/C8CP00540K.

(27) Politi, Y. Sea Urchin Spine Calcite Forms via a Transient Amorphous Calcium Carbonate Phase. *Science* **2004**, *306* (5699), 1161–1164. https://doi.org/10.1126/science.1102289.

(28) Addadi, L.; Raz, S.; Weiner, S. Taking Advantage of Disorder: Amorphous Calcium Carbonate and Its Roles in Biomineralization. *Adv. Mater.* **2003**, *15* (12), 959–970. https://doi.org/10.1002/adma.200300381.

(29) Beniash, E.; Metzler, R. A.; Lam, R. S. K.; Gilbert, P. U. P. A. Transient Amorphous Calcium Phosphate in Forming Enamel. *J. Struct. Biol.* **2009**, *166* (2), 133–143. https://doi.org/10.1016/j.jsb.2009.02.001.

(30) Combes, C.; Rey, C. Amorphous Calcium Phosphates: Synthesis, Properties and Uses in Biomaterials. *Acta Biomater.* **2010**, *6* (9), 3362–3378. https://doi.org/10.1016/j.actbio.2010.02.017.

(31) Raz, S.; Hamilton, P. C.; Wilt, F. H.; Weiner, S.; Addadi, L. The Transient Phase of Amorphous Calcium Carbonate in Sea Urchin Larval Spicules: The Involvement of Proteins and Magnesium Ions in Its Formation and Stabilization. *Adv. Funct. Mater.* **2003**, *13* (6), 480–486. https://doi.org/10.1002/adfm.200304285.

(32) Buljan Meić, I.; Kontrec, J.; Domazet Jurašin, D.; Njegić Džakula, B.; Štajner, L.; Lyons, D. M.; Dutour Sikirić, M.; Kralj, D. Comparative Study of Calcium Carbonates and Calcium Phosphates Precipitation in Model Systems Mimicking the Inorganic Environment for Biomineralization. *Cryst. Growth Des.* **2017**, *17* (3), 1103–1117. https://doi.org/10.1021/acs.cgd.6b01501.

(33) Gordon, L. M.; Cohen, M. J.; MacRenaris, K. W.; Pasteris, J. D.; Seda, T.; Joester, D. Amorphous Intergranular Phases Control the Properties of Rodent Tooth Enamel. *Science* **2015**, *347* (6223), 746–750. https://doi.org/10.1126/science.1258950.

(34) Belcher, A. M.; Wu, X. H.; Christensen, R. J.; Hansma, P. K.; Stucky, G. D.; Morse, D. E. Control of Crystal Phase Switching and Orientation by Soluble Mollusc-Shell Proteins. *Nature* **1996**, *381* (6577), 56–58. https://doi.org/10.1038/381056a0.

(35) Meldrum, F. C.; Cölfen, H. Controlling Mineral Morphologies and Structures in Biological and Synthetic Systems. *Chem. Rev.* **2008**, *108* (11), 4332–4432. https://doi.org/10.1021/cr8002856.

(36) Tertuliano, O. A.; Greer, J. R. The Nanocomposite Nature of Bone Drives Its Strength and Damage Resistance. *Nat. Mater.* **2016**, *15* (11), 1195–1202. https://doi.org/10.1038/nmat4719.

(37) Wang, Y.-W.; Kim, Y.-Y.; Stephens, C. J.; Meldrum, F. C.; Christenson, H. K. In Situ Study of the Precipitation and Crystallization of Amorphous Calcium

Carbonate (ACC). *Cryst. Growth Des.* **2012**, *12* (3), 1212–1217. https://doi.org/10.1021/cg201204s.

(38) Gower, L. B. Biomimetic Model Systems for Investigating the Amorphous Precursor Pathway and Its Role in Biomineralization. *Chem. Rev.* **2008**, *108* (11), 4551–4627. https://doi.org/10.1021/cr800443h.

(39) Natalio, F.; Corrales, T. P.; Panthofer, M.; Schollmeyer, D.; Lieberwirth, I.; Muller, W. E. G.; Kappl, M.; Butt, H.-J.; Tremel, W. Flexible Minerals: Self-Assembled Calcite Spicules with Extreme Bending Strength. *Science* **2013**, *339* (6125), 1298–1302. https://doi.org/10.1126/science.1216260.

(40) Sun, S.; Mao, L.-B.; Lei, Z.; Yu, S.-H.; Cölfen, H. Hydrogels from Amorphous Calcium Carbonate and Polyacrylic Acid: Bio-Inspired Materials for "Mineral Plastics." *Angew. Chem. Int. Ed.* **2016**, *55* (39), 11765–11769. https://doi.org/10.1002/anie.201602849.

(41) Koishi, A.; Fernandez-Martinez, A.; Ruta, B.; Jimenez-Ruiz, M.; Poloni, R.; di Tommaso, D.; Zontone, F.; Waychunas, G. A.; Montes-Hernandez, G. Role of Impurities in the Kinetic Persistence of Amorphous Calcium Carbonate: A Nanoscopic Dynamics View. *J. Phys. Chem. C* **2018**, *122* (29), 16983–16991. https://doi.org/10.1021/acs.jpcc.8b05189.

(42) Albéric, M.; Bertinetti, L.; Zou, Z.; Fratzl, P.; Habraken, W.; Politi, Y. The Crystallization of Amorphous Calcium Carbonate Is Kinetically Governed by Ion Impurities and Water. *Adv. Sci.* **2018**, *5* (5), 1701000. https://doi.org/10.1002/advs.201701000.

(43) Kababya, S.; Gal, A.; Kahil, K.; Weiner, S.; Addadi, L.; Schmidt, A. Phosphate–Water Interplay Tunes Amorphous Calcium Carbonate Metastability: Spontaneous Phase Separation and Crystallization vs Stabilization Viewed by Solid State NMR. *J. Am. Chem. Soc.* **2015**, *137* (2), 990–998. https://doi.org/10.1021/ja511869g.

(44) Cartwright, J. H. E.; Checa, A. G.; Gale, J. D.; Gebauer, D.; Sainz-Díaz, C. I. Calcium Carbonate Polyamorphism and Its Role in Biomineralization: How Many Amorphous Calcium Carbonates Are There? *Angew. Chem. Int. Ed.* **2012**, *51* (48), 11960–11970. https://doi.org/10.1002/anie.201203125.

(45) Gebauer, D.; Gunawidjaja, P. N.; Ko, J. Y. P.; Bacsik, Z.; Aziz, B.; Liu, L.; Hu, Y.; Bergström, L.; Tai, C.-W.; Sham, T.-K.; Edén, M.; Hedin, N. Proto-Calcite and Proto-Vaterite in Amorphous Calcium Carbonates. *Angew. Chem. Int. Ed.* **2010**, *49* (47), 8889–8891. https://doi.org/10.1002/anie.201003220.

(46) Farhadi-Khouzani, M.; Chevrier, D. M.; Zhang, P.; Hedin, N.; Gebauer, D. Water as the Key to Proto-Aragonite Amorphous $CaCO_3$. *Angew. Chem. Int. Ed.* **2016**, *55* (28), 8117–8120. https://doi.org/10.1002/anie.201603176.

(47) Tobler, D. J.; Rodriguez Blanco, J. D.; Sørensen, H. O.; Stipp, S. L. S.; Dideriksen, K. Effect of PH on Amorphous Calcium Carbonate Structure and Transformation. *Cryst. Growth Des.* **2016**, *16* (8), 4500–4508. https://doi.org/10.1021/acs.cgd.6b00630.

(48) Jensen, A. C. S.; Rodriguez, I.; Habraken, W. J. E. M.; Fratzl, P.; Bertinetti, L. Mobility of Hydrous Species in Amorphous Calcium/Magnesium Carbonates. *Phys. Chem. Chem. Phys.* **2018**, *20* (29), 19682–19688. https://doi.org/10.1039/C8CP01782D.

(49) Lippmann, F. Darstellung und kristallographische Daten von CaCO3�H2O. *Naturwissenschaften* **1959**, *46* (19), 553–554. https://doi.org/10.1007/BF00631281.

(50) Dickens, B.; Brown, W. E. Crystal Structure of Calcium Carbonate Hexahydrate at about -120.Deg. *Inorg. Chem.* **1970**, *9* (3), 480–486. https://doi.org/10.1021/ic50085a010.

(51) Németh, P.; Mugnaioli, E.; Gemmi, M.; Czuppon, G.; Demény, A.; Spötl, C. A Nanocrystalline Monoclinic $CaCO_3$ Precursor of Metastable Aragonite. *Sci. Adv.* **2018**, *4* (12), eaau6178. https://doi.org/10.1126/sciadv.aau6178.

(52) Zou, Z.; Habraken, W. J. E. M.; Matveeva, G.; Jensen, A. C. S.; Bertinetti, L.; Hood, M. A.; Sun, C.; Gilbert, P. U. P. A.; Polishchuk, I.; Pokroy, B.; Mahamid, J.; Politi, Y.; Weiner, S.; Werner, P.; Bette, S.; Dinnebier, R.; Kolb, U.; Zolotoyabko, E.; Fratzl, P. A Hydrated Crystalline Calcium Carbonate Phase: Calcium Carbonate Hemihydrate. *Science* **2019**, *363* (6425), 396–400. https://doi.org/10.1126/science.aav0210.

(53) Ihli, J.; Kulak, A. N.; Meldrum, F. C. Freeze-Drying Yields Stable and Pure Amorphous Calcium Carbonate (ACC). *Chem. Commun.* **2013**, *49* (30), 3134. https://doi.org/10.1039/c3cc40807h.

(54) Gower, L. B.; Odom, D. J. Deposition of Calcium Carbonate Films by a Polymer-Induced Liquid-Precursor (PILP) Process. *J. Cryst. Growth* **2000**, *210* (4), 719–734. https://doi.org/10.1016/S0022-0248(99)00749-6.

(55) Aizenberg, J.; Addadi, L.; Weiner, S.; Lambert, G. Stabilization of Amorphous Calcium Carbonate by Specialized Macromolecules in Biological and Synthetic Precipitates. *Adv. Mater.* **1996**, *8* (3), 222–226. https://doi.org/10.1002/adma.19960080307.

(56) Politi, Y.; Batchelor, D. R.; Zaslansky, P.; Chmelka, B. F.; Weaver, J. C.; Sagi, I.; Weiner, S.; Addadi, L. Role of Magnesium Ion in the Stabilization of Biogenic Amorphous Calcium Carbonate: A Structure−Function Investigation. *Chem. Mater.* **2010**, *22* (1), 161–166. https://doi.org/10.1021/cm902674h.

(57) Hu, H.; Li, X.; Huang, P.; Zhang, Q.; Yuan, W. Efficient Removal of Copper from Wastewater by Using Mechanically Activated Calcium Carbonate. *J. Environ. Manage.* **2017**, *203*, 1–7. https://doi.org/10.1016/j.jenvman.2017.07.066.

(58) Tsai, W.-T.; Yang, J.-M.; Hsu, H.-C.; Lin, C.-M.; Lin, K.-Y.; Chiu, C.-H. Development and Characterization of Mesoporosity in Eggshell Ground by Planetary Ball Milling. *Microporous Mesoporous Mater.* **2008**, *111* (1–3), 379–386. https://doi.org/10.1016/j.micromeso.2007.08.010.

(59) Polini, R.; Paci, B.; Generosi, A.; Marcheselli, G. Synthesis of Scheelite Nanoparticles by Mechanically Assisted Solid-State Reaction of Wolframite and Calcium Carbonate. *Miner. Eng.* **2019**, *138*, 133–138. https://doi.org/10.1016/j.mineng.2019.05.002.

(60) Huang, X.; Dong, K.; Liu, L.; Luo, X.; Yang, R.; Song, H.; Li, S.; Huang, Q. Physicochemical and Structural Characteristics of Nano Eggshell Calcium Prepared by Wet Ball Milling. *LWT* **2020**, *131*, 109721. https://doi.org/10.1016/j.lwt.2020.109721.

(61) Burns, J. H.; Bredig, M. A. Transformation of Calcite to Aragonite by Grinding. *J. Chem. Phys.* **1956**, *25* (6), 1281–1281. https://doi.org/10.1063/1.1743198.

(62) Criado, J. M.; Trillo, J. M. Effects of Mechanical Grinding on the Texture and Structure of Calcium Carbonate. *J. Chem. Soc. Faraday Trans. 1 Phys. Chem. Condens. Phases* **1975**, *71* (0), 961. https://doi.org/10.1039/f19757100961.

(63) Northwood, D. O.; Lewis, D. Transformation of Vaterite to Calcite during Grinding. *Am. Mineral.* **1968**, *53* (11–12), 2089–2092.

(64) Barriga, C.; Morales, J.; Tirado, J. L. Changes in Crystallinity and Thermal Effects in Ground Vaterite. *J. Mater. Sci.* **1985**, *20* (3), 941–946. https://doi.org/10.1007/BF00585738.

(65) Leukel, S.; Panthöfer, M.; Mondeshki, M.; Kieslich, G.; Wu, Y.; Krautwurst, N.; Tremel, W. Mechanochemical Access to Defect-Stabilized Amorphous Calcium

Carbonate. *Chem. Mater.* **2018**, *30* (17), 6040–6052. https://doi.org/10.1021/acs.chemmater.8b02339.

(66) Bots, P.; Benning, L. G.; Rodriguez-Blanco, J.-D.; Roncal-Herrero, T.; Shaw, S. Mechanistic Insights into the Crystallization of Amorphous Calcium Carbonate (ACC). *Cryst. Growth Des.* **2012**, *12* (7), 3806–3814. https://doi.org/10.1021/cg300676b.

(67) Rodriguez-Blanco, J. D.; Shaw, S.; Benning, L. G. The Kinetics and Mechanisms of Amorphous Calcium Carbonate (ACC) Crystallization to Calcite, Viavaterite. *Nanoscale* **2011**, *3* (1), 265–271. https://doi.org/10.1039/C0NR00589D.

(68) Wolf, S. E.; Böhm, C.; Harris, J.; Hajir, M.; Mondeshki, M.; Marin, F. Single Nanogranules Preserve Intracrystalline Amorphicity in Biominerals. *Key Eng. Mater.* **2016**, *672*, 47–59. https://doi.org/10.4028/www.scientific.net/KEM.672.47.

(69) Rodriguez-Navarro, C.; Kudłacz, K.; Cizer, Ö.; Ruiz-Agudo, E. Formation of Amorphous Calcium Carbonate and Its Transformation into Mesostructured Calcite. *CrystEngComm* **2015**, *17* (1), 58–72. https://doi.org/10.1039/C4CE01562B.

(70) Nebel, H.; Neumann, M.; Mayer, C.; Epple, M. On the Structure of Amorphous Calcium Carbonate□A Detailed Study by Solid-State NMR Spectroscopy. *Inorg. Chem.* **2008**, *47* (17), 7874–7879. https://doi.org/10.1021/ic8007409.

(71) Andersen, F. A.; Brečević, L.; Beuter, G.; Dell'Amico, D. B.; Calderazzo, F.; Bjerrum, N. J.; Underhill, A. E. Infrared Spectra of Amorphous and Crystalline Calcium Carbonate. *Acta Chem. Scand.* **1991**, *45*, 1018–1024. https://doi.org/10.3891/acta.chem.scand.45-1018.

(72) Parr, R. G.; Pearson, R. G. Absolute Hardness: Companion Parameter to Absolute Electronegativity. *J. Am. Chem. Soc.* **1983**, *105* (26), 7512–7516. https://doi.org/10.1021/ja00364a005.

(73) Tortet, L.; Gavarri, J. R.; Nihoul, G.; Dianoux, A. J. Study of Protonic Mobility in CaHPO4·2H2O (Brushite) and CaHPO4(Monetite) by Infrared Spectroscopy and Neutron Scattering. *J. Solid State Chem.* **1997**, *132* (1), 6–16. https://doi.org/10.1006/jssc.1997.7383.

(74) Brangule, A.; Gross, K. A. Importance of FTIR Spectra Deconvolution for the Analysis of Amorphous Calcium Phosphates. *IOP Conf. Ser. Mater. Sci. Eng.* **2015**, *77*, 012027. https://doi.org/10.1088/1757-899X/77/1/012027.

(75) Plyler, E. K.; Acquista, N. Infrared Absorption Spectra of Cyclo-Hydrocarbons. *J. Res. Natl. Bur. Stand.* **1949**, *43* (1), 37. https://doi.org/10.6028/jres.043.003.

(76) Hing, A. W.; Vega, S.; Schaefer, J. Transferred-Echo Double-Resonance NMR. *J. Magn. Reson. 1969* **1992**, *96* (1), 205–209. https://doi.org/10.1016/0022-2364(92)90305-Q.

(77) Rothwell, W. P.; Waugh, J. S.; Yesinowski, J. P. High-Resolution Variable-Temperature Phosphorus-31 NMR of Solid Calcium Phosphates. *J. Am. Chem. Soc.* **1980**, *102* (8), 2637–2643. https://doi.org/10.1021/ja00528a020.

(78) Catti, M.; Ferraris, G.; Filhol, A. Hydrogen Bonding in the Crystalline State. CaHPO4 (Monetite), P1 or P1? A Novel Neutron Diffraction Study. *Acta Crystallogr. B* **1977**, *33* (4), 1223–1229. https://doi.org/10.1107/S0567740877005706.

(79) Gras, P.; Baker, A.; Combes, C.; Rey, C.; Sarda, S.; Wright, A. J.; Smith, M. E.; Hanna, J. V.; Gervais, C.; Laurencin, D.; Bonhomme, C. From Crystalline to Amorphous Calcium Pyrophosphates: A Solid State Nuclear Magnetic Resonance Perspective. *Acta Biomater.* **2016**, *31*, 348–357. https://doi.org/10.1016/j.actbio.2015.10.016.

(80) Giordani, M.; Beruto, D. Effect of Vaporization Rate on Calcium Carbonate Nucleation from Calcium Hydrogen Carbonate Aqueous Solutions. *J. Cryst. Growth* **1987**, *84* (4), 679–682. https://doi.org/10.1016/0022-0248(87)90060-1.

(81) Beruto, D.; Giordani, M. Calcite and Aragonite Formation from Aqueous Calcium Hydrogencarbonate Solutions: Effect of Induced Electromagnetic Field on the Activity of CaCO3 Nuclei Precursors. *J. Chem. Soc. Faraday Trans.* **1993**, *89* (14), 2457. https://doi.org/10.1039/ft9938902457.

(82) *A Dictionary of Chemistry*, 6th ed.; Daintith, J., Ed.; Oxford paperback reference; Oxford University Press: New York, 2008.

(83) Shannon, R. D. Revised Effective Ionic Radii and Systematic Studies of Interatomic Distances in Halides and Chalcogenides. *Acta Crystallogr. Sect. A* **1976**, *32* (5), 751–767. https://doi.org/10.1107/S0567739476001551.

(84) Xu, B.; Hirsch, A.; Kronik, L.; Poduska, K. M. Vibrational Properties of Isotopically Enriched Materials: The Case of Calcite. *RSC Adv.* **2018**, *8* (59), 33985–33992. https://doi.org/10.1039/C8RA06608F.

(85) Rudolph, W. W.; Fischer, D.; Irmer, G. Vibrational Spectroscopic Studies and Density Functional Theory Calculations of Speciation in the CO_2 —Water System. *Appl. Spectrosc.* **2006**, *60* (2), 130–144. https://doi.org/10.1366/000370206776023421.

(86) Garand, E.; Wende, T.; Goebbert, D. J.; Bergmann, R.; Meijer, G.; Neumark, D. M.; Asmis, K. R. Infrared Spectroscopy of Hydrated Bicarbonate Anion Clusters: $HCO_3^-(H_2O)_{1-10}$. *J. Am. Chem. Soc.* **2010**, *132* (2), 849–856. https://doi.org/10.1021/ja9093132.

(87) Eckert, H. Dipolar 31P NMR Spectroscopy of Crystalline Inorganic Phosphorus Compounds. *Solid State Nucl. Mugnetic Reson.* **1992**, *1*, 73–83.

(88) Gee, B.; Eckert, H. Cation Distribution in Mixed-Alkali Silicate Glasses. NMR Studies by ^{23}Na−{^{7}Li} and ^{23}Na−{^{6}Li} Spin Echo Double Resonance. *J. Phys. Chem.* **1996**, *100* (9), 3705–3712. https://doi.org/10.1021/jp9521722.

(89) Eckert, H. Short and Medium Range Order in Ion-Conducting Glasses Studied by Modern Solid State NMR Techniques. *Z. Für Phys. Chem.* **2010**, *224* (10–12), 1591–1654. https://doi.org/10.1524/zpch.2010.0030.

(90) Van Vleck, J. H. The Dipolar Broadening of Magnetic Resonance Lines in Crystals. *Phys. Rev.* **1948**, *74* (9), 1168–1183. https://doi.org/10.1103/PhysRev.74.1168.

(91) Jansen, M.; Schön, J. C.; van Wüllen, L. The Route to the Structure Determination of Amorphous Solids: A Case Study of the Ceramic Si3B3N7. *Angew. Chem. Int. Ed.* **2006**, *45* (26), 4244–4263. https://doi.org/10.1002/anie.200504193.

(92) Hoeher, A.; Mergelsberg, S.; Borkiewicz, O. J.; Dove, P. M.; Michel, F. M. A New Method for *in Situ* Structural Investigations of Nano-Sized Amorphous and Crystalline Materials Using Mixed-Flow Reactors. *Acta Crystallogr. Sect. Found. Adv.* **2019**, *75* (5), 758–765. https://doi.org/10.1107/S2053273319008623.

(93) Ferrero, E. E.; Martens, K.; Barrat, J.-L. Relaxation in Yield Stress Systems through Elastically Interacting Activated Events. *Phys. Rev. Lett.* **2014**, *113* (24), 248301. https://doi.org/10.1103/PhysRevLett.113.248301.

(94) Pritzker, K. P. H. Calcium Pyrophosphate Crystal Formation and Dissolution. In *Calcium Phosphates in Biological and Industrial Systems*; Amjad, Z., Ed.; Springer US: Boston, MA, 1998; pp 277–301. https://doi.org/10.1007/978-1-4615-5517-9_12.

(95) Hahn, E. L. Spin Echoes. *Phys. Rev.* **1950**, *80* (4), 580–594. https://doi.org/10.1103/PhysRev.80.580.

(96) Makowka, C. D.; Slichter, C. P.; Sinfelt, J. H. Probe of the Surface of a Heterogeneous Catalyst: Double NMR of Carbon Monoxide Chemisorbed on Highly Dispersed Platinum. *Phys. Rev. Lett.* **1982**, *49* (6), 379–382. https://doi.org/10.1103/PhysRevLett.49.379.
(97) Dippel, A.-C.; Liermann, H.-P.; Delitz, J. T.; Walter, P.; Schulte-Schrepping, H.; Seeck, O. H.; Franz, H. Beamline P02.1 at PETRA III for High-Resolution and High-Energy Powder Diffraction. *J. Synchrotron Radiat.* **2015**, *22* (3), 675–687. https://doi.org/10.1107/S1600577515002222.
(98) Filik, J.; Ashton, A. W.; Chang, P. C. Y.; Chater, P. A.; Day, S. J.; Drakopoulos, M.; Gerring, M. W.; Hart, M. L.; Magdysyuk, O. V.; Michalik, S.; Smith, A.; Tang, C. C.; Terrill, N. J.; Wharmby, M. T.; Wilhelm, H. Processing Two-Dimensional X-Ray Diffraction and Small-Angle Scattering Data in *DAWN 2*. *J. Appl. Crystallogr.* **2017**, *50* (3), 959–966. https://doi.org/10.1107/S1600576717004708.
(99) Soper, A. K.; Barney, E. R. Extracting the Pair Distribution Function from White-Beam X-Ray Total Scattering Data. *J. Appl. Crystallogr.* **2011**, *44* (4), 714–726. https://doi.org/10.1107/S0021889811021455.

2.1.9 Supporting Information

Table S1. Quantification of ball-milled precursors by FTIR.

Sample	Fraction of crystalline phase
BM-calcite	29.1 %
BM-monetite	19.8 %

The quantification is based on the FTIR data. For ball-milled calcite the band of the ν_2 vibration mode was fitted using a bimodal pseudo Voigt function. The area ratio of the function is shown in Table S1 for the amorphous and crystalline phase. To quantify portion of ball-milled monetite the band of the $\nu_{P\text{-}O}$ vibration mode at ≈1000 cm^{-1} was fitted for the crystalline, ball-milled and amorphous phases. The full width at half maximum (FWHM) of the crystalline phase was set to “100% crystalline” and the FWHM of the amorphous phase to 0%. The ratios are in good agreement with the XRPD patterns (Figure S8).

Table S2. Positions of CO_3^{2-} bands in amorphous calcium carbonate/calcium hydrogen phosphate (aCCP), amorphous strontium carbonate/calcium hydrogen phosphate (aSCP) and amorphous barium carbonate/calcium hydrogen phosphate (aBCP).

	CO_3^{2-} vibration modes (cm^{-1})		
Sample	ν_2	ν_3	ν_4
aCCP 0.5	862	1410, 1493	693, 728
aSCP 0.5	864	1406, 1483	689, 724
aBCP 0.5	865	1397, 1470	683, 717

For the ν_2 vibration mode, the band are shifted to higher wave numbers for increasing cation mass. Soft Pearson acids lead to weaker interactions with the oxygen atoms of the carbonate ion. Therefore, the carbon atom polarizes a higher electron density on the oxygen atoms, and the out-of plane vibration appears at higher frequency. The ν_3 and ν_4 vibration modes are shifted to lower wave numbers with increasing cation mass. Sr^{2+} and Ba^{2+} ions polarize the electron density around the carbonate oxygen atoms less strongly. As a result, the stretching modes are shifted to lower frequencies.

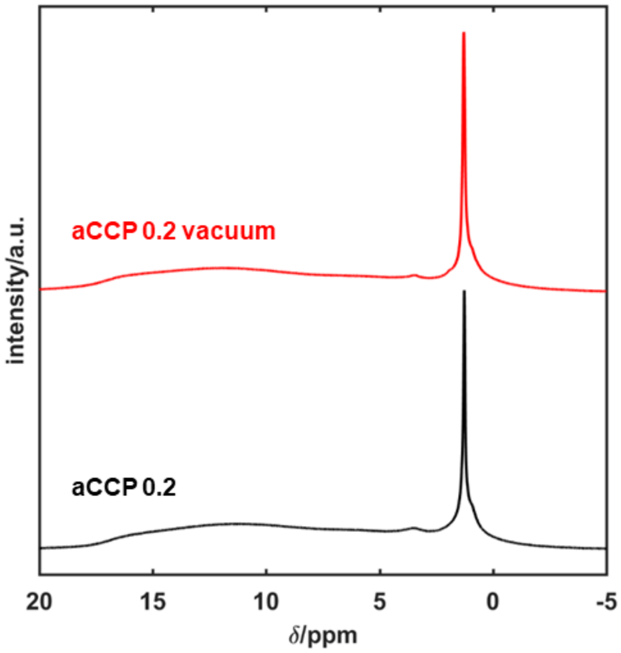

Figure S1. ^{1}H NMR spectra of aCCP 0.2 with and without drying in an vacuum oven at 40°C for 8 h.

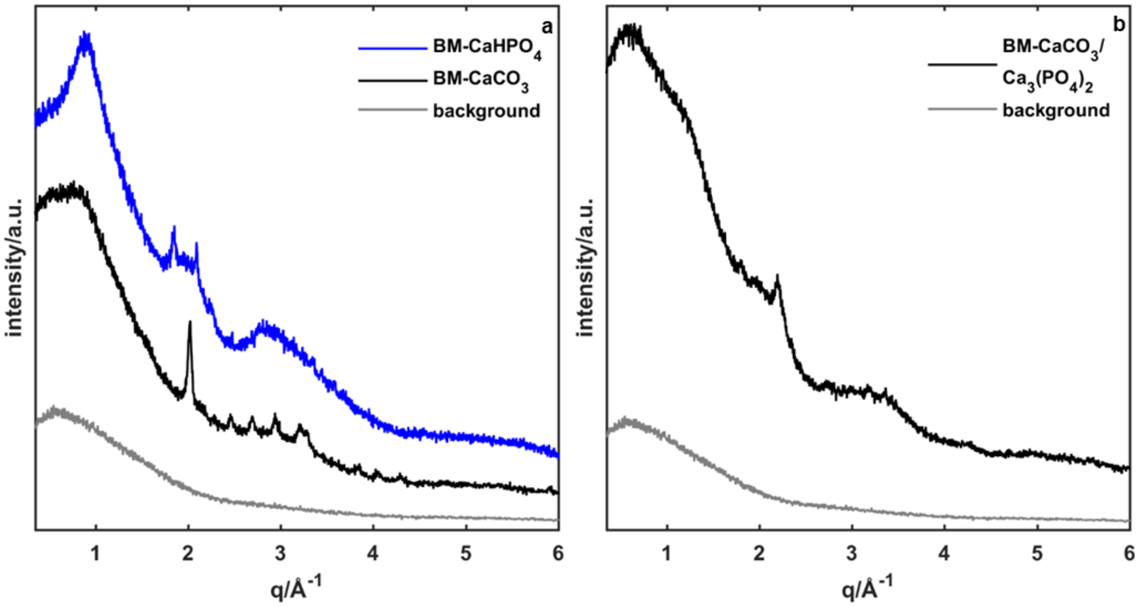

Figure S2. Powder diffractograms of the ball-milled starting materials (a, left) and a mixture of $CaCO_3$ (calcite) and tricalcium phosphate (b, right).

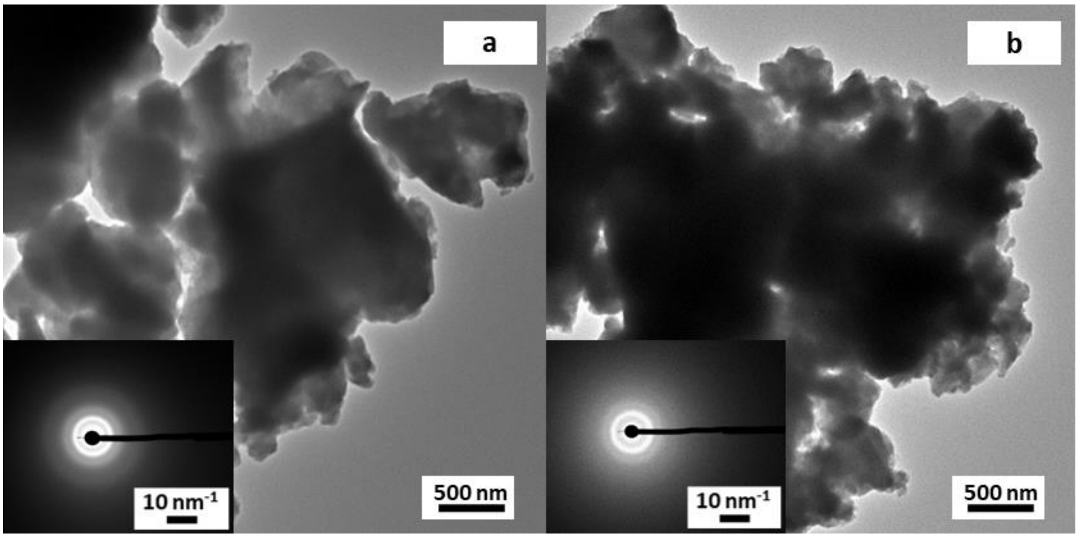

Figure S3. TEM images and associated diffraction patterns for (a) aSCP (0.5) and (b) aBCP (0.5).

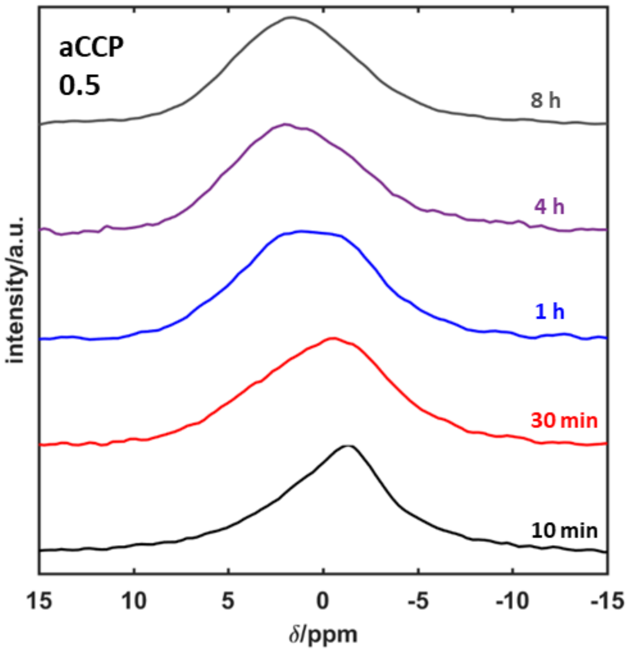

Figure S4. ^{31}P-MAS-ssNMR spectra of aCCP 0.5 as a function of milling time.

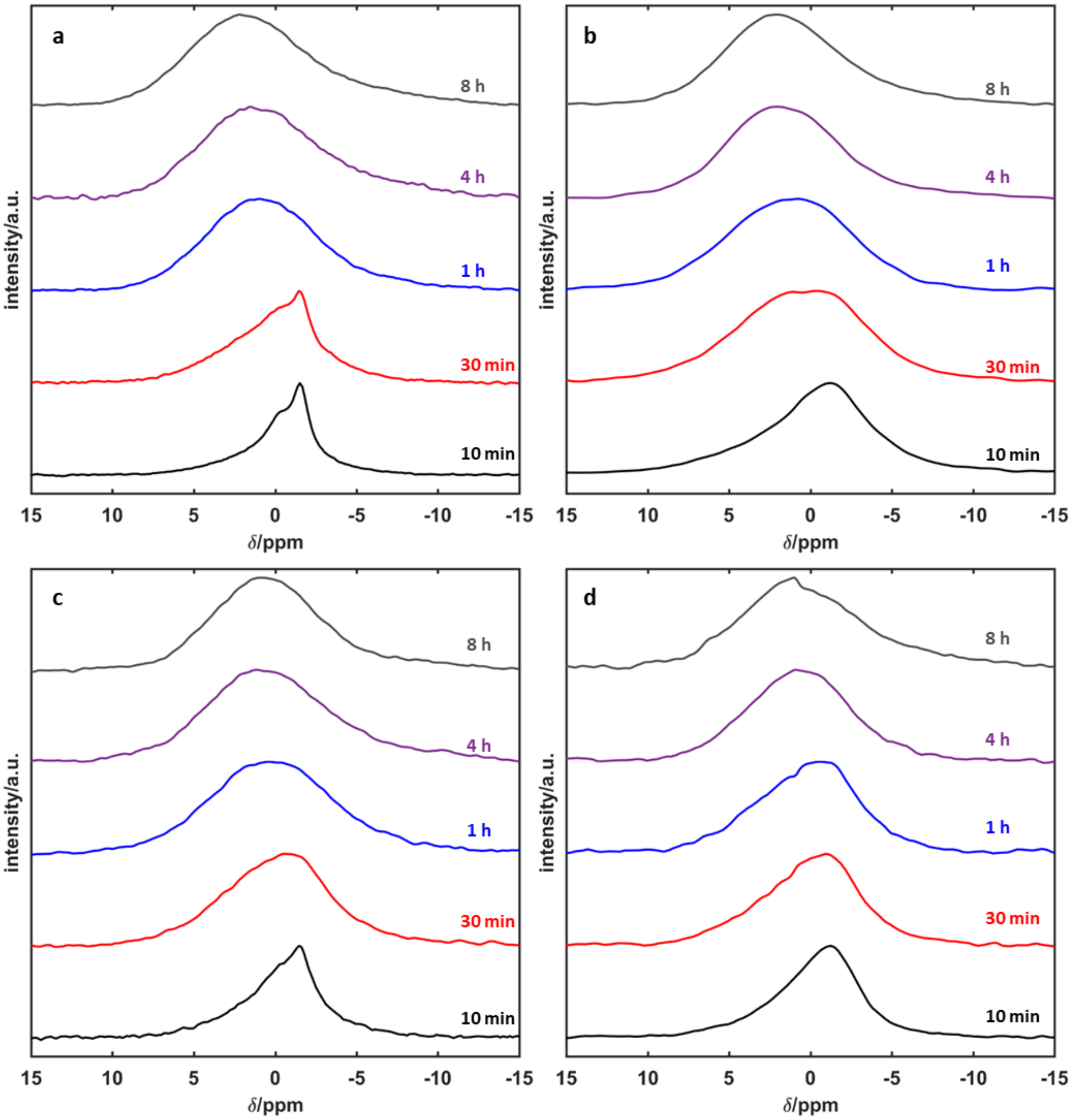

Figure S5. ^{31}P-MAS-ssNMR spectra of (a) $SrCO_3$ 0.2, (b) $SrCO_3$ 0.5, (c) $BaCO_3$ 0.2 and (d) $BaCO_3$ 0.5 as a function of milling time.

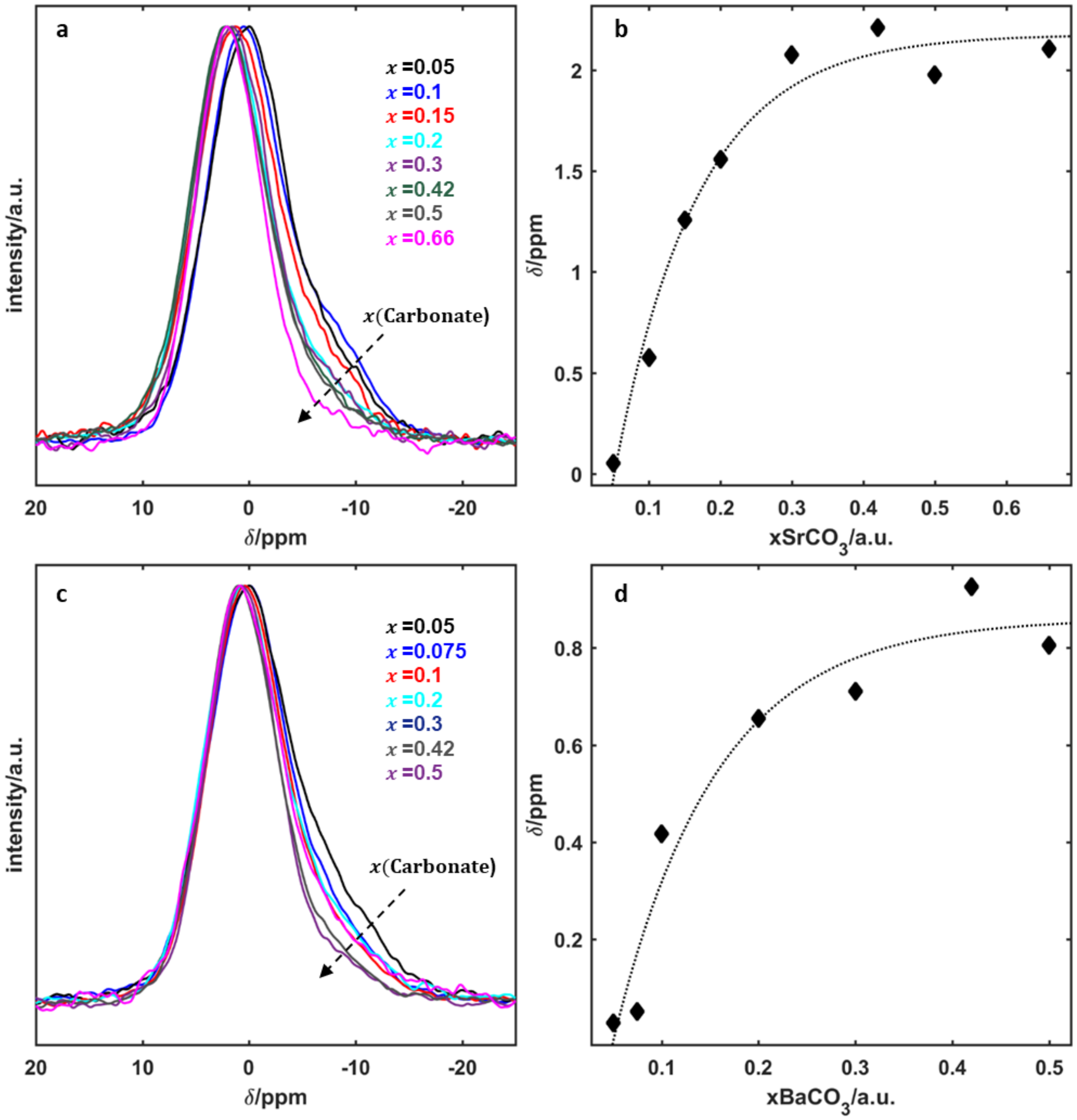

Figure S6. ^{31}P signals of ball-milled amorphous strontium (a) and barium (b) carbonate phosphates. Signal maxima of ball-milled amorphous strontium (b) and barium (d) carbonate phosphates as a function of the carbonate mole fraction χ(Carbonate).

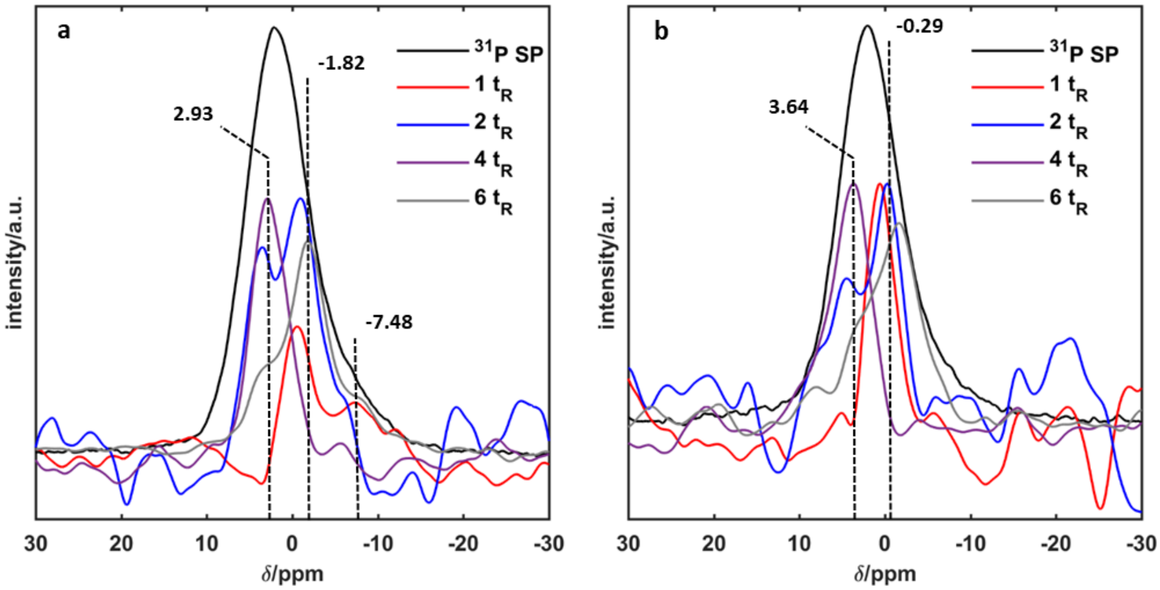

Figure S7. TEDOR spectra of (a) amorphous aSCP (χ(Carbonate) = 0.2) and (b) amorphous aSCP (χ(Carbonate) = 0.5) as a function of the rotor period recorded at 1, 2, 4, and 6 rotor periods (40, 80, 160 and 240 µs recoupling time respectively), with the respective ^{31}P single pulse excitation (SPE) spectra.

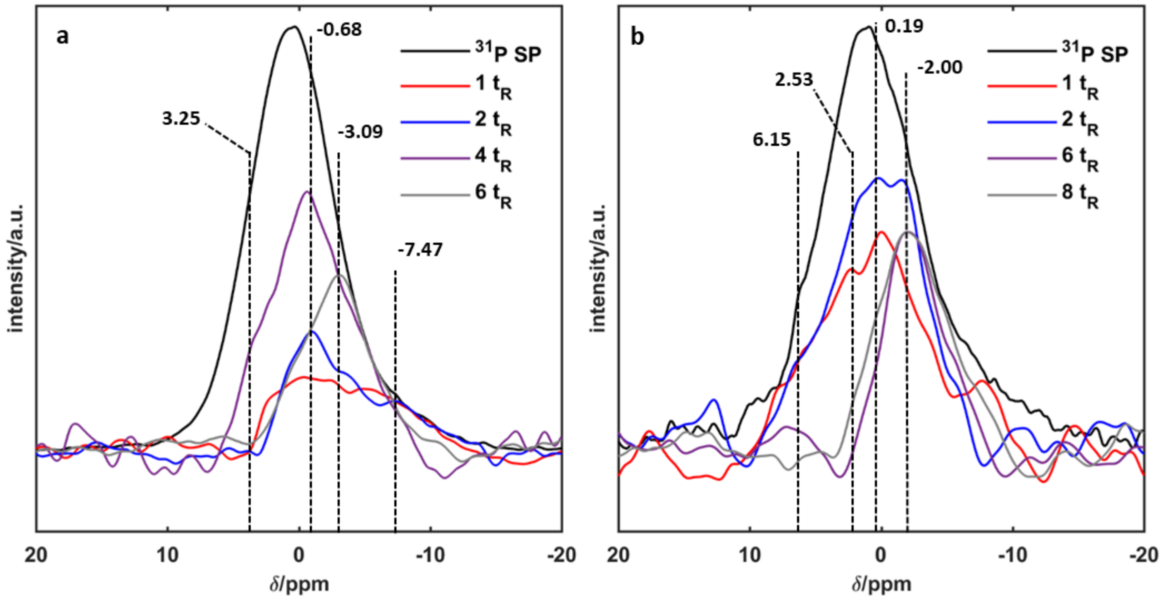

Figure S8. TEDOR spectra of (a) amorphous aBCP (χ(Carbonate)= 0.2) and (b) amorphous aBCP (χ(Carbonate)= 0.5) as a function of the rotor period recorded at 1, 2, 4, and 6 rotor periods (40, 80, 160 and 240 µs recoupling time respectively), with the respective ^{31}P single pulse excitation (SPE) spectra.

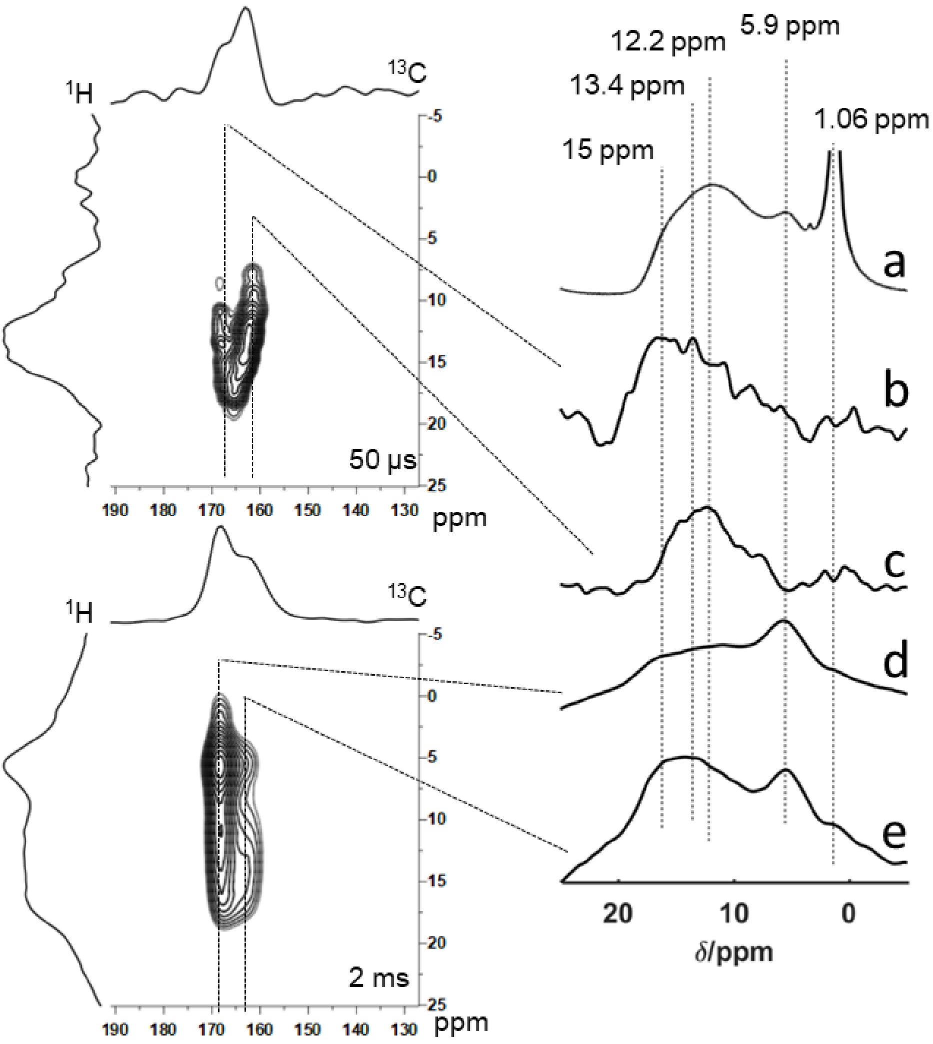

Figure S9. ^{1}H-^{13}C HETCOR spectra of aSCP (χ(Carbonate) = 0.5) recorded with contact times of 50 and 2000 µs and respective projections, in particular (a) ^{1}H SPE spectrum, (b) projection at 168 ppm with contact times of 50 µs, (c) projection at 162 ppm with contact times of 50 µs, (d) projection at 168 ppm with contact times of 2 ms, (e) projection at 162 ppm with contact times of 2 ms.

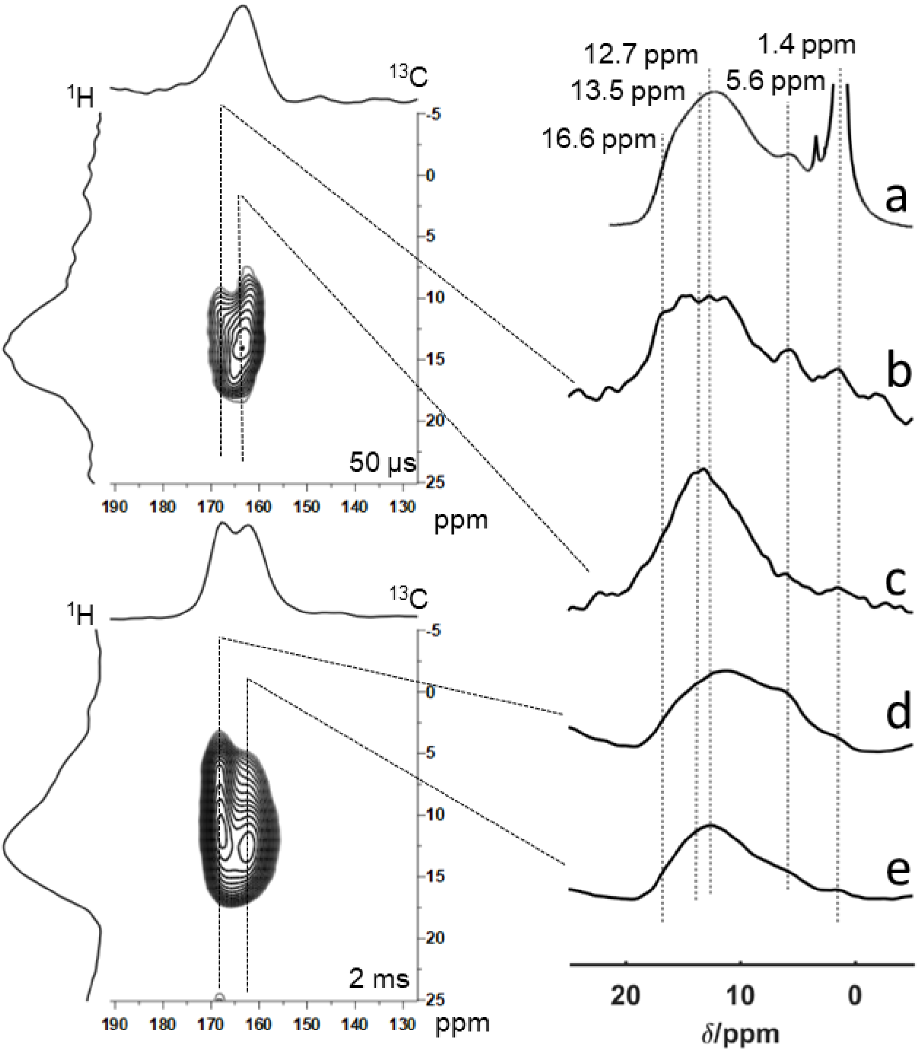

Figure S10. ^{1}H-^{13}C HETCOR spectra of aBCP (χ(Carbonate) = 0.5) recorded with contact times of 50 and 2000 μs and respective projections, in particular (a) ^{1}H SPE spectrum, (b) projection at 168 ppm with contact times of 50 μs, (c) projection at 162 ppm with contact times of 50 μs, (d) projection at 168 ppm with contact times of 2 ms, (e) projection at 162 ppm with contact times of 2 ms.

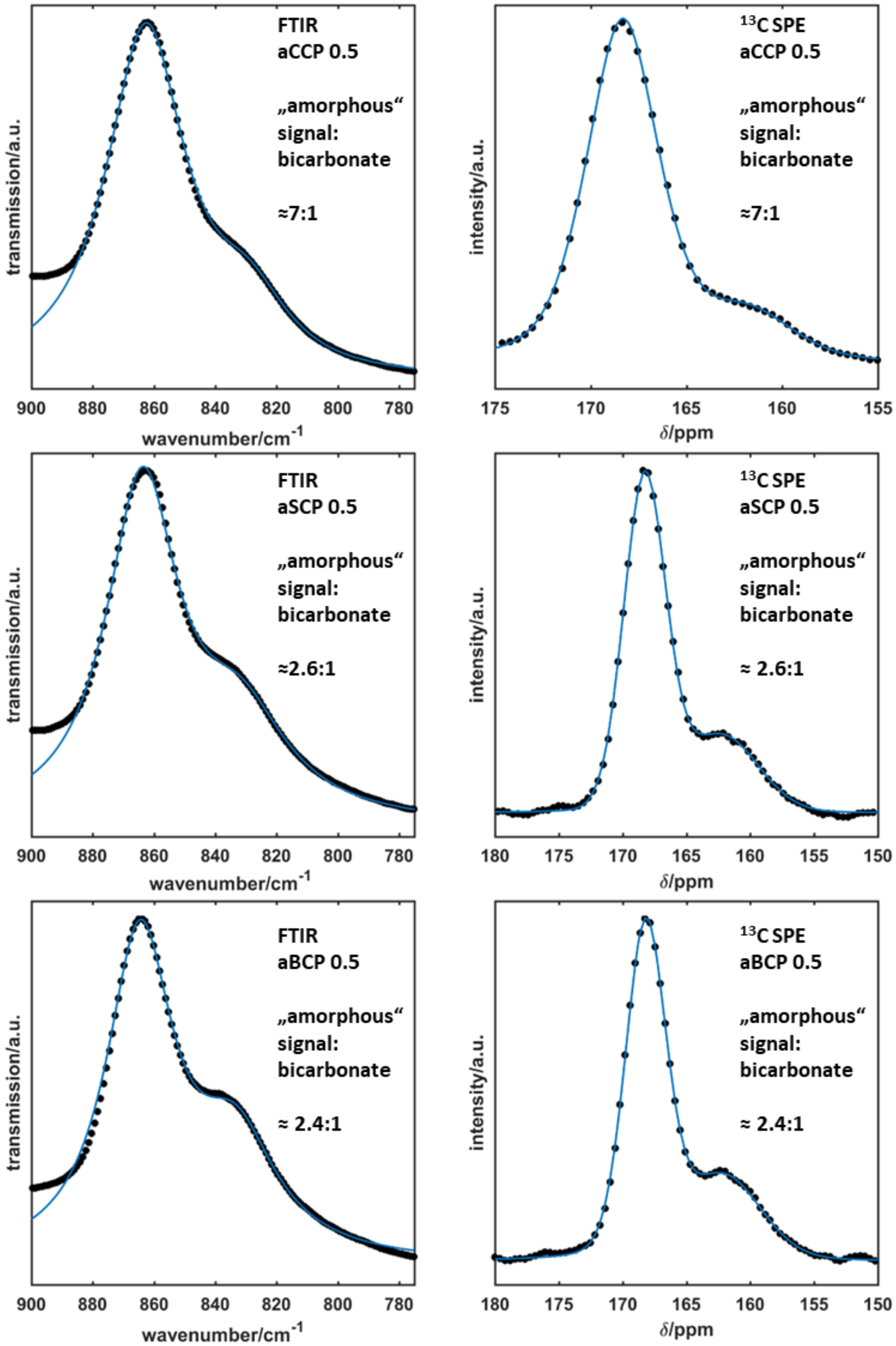

Figure S3. Comparison of the best fits (blue line) of the FTIR (left) and ^{13}C SPE (right) spectra. The ratio of the areas of the bimodal pseudo Voigt fits correspond to the carbonate to hydrogen carbonate ratio (top: aCCP, middle: aSCP, bottom: aBCP).

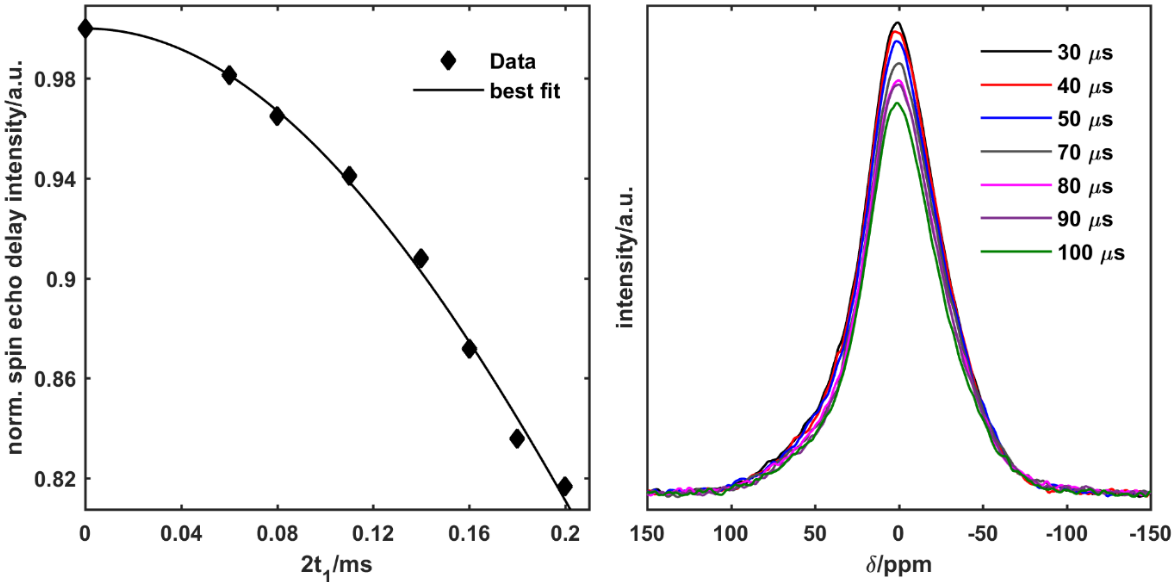

Figure S4. ^{31}P spin echo decay of aCCP 0.5 (left) with the corresponding static Hahn echo delay spectra (right). The solid line shows the best fit using the Gaussian function (equation 1).

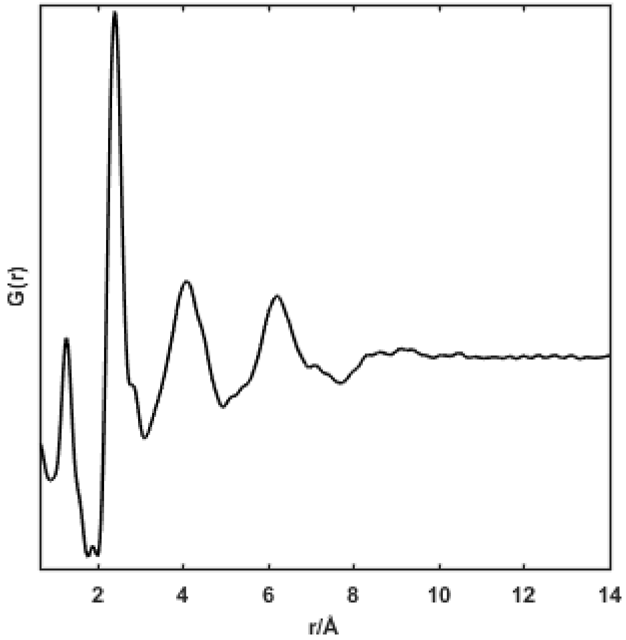

Figure S5. Pair distribtuion function of hydrous ACC (from previous study).

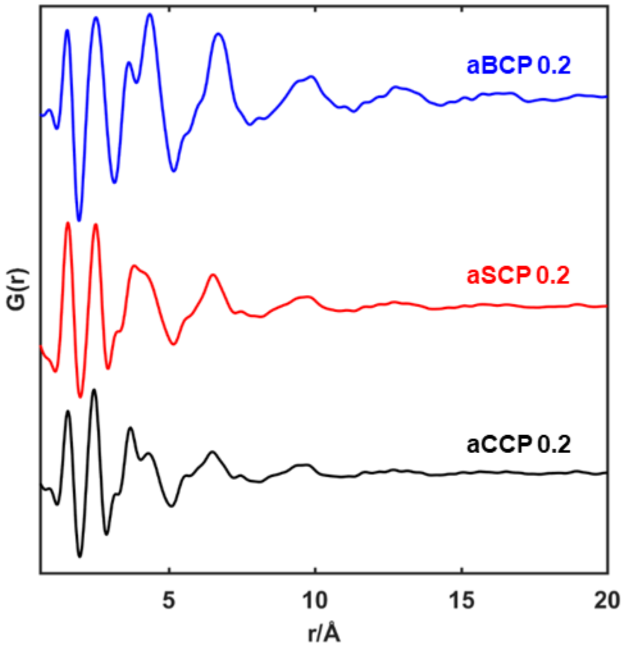

Figure S64. Pair distribtuion function of aSCP 0.2 (red) and aBCP 0.2 (blue). The PDFs show clear broad peaks beyond 10 Å. This proves a higher crystallinity in comparison to the aCCP samples.

Thermogravimetric and differential thermal analysis

DTA and TGA measurements were performed on samples of aXCP 0.2 and 0.5. The first endothermic effect at ≈ 91°C is caused by surface-bound solvents, e.g. cyclohexane, ethanol and water. This is supported by the observed mass changes (< 1%). The second endothermic effect at about 220 °C (depending on the cation) shows the evaporation of entrapped solvent (specifically cyclohexane), and it is followed with a significant weight loss. We assume that the solvents are encapsulated in cavities between grain boundaries of the amorphous phase. The thermal energy increases the diffusion. This can lead to cracking of grain boundaries and a rapid release of the gaseous solvent. In samples with a mol fraction $x = 0.2$ this occurs at higher temperatures for the heavier alkaline earth cations. As shown by Zhang *et al.*[1] hydrogen bonded hydroxyl groups have a large impact on the thermal stability of phases. Therefore, we assume that due to the higher hydrogen carbonate content (aCCP<aSCP<aBCP, Figure S10) more hydrogen bonded hydroxyl groups are present, which leads to the observed higher thermal stability. A small endothermic effect occurs at ~500°C. Thermally induced crystallization to calcite, tricalcium phosphate and several polyphosphates occurs at ~600°C. The mass loss at higher temperature is due to decarboxylation of calcium carbonate.

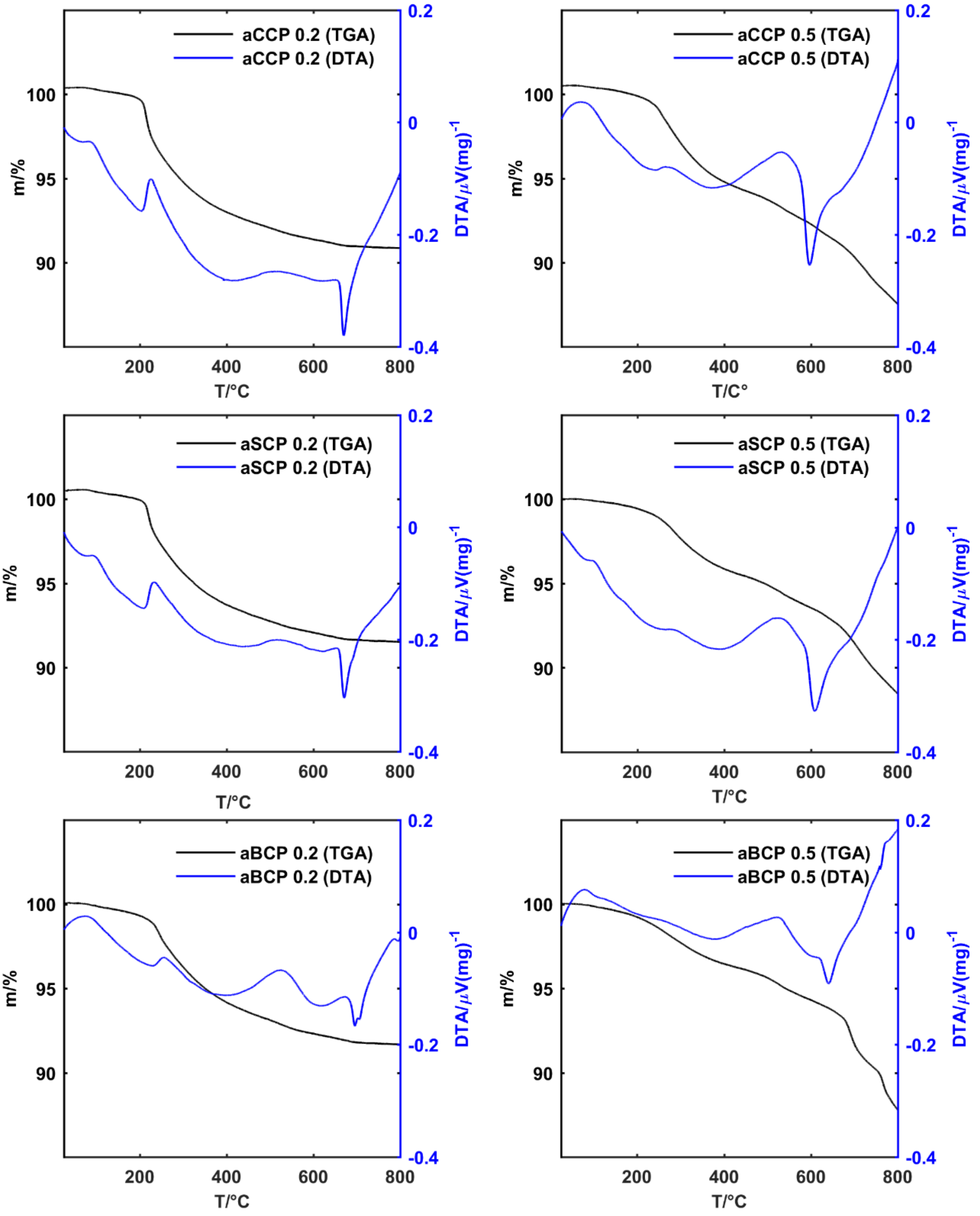

Figure S15. DTA and TGA traces for aXCP (top: X = Ca, middle; X = Sr, bottom: X = Ba. $x(Carbonate) = 0.2$ (left side). $x(Carbonate) = 0.5$ (right side).

Thermogravimetric analysis of samples subject to vacuum

Ex situ TGA measurements were performed to investigate the vacuum stability of the samples (Figure S14). In accordance with the XPCS data, the aCCP (0.2) sample shows a significant change under vacuum. This is another indication that hydroxyl groups (with hydrogen bonds) are either broken or reorganized. In contrast, the water loss of sample aCCP (0.5) is less affected by the vacuum treatment. This is consistent with the less extent of sample aging observed in XPCS experiments.

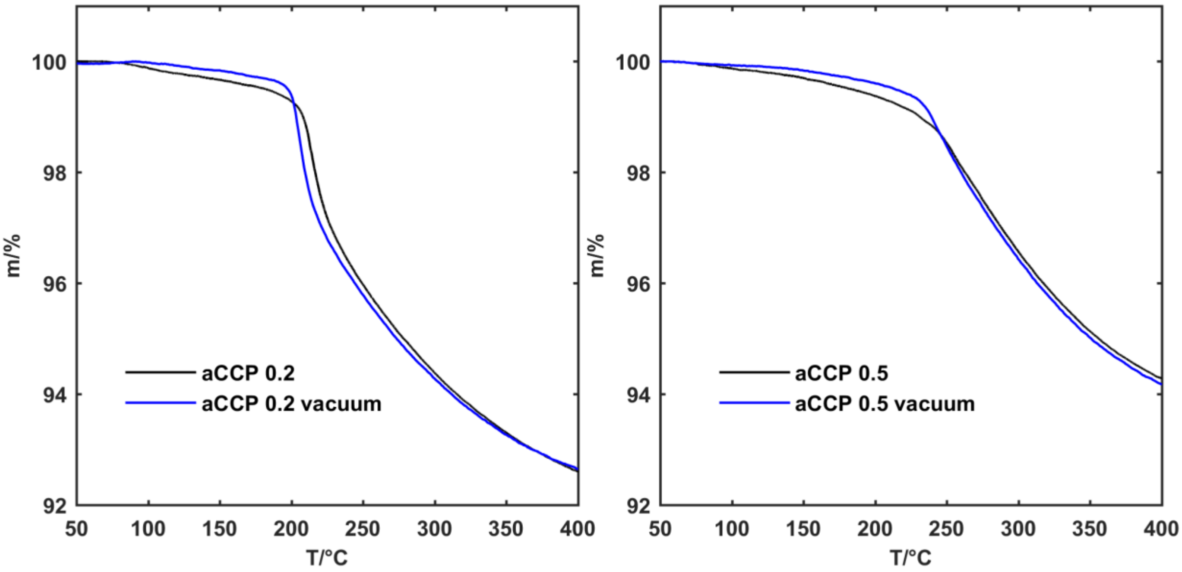

Figure S16. TGA traces under vacuum (blue line) and normal pressure (black line) for aCCP (0.2) (a, left) and aCCP 0.5 (b, right). The mass loss for aCCP 0.2 occurs at lower temperature (ΔT = 9°C) under vacuum conditions.

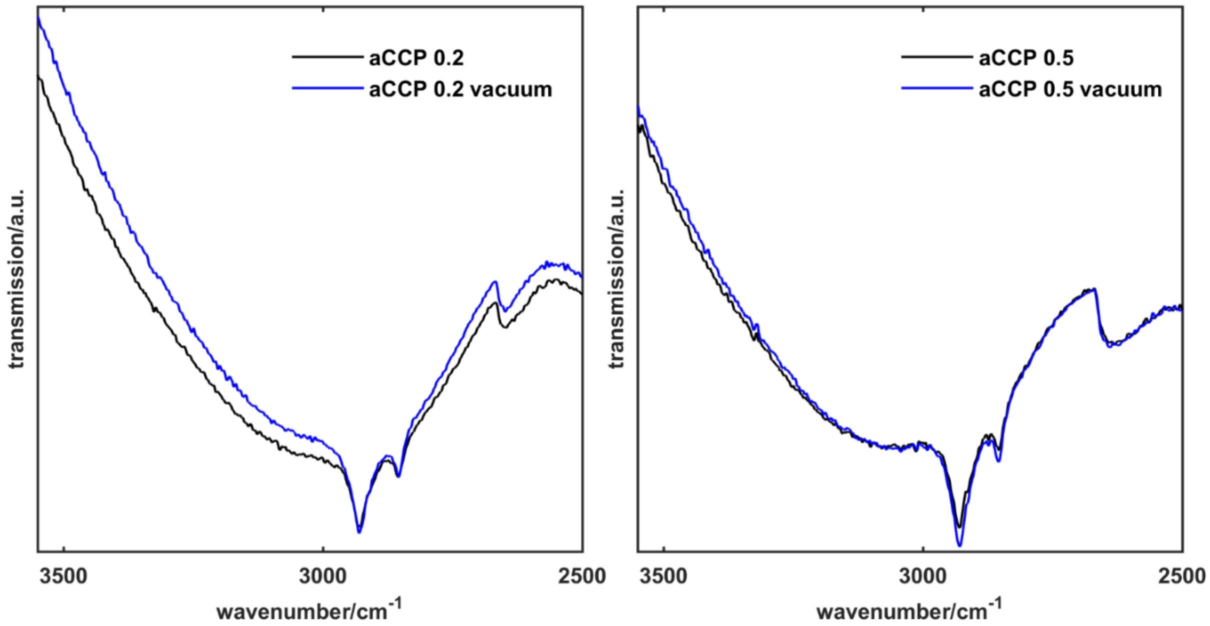

Figure S17. Vibrational region of the generalized VDOS for water at 300 K in aCCP for (left) χ(Carbonate) = 0.2 and (right) χ(Carbonate) = 0.5. The intensity is normalized to the unity within the 2500–3500 cm^{-1} range. Black lines represent data for aCCP in air, blue lines for aCCP under vacuum conditions.

X-ray Photon Correlation Spectroscopy.

A high-flux coherent X-ray beam is used to detect time-dependent intensity fluctuations of the “speckle pattern”, which directly relates to local dynamics, *e.g.* rearrangement of particles and density fluctuations in the probed volume.[2] The spatial size of the dynamics depends on the experimental q value, the scattering vector. The q-dependent intensity fluctuations are evaluated with the following autocorrelation function, which is a measure of the similarity of the intensity with itself after a lag time Δt.

$$g^{(2)}(\Delta t, q) = \frac{\langle I(t,q) I(t+\Delta t, q)\rangle}{\langle I(t,q)\rangle^2} \tag{3}$$

In order to obtain information about the dynamics of the system, the autocorrelation curve is fitted with the Kohlrausch-Williams-Watts model.

$$g^{(2)}(t) = 1 + c \cdot exp\left(-2\left(\frac{t}{\tau}\right)^{\beta}\right) \tag{4}$$

The parameter c is the setup-dependent contrast, τ is the structural relaxation time and β is the shape factor of the curve.”

References

(1) Zhang, K.; Han, L.; Nie, Y.; Szigeti, M. L.; Ishida, H. Examining the Effect of Hydroxyl Groups on the Thermal Properties of Polybenzoxazines: Using Molecular Design and Monte Carlo Simulation. *RSC Adv.* **2018**, *8* (32), 18038–18050.
(2) Synchrotron Light Sources and Free-Electron Lasers: Accelerator Physics, Instrumentation and Science Applications; Jaeschke, E., Khan, S., Schneider, J. R., Hastings, J. B., Eds.; Springer International Publishing: Cham, 2019.

3 Chapter 2

The contents of the following chapter are taken and partially adapted from Adv. Funct. Mater. 2021, 31, 2007830.

3.1 Insights into the *in vitro* Formation of Bone-Like Apatite from Mg-Stabilized Amorphous Calcium Carbonate

3.1.1 ABSTRACT.

"Biomimetic materials are of interest for use in bone replacement because they may provide regenerative alternatives for the use of autologous tissues for bone regeneration. In this study we describe a promising approach to a protein-free formation of bone-like apatite from amorphous precursors through ball-milling. The addition of Mg^{2+} ions is crucial to achieve full amorphization of calcium carbonate. Mg^{2+} incorporation generates defects which strongly retard a recrystallization of ball-milled Mg-doped amorphous calcium carbonate (BM-aMCC), which promotes the growth of osteoblastic and endothelial cells in simulated body fluid (SBF) and has no effect on endothelial cell gene expression. *Ex situ* snapshots of the processes with a combination of powder X-ray diffraction, transmission electron microscopy, Fourier-transform infrared and multimagic angle spinning nuclear magnetic resonance spectroscopy revealed the reaction mechanisms. For Mg contents of up to 30% a two phase system consisting of Mg-doped amorphous calcium carbonate and calcite "impurities" was formed. For high (>40%) Mg^{2+} contents BM-aMCC follows a different crystallization path *via* magnesian calcite and monohydrocalcite (MHC) to aragonite. While pure amorphous calcium carbonate crystallizes very rapidly to calcite in aqueous media, Mg-doped amorphous calcium carbonate forms in the presence of phosphate ions bone-like hydroxycarbonate apatite (HCA, dahllite), a single-phase carbonate apatite with carbonate substitution in both type A (OH^{-}) and type B (PO_4^{3-}) sites, which grows on calcite "impurities" *via* heterogeneous nucleation. This process was shown to produce an endotoxin-free material and makes BM-aMCC an excellent "ion storage buffer" that promotes cell growth by stimulating cell viability and metabolism with promising applications in the treatment of bone defects and bone degenerative diseases.

3.1.2 INTRODUCTION

The development of synthetic biomaterials with tailor-made properties that promote bone regeneration in orthopaedic and dental surgery has long been a goal of research.[1] Bone is a nanocomposite with a hierarchical structure ranging from the nano- to the macroscale.[2,3] Bone tissue engineering pursues different strategies to substitute biomaterials in native bone (e.g. hydroxyapatite (HA) and collagen).[1,4,5] Autocrafts (autologous bone) are considered as gold standard as they fulfill all requirements for bone regeneration in terms of osteoconduction, osteoinduction and osteogenesis.[6,7] Their limited supply leaves bone allo- or xenografts as alternatives for orthopaedic surgeons, as they are available in various forms and large quantities. They come, however, with drawbacks concerning biological variability and risk of viral or bacterial contaminations. Therefore, synthetic biomaterials are needed whose synthesis and manufacturing protocols must meet the demands and requirements of clinical applications.

These biomaterials include metals, polymers, ceramics, bioactive glasses, calcium sulfates, calcium carbonates and calcium phosphates (CaPs).[8] Fast-setting ionic cements are attractive materials for bone fillings. Calcium phosphate (CaP) cements are the most common bone replacement materials because of their bioactivity, osteoconductivity, injectability and moldability. Still, the rates of bioresorption of these cements must be enhanced to improve bone formation and regeneration.[9,10] Bioresorption critically depends on the solubility of the mineral constituents. Since calcium carbonate ($K_L \sim 10^{-8}$)[11] has a much higher solubility than apatite ($K_L \sim 10^{-54}$)[11] replacing calcium phosphate-based by calcium carbonate-based cements is a valid approach to obtain cements with improved and tuneable biodegradation rates.[12,13] Cements containing blends of calcium carbonate and calcium phosphate have been tested,[14] but only a few studies have dealt with cements containing exclusively calcium carbonate as mineral component.[15–18]

Calcium carbonate occurs in three anhydrous crystalline polymorphs, aragonite, calcite, and vaterite[19–23] as well as in two hydrated crystal phases, monohydrocalcite ($CaCO_3 \cdot 1H_2O$) (MHC)[24] and ikaite ($CaCO_3 \cdot 6H_2O$).[25] Calcite is the thermodynamically stable phase at ambient conditions, aragonite is the high-pressure form, vaterite is metastable and its occurrence associated with the early stages of $CaCO_3$ precipitation and nanosized crystal formation.[26,27] In waters with a Mg^{2+}/Ca^{2+} ratio > 1.5 (pH > 8.2)[28] and a saturation index of calcite < 0.8[29,30] aragonite formation is favored. The strong hydration of Mg^{2+} cations leads to changes of the crystallization pathways as shown by the formation of crystalline monoclinic hemihydrate $CaCO_3 \cdot ½H_2O$[31] and a monoclinic aragonite intermediate[32] with layered aragonite structure, where some carbonate anions are replaced by hydroxyl groups and up to 10 atomic % of Mg can be incorporated on the cation positions.

Amorphous calcium carbonate (ACC)[33,34] is a precursor of crystalline $CaCO_3$[35–38] which transforms into aragonite via anhydrous ACC[30] or via monohydrocalcite[39] through a series of ordering, dehydration, and crystallization processes.[40,41] Spectroccopic evidence suggested ACC to be a precursor of carbonated apatite,[42–44] the mineral building blocks of bone which contains a form of carbonated apatite similar to dahllite [$Ca_5(PO_4,CO_3)_3(OH)$], which is formed from an amorphous calcium phosphate (ACP) precursor.[45]

Applications of ACC as mineral component for bone regeneration have been hampered by its solubility, whereas the lower solubility of vaterite permits a slow transformation process from $CaCO_3$ to hydroxyapatite by acting as a solid ion buffer material.[17] The stability of ACC *in vivo* is controlled by a set of specialized proteins,[46] often in combination with Mg^{2+}. ACCs prepared *in vitro* at different pH have different solubility products and structural properties,[27,47] which lead to the hypothesis of ‘‘polyamorphous’’ $CaCO_3$.[48] Under *in vitro* conditions non-biogenic ACC can be stabilized by removal of water[49] or additives like (oligo)phosphates,[50], Mg^{2+} [51–53] or silica.[54]

Since biogenic ACCs contain Mg^{2+} ions and their Mg content is rather specific in different species and tissues,[36] structural information of Mg^{2+}-stabilized ACC (BM-aMCC) is needed to address the question of ‘‘amorphism’’ and crystallization. Importantly, any application of ACC, in particular of MgACC as support for bone regeneration requires its synthesis in large quantities with controlled and reproducible properties. Slow-diffusion processes that are popular for studying crystal growth[55] are difficult to scale-up. Typical large-scale routes to ACC are precipitation from solution,[56,57] but in typical single-batch processes only the initial reaction parameters (e.g. pH, supersaturation or ionic strength) are defined, and they change during the reaction. This lack of control makes scaling-up difficult and prevents intentional control of the parameters during the reaction. Ball-milling is a simple and established strategy for breaking down bulk materials to nano-size.[58,59] Defect formation over large scales leads to an amorphization of crystalline solids.[60] Still, the "molecular" processes during ball milling are not well understood, because standard *in situ* characterization tools for solids in the ball milling environment require crystalline analytes.[61–64] While non-crystalline solids elude structural analysis by diffraction, local probes like vibrational (IR, Raman)[65] and nuclear magnetic resonance (NMR) spectroscopy[66] or total scattering[64] can aid in their structural analysis. Since solid state transformations are typically diffusion limited and therefore slow, a step by step analysis, where “snapshots” are taken at different stages of the reaction, can be used to identify transient phases.[67,68]

We applied mechanochemistry for a large-scale synthesis of Mg^{2+}-stabilized ACC (BM-aMCC).[69] Mechanochemistry is useful for large applications because of its scalability. The transformation of calcite to aragonite in a mechanically operated mortar,[70] the reverse transformation from aragonite to calcite[71] or of vaterite to calcite[72,73] have been reported. We found that the insertion of Mg^{2+} into the ACC network retards the recrystallization of BM-aMCC dramatically and promotes the growth of osteoblastic and endothelial cells in simulated body fluid (SBF). Endothelial cells exhibited normal gene expression in the presence of BM-aMCC. The synthesis delivered large amounts to an endotoxin-free BM-aMCC material. We used powder X-ray diffraction (PXRD), *ex situ* Fourier transform infrared spectroscopy (FTIR), and magic angle spinning nuclear magnetic resonance ($^{1}H/^{13}C$ MAS NMR) spectroscopy as state of the art tools like to derive a picture of the crystallization pathways at the molecular level by studying the crystallinity, phase composition and the local atomic structure of the Ca^{2+} cations and the carbonate and phosphate groups.

3.1.3 RESULTS AND DISCUSSION

Synthesis

BM-aMCC was prepared by ball-milling. Basic magnesium carbonate ($4Mg(CO_3) \cdot Mg(OH)_2 \cdot 5(H_2O)$) and calcium carbonate (calcite) were dispersed in cyclohexane and ground in a planetary ball mill for 8 h at 720 rpm. Five different compositions of ball-milled amorphous magnesium calcium carbonate (BM-aMCC) were analyzed to find the optimum ratio of magnesium to calcium ions for clinical use. The values (10/20/30/40/50) indicate the percentage of magnesium carbonate in the starting material.

Structure analysis of amorphous starting materials

Figure 30a shows powder X-ray diffraction (PXRD) patterns of the products after 8 h of ball-milling. The absence of Bragg reflections and the modulation characteristics of the patterns are compatible with an “X-ray amorphous” product for BM-aMCC 50 %. For smaller magnesium contents, the prominent 104 reflection of the calcite starting material remained (Figure S18, Supporting Information). A minimum magnesium content of 30 % was required to achieve complete amorphization. We assume that a mixture of phase separated BM-aMCC and calcite is present for $MgCO_3$ contents $\leq$ 30%. Mg^{2+} cations are known to substitute Ca^{2+} in the calcite structure,[74] and we assume that a replacement of Ca^{2+} by Mg^{2+} cations stabilizes the non-crystalline phase after mechanochemical treatment.

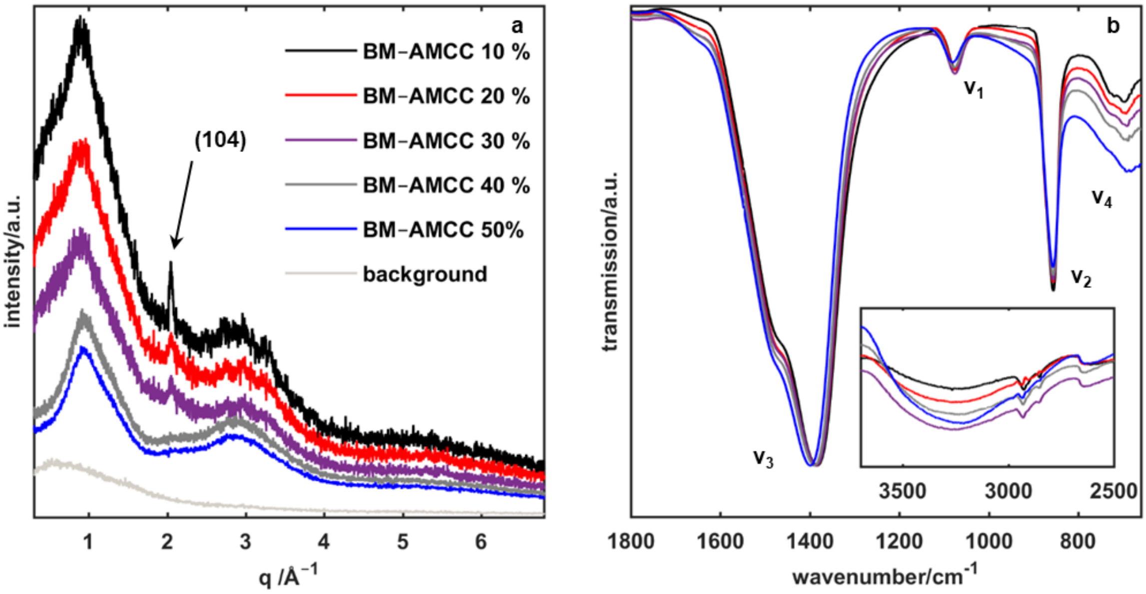

Figure 30. a) Powder X-ray diffractograms and b) FTIR spectra of ball-milled $CaCO_3$ and basic magnesian carbonate with different ratios (Mg/Ca 10-50 %).

Fourier-transform infrared (FT-IR) spectra of the amorphous products (Figure 30b) show the characteristic vibration modes of the carbonate ions in ACC: The symmetric stretch (ν_1 $\approx$ 1081 cm^{-1}), the out-of-plane mode ($\nu_2 \approx$ 857 cm^{-1}), the asymmetric stretch ($\nu_3 \approx$ 1400 and 1477 cm^{-1}) and the in-plane deformation mode ($\nu_4 \approx$ 689 and 733 cm^{-1}). All bands are broadened compared to those of the crystalline starting materials, indicating a less defined coordination of the carbonate anions. In addition, all bands are slightly shifted and the (symmetry forbidden in calcite) ν_1 band is present. The band at 1081 cm^{-1} can be assigned to the oxygen-hydrogen stretch (ν_{OH}) of basic magnesian carbonate. All samples are anhydrous, as supported by thermal analysis (Figure S19, Supporting Information). The bands at 2930 and 2852 cm^{-1} (asymmetric and symmetric C-H stretch of the CH_2 groups) are associated with cyclohexane, the dispersant medium. The bands remained, although the samples were dried in a vacuum oven. This indicates that the cyclohexane dispersant is trapped in inclusions of the amorphous solid (Figure S20, Supporting Information).

The loss of crystallinity with increasing Mg^{2+} cation content, which was observed in the X-ray diffractograms, is apparent from the FTIR spectra as well. The vibrational bands show slight positional shifts and changes in the full width at half maximum (FWHM) with increasing Mg^{2+} content. This can be explained by the change in crystallinity and the exchange of the (Pearson) softer[75] Ca^{2+} (Ca^{2+}: η=19.7) by harder Mg^{2+} (Mg^{2+}: η=32.5) cations.

Transmission electron microscopy (TEM) images and the associated diffraction patterns for BM-aMCC 30 and 50% confirm the complete lack of long-range order (Figure S20, Supporting Information). The morphology of the particles is very different compared to amorphous carbonates precipitated from solution,[76] and the particles have much larger diameters (up to 600 nm).

The crystallinity in the samples was quantified by deconvoluting the ν_2 band (of the out-of-plane mode) with a bimodal pseudo-Voigt function.[77] Since this vibrational mode is non-degenerate, the deconvoluted bands can be assigned to specific $CaCO_3$ phases (Figure S21, Supporting Information). Figure 31 shows the best fit results with the corresponding bands of the out-of-plane vibration mode. Samples with less than 30% magnesium content still contained a small portion of calcite. For a magnesium content of 40% the product was amorphous.

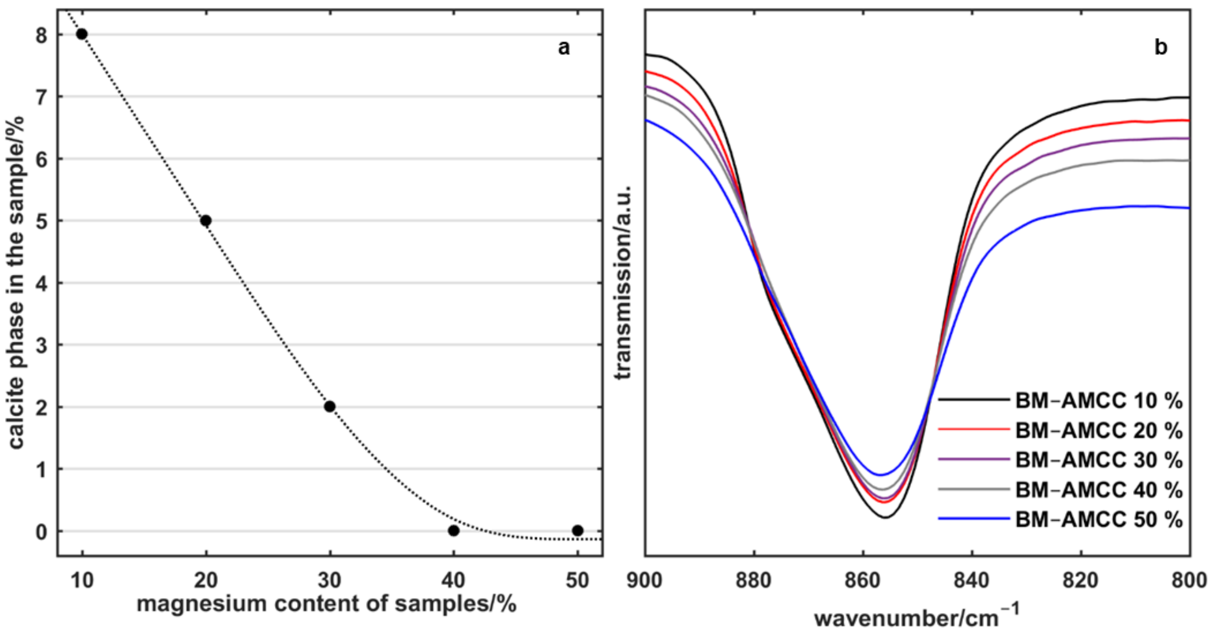

Figure 31. a) Contribution of crystalline calcite as a function of the Mg content (dotted black curve drawn to guide the eye). b) FTIR spectra that were used to determination the content of crystalline phases.

X-ray total-scattering experiments were performed to obtain insight into the local structure of the amorphous samples. The pair distribution function (PDF) was calculated from these data with *GudrunX4*. Figure 32 displays the PDF of humidic ACC from a previous study with 4 significant peaks. The first peak at 1.28 Å was assigned to the C-O distances of the carbonate anion. The most intense peak at 2.4 Å can be related to the Ca-O distances of the first coordination sphere. Further, the O-O distances contribute to this peak. The other two peaks at 4.1 Å and 6.2 Å result from a variety of different atomic distances (Figure S21, Supporting Information). We assume that the distances related with metal atoms have the most contribution to the intensity due to the in comparison higher atomic form factors. The PDF fade out clearly and become a virtually flat at about 7 Å indicating a lack of long-range order.

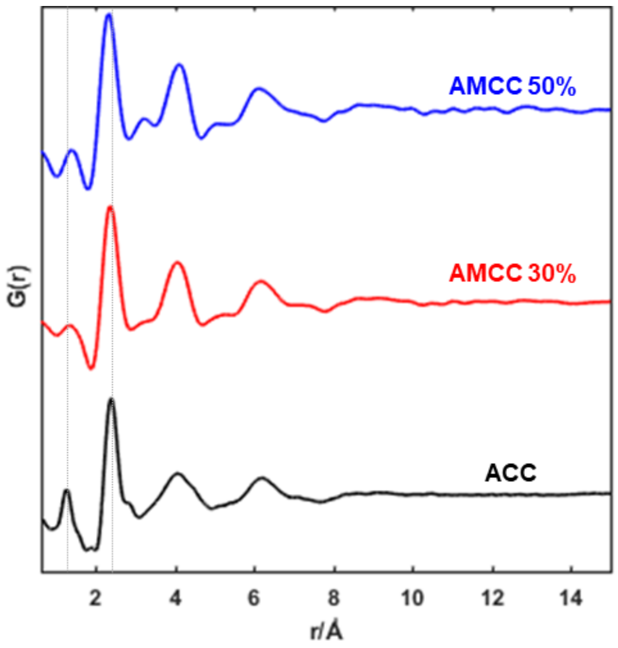

Figure 32. Pair distribution function (PDF) of humidic ACC (black), AMCC 30% (red) and AMCC 50% (blue).

The ball-milled samples are similar to the ACC reference. However, with higher magnesian content the C-O shifts to higher distances, in particular BM-aMCC 30% 1.36 Å and BM-aMCC 50% 1.4 Å. The magnesium ion polarizes the oxygen atom more strongly than the calcium ion which leads to an increase of the bond distance. Parallel to this the M-O distance decreases with higher magnesium content (BM-aMCC 30%: 2.38 Å; BM-aMCC 50%: 2.34 Å). An additonal peak at 3.24 Å appears for BM-aMCC 50%. Based on crystalline reference samples,[78] we assign this peak to Mg-Mg distances. These results indicate a stronger M-O binding (*vide* infra), which is a key aspect of the high hydration barrier of magnesian calcium carbonates.

The crystallization of the different BM-aMCCs in the presence of water was studied *ex situ* by FTIR spectroscopy. The crystallization of $CaCO_3$ is delayed kinetically in the presence of Mg^{2+} cations, which are known to have a large effect on $CaCO_3$ polymorph selection.[41,79] To evaluate the crystallization quantitatively, the ν_2 bands were fitted and their areas determined at different times of crystallization by normalizing to the areas of the respective crystalline or amorphous phases. Crystallization was assumed to proceeded according to the classical dissolution and recrystallization model. The dissolution process was fitted with a first-order kinetic model.[80] The formation of the thermodynamically stable phase was described kinetically with the Johnson-Mehl-Avrami-Kolmogorov (JMAK) model.[81,82]

(Supporting Information) Figure 33 shows the results of *ex situ* crystallization experiments for BM-aMCC (10, 20 and 30%) and the corresponding FTIR spectra for BM-aMCC 30%.

The phase transition of BM-aMCC 10, 20, and 30 % to calcite took essentially the same time in all cases. The crystallization rate decreased only slightly with increasing Mg content because of the calcite "nanograins" remaining after ball milling (Figure 33, *vide supra*). We assume that these calcite nanograins can act as seeds for heterogeneous nucleation and growth. This allows crystallization to proceed much faster than expected. Therefore, there is no clear trend in the rate constants except for the BM-aMCC 30% sample (with ~2% crystalline phase remaining), where the crystallization is slower.

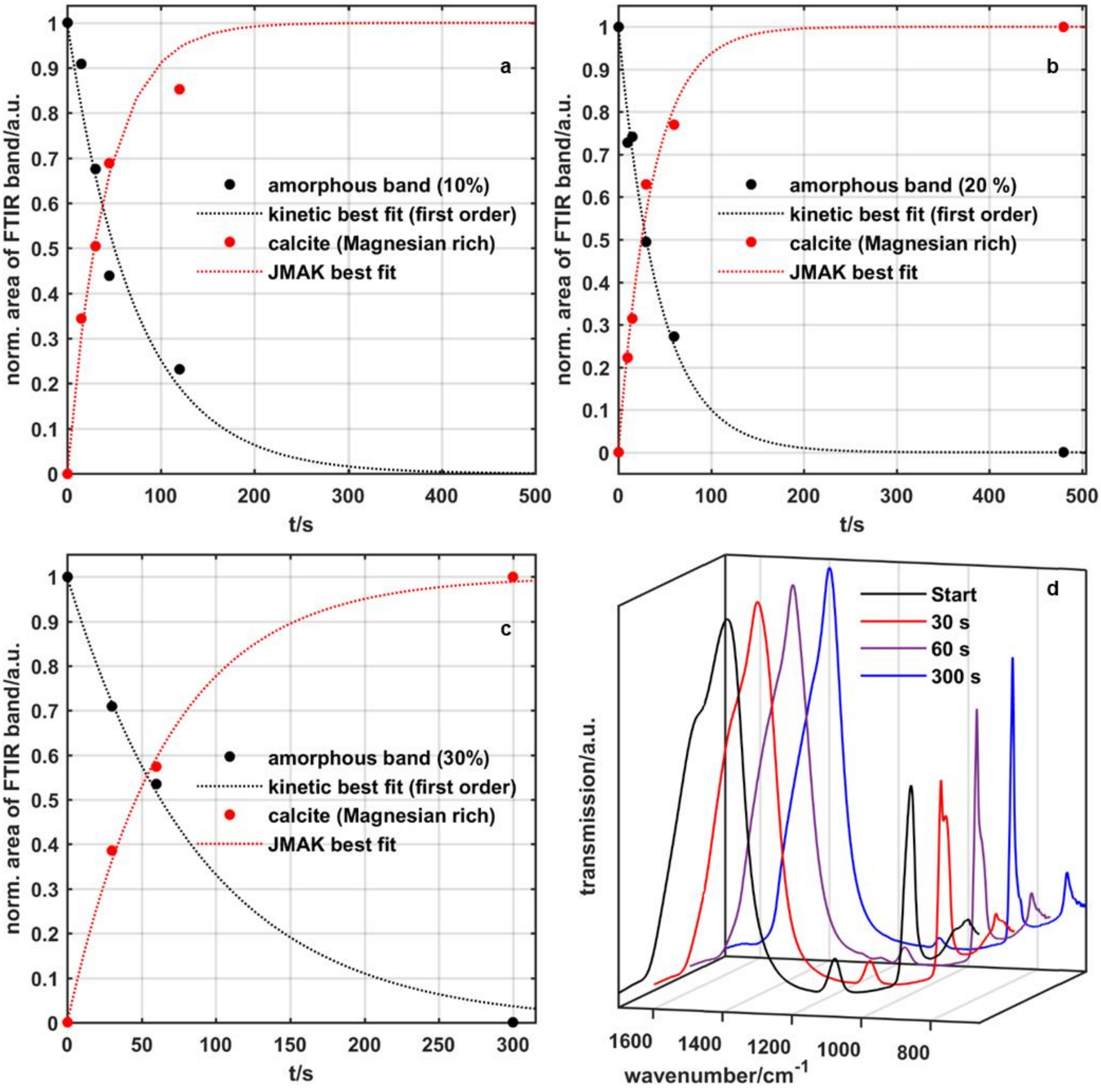

Figure 33. *Ex situ* (re-)crystallization curves of BM-aMCC 10-30 % a-c). The normalized area of the deconvoluted FTIR bands (ν_2 vibration mode) of the amorphous phase (black) and the calcite phase (red) are shown as a function of crystallization time in MQ water. The black dotted lines show a kinetic fit modelling

the solution process of the amorphous species. The red dotted curves display the best fit of a JMAK function. d) FTIR spectra for the (re-) crystallization of BM-aMCC 30 %.

However, the crystallization of BM-aMCC was significantly different when BM-aMCC 40 % was used as starting material. Here, the dissolution and recrystallization process required several days (Figure 34). Furthermore, the crystallization of BM-aMCC proceeded *via* magnesian calcite, and monohydrocalcite (MHC) to aragonite. Since the bands of the ν_2 vibration mode of MHC and magnesium rich calcite appear almost at the same wavenumbers, we could not perfom JMAK fits. A trend line describes the simultaneous formation and dissolution of both phases.

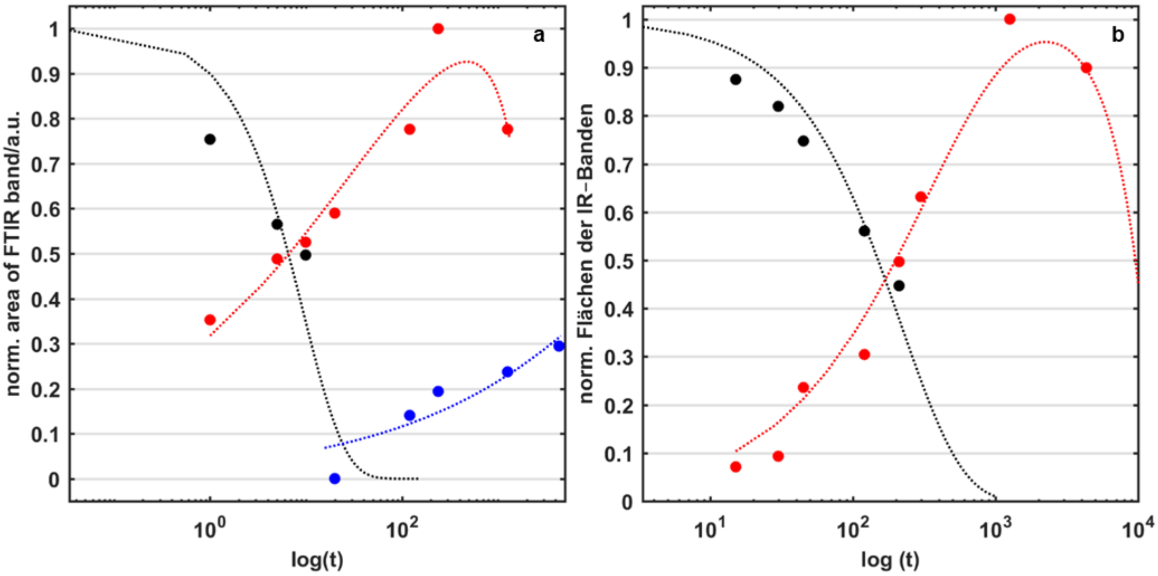

Figure 34. *Ex situ* (re-)crystallization curves of BM-aMCC 40-50 % a-b). Logarithmic plot of normalized area of the deconvoluted FTIR bands (ν_2 vibration mode) of the amorphous phase (black) , calcite phase (red) and aragonite phase (blue) are shown as a function of crystallization time in MQ water. The red lines diplays a guide line for the recrystallization and solution of a mixture of magnesian rich calcite as well as monohydro calcite.

It has been shown before that MHC is formed in the presence of high Mg^{2+} concentrations during the crystallization of calcium carbonate.[83] Magnesium-rich calcite is highly soluble at high Mg^{2+} concentrations. In addition, MHC can accommodate large amounts of Mg^{2+} cations. Therefore, the Pearson-hard Mg^{2+} cation is not fully dehydrated, thereby kinetically and energetically stabilizing the MHC phase (enthalpy of hydration: $\Delta H_{Mg^{2+}} = -1908\ \frac{kJ}{mol}, \Delta H_{Ca^{2+}} = -1577\ \frac{kJ}{mol}$). Finally, phase separation occurs, when aragonite is formed. Mg^{2+} cations are not incorporated into the aragonite structure because the ionic radius of Mg^{2+} is too small to be compatible with coordination number (CN) 9.[30]

Incubation in simulated body fluid

Based on the crystallization behavior, we selected a “stabilized” material (30%) with a suitable reactivity for transforming into a bone-like material in SBF. For a BM-aMCC 30% sample we tested whether its (i) dissolution and recrystallization leads to one of the $CaCO_3$ phases, (ii) whether the amorphous phase is sufficiently stabilized and (iii) whether very high Mg^{2+} concentrations concentrations have a stimulating effect on the growth of osteoblastic MG63 and primary human umbilical vein endothelial cells (HUVEC) cells.

For this purpose, BM-aMCC was incubated at 37°C in SBF. The incubation was monitored *ex situ* by FTIR spectroscopy. Figure 35 shows the FTIR spectra of BM-aMCC 30% (with ACC as reference) as a function of time. Table 2 summarizes the vibrational modes of the carbonate and phosphate ions before and after incubation. During incubation of ACC the ν_2 band of the CO_3^{2-} anion shifted to higher wavenumbers and an additional band appeared at 711 cm^{-1}. Both, the shift of the ν_2 band and the presence of the ν_4 band (in-plane deformation mode) of the CO_3^{2-} anion at 711 cm^{-1} clearly show the formation of calcite.[84] The progression in the ν_2 (out-of-plane) band at 872 cm (Figure 35b) indicates that the amount of calcite remained constant, and apatite started to form after 6 h (Table 2). The band at 962 cm^{-1} indicated the formation of crystalline apatite.[85] The position and intensity of the vibrational bands show the simultaneous formation of a two phase system consisting of calcite and hydroxyapatite, because pure and non-stabilized ACC is metastable and recrystallizes as calcite after spontaneous dissolution in water. This dissolution/recrystallization process of ACC occurs very rapidly. Therefore, hydroxyapatite crystallites grow on calcite particles through heterogeneous nucleation or precipitation due to the increasing Ca^{2+} concentration.

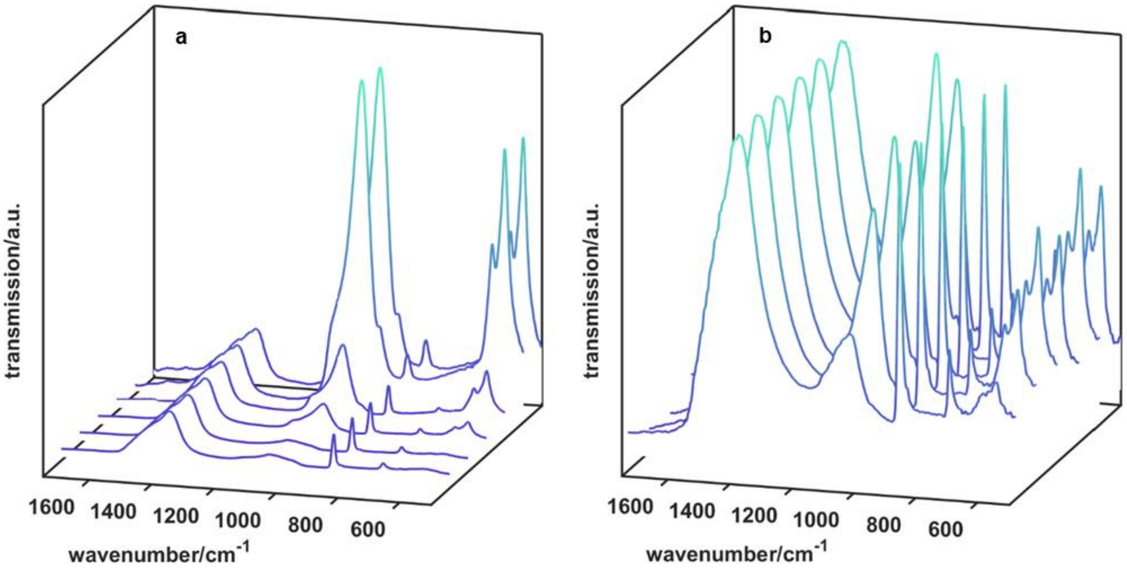

Figure 35. Incubation of a) BM-aMCC (0.2 mg/mL) and b) ACC (0.2 mg/mL) in simulated body fluid (SBF) after 6, 12, 24, 48, 72 h and 7d. After 48 hours the FTIR spectra of BM-aMCC show a rapid growth of a semi-crystalline carbonate rich apatite. In contrast, incubation of ACC with SFB shows the crystallization of phase separated calcite and hydroxy apatite.

In contrast, apatite and calcite formation is strongly retarded kinetically with BM-aMCC 30%. Phosphate bands indicating the formation of a calcium phosphates were detected after 12 h of incubation in SBF. The initial broadening of the bands and the weak splitting of the P-O band indicate the formation of an amorphous phosphate; the splitting became more pronounced during incubation according to Ostwald-Volmer rule.[86] In BM-aMCC, the ν_1 and ν_4 bands of the phosphate group are shifted to lower wavenumbers compared to their positions in HA or to the bands of ACC incubated with SBF. The ν_4 band of the CO_3^{2-} anion vanishes completely. This indicates the formation of a (bone-like) hydroxycarbonate apatite (HCA, dahllite), a single-phase carbonate apatite, with carbonate substitutions in both type A ($OH^–$) and type B ($PO_4^{3–}$) sites.[87] The compatibility with the poorly defined and strongly broadened ν_1 band indicates the presence of small and strongly disordered domains due to the carbonate substitution.[88]

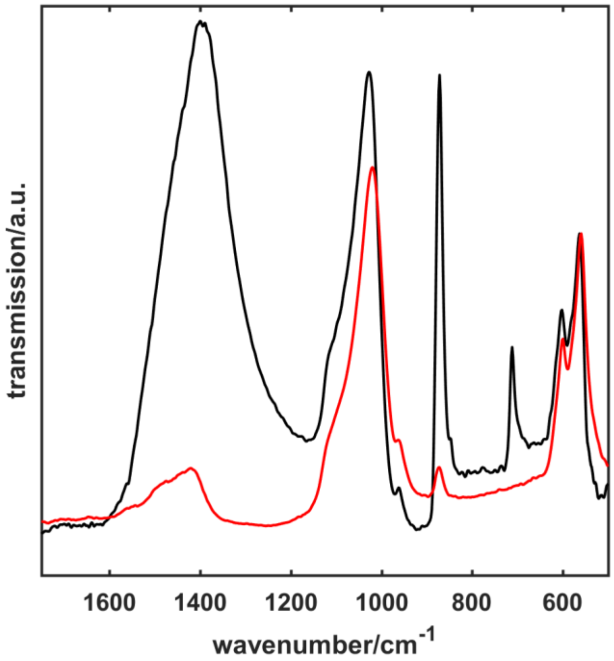

Figure 36. Comparison of the FTIR spectra of aMCC (red) and ACC (black) after an incubation time of 7 days (without background correction).

Table 3. Vibrational modes of the carbonate (ν_1 symmetric stretch, ν_2 out-of-plane, ν_3 asymmetric stretch, ν_4 in-plane deformation) and phosphate ions (ν_1 symmetric stretch, ν_3 asymmetric stretch, ν_4 in-plane deformation) in ACC, aMCC, calcite, ACC, and aMCC in SBF, HA, and bone.

		ACC	aMCC	Calcite	ACC in SBF	aMCC in SBF	HA *nano*	bone
CO_3^{2-}	ν_1	1074	1081	1089	–	–	–	–
	ν_2	860	857	872	872	874	–	873
	ν_3	1389	1400 1477	1388	1398	1420 ≈1450	–	1420 1448
	ν_4	–	689 733	711	712	–	–	–
PO_4^{3-}	ν_1	–	–	–	962	962	962	962
	ν_3	–	–	–	1030	1020	1031	1022
	ν_4	–	–	–	563 579 602	560 578 602	562 575 603	561 600

Figure 36 shows the FTIR spectra at the end of the incubation period. Table 3 compiles the positions of the bands with the corresponding assignments. The ACC sample (incubated with SBF) contains crystalline calcite and hydroxyapatite, but incubation of BM-aMCC 30 % leads to the formation of a carbonate apatite with the typical band positions listed in Table 3. The BM-aMCC 30% sample shows plate-like morphology (S22, Supporting Information).

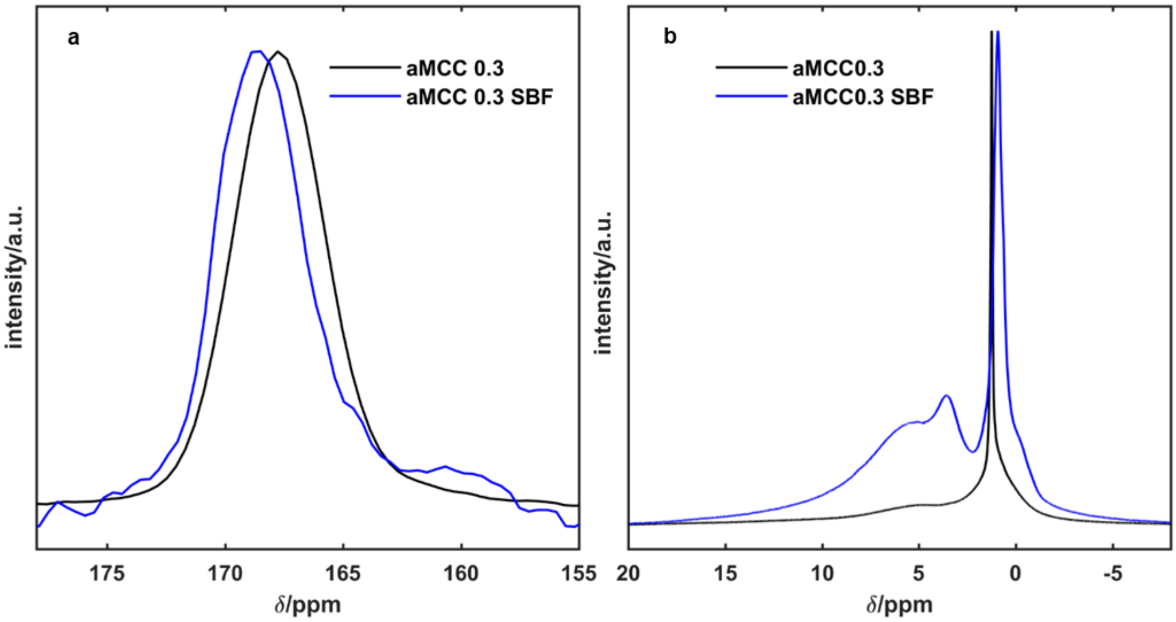

Figure 37. a) ^{13}C CP-MAS-NMR and b) ^{1}H-MAS-NMR spectra of aMCC before (black line) and after (blue line) incubation.

Solid-State NMR Spectroscopy

^{13}C-NMR spectroscopy can distinguish between different carbonate phases due to its sensitivity to the specific electronic environments of the carbonate groups.[84] The FWHM of the resonance bands provides information about the crystallinity of the samples.[89] Sharp resonances are characteristic for a crystalline sample, boad resonances indicate structurally disordered or nanocrystalline samples. Figure 37 shows ^{13}C-CP-MAS-NMR spectra of BM-aMCC with 2 ms contact times before (Figure 37a) and after (Figure 37b) incubation. The spectrum of the BM-aMCC sample shows a broad signal (FWHM=449.3 Hz) at 167.7 ppm, which is typical for amorphous calcium carbonate. After incubation in SBF, the signal becomes asymmetric and shifts downfield. Deconvolution of the spectrum reveals three different carbonate environments (Figure S23, Supporting Information). The signal at 168.4 ppm is due to to low crystalline calcite (FWHM=366.4 Hz), the signal at 165 ppm is due to the potassium hydrogen carbonate from the simulated body fluid buffer, and the signal at 170.0 ppm results from the carbonate apatite. The signals at ~56 ppm are due to the TRIS buffer of the simulated body fluid (Figure S24, Supporting Information).

The ^{1}H-MAS-NMR spectrum of BM-aMCC displays three signals. The sharp signal at 1.2 ppm is associated with cyclohexane trapped in grain boundaries (*vide* FTIR spectra), the signal at -0.2 ppm is due to hydroxide ions of the basic magnesian carbonate starting material. The broad signal at ~5 ppm is related to small amounts of structural water. After incubation in SBF the ^{1}H-MAS-NMR spectrum of BM-aMCC displays 4 resonances, which are related to the organic buffer and the washing agent ethanol (0.9 and 3.5 ppm), entrapped water (~ 5.0 ppm), and hydroxide ions of hydroxyapatite and basic magnesian carbonate (~ -0.2 ppm). The resonance related to entrapped cyclohexane has vanished, indicating a rearrangement of BM-aMCC after incubation in SBF.

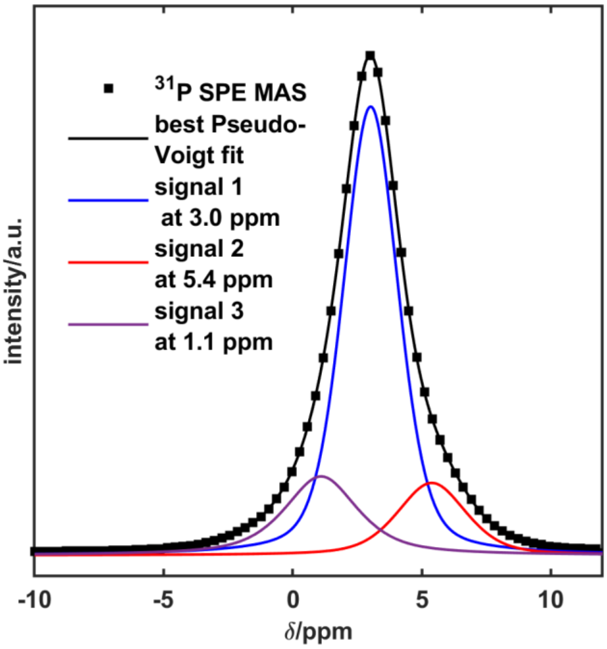

Figure 38. ^{31}P-SPE-MAS NMR spectrum of BM-aMCC 30 % after incubation in SBF. After deconvolution, the signal displays three different electronic environments.

Figure 38 shows the ^{31}P-SPE-MAS NMR spectrum of incubated BM-aMCC 30%. The signal is dominated by a broad resonance at 3.0 ppm (FWHM=178.0 Hz), which is assigned to bulk orthophosphate. Since deprotonated phosphate groups are less shielded, the signal at 5.4 ppm is associated with deprotonated surface phosphate groups (FWHM=404.7 Hz). The signal at ~1.1 ppm (FWHM=534.2 Hz) shows the presence of hydrogen phosphate groups. The signals are broad, indicating a nano-crystalline or a disordered system.

Figure 39 shows the ^{1}H-^{31}P HETCOR spectrum of BM-aMCC 30% incubated in SBF, recorded with contact times of 20 and 2000 μs. The HETCOR spectrum recorded with a short-range contact time of 20 μs reveals correlations between the proton signal at 11.0 ppm and the broad signal at ~2.0 ppm. This signal is related to HPO_4^{2-} ions, which have been reported for bone minerals and Ca-deficient apatite minerals.[90] The broad resonance at ~6 ppm in the ^{31}P spectrum with short-range contact time (20 μs) shows no correlation with any ^{1}H resonance. This indicates that this signal is related to deprotonated surface phosphate groups. Long-range contact times show correlations of the phosphor resonance with the resonances at -0.53 (presumably HA) and 5.3 ppm (structural water).

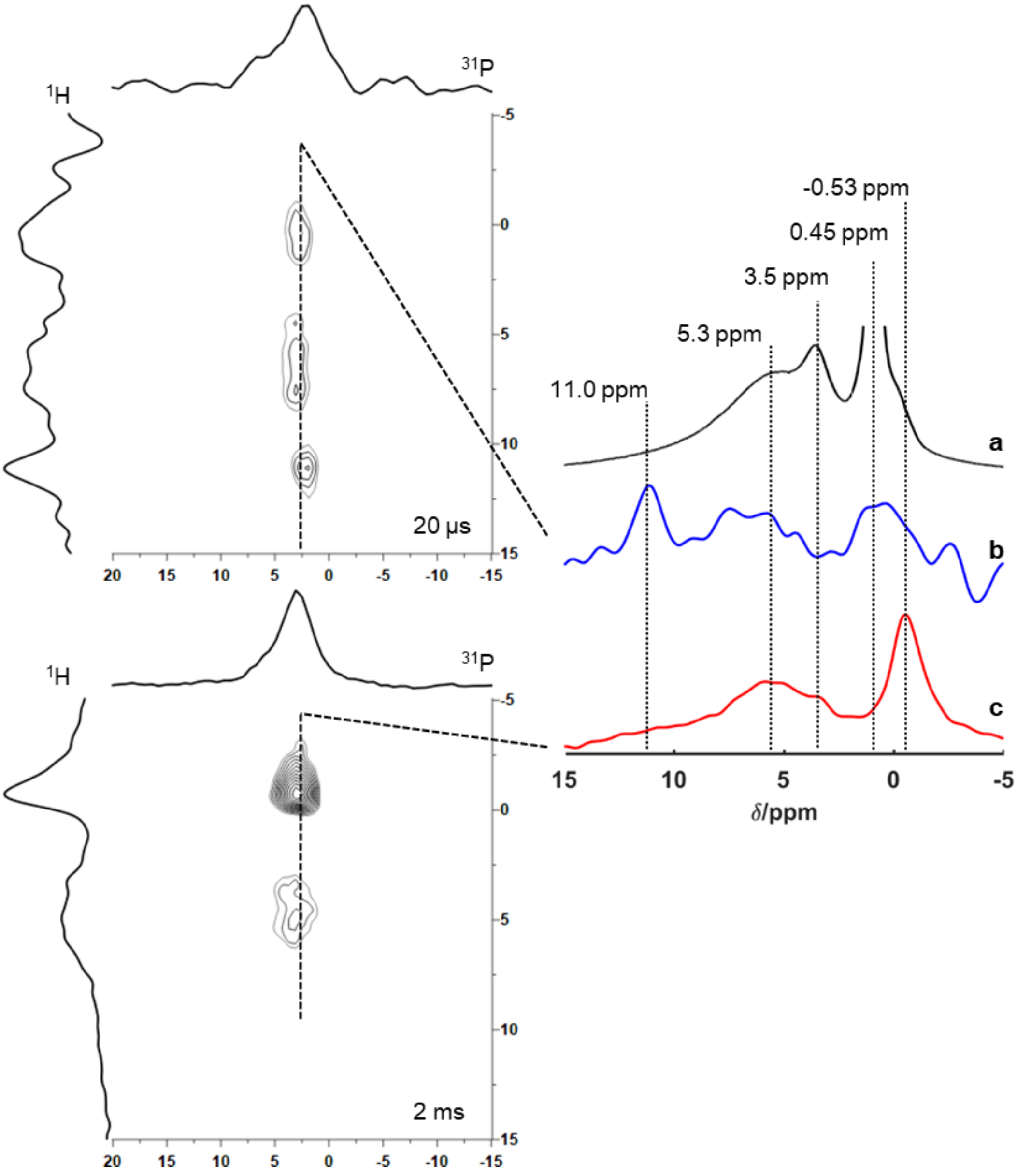

Figure 39. ^{1}H-^{31}P HETCOR spectra of BM-aMCC 30 % incubated in SBF with short range contact times (top left) and long range contact times (bottom left). The corresponding ^{1}H projections are shown on the right side.

Cyctotoxicity and Cell Viability of BM-aMCC *in vitro*

The cell compatibility of BM-aMCC particles was investigated using two complementary methods, The cellular metabolic activity was tested with a resazurin (RES) cell viability assay. Resazurin is a non-fluorescent dye that is taken up by cells. Viable cells with active metabolism can reduce resazurin to resorufin product which is pink and fluorescent. The integrity of the cell membrane after particle exposure was determined with an lactate dehydrogenase (LDH) assay.[91] The occurance of LDH in cell supernatants is an indicator of damage to the cell membrane which in turn is an indicator of cell death. It is used to determine cytoxicity. The results are illustrated side by side in Figure 40.

The RES assay shows no significant changes during incubation times up to 72 h and for particle exposure concentrations of up to 250µg/mL. Exposure of the osteoblast cell line MG-63 to BM-aMCC particles did not lead to a decrease of the cell metabolic activity, i.e., the viability of the cells is not effected by increasing concentrations of BM-aMCC and longer exposure times. Similarly, physiologically very low LDH concentrations were observed in all cell supernatants from cells exposed to varying concentrations of BM-aMCC at various time points of exposure (Figure 40b). They were comparable to LDH values observed in the supernatant of untreated cells. Increasing concentrations of BM-aMCC for varying time points had no effect on cell metabolism or cytotoxic effects. This indicates that BM-aMCC is highly cell-compatible.

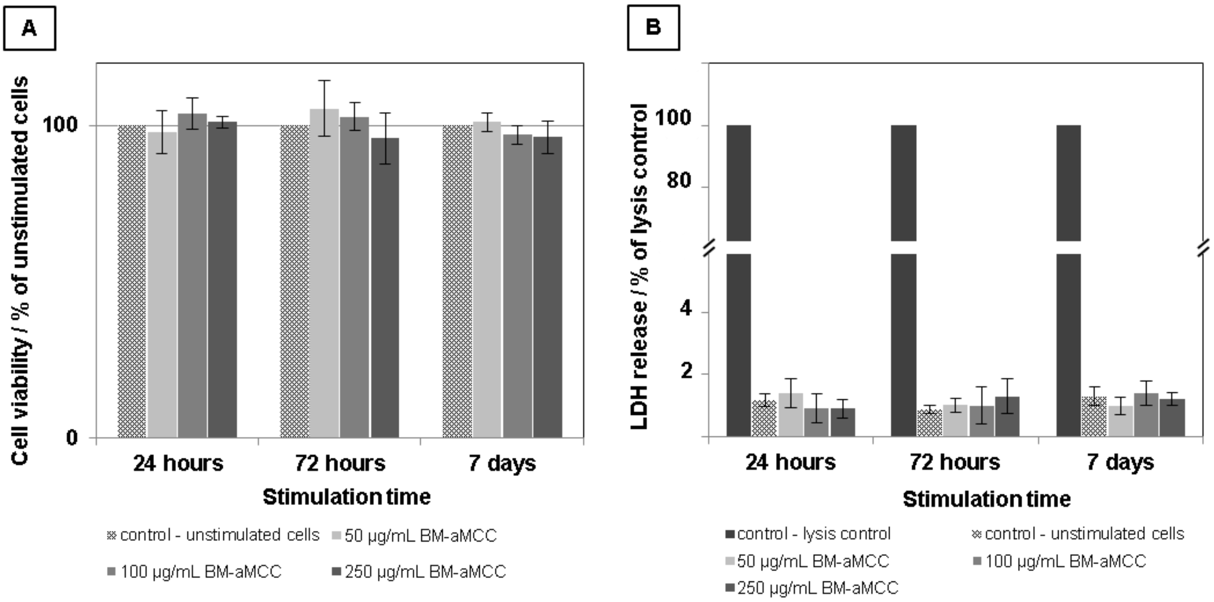

Figure 40. Analysis of the metabolism and membrane integrity of cells cultured with increasing concentrations of BM-aMCC at various time points. a) shows the metabolism of cells exposed to BM-aMCC compared to control cells by measuring the conversion of resazurin to resorufin, b) the membrane integrity as measure by the amount of LDH present in the supernatant as described in the Experimental Section.

Cell proliferation and biocompatibility

Cell biocompatibility is essential for *in vivo* experiments and futher clinical applications.[92] The cell biocompatibility of BM-aMCC was examined using two different cell types by monitoring cell growth in the presence of BM-aMCC with the fluorescent dye calcein-AM dye. The dye is taken up and retained in living cells with an intact membrane[92] and converted into the membrane-nonpermeable and fluorescent calcein dye by intracellular esterases. In this way,

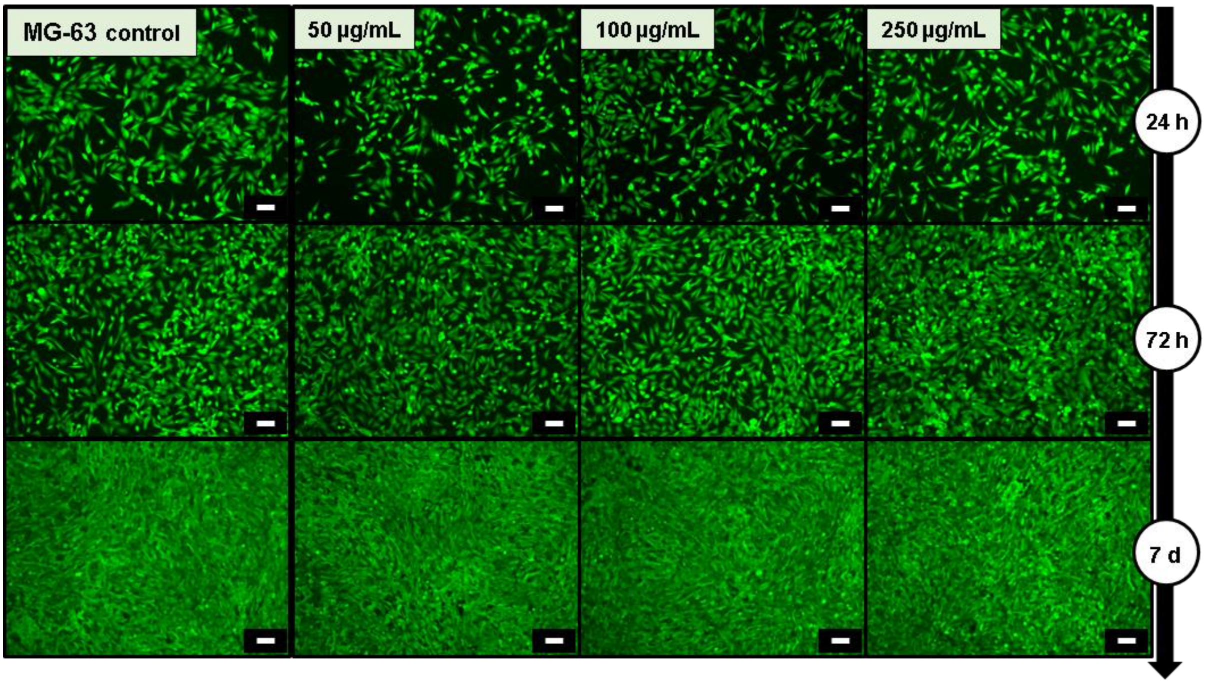

Figure 41. Cell biocompatibility of BM-aMCC particles tested on MG-63. Cells were treated with different concentrations (50 µg/mL, 100 µg/mL, 250 µg/mL) of BM-aMCC for 1, 3 and 7 days under cell culture conditions. Viable cells are indicated by green fluorescence (calcein-AM staining). Scale bar corresponds to 100 nm.

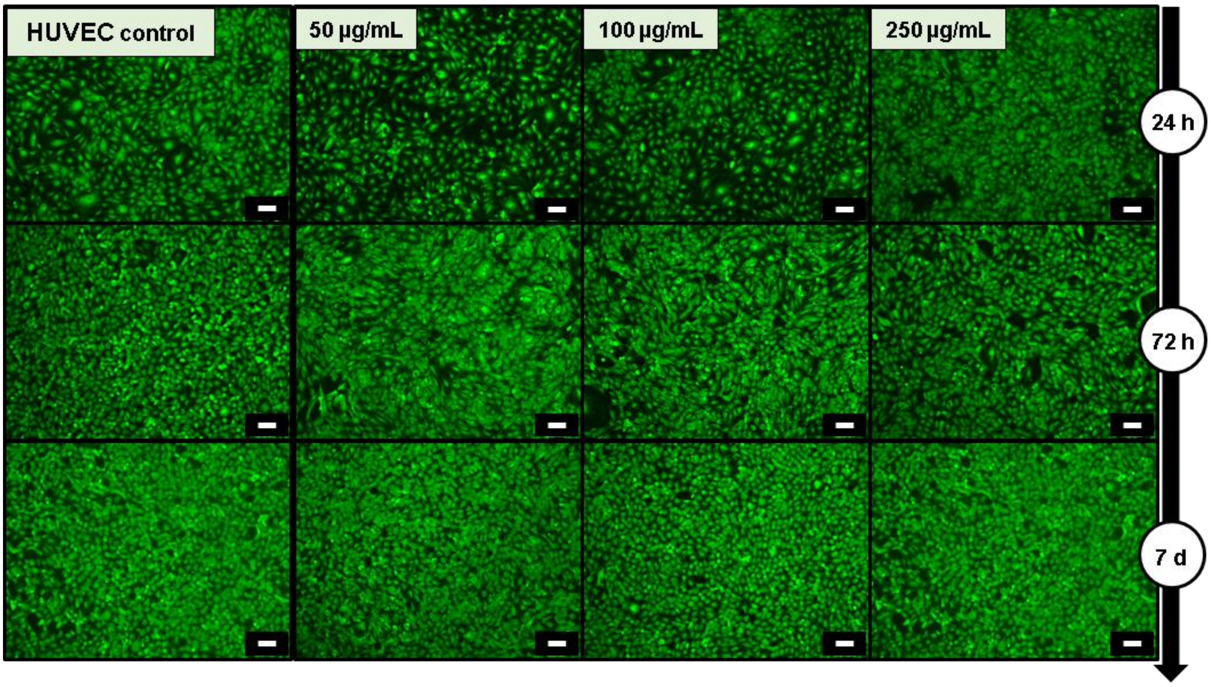

Figure 42. Cell biocompatibility of BM-aMCC particles tested on HUVEC. Cells were treated with different BM-aMCC concentrations (50 µg/mL, 100 µg/mL, 250 µg/mL) for 1, 3 and 7 days under cell culture conditions. Viable cells are indicated by green fluorescence (calcein-AM staining). Scale bars correspond to 100 nm.

cell proliferation and cell morphology can be investigated to evaluate the cell viability and cell biocompatibility. Figure 41 and 42 show fluorescence microscopy images of the osteoblastic cell line MG63 and the primary human umbilical vein endothelial cells (HUVEC) cells at various time points up to 7 days after the addition of varying concentrations of BM-aMCC particles (50µg/mL, 100µg/mL, 250µg/mL) and in the absence of BM-aMCC.

Figure 12 and 13 show that both osteoblast and endothelial cells proliferated with time. Similar amounts of cells were observed with increasing concentration of BM-aMCC. Monolayers of cells exhibited a morphology similar to monolayers in non-exposed cells were. No rounded-up, detached cells were observed with increasing concentration of BM-aMCC or with increasing time. This indicated that BM-aMCC had no effect on cell morphology or the attachment of cells. Overall, the presence of BM-aMCC particles have no effect on cell attachment, viability, metabolism and proliferation indicating that BM-aMCC is highly cell compatible.

Endotoxin presence and effects on endothelial cell gene expression by BM-aMCC

The absence of endotoxin in a compound/material designated for use in humans is essential. Also, a material should have no effect on the gene expression of endothelial cells making up the vasculature and cells that responsible for the first response to a foreign material introduced into the body. The rapid induction of E-selectin in endothelial cells in the presence of endotoxin has been previously reported and has been adapted as a rapid test for the presence of endotoxin in biomaterials.[93] Figure 43a shows the expression of E-selectin (green stain within the cell) after stimulation of cells for 4 h with endotoxin (LPS) and Figure 43b shows the control HUVEC (no LPS, no green staining). Figure 43c shows that BM-aMCC cultured with HUVEC resulted in no induction of E-selectin, indicating that the synthesis procedure of BM-aMCC was not contaminated with endotoxin. This same test can also be used to examine the effects of a biomaterial on normal endothelial cell gene expression.[94] HUVEC will show an induction of E-selectin under inflammatory conditions when in contact with a biomaterial. Figure 43d shows that HUVEC cultured with BM-aMCC expressed E-selectin when inflammatory stimulating conditions were applied (mimicked by the addition of LPS). Thus, HUVEC growing with BM-aMCC exhibit normal endothelial cell gene expression in response to an inflammatory agent.

3.1.4 CONCLUSIONS

We have demonstrated a promising alternative for the use of biodegradable materials with potential bone targeting capability based on a magnesium substituted amorphous calcium carbonate nanoparticles prepared in large amounts by ball milling. Amorphous calcium carbonate is inherently labile to ensure the presence of an "ion buffer" for bone regeneration, while still being sufficiently reactive to form hydroxycarbonate apatite. A combination of powder X-ray diffractometry, transmission electron microscopy, multimagic angle spinning nuclear magnetic resonance spectroscopy and *in-situ* FT-IR spectroscopy showed the transformation of BM-aMCC nanoparticles to hydroxycarbonate apatite crystals with low crystallinity upon incubation in simulated body fluid at human body temperature.

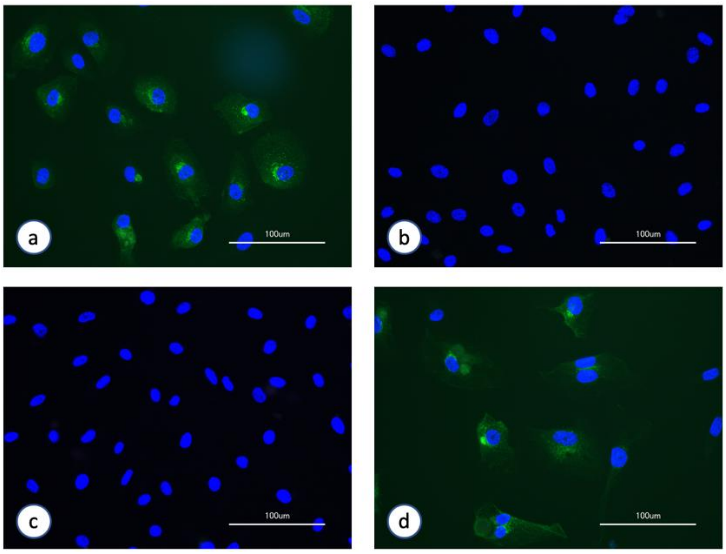

Figure 43. Evaluation of the presence of endotoxin and induction of E-selectin of endothelial cells in the presence of BM-aMCC. Nuclei were stained blue (DAPI) and the presence of E-selectin on cells was stained green via immunostaining as described in the Experimental Section. a) HUVEC cells cultured with LPS showing induction of E-selectin (green). b) HUVEC cells cultured without LPS showing absence of E-selectin. c) HUVEC cells in the presence of BM-aMCC showing no induction of E-selectin (no green staining) indicating the absence of endotoxin. d) HUVEC cells in the presence of BM-aMCC and LPS showing induction of E-selectin indicating no inhibition of E-selectin induction by BM-aMCC when cells are stimulated with an inflammatory agent (LPS). This indicates normal endothelial gene functioning when cells are grown with BM-aMCC.

Addition of Mg^{2+} ions is crucial to achieve full amorphization of calcium carbonate in ball milling reactions. The incorporation of Mg^{2+} cations generates defects that strongly retard a recrystallization of ball-milled Mg-doped amorphous calcium carbonate. Mg^{2+}

incorporation also promotes the growth of osteoblastic and endothelial cells in simulated body fluid (SBF). A combination of powder X-ray diffraction, transmission electron microscopy, Fourier-transform infrared and multimagic angle spinning nuclear magnetic resonance spectroscopy revealed the mechanistic reaction paths for Mg-doped ACC for different Mg contents. While pure amorphous calcium carbonate crystallizes very rapidly to calcite in aqueous media, a two phase system consisting of Mg-doped amorphous calcium carbonate and calcite "impurities" was formed for Mg contents of up to 30%. For higher (>30%) Mg^{2+} contents BM-aMCC follows a different crystallization path *via* magnesian calcite and monohydrocalcite (MHC) to aragonite. For Mg contents < 30% Mg-doped amorphous calcium carbonate forms in the presence of phosphate ions bone-like hydroxycarbonate apatite (HCA, dahllite), a single-phase carbonate apatite with carbonate substitution in both type A (OH^-) and type B (PO_4^{3-}) sites, which grows on calcite "impurities" through heterogeneous nucleation. BM-aMCC is fully biodegradable as it serves as a *storage buffer material for bone-forming cells* for regeneration of new bone tissue. BM-aMCC was shown to be free of endotoxin and to exhibit no inflammatory potential. This may have prospects for future applications in the treatment of bone defects and bone degenerative diseases. The results presented in this work demonstrate important aspects of BM-aMCC crystallization, which contributes to the understanding of composite material design.

3.1.5 Experimental Section

Materials. Calcite (98%, Socal 31, Solvay), calcium carbonate-^{13}C (99 atom % ^{13}C, isotec), cyclohexane (Analytical reagent grade, Fisher Chemicals), ethanol (absolute 99.8+%, Fisher Chemicals) and milliQ deionized water.

Synthesis of Amorphous Calcium Magnesian Carbonate. Calcite (0.100 g, 1 mmol) was treated with different amounts of basic magnesian carbonate (*e.g.* aMCC 0.5: 0.064 g, 1 mmol per magnesian ion) in a planetary ball mill (Pulverisette 7 Classic, Fritsch). The starting materials and 10 mL of cyclohexane were transferred together with 3.65 grams of grinding balls (about 1100 balls, 1 mm diameter, ZrO_2) into ZrO_2 grinding jars. The mixture was milled for certain times at 720 rpm. To avoid overheating, alternate 10 minutes of grinding and then a 10 minute rest phase were used. Therefore, 480 min of ball milling results in 950 minutes of reaction time. Afterward, the cyclohexane was removed with a pipette. The product was dispersed in ethanol and separated from the grinding balls by decanting. The product was isolated by centrifugation and dried *in vacuo*.

Characterization

X-ray Powder Diffraction. X-ray diffractograms were recorded with a STOE Stadi P equipped with a Mythen 1k detector using Mo Kα_1 radiation (λ=0.7093 Å). The dry samples were prepared between polyvinyl acetate foils in perfluoroether (Fomblin Y, Aldrich). The measurements were performed in the 2θ range from 2° to 45° with a step size of 0.015° (continuous scan, 150 s/deg). Crystalline phases were identified according to the PDF-2 database using Bruker AXS.

ATR-FTIR Spectroscopy. The attenuated total reflection (ATR) FTIR spectra were recorded on a Nicolet iS10 spectrometer (Thermo scientific) using a frequency range from 650 to 4000 cm^{-1} with a resolution of 1.4 cm^{-1} per data point.

Solid-State NMR Spectroscopy. All solid state NMR spectra were recorded on a Bruker Advance 400 DSX NMR spectrometer (Bruker BioSpin GmbH, Rheinstteten, Germany operated by Topspin 1.3, 2007, patchlevel 8) at a ^{1}H frequency of 399.87 MHz, ^{13}C frequency of 100.55 MHz and ^{31}P frequency of 161.87 MHz. A commercial 3 channel 4 mm Bruker probe head at 10 kHz magic angle spinning (MAS) was used for all experiments. The ^{1}H NMR spectra and ^{1}H background corrected spectra were recorded averaging 32 transients with 8 s recycle delay. For all solid-state ^{13}C cross-polarization (CP) magic angle spinning (MAS) NMR experiments, an initial 90° pulse with 4.0 μs length and 5 s recycle delay were used. A ramped CP pulse (from 64 to 100%) with duration of 20 μs, 50 μs, 100 μs, 200 μs, 500 μs, 1 ms, 2 ms, 3 ms, 5 ms and 7 ms was used for recording the CP build-up curves. Two pulse phase modulation (TPPM) ^{1}H decoupling scheme was used while acquiring the ^{13}C signal. 512 transients were averaged for the CP experiments. The spectra were baseline-corrected and a broadening of 30 Hz was applied. Quantitative ^{13}C single pulse excitation experiments allowing full relaxation have been recorded averaging 16 transients with a recycle delay of 2200 s and TPPM heteronuclear decoupling. The spectrum was background corrected and a broadening of 30 Hz was applied. The ^{1}H-^{13}C heteronuclear correlation (HETCOR) 2D NMR spectra were acquired using ^{1}H-^{13}C magnetization transfer with contact times of 50 and 2000 μs and 256 transients/t1. The data points recorded were 1 k (t1) and 96 or 128 (t2) and zero-filled to 4 k (t1) and 256 (t2) before the 2D Fourier transformation. The other parameters were identical to those for the 1D CP NMR experiments. Single pulse excitation ^{31}P experiments were recorded using 60 s recycle delay averaging 16 scans under TPPM heteronuclear decoupling while acquiring the NMR signal. For all ^{31}P cross-polarization (CP) magic angle spinning (MAS) NMR experiments, an initial 90° pulse with 4.0 μs length and 5 s recycle delay were used. A ramped CP pulse (from 64 to 100%) with duration of 20 μs, 50 μs, 100 μs, 250 μs, 500 μs, 1 ms, 2 ms, 3 ms, 4 ms and 5 ms was used for recording the CP build-up curves. Two pulse phase modulation (TPPM) ^{1}H decoupling scheme was used while acquiring the ^{31}P signal. Transients of 64 were averaged for the CP experiments. The spectra were baseline-corrected and a broadening of 30 Hz was applied. The ^{1}H-^{31}P heteronuclear correlation (HETCOR) 2D NMR spectra were acquired using ^{1}H-^{31}P magnetization transfer with contact times of 20 and 2000 µs and 64 transients/t1. The data points recorded were 2 k (t1) and 128 (t2) and zero-filled to 4 k (t1) and 256 (t2) before the 2D Fourier transformation. The other experimental parameters were identical to those for the 1D CP NMR experiments. Spectral deconvolution and fitting the intensity decrease in the spin-echo experiments were performed using self-written MatLab scripts (version 2017b).

Thermal Analysis. Coupled thermogravimetry-differential thermal analysis (TG-DTA) was carried out at a Netzsch STA 449 F3 Jupiter device. About 10 mg of the sample was heated in an alumina cup in argon atmosphere from 50 to 900 °C at a heating rate of 10 K/min.

Transmission Electron Microscopy (TEM). Samples were prepared by drop-casting 20 µL of the respective sample dispersion on 400 mesh carbon copper grids (Plano GmbH, Wetzlar, Germany) and measured with a Technai Spirit G2 at 120 kV acceleration voltage, equipped with a standard 4K CCD camera.

Total Scattering. Total scattering measurements of amorphous earth alkali metal carbonate hydrogen phosphates were performed at beamline P02.1 at Petra III, DESY, Germany using an X-ray energy of 60 keV ($\lambda = 0.20724$ Å). All samples were prepared in a 0.5 mm borosilicate capillary and measured in transmission mode with a 2D Perkin Elmer area detector with 2048 x 2048 pixels. The exposure time for each sample was 15 min. The resulted 2D images were integrated by using the program DAWNscience. The analysis of the atomic pair distribution function (PDF) was performed utilizing the Gudrun X software using an empty capillary (0.5 mm) for background subtraction with Qmax = 24 Å-1.

Synthesis of SBF (Simulated Body Fluid). Simulated body fluid was prepared using the method of synthesis described by Kokubo and Takadama.[95] The pH of the SBF solution was adjusted to pH 7.37 at 37°C with 1M HCl.

Cells and Growth Conditions. Two different cell types were used for the *in vitro* studies. The human osteoblast cell line MG-63 (ATCC® CRL-1427®, LGC Promochem) was cultivated in Dulbecco's Modified Eagle Medium ([DMEM], high glucose, Sigma Aldrich), 10% fetal bovine serum ([FBS], Sigma Aldrich) + 2mM Glutamax I (Gibco® Thermo Fisher Scientific) + 100 U/100 µg/mL penicillin/streptomycin (Gibco® Thermo Fisher Scientific).

Human endothelial cells were isolated from the umbilical cord (human umbilical vein endothelial cells [HUVEC]) from various donors according to the procedure of Jaffe et al.[96] HUVEC were cultured in M199 (Sigma Aldrich) + 20% FBS (Sigma Aldrich) + 2mM Glutamax I (Gibco Thermo

Fisher Scientific) + 100 U/100 µg/ml penicillin/streptomycin (Gibco Thermo Fisher Scientific) + 25 µg/ml endothelial growth factor supplement (ECGS; Becton Dickinson and Company) + 25 µg/ml heparin sodium salt (Sigma Aldrich) in a humidified atmosphere at 37 °C and 5% CO_2.

In Vitro Cyctoxicity and Cell Viability. The cytotoxicity and viability tests were carried out with the MG-63 cell line. The tests were performed by seeding 25,000 cells per well in a sterile flat-bottom 96-well cell culture plate (Greiner, bio-one Cellstar) and cultivated for 24 hours prior to adding BM-aMCC particles at concentrations of 50 µg/mL, 100 µg/mL and 250 µg/mL. Cells with particles were incubated for 24 and 72 hours and for 7 days. In addition, unstimulated cells and wells with the equivalent particle concentrations but without cells were prepared as controls. All experiments were carried out three times and with three technical replicates. The results of the resazurin (RES) assay (see belwo) were presented as a percentage of the unstimulated cell control. The viability of the cell control was set at 100% for this analysis. The results of lactate dehydrogenase (LDH) assay were presented as percent of lysis of the cell control cytotoxicity set to 100%. A student's t-test Type 3 was performed for statistical significance and is indicated as $*p < 0.05$.

RES Assay. The resazurin cell viability assay is a fluorescence assay that detects cellular metabolic activities. The non-fluorescent, deep purple resazurin dye is irreversibly reduced by dehydrogenases in metabolically active cells to deep red, strongly red-fluorescent resorufin. The fluorescence can be measured at an excitation wavelength of 530 - 560 nm and an emission wavelength of 580 – 600 nm using a Tecan spark plate reader. Resazurin was prepared by dissolving 20 mg resazurin (Sigma) in 100 ml Hanks' balanced salt solution with Mg^{2+} and Ca^{2+} (Sigma). At the respective time points, 20 µl of this solution was added to each 96-well and incubated for 3 hr. After this, fluorescene in wells was determined using wavelengths described above. The fluorescence signal is proportional to the number of living cells.

LDH Assay. The toxicity of exposure to BM-aMCC particles on MG-63 cells was determined by measuring LDH released into the cell supernatant. The LDH was measured using the LDH CytoTox 96® nonradio cytotoxicity assay (Promega, G1780) following the manufacturer's instructions.

Cell Proliferation and Biocompatibility Studies. Cell biocompatibility of BM-aMCC particles was evaluated with the MG-63 cell line as well as with primary HUVEC cells. Cells were seeded at 50,000 cells per well with MG-63 or 80,000 cells per well with HUVEC in a 24-well cell culture plate (Greiner bio-one Cellstar) and cultivated for 24h in a humidified atmosphere prior to adding various concentartions (50 µg/mL, 100 µg/mL 250 µg/mL) of BM-aMCC. All cell culture plates with HUVEC were coated with gelatin (0.2%, Sigma–Aldrich) prior to the addition of cells and were performed with three different donors, each in passage 3. The studies with MG-63 were double determinations using 2 different passages of the cells. Untreated cells were used as controls. The cells were evaluated optically using fluorescence microscopy (BZ-9000E BIOREVO, Keyence) at three different time points (24 hours, 72 hours, 7 days). To detect live cells, 10 µg/mL of the fluorescent dye calcein-AM (ThermoFischer) was added to each well and incubated for 10 min at humidified atmosphere[92] prior to examination.

Endotoxin and Gene Regulation Studies. Testing for the presence of endotoxin in BM-aMCC and examining endothelial gene expression was carried out as previously described.[97] HUVEC were plated into 8-well chamber slides (Nunc, Sigma-Aldrich, Germany) and were incubated overnight. The next day, 1 µg of BM-aMCC, 1 µg of LPS in PBS (E. coli lipopolysaccharide, Sigma-Aldrich, Germany) or a combination of both was added to individual wells with the cells and incubated for 4 h. Non-treated cells acted as control. After 4 h, cells were rinsed briefly with PBS and then fixed with 4% paraformaldehyde in PBS for 15 min at room temperature, washed 4X with PBS and then permeabilized with 0.5% Triton-X 100 for 10min. After washing four times with PBS, antibody (1:100, E-selectin, Monosan, Netherlands) was added and incubated overnight at 4˚C. Cells were then washed four times with PBS and the secondary antibody (1:1000, anti-mouse Alexa Fluor 488, Molecular Probes) was added and incubated for 1 h at room temperature. After washing 3X with PBS, cells were stained with Hoechst 33342 (1:10,000 in PBS, Thermo Fisher Scientific, Dreieich, Germany) for 5 min RT and washed three times. Finally, the transwell chamber was removed and the cells on the slide were mounted with Fluoromount-GTM (Southern Biotech, Birmingham, AL, USA). Images were obtained using a fluorescence microscope (BZ-9000E BIOREVO, Keyence, Germany).”

3.1.6 REFERENCES

(1) Amini, A. R.; Laurencin, C. T.; Nukavarapu, S. P. Bone Tissue Engineering: Recent Advances and Challenges. *Crit. Rev. Biomed. Eng.* **2012**, *40* (5), 363–408. https://doi.org/10.1615/critrevbiomedeng.v40.i5.10.

(2) Gupta, H. S.; Seto, J.; Wagermaier, W.; Zaslansky, P.; Boesecke, P.; Fratzl, P. Cooperative Deformation of Mineral and Collagen in Bone at the Nanoscale. *Proc. Natl. Acad. Sci.* **2006**, *103* (47), 17741–17746. https://doi.org/10.1073/pnas.0604237103.

(3) Gong, T.; Xie, J.; Liao, J.; Zhang, T.; Lin, S.; Lin, Y. Nanomaterials and Bone Regeneration. *Bone Res.* **2015**, *3* (1), 15029. https://doi.org/10.1038/boneres.2015.29.

(4) Place, E. S.; Evans, N. D.; Stevens, M. M. Complexity in Biomaterials for Tissue Engineering. *Nat. Mater.* **2009**, *8* (6), 457–470. https://doi.org/10.1038/nmat2441.

(5) Wegst, U. G. K.; Bai, H.; Saiz, E.; Tomsia, A. P.; Ritchie, R. O. Bioinspired Structural Materials. *Nat. Mater.* **2015**, *14* (1), 23–36. https://doi.org/10.1038/nmat4089.

(6) Bauer, T. W.; Muschler, G. F. Bone Graft Materials. An Overview of the Basic Science. *Clin. Orthop.* **2000**, No. 371, 10–27.

(7) Wang, W.; Yeung, K. W. K. Bone Grafts and Biomaterials Substitutes for Bone Defect Repair: A Review. *Bioact. Mater.* **2017**, *2* (4), 224–247. https://doi.org/10.1016/j.bioactmat.2017.05.007.

(8) Habraken, W.; Habibovic, P.; Epple, M.; Bohner, M. Calcium Phosphates in Biomedical Applications: Materials for the Future? *Mater. Today* **2016**, *19* (2), 69–87. https://doi.org/10.1016/j.mattod.2015.10.008.

(9) Tsai, C.-H.; Lin, R.-M.; Ju, C.-P.; Chern Lin, J.-H. Bioresorption Behavior of Tetracalcium Phosphate-Derived Calcium Phosphate Cement Implanted in Femur of Rabbits. *Biomaterials* **2008**, *29* (8), 984–993. https://doi.org/10.1016/j.biomaterials.2007.10.014.

(10) O'Neill, R.; McCarthy, H. O.; Montufar, E. B.; Ginebra, M.-P.; Wilson, D. I.; Lennon, A.; Dunne, N. Critical Review: Injectability of Calcium Phosphate Pastes and Cements. *Acta Biomater.* **2017**, *50*, 1–19. https://doi.org/10.1016/j.actbio.2016.11.019.

(11) Ball, J. W.; Nordstrom, D. K. WATEQ4F -- User's Manual with Revised Thermodynamic Data Base and Test Cases for Calculating Speciation of Major, Trace and Redox Elements in Natural Waters. *Open-File Rep.* **1991**, 90–129.

(12) Heughebaert, J. C.; Nancollas, G. H. Kinetics of Crystallization of Octacalcium Phosphate. *J. Phys. Chem.* **1984**, *88* (12), 2478–2481. https://doi.org/10.1021/j150656a012.

(13) Brečević, L.; Nielsen, A. E. Solubility of Amorphous Calcium Carbonate. *J. Cryst. Growth* **1989**, *98* (3), 504–510. https://doi.org/10.1016/0022-0248(89)90168-1.

(14) Khairoun, I.; Boltong, M. G.; Driessens, F. C. M.; Planell, J. A. Effect of Calcium Carbonate on the Compliance of an Apatitic Calcium Phosphate Bone Cement. *Biomaterials* **1997**, *18* (23), 1535–1539. https://doi.org/10.1016/S0142-9612(97)80005-1.

(15) Combes, C.; Miao, B.; Bareille, R.; Rey, C. Preparation, Physical–Chemical Characterisation and Cytocompatibility of Calcium Carbonate Cements. *Biomaterials* **2006**, *27* (9), 1945–1954. https://doi.org/10.1016/j.biomaterials.2005.09.026.

(16) Tolba, E.; Müller, W. E. G.; Abd El-Hady, B. M.; Neufurth, M.; Wurm, F.; Wang, S.; Schröder, H. C.; Wang, X. High Biocompatibility and Improved Osteogenic Potential of Amorphous Calcium Carbonate/Vaterite. *J. Mater. Chem. B* **2016**, *4* (3), 376–386. https://doi.org/10.1039/C5TB02228B.

(17) Schröder, R.; Pohlit, H.; Schüler, T.; Panthöfer, M.; Unger, R. E.; Frey, H.; Tremel, W. Transformation of Vaterite Nanoparticles to Hydroxycarbonate Apatite in a Hydrogel Scaffold: Relevance to Bone Formation. *J. Mater. Chem. B* **2015**, *3* (35), 7079–7089. https://doi.org/10.1039/C5TB01032B.

(18) Schröder, R.; Besch, L.; Pohlit, H.; Panthöfer, M.; Roth, W.; Frey, H.; Tremel, W.; Unger, R. E. Particles of Vaterite, a Metastable $CaCO_3$ Polymorph, Exhibit High Biocompatibility for Human Osteoblasts and Endothelial Cells and May Serve as a Biomaterial for Rapid Bone Regeneration. *J. Tissue Eng. Regen. Med.* **2018**, *12* (7), 1754–1768. https://doi.org/10.1002/term.2703.

(19) De Keyser, W. L.; Degueldre, L. Contribution à l’étude de La Formation de La Calcite, Aragonite et Vatérite. *Bull. Sociétés Chim. Belg.* **2010**, *59* (1–2), 40–71. https://doi.org/10.1002/bscb.19500590105.

(20) Wray, J. L.; Daniels, F. Precipitation of Calcite and Aragonite. *J. Am. Chem. Soc.* **1957**, *79* (9), 2031–2034. https://doi.org/10.1021/ja01566a001.

(21) Swanson, H. E.; Fuyat, Ruth K.; Ugrinic, G. M. *Standard X-Ray Diffraction Powder Patterns*; National Bureau of Standards, 1953; Vol. 4.

(22) Huggins, M. L. The Crystal Structures of Aragonite (CaC O 3) and Related Minerals. *Phys. Rev.* **1922**, *19* (4), 354–362. https://doi.org/10.1103/PhysRev.19.354.

(23) Mugnaioli, E.; Andrusenko, I.; Schüler, T.; Loges, N.; Dinnebier, R. E.; Panthöfer, M.; Tremel, W.; Kolb, U. Ab Initio Structure Determination of Vaterite by Automated Electron Diffraction. *Angew. Chem. Int. Ed.* **2012**, *51* (28), 7041–7045. https://doi.org/10.1002/anie.201200845.

(24) Effenberger, H. Kristallstruktur und Infrarot-Absorptionsspektrum von synthetischem Monohydrocalcit, CaCO3�H2O. *Monatshefte F�r Chem.* **1981**, *112* (8–9), 899–909. https://doi.org/10.1007/BF00905061.

(25) Marland, G. The Stability of CaCO3·6H2O (Ikaite). *Geochim. Cosmochim. Acta* **1975**, *39* (1), 83–91. https://doi.org/10.1016/0016-7037(75)90186-6.

(26) Morse, J. W.; Arvidson, R. S.; Lüttge, A. Calcium Carbonate Formation and Dissolution. *Chem. Rev.* **2007**, *107* (2), 342–381. https://doi.org/10.1021/cr050358j.

(27) Gebauer, D.; Völkel, A.; Cölfen, H. Stable Prenucleation Calcium Carbonate Clusters. *Science* **2008**, *322* (5909), 1819–1822. https://doi.org/10.1126/science.1164271.

(28) De Choudens-Sanchez, V.; Gonzalez, L. A. Calcite and Aragonite Precipitation Under Controlled Instantaneous Supersaturation: Elucidating the Role of CaCO3 Saturation State and Mg/Ca Ratio on Calcium Carbonate Polymorphism. *J. Sediment. Res.* **2009**, *79* (6), 363–376. https://doi.org/10.2110/jsr.2009.043.

(29) Riechelmann, S.; Schröder-Ritzrau, A.; Wassenburg, J. A.; Schreuer, J.; Richter, D. K.; Riechelmann, D. F. C.; Terente, M.; Constantin, S.; Mangini, A.; Immenhauser, A. Physicochemical Characteristics of Drip Waters: Influence on Mineralogy and Crystal Morphology of Recent Cave Carbonate Precipitates. *Geochim. Cosmochim. Acta* **2014**, *145*, 13–29. https://doi.org/10.1016/j.gca.2014.09.019.

(30) Sun, W.; Jayaraman, S.; Chen, W.; Persson, K. A.; Ceder, G. Nucleation of Metastable Aragonite $CaCO_3$ in Seawater. *Proc. Natl. Acad. Sci.* **2015**, *112* (11), 3199–3204. https://doi.org/10.1073/pnas.1423898112.

(31) Zou, Z.; Habraken, W. J. E. M.; Matveeva, G.; Jensen, A. C. S.; Bertinetti, L.; Hood, M. A.; Sun, C.; Gilbert, P. U. P. A.; Polishchuk, I.; Pokroy, B.; Mahamid, J.; Politi, Y.; Weiner, S.; Werner, P.; Bette, S.; Dinnebier, R.; Kolb, U.; Zolotoyabko, E.; Fratzl, P. A Hydrated Crystalline Calcium Carbonate Phase: Calcium Carbonate Hemihydrate. *Science* **2019**, *363* (6425), 396–400. https://doi.org/10.1126/science.aav0210.

(32) Németh, P.; Mugnaioli, E.; Gemmi, M.; Czuppon, G.; Demény, A.; Spötl, C. A Nanocrystalline Monoclinic $CaCO_3$ Precursor of Metastable Aragonite. *Sci. Adv.* **2018**, *4* (12), eaau6178. https://doi.org/10.1126/sciadv.aau6178.

(33) Gower, L. B.; Odom, D. J. Deposition of Calcium Carbonate Films by a Polymer-Induced Liquid-Precursor (PILP) Process. *J. Cryst. Growth* **2000**, *210* (4), 719–734. https://doi.org/10.1016/S0022-0248(99)00749-6.

(34) Gower, L. B. Biomimetic Model Systems for Investigating the Amorphous Precursor Pathway and Its Role in Biomineralization. *Chem. Rev.* **2008**, *108* (11), 4551–4627. https://doi.org/10.1021/cr800443h.

(35) Addadi, L.; Raz, S.; Weiner, S. Taking Advantage of Disorder: Amorphous Calcium Carbonate and Its Roles in Biomineralization. *Adv. Mater.* **2003**, *15* (12), 959–970. https://doi.org/10.1002/adma.200300381.

(36) Weiner, S. STRUCTURAL BIOLOGY: Choosing the Crystallization Path Less Traveled. *Science* **2005**, *309* (5737), 1027–1028. https://doi.org/10.1126/science.1114920.

(37) Farhadi-Khouzani, M.; Chevrier, D. M.; Zhang, P.; Hedin, N.; Gebauer, D. Water as the Key to Proto-Aragonite Amorphous $CaCO_3$. *Angew. Chem. Int. Ed.* **2016**, *55* (28), 8117–8120. https://doi.org/10.1002/anie.201603176.

(38) Walker, J. M.; Marzec, B.; Nudelman, F. Solid-State Transformation of Amorphous Calcium Carbonate to Aragonite Captured by CryoTEM. *Angew. Chem. Int. Ed.* **2017**, *56* (39), 11740–11743. https://doi.org/10.1002/anie.201703158.

(39) Zhang, Z.; Xie, Y.; Xu, X.; Pan, H.; Tang, R. Transformation of Amorphous Calcium Carbonate into Aragonite. *J. Cryst. Growth* **2012**, *343* (1), 62–67. https://doi.org/10.1016/j.jcrysgro.2012.01.025.

(40) Radha, A. V.; Forbes, T. Z.; Killian, C. E.; Gilbert, P. U. P. A.; Navrotsky, A. Transformation and Crystallization Energetics of Synthetic and Biogenic Amorphous Calcium Carbonate. *Proc. Natl. Acad. Sci.* **2010**, *107* (38), 16438–16443. https://doi.org/10.1073/pnas.1009959107.

(41) Albéric, M.; Bertinetti, L.; Zou, Z.; Fratzl, P.; Habraken, W.; Politi, Y. The Crystallization of Amorphous Calcium Carbonate Is Kinetically Governed by Ion Impurities and Water. *Adv. Sci.* **2018**, *5* (5), 1701000. https://doi.org/10.1002/advs.201701000.

(42) Bentov, S.; Zaslansky, P.; Al-Sawalmih, A.; Masic, A.; Fratzl, P.; Sagi, A.; Berman, A.; Aichmayer, B. Enamel-like Apatite Crown Covering Amorphous Mineral in a Crayfish Mandible. *Nat. Commun.* **2012**, *3* (1), 839. https://doi.org/10.1038/ncomms1839.

(43) Ibsen, C. J. S.; Chernyshov, D.; Birkedal, H. Apatite Formation from Amorphous Calcium Phosphate and Mixed Amorphous Calcium Phosphate/Amorphous Calcium Carbonate. *Chem. - Eur. J.* **2016**, *22* (35), 12347–12357. https://doi.org/10.1002/chem.201601280.

(44) Nitiputri, K.; Ramasse, Q. M.; Autefage, H.; McGilvery, C. M.; Boonrungsiman, S.; Evans, N. D.; Stevens, M. M.; Porter, A. E. Nanoanalytical Electron Microscopy Reveals a Sequential Mineralization Process Involving Carbonate-Containing Amorphous Precursors. *ACS Nano* **2016**, *10* (7), 6826–6835. https://doi.org/10.1021/acsnano.6b02443.

(45) Wang, Y.; Von Euw, S.; Fernandes, F. M.; Cassaignon, S.; Selmane, M.; Laurent, G.; Pehau-Arnaudet, G.; Coelho, C.; Bonhomme-Coury, L.; Giraud-Guille, M.-M.; Babonneau, F.; Azaïs, T.; Nassif, N. Water-Mediated Structuring of Bone Apatite. *Nat. Mater.* **2013**, *12* (12), 1144–1153. https://doi.org/10.1038/nmat3787.

(46) Aizenberg, J.; Lambert, G.; Weiner, S.; Addadi, L. Factors Involved in the Formation of Amorphous and Crystalline Calcium Carbonate: A Study of an Ascidian Skeleton. *J. Am. Chem. Soc.* **2002**, *124* (1), 32–39. https://doi.org/10.1021/ja016990l.

(47) Gebauer, D.; Gunawidjaja, P. N.; Ko, J. Y. P.; Bacsik, Z.; Aziz, B.; Liu, L.; Hu, Y.; Bergström, L.; Tai, C.-W.; Sham, T.-K.; Edén, M.; Hedin, N. Proto-Calcite and Proto-Vaterite in Amorphous Calcium Carbonates. *Angew. Chem. Int. Ed.* **2010**, *49* (47), 8889–8891. https://doi.org/10.1002/anie.201003220.

(48) Cartwright, J. H. E.; Checa, A. G.; Gale, J. D.; Gebauer, D.; Sainz-Díaz, C. I. Calcium Carbonate Polyamorphism and Its Role in Biomineralization: How Many Amorphous Calcium Carbonates Are There? *Angew. Chem. Int. Ed.* **2012**, *51* (48), 11960–11970. https://doi.org/10.1002/anie.201203125.

(49) Ihli, J.; Kulak, A. N.; Meldrum, F. C. Freeze-Drying Yields Stable and Pure Amorphous Calcium Carbonate (ACC). *Chem. Commun.* **2013**, *49* (30), 3134. https://doi.org/10.1039/c3cc40807h.

(50) Müller, W. E. G.; Neufurth, M.; Huang, J.; Wang, K.; Feng, Q.; Schröder, H. C.; Diehl-Seifert, B.; Muñoz-Espí, R.; Wang, X. Nonenzymatic Transformation of Amorphous $CaCO_3$ into Calcium Phosphate Mineral after Exposure to Sodium Phosphate in Vitro: Implications for in Vivo Hydroxyapatite Bone Formation. *ChemBioChem* **2015**, *16* (9), 1323–1332. https://doi.org/10.1002/cbic.201500057.

(51) Yang, S.-Y.; Chang, H.-H.; Lin, C.-J.; Huang, S.-J.; Chan, J. C. C. Is Mg-Stabilized Amorphous Calcium Carbonate a Homogeneous Mixture of Amorphous Magnesium Carbonate and Amorphous Calcium Carbonate? *Chem. Commun.* **2016**, *52* (77), 11527–11530. https://doi.org/10.1039/C6CC04522G.

(52) Purgstaller, B.; Goetschl, K. E.; Mavromatis, V.; Dietzel, M. Solubility Investigations in the Amorphous Calcium Magnesium Carbonate System. *CrystEngComm* **2019**, *21* (1), 155–164. https://doi.org/10.1039/C8CE01596A.

(53) Zhang, J.; Dong, C.; Sun, Y.; Yu, J. Mechanism of Magnesium's Influence on Calcium Carbonate Crystallization: Kinetically Controlled Multistep Crystallization. *Cryst. Res. Technol.* **2018**, *53* (8), 1800075. https://doi.org/10.1002/crat.201800075.

(54) Kellermeier, M.; Melero-García, E.; Glaab, F.; Klein, R.; Drechsler, M.; Rachel, R.; García-Ruiz, J. M.; Kunz, W. Stabilization of Amorphous Calcium Carbonate in Inorganic Silica-Rich Environments. *J. Am. Chem. Soc.* **2010**, *132* (50), 17859–17866. https://doi.org/10.1021/ja106959p.

(55) Peh, E.; Taubert, A.; Tauer, K. Ammonium Carbonate Gas Diffusion Crystallization in a Continuous Organic Medium Leads to Dendritic Calcium Carbonate. *Matters* **2017**. https://doi.org/10.19185/matters.201706000012.

(56) Faatz, M.; Gröhn, F.; Wegner, G. Amorphous Calcium Carbonate: Synthesis and Potential Intermediate in Biomineralization. *Adv. Mater.* **2004**, *16* (12), 996–1000. https://doi.org/10.1002/adma.200306565.

(57) Declet, A.; Reyes, E.; Suárez, O. M. Calcium Carbonate Precipitation: A Review of the Carbonate Crystallization Process and Applications in Bioinspired Composites. *Rev. Adv. Mater. Sci.* **2016**, *44* (1), 87–107.

(58) Fecht, H. J.; Hellstern, E.; Fu, Z.; Johnson, W. L. Nanocrystalline Metals Prepared by High-Energy Ball Milling. *Metall. Trans. A* **1990**, *21* (9), 2333–2337. https://doi.org/10.1007/BF02646980.

(59) Annenkov, M.; Blank, V.; Kulnitskiy, B.; Larionov, K.; Ovsyannikov, D.; Perezhogin, I.; Popov, M.; Sorokin, P. Boron Carbide Nanoparticles for High-Hardness Ceramics: Crystal Lattice Defects after Treatment in a Planetary Ball Mill. *J. Eur. Ceram. Soc.* **2017**, *37* (4), 1349–1353. https://doi.org/10.1016/j.jeurceramsoc.2016.12.001.

(60) Weeber, A. W.; Bakker, H. Amorphization by Ball Milling. A Review. *Phys. B Condens. Matter* **1988**, *153* (1–3), 93–135. https://doi.org/10.1016/0921-4526(88)90038-5.

(61) Katsenis, A. D.; Puškarić, A.; Štrukil, V.; Mottillo, C.; Julien, P. A.; Užarević, K.; Pham, M.-H.; Do, T.-O.; Kimber, S. A. J.; Lazić, P.; Magdysyuk, O.; Dinnebier, R. E.; Halasz, I.; Friščić, T. In Situ X-Ray Diffraction Monitoring of a Mechanochemical Reaction Reveals a Unique Topology Metal-Organic Framework. *Nat. Commun.* **2015**, *6* (1), 6662. https://doi.org/10.1038/ncomms7662.

(62) Fischer, F.; Wenzel, K.-J.; Rademann, K.; Emmerling, F. Quantitative Determination of Activation Energies in Mechanochemical Reactions. *Phys. Chem. Chem. Phys.* **2016**, *18* (33), 23320–23325. https://doi.org/10.1039/C6CP04280E.

(63) Michalchuk, A. A. L.; Hope, K. S.; Kennedy, S. R.; Blanco, M. V.; Boldyreva, E. V.; Pulham, C. R. Ball-Free Mechanochemistry: *In Situ* Real-Time Monitoring of Pharmaceutical Co-Crystal Formation by Resonant Acoustic Mixing. *Chem. Commun.* **2018**, *54* (32), 4033–4036. https://doi.org/10.1039/C8CC02187B.

(64) Kulla, H.; Haferkamp, S.; Akhmetova, I.; Röllig, M.; Maierhofer, C.; Rademann, K.; Emmerling, F. In Situ Investigations of Mechanochemical One-Pot Syntheses. *Angew. Chem. Int. Ed.* **2018**, *57* (20), 5930–5933. https://doi.org/10.1002/anie.201800147.

(65) Sottmann, J.; Di Michiel, M.; Fjellvåg, H.; Malavasi, L.; Margadonna, S.; Vajeeston, P.; Vaughan, G. B. M.; Wragg, D. S. Chemical Structures of Specific Sodium Ion Battery Components Determined by Operando Pair Distribution Function and X-Ray Diffraction Computed Tomography. *Angew. Chem. Int. Ed.* **2017**, *56* (38), 11385–11389. https://doi.org/10.1002/anie.201704271.

(66) Baxter, E. F.; Bennett, T. D.; Cairns, A. B.; Brownbill, N. J.; Goodwin, A. L.; Keen, D. A.; Chater, P. A.; Blanc, F.; Cheetham, A. K. A Comparison of the Amorphization of Zeolitic Imidazolate Frameworks (ZIFs) and Aluminosilicate Zeolites by Ball-Milling. *Dalton Trans.* **2016**, *45* (10), 4258–4268. https://doi.org/10.1039/C5DT03477A.

(67) Leukel, S.; Panthöfer, M.; Mondeshki, M.; Kieslich, G.; Wu, Y.; Krautwurst, N.; Tremel, W. Trapping Amorphous Intermediates of Carbonates – A Combined Total Scattering and

NMR Study. *J. Am. Chem. Soc.* **2018**, *140* (44), 14638–14646. https://doi.org/10.1021/jacs.8b06703.

(68) Stawski, T. M.; Roncal-Herrero, T.; Fernandez-Martinez, A.; Matamoros-Veloza, A.; Kröger, R.; Benning, L. G. “On Demand” Triggered Crystallization of CaCO $_3$ from Solute Precursor Species Stabilized by the Water-in-Oil Microemulsion. *Phys. Chem. Chem. Phys.* **2018**, *20* (20), 13825–13835. https://doi.org/10.1039/C8CP00540K.

(69) Leukel, S.; Panthöfer, M.; Mondeshki, M.; Kieslich, G.; Wu, Y.; Krautwurst, N.; Tremel, W. Mechanochemical Access to Defect-Stabilized Amorphous Calcium Carbonate. *Chem. Mater.* **2018**, *30* (17), 6040–6052. https://doi.org/10.1021/acs.chemmater.8b02339.

(70) Burns, J. H.; Bredig, M. A. Transformation of Calcite to Aragonite by Grinding. *J. Chem. Phys.* **1956**, *25* (6), 1281–1281. https://doi.org/10.1063/1.1743198.

(71) Criado, J. M.; Trillo, J. M. Effects of Mechanical Grinding on the Texture and Structure of Calcium Carbonate. *J. Chem. Soc. Faraday Trans. 1 Phys. Chem. Condens. Phases* **1975**, *71* (0), 961. https://doi.org/10.1039/f19757100961.

(72) Northwood, D. O.; Lewis, D. Transformation of Vaterite to Calcite during Grinding. *Am. Mineral.* **1968**, *53* (11–12), 2089–2092.

(73) Barriga, C.; Morales, J.; Tirado, J. L. Changes in Crystallinity and Thermal Effects in Ground Vaterite. *J. Mater. Sci.* **1985**, *20* (3), 941–946. https://doi.org/10.1007/BF00585738.

(74) Goldsmith, J. R.; Graf, D. L.; Heard, H. C. Lattice Constants of the Calcium-Magnesium Carbonates. *Am. Mineral.* **1961**, *46*, 453–459.

(75) Parr, R. G.; Pearson, R. G. Absolute Hardness: Companion Parameter to Absolute Electronegativity. *J. Am. Chem. Soc.* **1983**, *105* (26), 7512–7516. https://doi.org/10.1021/ja00364a005.

(76) Rodriguez-Navarro, C.; Kudłacz, K.; Cizer, Ö.; Ruiz-Agudo, E. Formation of Amorphous Calcium Carbonate and Its Transformation into Mesostructured Calcite. *CrystEngComm* **2015**, *17* (1), 58–72. https://doi.org/10.1039/C4CE01562B.

(77) Reilly, J. T.; Walsh, J. M.; Greenfield, M. L.; Donohue, M. D. Analysis of FT-IR Spectroscopic Data: The Voigt Profile. *Spectrochim. Acta Part Mol. Spectrosc.* **1992**, *48* (10), 1459–1479. https://doi.org/10.1016/0584-8539(92)80154-O.

(78) Fiquet, G.; Guyot, F.; Kunz, M.; Matas, J.; Andrault, D.; Hanfland, M. Structural Refinements of Magnesite at Very High Pressure. *Am. Mineral.* **2002**, *87* (8–9), 1261–1265. https://doi.org/10.2138/am-2002-8-927.

(79) Rodriguez-Blanco, J. D.; Shaw, S.; Bots, P.; Roncal-Herrero, T.; Benning, L. G. The Role of PH and Mg on the Stability and Crystallization of Amorphous Calcium Carbonate. *J. Alloys Compd.* **2012**, *536*, S477–S479. https://doi.org/10.1016/j.jallcom.2011.11.057.

(80) Christy, A. G.; Putnis, A. The Kinetics of Barite Dissolution and Precipitation in Water and Sodium Chloride Brines at 44–85°C. *Geochim. Cosmochim. Acta* **1993**, *57* (10), 2161–2168. https://doi.org/10.1016/0016-7037(93)90557-D.

(81) Avrami, M. Kinetics of Phase Change. I General Theory. *J. Chem. Phys.* **1939**, *7* (12), 1103–1112. https://doi.org/10.1063/1.1750380.

(82) Kolmogoroff, A. Zur Statistik der Kristallisationsvorgänge in Metallen. *Izv Akad Nauk SSSR Ser Mat* **1937**, *1*, 355–359.

(83) Rodriguez-Blanco, J. D.; Shaw, S.; Bots, P.; Roncal-Herrero, T.; Benning, L. G. The Role of Mg in the Crystallization of Monohydrocalcite. *Geochim. Cosmochim. Acta* **2014**, *127*, 204–220. https://doi.org/10.1016/j.gca.2013.11.034.

(84) Nebel, H.; Neumann, M.; Mayer, C.; Epple, M. On the Structure of Amorphous Calcium Carbonate□A Detailed Study by Solid-State NMR Spectroscopy. *Inorg. Chem.* **2008**, *47* (17), 7874–7879. https://doi.org/10.1021/ic8007409.

(85) Rehman, I.; Bonfield, W. Characterization of Hydroxyapatite and Carbonated Apatite by Photo Acoustic FTIR Spectroscopy. *J. Mater. Sci. Mater. Med.* **1997**, *8* (1), 1–4. https://doi.org/10.1023/A:1018570213546.

(86) Ostwald, W. Studien Über Die Bildung Und Umwandlung Fester Körper. *Z. Für Phys. Chem.* **1897**, *22U* (1). https://doi.org/10.1515/zpch-1897-2233.

(87) LeGeros, R. Z.; Trautz, O. R.; Klein, E.; LeGeros, J. P. Two Types of Carbonate Substitution in the Apatite Structure. *Experientia* **1969**, *25* (1), 5–7. https://doi.org/10.1007/BF01903856.

(88) *Biomaterials Research Advances*; Kendall, J. B., Ed.; Nova Science Publishers: New York, 2007.

(89) Wolf, S. E.; Böhm, C.; Harris, J.; Hajir, M.; Mondeshki, M.; Marin, F. Single Nanogranules Preserve Intracrystalline Amorphicity in Biominerals. *Key Eng. Mater.* **2016**, *672*, 47–59. https://doi.org/10.4028/www.scientific.net/KEM.672.47.

(90) Jarlbring, M.; Sandström, D. E.; Antzutkin, O. N.; Forsling, W. Characterization of Active Phosphorus Surface Sites at Synthetic Carbonate-Free Fluorapatite Using Single-Pulse ^{1} H, ^{31} P, and ^{31} P CP MAS NMR. *Langmuir* **2006**, *22* (10), 4787–4792. https://doi.org/10.1021/la052837j.

(91) Riss, T.; Niles, A.; Moravec, R.; Karassina, N.; Vidugiriene, J. Cytotoxicity Assays: In Vitro Methods to Measure Dead Cells. In *Assay Guidance Manual*; Sittampalam, G. S., Grossman, A., Brimacombe, K., Arkin, M., Auld, D., Austin, C. P., Baell, J., Bejcek, B., Caaveiro, J. M. M., Chung, T. D. Y., Coussens, N. P., Dahlin, J. L., Devanaryan, V., Foley, T. L., Glicksman, M., Hall, M. D., Haas, J. V., Hoare, S. R. J., Inglese, J., Iversen, P. W., Kahl, S. D., Kales, S. C., Kirshner, S., Lal-Nag, M., Li, Z., McGee, J., McManus, O., Riss, T., Saradjian, P., Trask, O. J., Weidner, J. R., Wildey, M. J., Xia, M., Xu, X., Eds.; Eli Lilly & Company and the National Center for Advancing Translational Sciences: Bethesda (MD), 2004.

(92) Unger, R. E.; Huang, Q.; Peters, K.; Protzer, D.; Paul, D.; Kirkpatrick, C. J. Growth of Human Cells on Polyethersulfone (PES) Hollow Fiber Membranes. *Biomaterials* **2005**, *26* (14), 1877–1884. https://doi.org/10.1016/j.biomaterials.2004.05.032.

(93) Unger, R. E.; Peters, K.; Sartoris, A.; Freese, C.; Kirkpatrick, C. J. Human Endothelial Cell-Based Assay for Endotoxin as Sensitive as the Conventional Limulus Amebocyte Lysate Assay. *Biomaterials* **2014**, *35* (10), 3180–3187. https://doi.org/10.1016/j.biomaterials.2013.12.059.

(94) Santos, M. I.; Fuchs, S.; Gomes, M. E.; Unger, R. E.; Reis, R. L.; Kirkpatrick, C. J. Response of Micro- and Macrovascular Endothelial Cells to Starch-Based Fiber Meshes for Bone Tissue Engineering. *Biomaterials* **2007**, *28* (2), 240–248. https://doi.org/10.1016/j.biomaterials.2006.08.006.

(95) Kokubo, T.; Takadama, H. How Useful Is SBF in Predicting in Vivo Bone Bioactivity? *Biomaterials* **2006**, *27* (15), 2907–2915. https://doi.org/10.1016/j.biomaterials.2006.01.017.

(96) Jaffe, E. A.; Nachman, R. L.; Becker, C. G.; Minick, C. R. Culture of Human Endothelial Cells Derived from Umbilical Veins. IDENTIFICATION BY MORPHOLOGIC AND IMMUNOLOGIC CRITERIA. *J. Clin. Invest.* **1973**, *52* (11), 2745–2756. https://doi.org/10.1172/JCI107470.

(97) Unger, R. E. Essential Criteria That Must Be Met by Novel Biomaterials Prior to Further in Vitro and in Vivo Biological Evaluation. *Adv. Biomater. Devices Med.* **2014**, *1*, 38–45. https://doi.org/10.24411/2409-2568-2014-00005.

3.1.7 Supporting Information

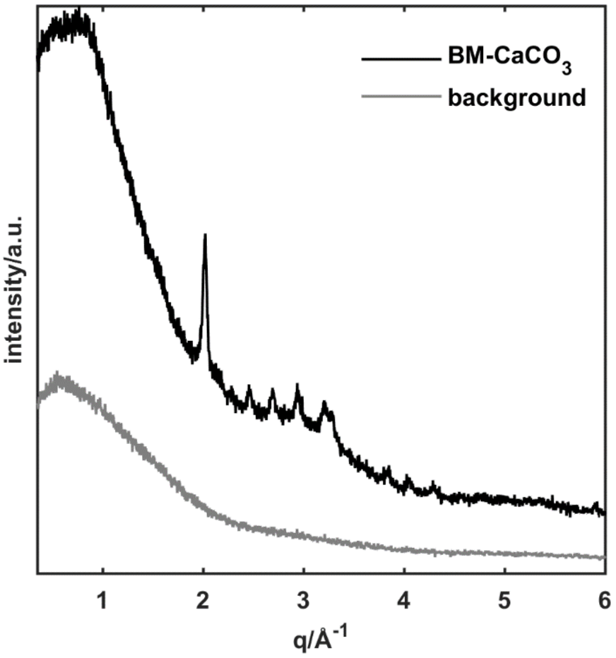

Figure S18. Powder X-ray diffractrogram of ball milled calcite.

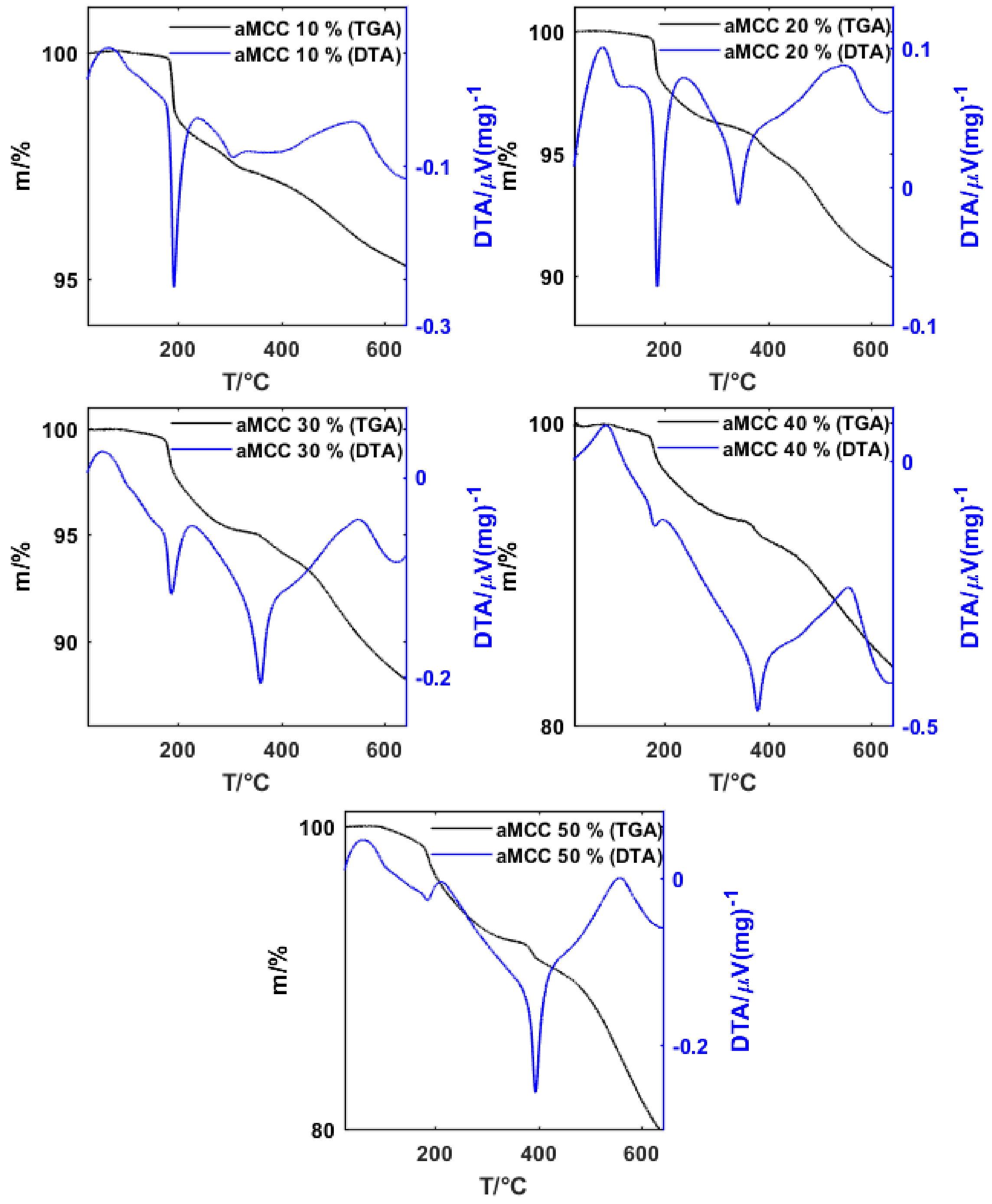

Figure S19. DTA and TGA traces for BM-aMCC (top: BM-aMCC 10% (left), BM-aMCC 20% (right); middle: BM-aMCC 30% (left), BM-aMCC 40% (right), bottom: BM-aMCC 50%).

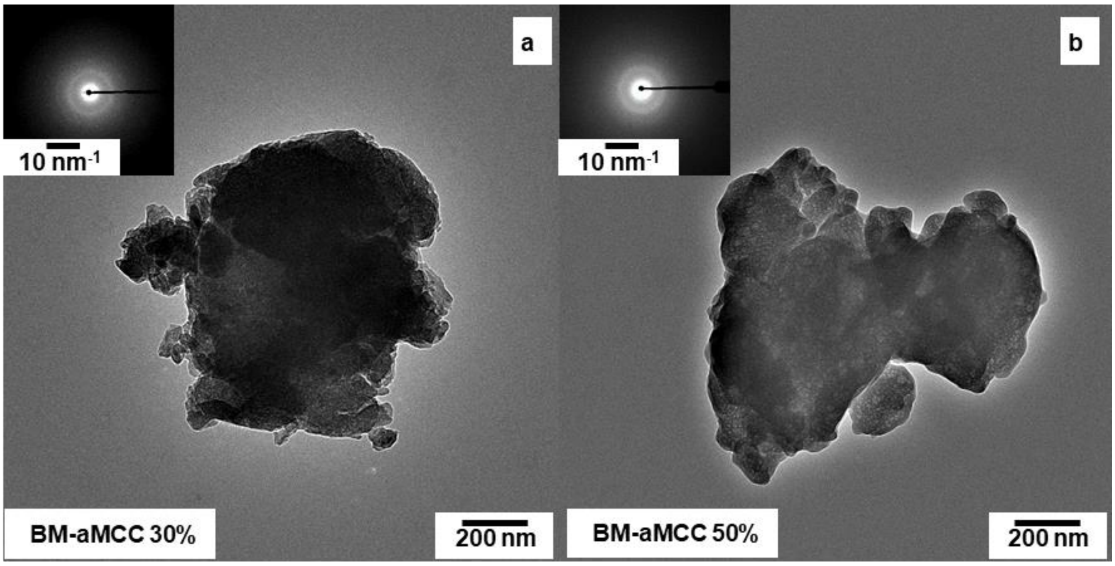

Figure S20. TEM images and associated diffraction patterns for (a) BM-aMCC 30% and (b) aMCC 50%.

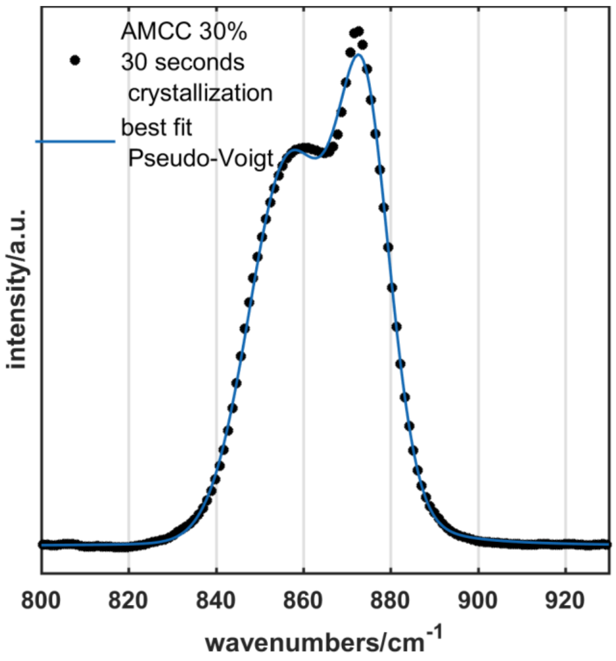

Figure S21. Section of the FTIR spectrum showing the band of the ν₂ vibration mode of calcium carbonate. Best Peudo-Voigt fit used for crystallization curves.

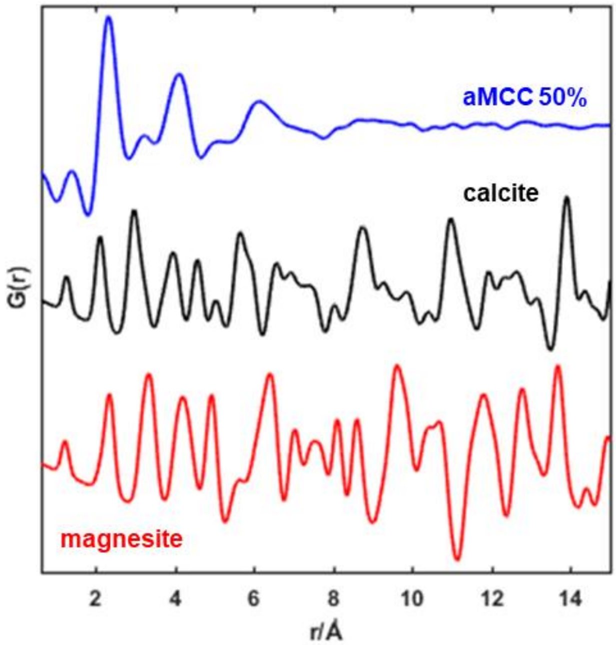

Figure S22. Pair distribution function of aMCC in comparison to simulated PDFs of crystalline calcite and magnesite. The peaks at about 4.1 and 6.2 Å can be mainly assingned to metal-metal distances of the first and second homonuclear coordination spheres (due to the higher scattering cross section).

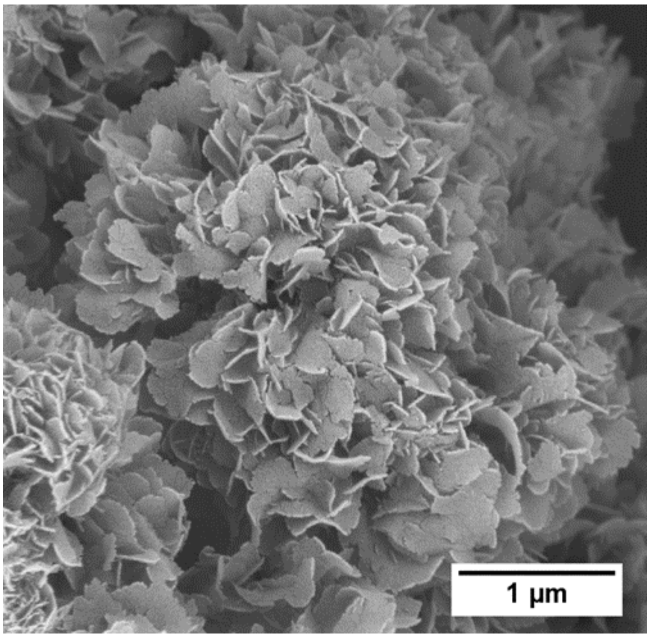

Figure S23. Scanning electron microscopy (SEM) images of aMCC 30% after incubation of SBF. The plate-shaped agglomerates shows typical morphology.[1]

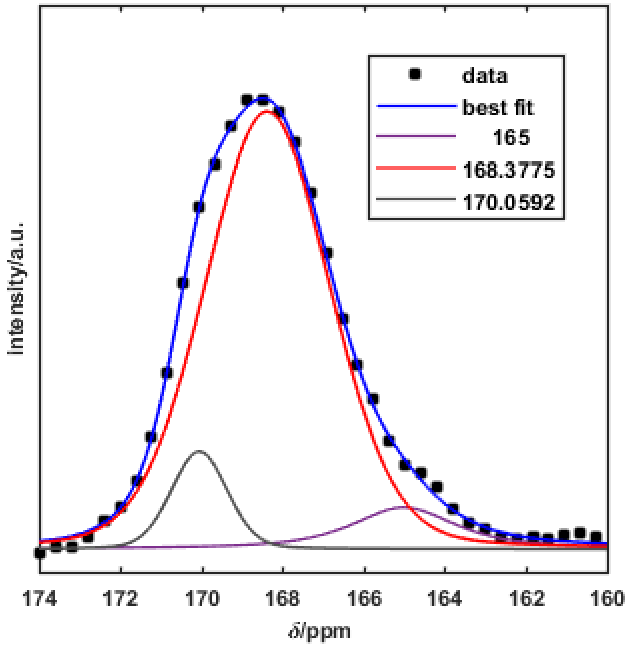

Figure S24. ^{13}C cross polarization of BM-aMCC 30% incubated in SBF with contact time of 2 ms. Best Pseudo-Voigt fit.

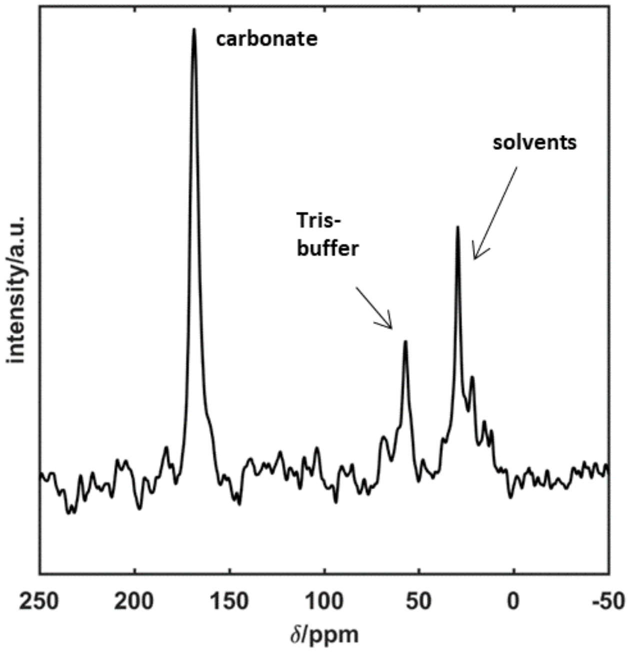

Figure S25. ^{13}C cross polarization of BM-aMCC 30% incubated in SBF with contact time of 2 ms. The washing solvents (ethanol, acetone) and buffer is assingend in the spectrum.

Avrami equation:

$$x(t) = 1 - e^{\left(-\left(\frac{t}{\tau}\right)^{2}\right)} \tag{1}$$

n : Avrami exponent (dimension of nucleation)

τ : kinetic constant

t : time

x : fraction of transformed material

Table S3. Results of the best Avrami fits.

	Avrami exponent n/ dimensionless	**Kinetic constant $\tau/1\mathrm{s}^{-1}$**	**Error $\tau/1\mathrm{s}^{-1}$**
AMCC 10%	1	$2.43 \cdot 10^{-2}$	$5.3 \cdot 10^{-3}$
AMCC 20%	1	$2.77 \cdot 10^{-2}$	$5.4 \cdot 10^{-3}$
AMCC 30%	1	$1.50 \cdot 10^{-2}$	$2.2 \cdot 10^{-3}$
AMCC 40%	-		
AMCC 50%			

Table S4. Amount of starting materials for the corresponding sample.

	$n_{bas.\ MgCO_3}$/mmol	$m_{bas.\ MgCO_3}$/mg	n_{CaCO_3}/mmol	m_{CaCO_3}/mg
AMCC 10%	0.2	13.5	1.8	180.0
AMCC 20%	0.4	27.0	1.6	160.0
AMCC 30%	0.6	40.4	1.4	140.0
AMCC 40%	0.8	53.9	1.2	120.0
AMCC 50%	1	67.4	1	100.0

References

(1) R. Schröder, H. Pohlit, T. Schüler, M. Panthöfer, R. E. Unger, H. Frey, W. Tremel, *J. Mater. Chem. B* **2015**, *3*, 7079.

4 Chapter 3

The contents of the following chapter are taken and partially adapted from Science 2021, submitted.

4.1 Arrested precipitation from amorphous precursors as a tool to explore pathways of mineral precipitation

4.1.1 ABSTRACT

“The synthesis of solids with limited phase stabilities is a challenging task. While traditional solid state reactions are diffusion limited, characterized by high temperatures and thermodynamically controlled, precipitation of ionic solids from liquids is typically nucleation limited and kinetically controlled. Understanding and controlling the competition between thermodynamics and kinetics is a fundamental step in elucidating reaction pathways. This can be realized by reducing transport pathways in amorphous intermediates and by reducing solvent concentrations to the interfacial level, enabling low activated reactions. The approach is the experimental counterpart of the simulated annealing approach used for computational prediction of inorganic solids. Its feasibility was tested for calcium sulfate, an important mineral in natural and industrial processes. The amorphous precursor is formed in a multistep reaction from $CaCO_3$ and $NaHSO_4$ *via* Na_2SO_4 and $Ca(HCO_3)_2$ followed by a hydrated sodium calcium sulfate ($Na_2Ca_5(SO_4)_6 \cdot 3H_2O$). We discovered a new mineral, $Ca_2Na_4(SO_4)_3(CO_3) \cdot 3H_2O$ (*mainzite*) during the crystallization of bassanite ($CaSO_4 \cdot ½H_2O$), gypsum ($CaSO_4 \cdot 2H_2O$) and glauberite, depending on the solvent concentration. This could benefit setting reactions of cement and may have implications in (bio)mineralization, geology, and industrial processes based on the hydration of $CaCO_3$ and $CaSO_4$.

4.1.2 INTRODUCTION

Understanding how solids form is important not only for materials synthesis[1], but also for geo- and atmospheric science[2,3], biomineralization[2], structural biology [4] or pharmaceutical chemistry.[5] The formation of solids illustrates the interplay of thermodynamics and kinetics. The elucidation of reaction pathways is related to the question whether a particular reaction is under kinetic ("what forms first") or thermodynamic control ("what is stable"). Conventional solid-state synthesis is based on the reaction of solid reactants with grain sizes on a macroscopic scale compared to atomic distances. Since diffusion coefficients in the solid state are only at the order of 10^{-12} cm^2/s, solid-state reactions are diffusion limited and require high thermal activation, favoring thermodynamic control and thermodynamically stable products. This precludes the formation of metastable and low-temperature phases. Current limitations to discover these "missing" compounds are due do the challenge of predicting the energy landscape to assess potential metastability theoretically.[6] From a practical perspective there is a lack of synthetic routes.

Diffusion barriers for reactions between ions or molecules in homogeneous fluids are lower and diffusion rates are orders of magnitude higher. Thus, the formation of ionic solids in fluids is typically nucleation limited. Fast diffusion allows much of the energy landscape to be explored, but with limited ability to control what crystallizes. According to bulk thermodynamics the least soluble and most stable crystalline compound precipitates from supersaturated solutions[7] stepwise *via* increasingly favorable intermediates.[8] Still, many compounds precipitate non-classically *via* multi-stage pathways where a parent phase (e.g., a solution) first transforms into an transient phase (e.g., a dense liquid or clusters) [9] before the stable solid emerges.[10–12] It is a matter of debate whether a final, stable phase nucleates directly from solution or forms in a multi-stage process.[11,12] In addition, the chemistry of the solution from which precipitation occurs can govern phase selection. Although the solution does not change the relative stability of the phases, it can affect the surface energy at the solvent/crystal interface [13]. As nuclei form at the nanoscale, the stabilization of a specific phase through its surface energy may be relevant for structure selection [13]. Metastable phases with lower surface energy can surpass the steady state nucleation barrier of a stable phase, if they have lower nucleation barriers.[14] The fundamental importance of nucleation has prompted many experimental and theoretical studies (*10, 11, 14-17*). The physicochemical conditions in model systems (such as the $CaCO_3$ or $CaSO_4$

systems)(*10,11,14,15*), from which most precipitates form, are close to ideal, whereas in real systems the supersaturations or alkalinities (e.g., during cement hardening) (*18*) are high or crystallization proceeds in restricted confined spaces. This hampers for example our ability to direct cement nucleation for healing fractures and pores in engineered structures.

Diffusional control can be circumvented by reducing transport distances to atomic dimensions. Liquid-phase routes, chemical vapor transport and topochemical reactions enable access to new materials by reducing diffusional barriers and studying solid-state reaction mechanisms (*19*). This allow to modify solids in a predictable manner to generate new materials under diffusional control. A seminal approach by Johnson used reactions in modulated layers of elemental reactants to generate amorphous precursors of the targeted compounds whose constituents are mixed at the atomic level in an appropriate ratio.(*19, 20*) Thus, nucleation becomes the rate-limiting step of the synthesis of metastable solids because the system is trapped in a local energy minimum under the reaction conditions. The approach proved useful for metal alloys that can be vapor deposited onto a support, but is not suitable for ionic solids with high melting points and low vapor pressures.

We have used ball milling to prepare an amorphous intermediate where the ionic constituents of the targeted product are mixed on a molecular level and in an appropriate ratio. This randomly “frozen” mixture of ions serves as starting point for a solid-state synthesis from the ionic building blocks, where a solvent is added in very small amounts to allow a reordering of the structural constituents. Ion hydration and transport at interfaces are relevant in many applied and natural processes. Interfacial effects are pronounced in confined geometries such as nanopores, where the mechanisms of ion transport in bulk solutions may not apply.(*20*) Our approach experimentally reproduces the “simulated annealing” concept, which has been employed for predicting inorganic solids and their crystal structures [21]. It allows to explore the energy landscape of the reaction system by controlling the supersaturation *via* the solvent concentration. Depending on the reaction conditions, different – and partly still unknown – mineral phases were formed.

The $CaSO_4/CaCO_3$ system was selected for testing the feasibility of our approach. Both minerals are important raw materials and fillers in the cement and polymer industry,[22] and they are textbook examples for the study of precipitation mechanisms and polymorphism [2,9,11–13,23–25]. Calcium sulfate is one of the most common evaporitic minerals on earth, which occurs in three polymorphs (gypsum, bassanite and anhydrite) [26]. The thermodynamic (meta)stability of the three $CaSO_4$ polymorphs is dictated by the variables temperature, pressure, and ionic strength. At ambient temperature and pressure gypsum ($CaSO_4·2H_2O$) represents the thermodynamically stable modification. It is formed in several distinct steps [27] *via* aggregation of nanometer-sized primary species [24] and nanoparticles [28,29] followed by the precipitation of bassanite, the hemihydrate ($CaSO_4·½H_2O$), by an oriented attachment of nanocrystals into elongated rods that finally transform into $CaSO_4·2H_2O$ [12].

Calcium carbonate is a main component of limestone from deep-sea sediments and forms many important minerals on earth. It is a model system for understanding crystal nucleation. For many years, three anhydrous and two hydrated polymorphs were assumed to exist: Calcite, the thermodynamically stable polymorph at ambient conditions, aragonite, metastable at Earth's near-surface conditions but common in marine and terrestrial environments, and vaterite, whose stability field is not well established [30]. Recently, an aragonite precursor phase (mAra) was found to coexist with hydromagnesite ($Mg_5(CO_3)_4(OH)_2·4H_2O$) and magnesite ($MgCO_3$) in stalactite drip water and flowstone [31]. In addition to the known hydrated phases monohydrocalcite ($CaCO_3·H_2O$) [30] and ikaite ($CaCO_3·6H_2O$),[30] a new hemihydrate ($CaCO_3·½H_2O$) was discovered recently that forms in solution from amorphous calcium carbonate (ACC) in the presence of Mg^{2+} ions for Mg/Ca molar ratios of ~5/1 [32].

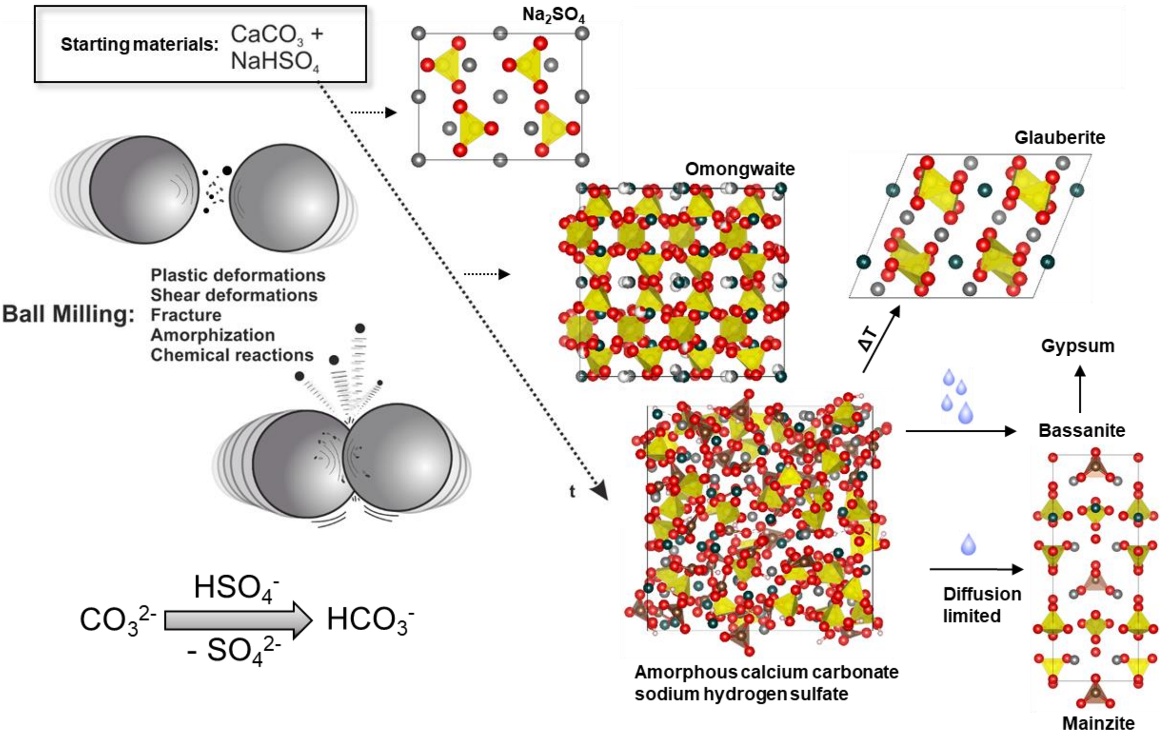

Fig. 44. Overview of amorphization and crystallization paths highlighting reaction intermediates and final products for different conditions.

4.1.3 RESULTS AND DISCUSSION

The experimental realization of the concept is outlined in Fig. 44. The reactants, $CaCO_3$ and $NaHSO_4$, were brought into a reactive amorphous form (calcium carbonate/sodium hydrogensulfate (aCCSHS)) by ball milling in a multistep reaction. Phase purity of the calcite and $NaHSO_4$ precursors was confirmed by PXRD (fig. S26). Equimolar mixtures of calcite and $NaHSO_4$ were ground for milling times between 10 min and 940 min with cyclohexane as dispersion medium. This reaction time was chosen to complete the reaction and reach mechanochemical equilibrium [33].

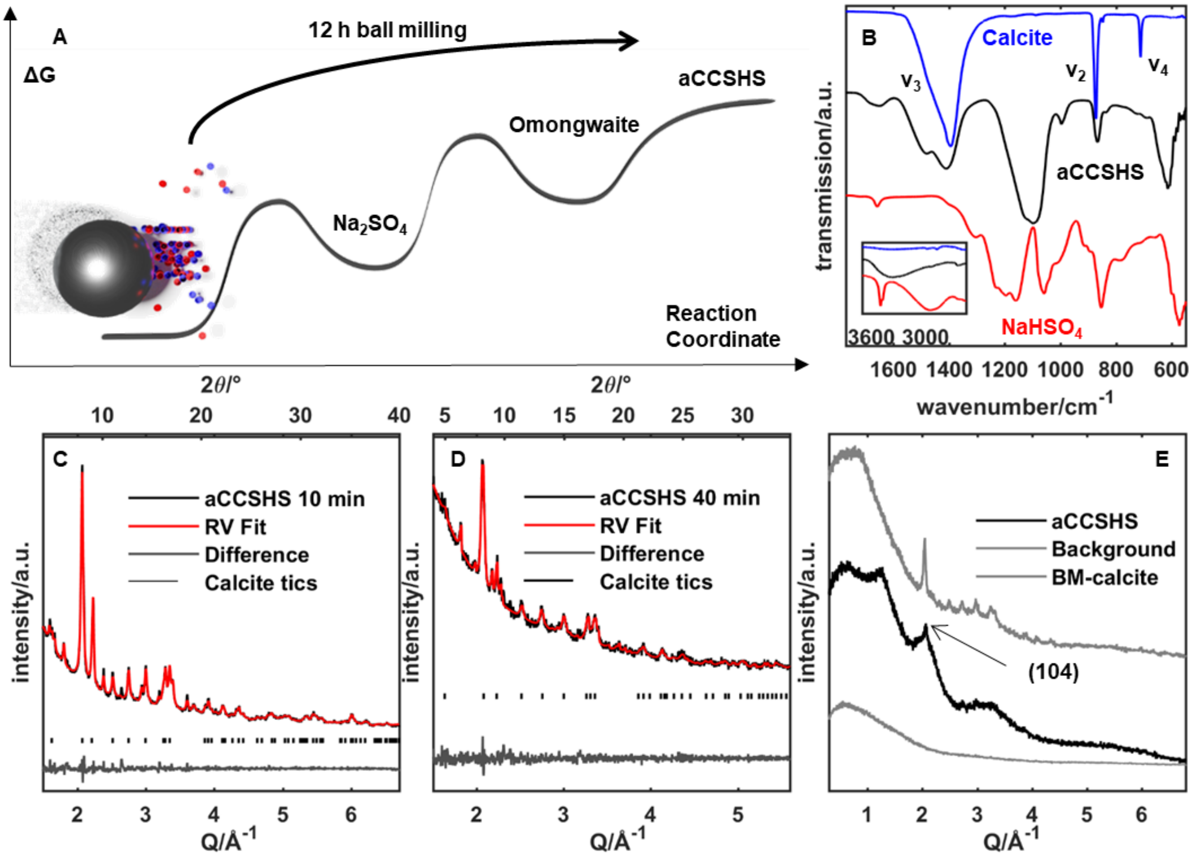

Fig. 45. (a) Energy landscape of the mechanochemical amorphization path of the starting materials calcite and sodium hydrogen sulfate. (b) FTIR spectra of aCCSS (black line) with the corresponding starting materials calcite (blue line) and sodium hydrogen sulfate (red line). (c) X-ray powder diffractogram of the

first formed intermediate $NaSO_4$. (d) X-ray powder diffractogram of the intermediate omongwaite. (e) X-ray powder diffractograms of aCCSHS (black) and ball-milled calcite (grey) with the corresponding background.

Reflection broadening shows that milling of pure calcite decreases the crystallite size. After 10 min the reflections of a first (Na_2SO_4, thenardite) intermediate appeared (Fig. 45C). The diffractogram was refined using the Rietveld method applying the thenardite Na_2SO_4 structure[34]. After 40 min the reflections of a omongwaite [35], a rare mineral from salt lake deposits in Namibia ($Na_2Ca_5(SO_4)_6 \bullet 3H_2O$), were identified (Fig. 45D) by Rietveld fitting [36]. Omongwaite occurs naturally as inclusion in gypsum crystals, but has been prepared in the laboratory as well [37]. The formation of thenardite and omongwaite are compatible with a proton transfer from the HSO_4^- (stronger acid) to the CO_3^{2-} anion (stronger base). Results were supported using ex situ XRPD and ^{23}Na ssNMR (fig. S27).

Vibrational spectroscopy is sensitive to the crystallinity of a compound due to the ability to measure lattice vibrations, in particular at low wavenumbers. The Raman spectrum of calcite shows a lattice mode at 283 cm^{-1} which is absent in the spectrum of the ball-milled calcium carbonate/sodium hydrogensulfate (aCCSHS) composite (fig. S28). The broadening of all bands in the Fourier transform infrared (FTIR) spectra (Fig 2B), in particular of the ν_3 band (asymmetric stretch) of the CO_3^{2-} group at ~1400 cm^{-1} with milling time indicates a loss of long-range order and increasing amorphization. The ν_2 (out-of-plane deformation) band of the CO_3^{2-} group at ~850 cm^{-1} broadens and a HCO_3^- band evolves at 870 cm^{-1} after 160 min. The ν_4 (in-plane deformation) band of the CO_3^{2-} group at ~713 cm^{-1} vanishes and two bands appear at 690 and 730 cm^{-1}. The ν_1 (symmetric stretch) band of the CO_3^{2-} group at ~1010 cm^{-1} overlaps with the ν_3 (asymmetric stretch) band of the SO_4^{2-} group. Two new bands at 835 cm^{-1} and 1650 cm^{-1} associated with the HCO_3^- appear while the O-H stretch of the HSO_4^- group at 3496 cm^{-1} is lost and indicates a protonation of the CO_3^{2-} anion (stronger base) by the HSO_4^- anion (stronger acid) during the ball milling reaction. This is supported by the FTIR spectra of ^{13}C enriched aCCSHS (fig. S29) which facilitate a spectral assignment, because the higher mass of the ^{13}C isotope shifts bands associated with the carbonate group to lower wavenumbers, the ν_4 band being the only exception. The ν_2 ($HO\text{-}CO_2$ in-plane deformation) and ν_3 ($HO\text{-}CO_2$ in-plane stretch) bands are strongly shifted. Since the ν_2 mode of the carbonate group is non-degenerate, the splitting of the band indicates the formation of a second phase. The bands at higher (1484 cm^{-1}) and lower (1413 cm^{-1}) are assigned to the CO_3^{2-} and $HOCO_2^-$ groups in aCCSHS. The bands of the sulfate groups (ν_{as}: 1120 and 1086 cm^{-1}; ν_s: 995 cm^{-1})

remained unaffected by the ^{13}C substitution. Transmission electron microscopy (TEM) images and the associated diffraction patterns for aCCSHS confirm the complete lack of long-range order (fig. S30).

Complementary information about the chemical environment of the carbonate group in aCCSHS was obtained by ^{13}C single pulse excitation (SPE) and cross-polarization (CP) MAS NMR spectroscopy (Fig. 46A). The ^{13}C SPE NMR spectrum (fig. S31) recorded with 2400 s recycle delay to ensure complete relaxation is characterized by two resonances at 168 ppm with full width at half height (fwhh) of 375Hz and at 162 ppm (fwhh of 655 Hz) with an integral ratio of 4.5 : 1. The former signal is compatible with ACC considering that calcite resonates at 168.2 ppm with fwhh of ca 100 Hz (Figure 3a black line) and that the typical BM-ACC is detected at ca. 168 ppm, but with a significantly higher fwhh of 1400 Hz (*37*). The high field shifted ^{13}C resonance at 162 ppm is characteristic for HCO_3^- groups (as in solid $NaHCO_3$ or $KHCO_3$) (*37,38*). Further confirmation of this assignment is found in the ^{13}C CP NMR experiment. The intensity of the signal at 162 ppm is significantly increased compared to the SPE spectrum most probably due to the ^{1}H-^{13}C dipole-dipole coupling with the bicarbonate proton. It should be noted that the ACC ^{13}C signal is also detected in this experiment which proves the presence of proton species in the vicinity of the carbonate group unlike in the crystalline calcite.

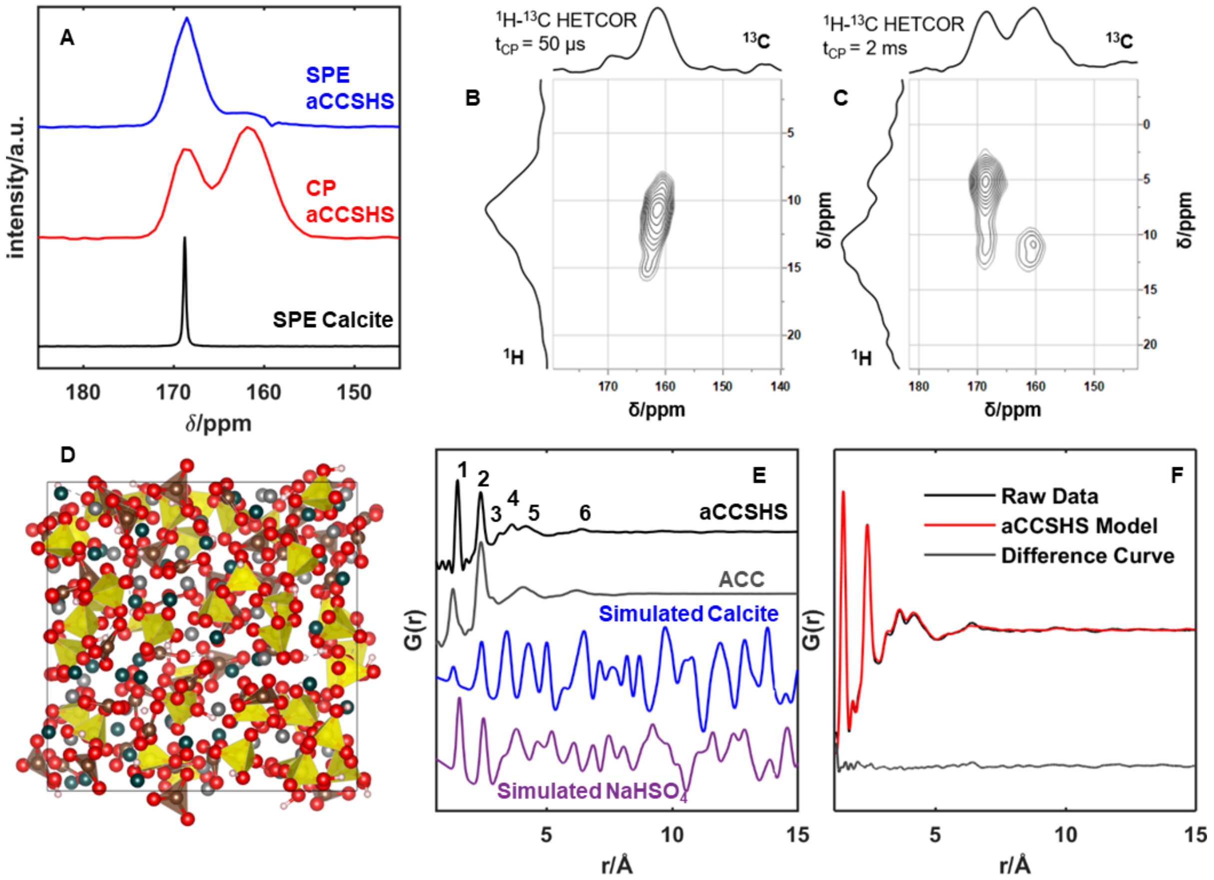

Fig. 46. (a) ^{13}C-MAS-NMR single pulse excitation (SPE) spectrum (blue line), cross polarization (CP) spectrum (red line) and SPE spectrum of the starting material calcite (black line). The CP experiment highlights two different ^{13}C environments corresponding to carbonate and hydrogen carbonate. ^{1}H-^{13}C heteronuclear correlation (HETCOR) spectrum of aCCSHS recorded with a contact time of 50 μs (b) and 2 ms (c). Short contact time HETCOR spectrum confirms the appearance of hydrogen carbonate anions. (d) Model of aCCSHS obtained by simulated annealing. (e) Pair distribution functions (PDF) of aCCSHS (black line), amorphous calcium carbonate (ACC) grey line. Simulated PDFs of crystalline calcite (blue line) and crystalline sodium hydrogen sulfate (purple line) are shown for comparison. (f) PDF of the aCCSHS model (red line) and the experimental aCCSHS (black line). The grey line shows the difference of the modelled PDF to the experimental PDF.

The emerging component of the aCCSHS composite is detected in the {^{1}H,^{13}C} 2D heteronuclear correlation (HETCOR) spectra (Fig. 46B & C) that establish connectivities within the carbonate/hydrogen system and so refine the characterization of the interactions between them. Short contact times (50 μs) map the protons in close proximity, while long contact times (2000 μs) map the protons at larger separations. The HETCOR spectrum recorded with a contact time 50 μs shows only the correlation between the bicarbonate proton and the respective ^{13}C signal at 162 ppm. Since this proton is in close proximity of the ^{13}C atom with a typical shift for hydrogen carbonate units this assignment is in harmony with the IR spectroscopic results. Correlations over large spatial separations are mapped in HETCOR experiments due to heteronuclear dipole-dipole coupling with contact times of 2000 μs. In addition to the bicarbonate correlation peak two more signals related with the carbonate carbon appear in this HETCOR spectrum. The ^{13}C signal of ACC is strongly correlated with the water signal at 5 ppm which proves that the amorphization of ACC is partially due to the incorporation of water in the lattice. Another weaker correlation with the proton at 11 ppm is also observed (^{1}H SPE spectrum of aCCSHS, fig. S32). Therefore, this signal is related to both hydrogen atoms of the hydrogen sulfate and hydrogen carbonate anions (^{1}H SPE spectrum of $NaHSO_4$, fig. S33).

Another piece of information was gathered by pair distribution function (PDF) analysis. X-ray total-scattering data, obtained at beamline ID 15-1 of Diamond Light Source and extracted with the program GUDRUN4 revealed six pronounced peaks at 1.46 Å, 2.38 Å, 3.14 Å, 3.62 Å, 4.18 Å and 6.40 Å (Fig. 46E). Beyond 7 Å the PDF was virtually a featureless line, underlining the amorphous character of aCCSHS, i.e., the long-range order of the reactants is lost during milling. In contrast, the simulated PDF functions of calcite and $NaHSO_4$ show a multitude of distinct maxima, even at higher *r* values. The first maximum can be assigned mainly to the sulfur-oxygen (sulfate ion) distance at 1.46 Å. We assume that carbon-oxygen (carbonate ion) separations contribute to this peak as well. The effective shift is small as the peak is a superposition of both, the S-O and the C-O distances, with the C-O portion contributing much less because the atomic form factors of carbon and oxygen keep the contribution of the C-O pairs small. A C-O distance of 1.3 Å could be an explanation for the merged peak as well [40]. The peak height is not only a measure of the coordination number, but also the total number and product of the atomic form factors. The second peak at 2.38 Å arises mainly from metal to oxygen (M-O) distances, and O-O distances contribute to the peak as well. M-S distances contributes to the third peak at 3.14 Å. The PDF data was modelled with TOPAS Academic V6 [41]. Fig. 46F shows a converged model with a residual of R_{wp}= 8.5. All runs converge into a model showing a solid solution of the starting materials (Fig. 46D). In no case phase separation or domains with a higher degree of sulfate or carbonate occur. Due to the small scattering cross section of the hydrogen atoms, it is not possible to detect any hydrogen positions. We used the ssNMR results to determine the ratio of hydrogen carbonate and carbonate anions. Thus, we have been able to extrapolate the amount of hydrogen carbonate and hydrogen sulfate ions and model them as rigid bodies. The PDF of aCCSHS has some truncation oscillations at low distances, therefore, the data below 1.2 Å have been neglected for the modelling.

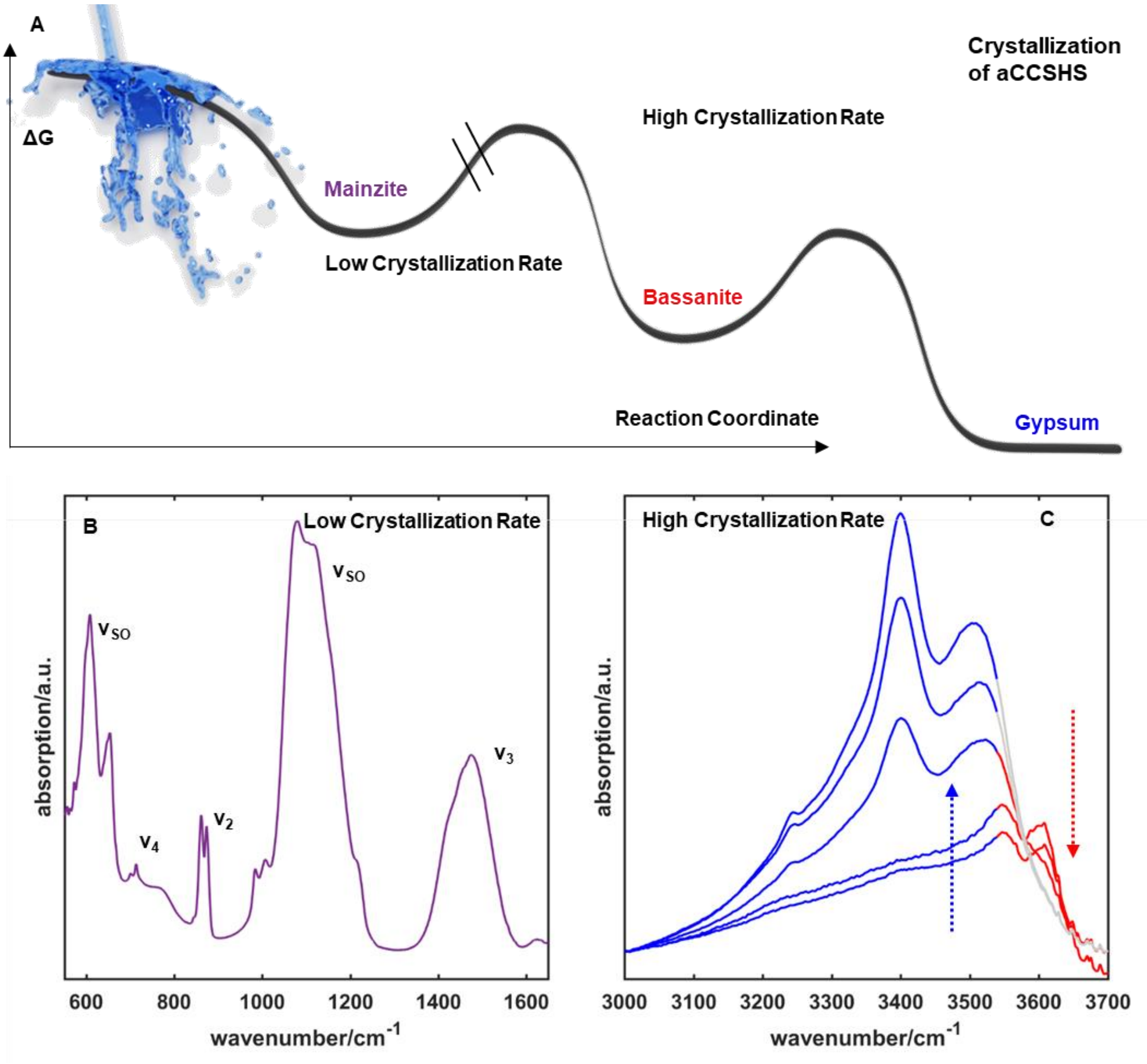

Fig. 47. (a) Energy landscape of the crystallization path of aCCSHS. (b) FTIR spectrum mainzite. (c) FTIR spectra of the dissolution and crystallization process from aCCSHS *via* bassanite (red) to gypsum (blue) as a function of time (from bottom to top: 10 s, 60 s, 600 s, 3600 s).

Crystallization of aCCSHS. Upon heating (TGA/TG traces fig. S34) aCCSHS gradually loses cyclohexane solvate. At ~400 °C crystallization occurs into anhydrite ($CaSO_4$) and glauberite ($Na_2Ca(SO_4)_2$), a mineral that is associated with anhydrite or gypsum and typically forms in continental and marine evaporites (X-ray powder diffractogram fig. S35). Further heating to 700 °C leads to the formation of a mixture of CaO, Na_2O, $CaSO_4$ and Na_2SO_4 by release CO_2 (fig. S36).

When exposing aCCSHS to water, calcite was formed within seconds as shown by FTIR spectroscopy. The crystallization of the sulfate component (ν_1=1008 cm^{-1}, ν_3=1110 and 1140 cm^{-1}, ν_2=660 cm^{-1}) proceeded more slowly (Fig. 47A). After 10 s bassanite with the characteristic sharp bands of structural water at 3500 cm^{-1} (ν_1) and 3600 cm^{-1} (ν_3) was formed [42]. After 10 min bassanite transformed to gypsum ($CaSO_4 \times 2H_2O$) (water bands ν_1 = 3400 cm^{-1} and 3500 cm^{-1}, ν_3 = 3550 cm^{-1}) by dissolution/recrystallization (Fig. 47B). The fast formation of bassanite has practical implications as it indicates a fast and cost-effective pathway for bassanite formation at ambient temperature. About 100 megatons of bassanite per year are produced for construction purposes ("plaster of Paris") by slow thermal dehydration of gypsum. A fast aqueous route to bassanite at ambient temperature could reduce the energy cost of the high-temperature process by orders of magnitude.

The crystallization rate was reduced significantly in water/acetonitrile (2.5/97.5) mixtures. (Fig. 47C) Acetonitrile is readily miscible with water and – different from alcohols [42,43] – does not affect the crystallization of the carbonate component. After 24 h the characteristic bands of the sulfate anion appeared, but the ν_2 band of the CO_3^{2-} anion at 870 cm^{-1} was split, indicating the formation of a second phase. Since the characteristic ν_1 band of bassanite at 3500 cm^{-1} associated with structural water appeared only after 24 h (whereas bassanite in pure water formed within 10 s), the formation of an intermediate phase was assumed. When exposing aCCSHS to atmospheric air, a material with identical IR spectrum was formed after 4 days. These findings could be verified by crystallization in paraffin oil, monitored *ex situ* using X-ray powder diffraction (fig. S37).

We carried out a structure analysis from powders, but the synchrotron X-ray powder diffraction data (SXPRD) did not match with any known carbonate or sulfate phase. Since *ab initio* crystal structure solution based on PXRD data was not possible, we applied three-dimensional electron diffraction (3D ED) to determine the crystal structure from single nanocrystals [44]. Our three-dimensional reconstruction of 3D ED data taken from crystals with unspecific morphology (inset Fig. 48A) revealed an orthorhombic unit cell for $Ca_2Na_4(SO_4)_3(CO_3)\cdot(H_2O)_3$ with the acentric space group $Pcm2_1$ (No. 26) and lattice parameters a = 6.43 Å, b = 6.91 Å and c = 18.32 Å. In the reconstructed crystallographic sections $h0l$ and $hk0$ (Fig. 48A and C) additional reflections for $h = 0.5\cdot n$ are visible indicating a superstructure with $a' = 2a$. In addition, diffuse scattering appears along $\boldsymbol{c^*}$. The solution of the average crystal structure based on the original a axis using direct methods resulted in an residual R(F) of 17.13 % (Table S5) and yielded the atomic positions of the Ca^{2+} and Na^+ cations, of the SO_4^{2-} and CO_3^{2-} anions and the position of additional O atoms from water molecules. (Table S6)

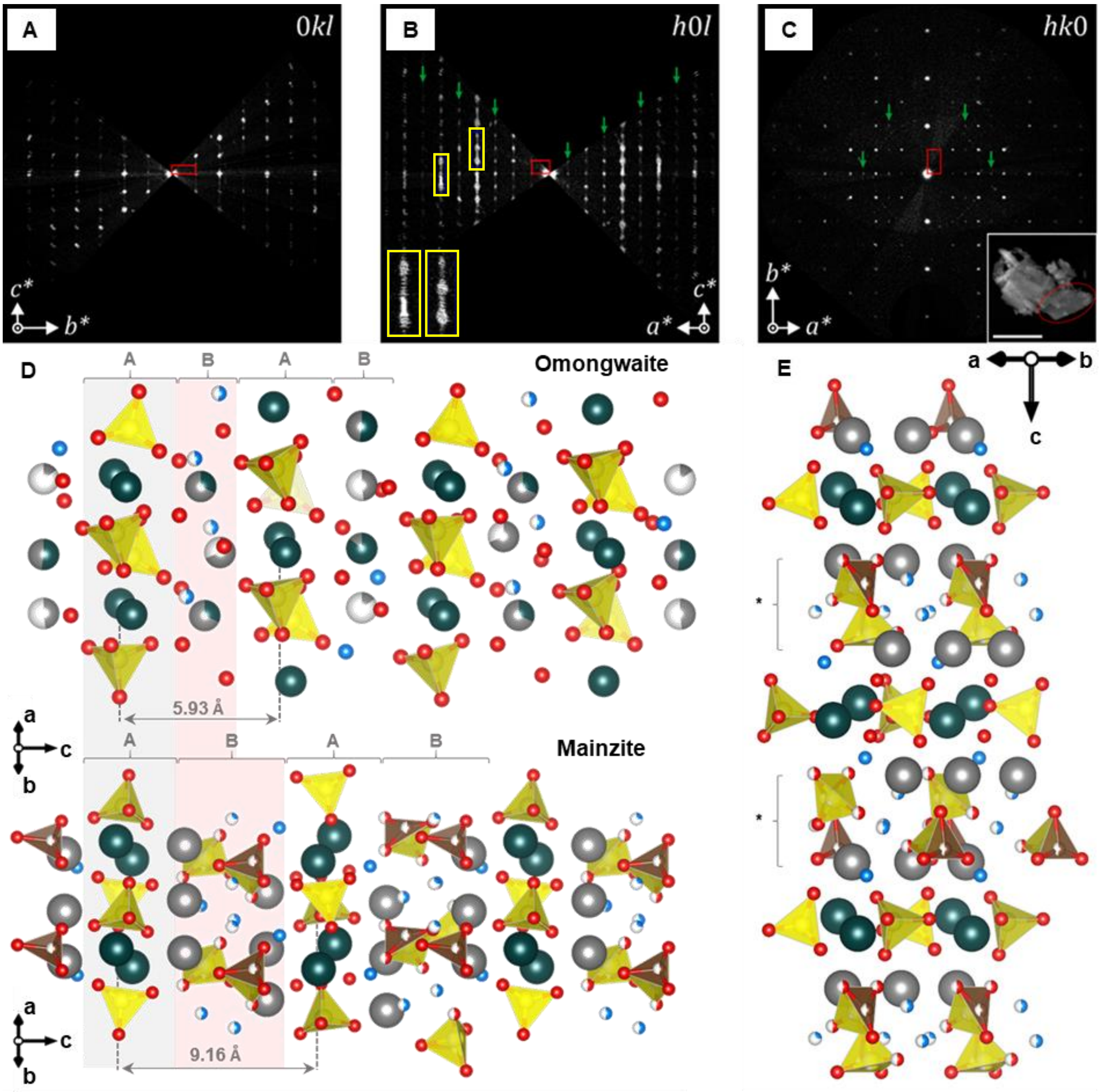

Fig. 48. Crystal structure of $Ca_2Na_4(SO_4)_3(CO_3)\cdot 3H_2O$ (mainzite) determined from 3D ED data and comparison with the structure of $Ca_5Na_2(SO_4)_6\cdot 3H_2O$ (omongwaite). Mainzite: space group $Pcm2_1$ (a = 6.43 Å, b = 6.91 Å, c = 18.32 Å). Three-dimensional reconstructed crystallographic sections 0kl, h0l and hk0. The projected reciprocal unit cell displayed as a red rectangle. (**A, B, C**) Additional reflections indicating a superstructure with **a'** = 2**a** marked with green arrows. (**B, C**) Enlarged regions of strong diffuse scattering along the **c*** axis with yellow frames. **(B)** STEM image: mainzite marked with red circle (scale bar 0.5 µm). (inset **C**); Comparison of the crystal structure of omongwaite in A2 setting (top) and mainzite (bottom) projected along the c axis. Planes containing sulfate and carbonate anions highlighted in light pink (**D**); Projection of mainzite along the c axis. (**E**) Blue-green spheres represents Ca, grey spheres Na, red spheres O (SO_4^{2-}/CO_3^{2-}: 0.66 and 0.33 for pair 1 and 2), brown spheres C, and blue spheres O (of the water molecules, H atoms not shown). Na^+ cations in heptagon coordination (2.24-2.65 Å) with additional contacts (2.93-3.02 Å). Ca^{2+} cations 8–fold coordination, Ca-O (2.31-2.81 Å) (Fig. S40, Tables S6-S8).

The structure of mainzite is related to the structure of the mineral omongwaite (Fig. 48D). Both structures contain layers of Ca^{2+} cations 8-fold coordinated by SO_4^{2-}/$CO3^{2-}$ anions and a water molecule. In the structure of omongwaite, these layers alternate with mixed $CaSO_4$/$NaSO_4$ layers containing channels filled with hydrated Na^+ cations. In the structure of mainzite this mixed layer contains additional SO_4^{2-}/CO_3^{2-} anions and Na^+ cations with a hydrate water molecule. This leads to an increased (from 5.93 to 9.16 Å) separation between the $CaSO_4$ layers compared to omongwaite (Fig. 48D). The superstructure along *a* is caused by an inhomogeneous distribution of anions (SO_4^{2-}/CO_3^{2-}: 2/1 and 1/2, respectively) associated with evidence of stacking faults (Fig. 48E). The doubling of the *a* axis is indicated by a reflection at $2\theta = 2.05°$ ($Q = 0.49$ Å^{-1}) in the powder diffractogram (Fig. 49). A structure determination in the supercell with $a' = 2a$ provided the $CaSO_4$ layers and parts of the intermediate layer. The achieved completeness and data quality allowed only an approximate determination of the distribution of carbonate and sulfate ions.

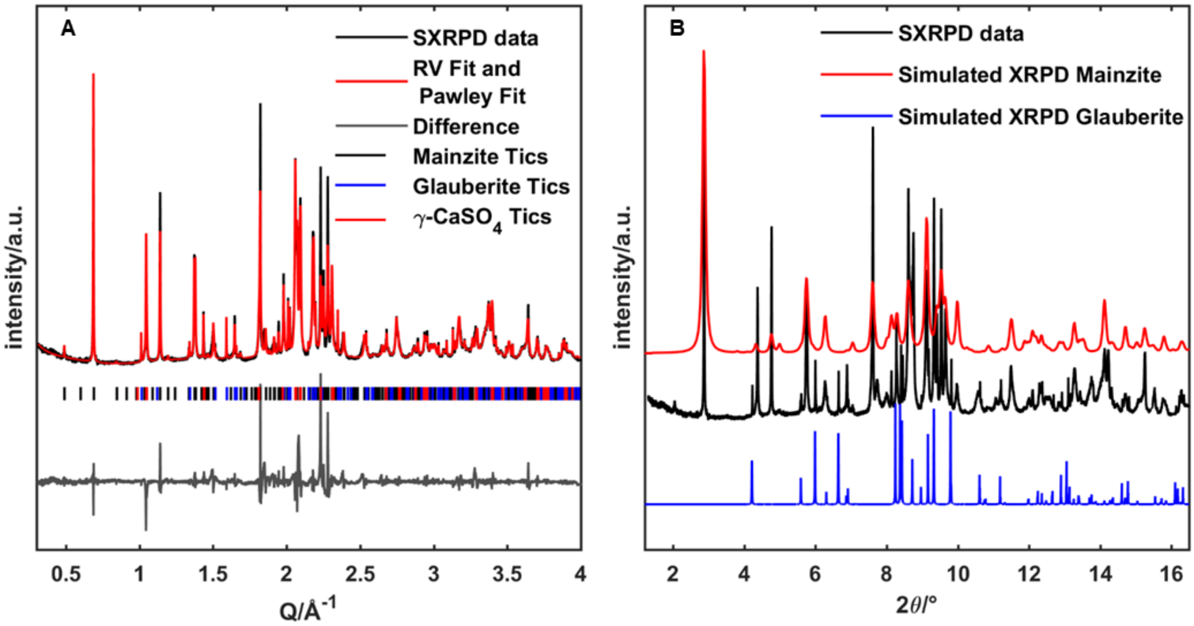

Fig. 49. Synchrotron X-ray powder diffraction pattern (SXRPD) of mainzite ($Ca_2Na_4(SO_4)_3(CO_3)\cdot 3H_2O$) (black line). (**A**) Pawley fit of mainzite (*Pmc2₁*) and Rietveld fit of glauberite and γ-$CaSO_4$. (**B**) Simulated X-ray powder diffractograms (XRPD) of the mainzite model (red line) and glauberite (blue line).

Pawley refinement against synchrotron X-ray powder diffraction data in the acentric space group $Pcm2_1$ showed a moderate fit (Fig. 49) and converged at relatively high residuals (even for nanocrystalline samples). In addition to mainzite, glauberite and γ-$CaSO_4$ were identified in the powder sample by Rietveld refinement. Refinement based on the mainzite structure model was not possible due to the doubling of the *a* axis, the high disorder of the material and the relatively low crystallinity. Definite proof of the microstructure model would require simulations [45] using stacking models with different layer constitutions or specific faults within each individual regime, which is currently not possible.

Mechanism of mainzite formation. The formation of $Ca_2Na_4(SO_4)_3(CO_3)\cdot 3H_2O$ competes with that of gypsum and calcite in sulfate- and carbonate-rich environments. A central question is which driving forces govern the crystallization pathway, in particular when an amorphous precursor phase is involved. When anhydrous aCCSHS is exposed to excess water, the crystallization of $CaCO_3$ competes with that of $CaSO_4$. Calcite is formed within seconds, because it has a much lower solubility ($pK_L = 8.48$) than gypsum or bassanite ($pK_L = 4.58$ and 4.05).[46] When the water concentration is reduced by two orders of magnitude in acetonitrile/water mixtures (or by vapor diffusion), the concentrations of the Ca^{2+}, SO_4^{2-} and HCO_3^- ions are increased accordingly. SO_4^{2-} and Mg^{2+} ions are known to affect calcite growth, dissolution and surface enrgy.[47,48] Therefore, the growth of calcite appears to be inhibited and mainzite to crystallize in the presence of SO_4^{2-} anions. This is in harmony with control experiments, where aMgCSHS (the Mg counterpart of aCCSHS, fig. S38) formed aragonite (based on vibrational spectroscopy analysis), which transformed to basic magnesium carbonate ($Mg(CO_3)\cdot Mg(OH)_2$) after 24 h while sulfate dissolved. Addition of Mg^{2+} slowed down the crystallization considerably, as indicated by the crystallization times in pure water. The presence of Mg^{2+} allowed the formation amorphous precursors and enforced phase separation into aragonite, basic magnesium carbonate and (water soluble) $NaHSO_4$.

The solubility window for gypsum, calcite and mainzite in water was estimated with PHREEQC.[49] The solubility of gypsum is hardly affected by carbonate anions in the relevant concentration range. As no thermodynamic data are available for mainzite, the behavior was approximated with the $Ca_2(SO_4)(CO_3)\cdot 4H_2O$ mineral.(fig. S39) For $CaCO_3$ ($c \sim 0.54$ mol/L, corresponding to the amount of $CaCO_3$ in aCCSHS) large sulfate concentrations are required for precipitation, but the high ionic strengths limit the validity of the calulations. Inhibition of calcite precipitation and water diffusion appear critical for the formation to mainzite.[50]

4.1.4 CONCLUSIONS

In conclusion, we have unraveled the chemistry of the calcium carbonate/sulfate reaction system by balancing the effects of nucleation and diffusion. The nucleation kinetics was controlled by the diffusion by the concentration of water in acetonitrile/water solvent mixtures. For high water concentrations calcite was formed instantaneously. Bassanite and gypsum were formed time-delayed for low water concentrations, and a new ternary mineral was formed for still lower concentrations of water. The average composition of the amorphous intermediate prevents binary precipitation of the binary minerals calcium sulfate and calcium carbonate, i.e., the synthetic approach gives access to rare compounds which would be difficult or even impossible to prepare at ambient temperature using conventional precipitation routes. The discovery of these minerals, their formation pathways, and their complete structure determination using X-ray powder or electron diffraction substantially expand our knowledge of the $CaSO_4$ and $CaCO_3$ families. The results could have practical implications in geochemical, industrial or (bio)mineralization processes involving the hydration of calcium carbonate and calcium sulfate.

4.1.5 References and Notes

(1) Chamorro, J. R.; McQueen, T. M. Progress toward Solid State Synthesis by Design. *Acc. Chem. Res.* **2018**, *51* (11), 2918–2925. https://doi.org/10.1021/acs.accounts.8b00382.

(2) Yoreo, J. J. D.; Gilbert, P. U. P. A.; Sommerdijk, N. A. J. M.; Penn, R. L.; Whitelam, S.; Joester, D.; Zhang, H.; Rimer, J. D.; Navrotsky, A.; Banfield, J. F.; Wallace, A. F.; Michel, F. M.; Meldrum, F. C.; Cölfen, H.; Dove, P. M. Crystallization by Particle Attachment in Synthetic, Biogenic, and Geologic Environments. *Science* **2015**, *349* (6247). https://doi.org/10.1126/science.aaa6760.

(3) Bogdan, A. Ice Clouds: Atmospheric Ice Nucleation Concept versus the Physical Chemistry of Freezing Atmospheric Drops. *J. Phys. Chem. A* **2018**, *122* (39), 7777–7781. https://doi.org/10.1021/acs.jpca.8b07926.

(4) Galkin, O.; Vekilov, P. G. Are Nucleation Kinetics of Protein Crystals Similar to Those of Liquid Droplets? *J. Am. Chem. Soc.* **2000**, *122* (1), 156–163. https://doi.org/10.1021/ja9930869.

(5) Bučar, D.-K.; Lancaster, R. W.; Bernstein, J. Disappearing Polymorphs Revisited. *Angew. Chem. Int. Ed.* **2015**, *54* (24), 6972–6993. https://doi.org/10.1002/anie.201410356.

(6) Sun, W.; Dacek, S. T.; Ong, S. P.; Hautier, G.; Jain, A.; Richards, W. D.; Gamst, A. C.; Persson, K. A.; Ceder, G. The Thermodynamic Scale of Inorganic Crystalline Metastability. *Sci. Adv.* **2016**, *2* (11), e1600225. https://doi.org/10.1126/sciadv.1600225.

(7) Becker, R.; Döring, W. Kinetische Behandlung Der Keimbildung in Übersättigten Dämpfen. *Ann. Phys.* **1935**, *416* (8), 719–752. https://doi.org/10.1002/andp.19354160806.

(8) Ostwald, W. File: Wilhelm Ostwald-Studien Über Die Bildung Und Umwandlung Fester Körper. Pdf. *Z. Für Phys. Chem.* **1897**, *22*, 289–330.

(9) Jehannin, M.; Rao, A.; Cölfen, H. New Horizons of Nonclassical Crystallization. *J. Am. Chem. Soc.* **2019**, *141* (26), 10120–10136. https://doi.org/10.1021/jacs.9b01883.

(10) Chung, S.-Y.; Kim, Y.-M.; Kim, J.-G.; Kim, Y.-J. Multiphase Transformation and Ostwald's Rule of Stages during Crystallization of a Metal Phosphate. *Nat. Phys.* **2009**, *5* (1), 68–73. https://doi.org/10.1038/nphys1148.

(11) Nielsen, M. H.; Aloni, S.; De Yoreo, J. J. In Situ TEM Imaging of CaCO3 Nucleation Reveals Coexistence of Direct and Indirect Pathways. *Science* **2014**, *345* (6201), 1158–1162. https://doi.org/10.1126/science.1254051.

(12) Van Driessche, A. E. S.; Benning, L. G.; Rodriguez-Blanco, J. D.; Ossorio, M.; Bots, P.; García-Ruiz, J. M. The Role and Implications of Bassanite as a Stable Precursor Phase to Gypsum Precipitation. *Science* **2012**, *336* (6077), 69–72. https://doi.org/10.1126/science.1215648.

(13) Navrotsky, A. Nanoscale Effects on Thermodynamics and Phase Equilibria in Oxide Systems. *ChemPhysChem* **2011**, *12* (12), 2207–2215. https://doi.org/10.1002/cphc.201100129.

(14) Stranski, I. N.; Totomanow, D. Rate of Formation of (Crystal) Nuclei and the Ostwald Step Rule. *Z Phys Chem* **1933**, *163*, 399–408.

(15) Wolf, S. E.; Leiterer, J.; Kappl, M.; Emmerling, F.; Tremel, W. Early Homogenous Amorphous Precursor Stages of Calcium Carbonate and Subsequent Crystal Growth in Levitated Droplets. *J. Am. Chem. Soc.* **2008**, *130* (37), 12342–12347. https://doi.org/10.1021/ja800984y.

(16) Gebauer, D.; Völkel, A.; Cölfen, H. Stable Prenucleation Calcium Carbonate Clusters. *Science* **2008**, *322* (5909), 1819–1822. https://doi.org/10.1126/science.1164271.

(17) Raiteri, P.; Gale, J. D. Water Is the Key to Nonclassical Nucleation of Amorphous Calcium Carbonate. *J. Am. Chem. Soc.* **2010**, *132* (49), 17623–17634. https://doi.org/10.1021/ja108508k.

(18) Rieger, J.; Kellermeier, M.; Nicoleau, L. Formation of Nanoparticles and Nanostructures-An Industrial Perspective on $CaCO_3$, Cement, and Polymers. *Angew. Chem. Int. Ed.* **2014**, n/a-n/a. https://doi.org/10.1002/anie.201402890.

(19) Cordova, D. L. M.; Johnson, D. C. Synthesis of Metastable Inorganic Solids with Extended Structures. *ChemPhysChem* **2020**, *21* (13), 1345–1368. https://doi.org/10.1002/cphc.202000199.

(20) Bauers, S. R.; Wood, S. R.; Jensen, K. M.; Blichfeld, A. B.; Iversen, B. B.; Billinge, S. J.; Johnson, D. C. Structural Evolution of Iron Antimonides from Amorphous Precursors to Crystalline Products Studied by Total Scattering Techniques. *J. Am. Chem. Soc.* **2015**, *137* (30), 9652–9658.

(21) Kirkpatrick, S.; Gelatt, C. D.; Vecchi, M. P. Optimization by Simulated Annealing. *Science* **1983**, *220* (4598), 671–680. https://doi.org/10.1126/science.220.4598.671.

(22) Kogel, J. E.; Society for Mining, M., and Exploration (U. S.). *Industrial Minerals & Rocks: Commodities, Markets, and Uses.*; Society for Mining, Metallurgy, and Exploration: Littleton, 2006.

(23) Stawski, T. M.; van Driessche, A. E. S.; Ossorio, M.; Diego Rodriguez-Blanco, J.; Besselink, R.; Benning, L. G. Formation of Calcium Sulfate through the Aggregation of Sub-3 Nanometre Primary Species. *Nat. Commun.* **2016**, *7* (1), 11177. https://doi.org/10.1038/ncomms11177.

(24) Gower, L. B. Biomimetic Model Systems for Investigating the Amorphous Precursor Pathway and Its Role in Biomineralization. *Chem. Rev.* **2008**, *108* (11), 4551–4627. https://doi.org/10.1021/cr800443h.

(25) Meldrum, F. C.; Cölfen, H. Controlling Mineral Morphologies and Structures in Biological and Synthetic Systems. *Chem. Rev.* **2008**, *108* (11), 4332–4432. https://doi.org/10.1021/cr8002856.

(26) Warren, J. K. *Evaporites: Sedimentology, Resources and Hydrocarbon*; Springer: Berlin, 2006.

(27) Wang, Y.-W.; Kim, Y.-Y.; Christenson, H. K.; Meldrum, F. C. A New Precipitation Pathway for Calcium Sulfate Dihydrate (Gypsum) via Amorphous and Hemihydrate Intermediates. *Chem Commun* **2012**, *48* (4), 504–506. https://doi.org/10.1039/C1CC14210K.

(28) Stawski, T. M.; Besselink, R.; Chatzipanagis, K.; Hövelmann, J.; Benning, L. G.; Van Driessche, A. E. S. Nucleation Pathway of Calcium Sulfate Hemihydrate (Bassanite) from Solution: Implications for Calcium Sulfates on Mars. *J. Phys. Chem. C* **2020**, *124* (15), 8411–8422. https://doi.org/10.1021/acs.jpcc.0c01041.

(29) Tritschler, U.; Van Driessche, A. E. S.; Kempter, A.; Kellermeier, M.; Cölfen, H. Controlling the Selective Formation of Calcium Sulfate Polymorphs at Room Temperature. *Angew. Chem. Int. Ed.* **2015**, *54* (13), 4083–4086. https://doi.org/10.1002/anie.201409651.

(30) Morse, J. W.; Arvidson, R. S.; Lüttge, A. Calcium Carbonate Formation and Dissolution. *Chem. Rev.* **2007**, *107* (2), 342–381. https://doi.org/10.1021/cr050358j.

(31) Németh, P.; Mugnaioli, E.; Gemmi, M.; Czuppon, G.; Demény, A.; Spötl, C. A Nanocrystalline Monoclinic $CaCO_3$ Precursor of Metastable Aragonite. *Sci. Adv.* **2018**, *4* (12), eaau6178. https://doi.org/10.1126/sciadv.aau6178.

(32) Zou, Z.; Habraken, W. J. E. M.; Matveeva, G.; Jensen, A. C. S.; Bertinetti, L.; Hood, M. A.; Sun, C.; Gilbert, P. U. P. A.; Polishchuk, I.; Pokroy, B.; Mahamid, J.; Politi, Y.; Weiner, S.; Werner, P.; Bette, S.; Dinnebier, R.; Kolb, U.; Zolotoyabko, E.; Fratzl, P. A Hydrated Crystalline Calcium Carbonate Phase: Calcium Carbonate Hemihydrate. *Science* **2019**, *363* (6425), 396–400. https://doi.org/10.1126/science.aav0210.

(33) Leukel, S.; Panthöfer, M.; Mondeshki, M.; Kieslich, G.; Wu, Y.; Krautwurst, N.; Tremel, W. Mechanochemical Access to Defect-Stabilized Amorphous Calcium Carbonate. *Chem. Mater.* **2018**, *30* (17), 6040–6052. https://doi.org/10.1021/acs.chemmater.8b02339.

(34) Hawthorne, F. C.; Ferguson, R. B. Anhydrous Sulphates; I, Refinement of the Crystal Structure of Celestite with an Appendix on the Structure of Thenardite. *Can. Mineral.* **1975**, *13* (2), 181–187.

(35) Mees, F.; Hatert, F.; Rowe, R. Omongwaite, Na2Ca5(SO4)6.3H2O, a New Mineral from Recent Salt Lake Deposits, Namibia. *Mineral. Mag.* **2008**, *72* (6), 1307–1318. https://doi.org/10.1180/minmag.2008.072.6.1307.

(36) Rietveld, H. M. A Profile Refinement Method for Nuclear and Magnetic Structures. *J. Appl. Crystallogr.* **1969**, *2* (2), 65–71. https://doi.org/10.1107/S0021889869006558.

(37) Freyer, D.; Reck, G.; Bremer, M.; Voigt, W. Thermal Behaviour and Crystal Structure of Sodium-Containing Hemihydrates of Calcium Sulfate. *Monatshefte Für ChemieChemical Mon.* **1999**, *130* (10), 1179–1193.

(38) Swain, D.; Guru Row, T. N. Analysis of Phase Transition Pathways in X3H (SO4) 2 (X= Rb, NH4, K, Na): Variable Temperature Single-Crystal X-Ray Diffraction Studies. *Inorg. Chem.* **2007**, *46* (11), 4411–4421.

(39) Xue, X.; Kanzaki, M. Proton Distributions and Hydrogen Bonding in Crystalline and Glassy Hydrous Silicates and Related Inorganic Materials: Insights from High-Resolution Solid-State Nuclear Magnetic Resonance Spectroscopy. *J. Am. Ceram. Soc.* **2009**, *92*, 2803–2830. https://doi.org/10.1111/j.1551-2916.2009.03468.x.

(40) Hoeher, A.; Mergelsberg, S.; Borkiewicz, O. J.; Dove, P. M.; Michel, F. M. A New Method for *in Situ* Structural Investigations of Nano-Sized Amorphous and Crystalline Materials Using Mixed-Flow Reactors. *Acta Crystallogr. Sect. Found. Adv.* **2019**, *75* (5), 758–765. https://doi.org/10.1107/S2053273319008623.

(41) Coelho, A. A. *TOPAS* and *TOPAS-Academic* : An Optimization Program Integrating Computer Algebra and Crystallographic Objects Written in C++. *J. Appl. Crystallogr.* **2018**, *51* (1), 210–218. https://doi.org/10.1107/S1600576718000183.

(42) Leukel, S.; Panthöfer, M.; Mondeshki, M.; Schärtl, W.; Plana-Ruiz, S.; Tremel, W. Calcium Sulfate Nanoparticles with Unusual Dispersibility in Organic Solvents for Transparent Film Processing. *Langmuir* **2018**, *34* (24), 7096–7105. https://doi.org/10.1021/acs.langmuir.8b00927.

(43) Leukel, S.; Tremel, W. Water-Controlled Crystallization of CaCO3, SrCO3, and MnCO3 from Amorphous Precursors. *Cryst. Growth Des.* **2018**, *18* (8), 4662–4670. https://doi.org/10.1021/acs.cgd.8b00627.

(44) Kolb, U.; Krysiak, Y.; Plana-Ruiz, S. Automated Electron Diffraction Tomography – Development and Applications. *Acta Crystallogr. Sect. B Struct. Sci. Cryst. Eng. Mater.* **2019**, *75* (4), 463–474. https://doi.org/10.1107/S2052520619006711.

(45) Treacy, M. M. J.; Newsam, J. M.; Deem, M. W. A General Recursion Method for Calculating Diffracted Intensities from Crystals Containing Planar Faults. *Proc. R. Soc. Lond. Ser. Math. Phys. Sci.* **1991**, *433* (1889), 499–520. https://doi.org/10.1098/rspa.1991.0062.

(46) Ball, J. W.; Nordstrom, D. K. WATEQ4F -- User’s Manual with Revised Thermodynamic Data Base and Test Cases for Calculating Speciation of Major, Trace and Redox Elements in Natural Waters. *Open-File Rep.* **1991**, 90–129.

(47) Nielsen, M. R.; Sand, K. K.; Rodriguez-Blanco, J. D.; Bovet, N.; Generosi, J.; Dalby, K. N.; Stipp, S. L. S. Inhibition of Calcite Growth: Combined Effects of Mg2+ and SO42–. *Cryst. Growth Des.* **2016**, *16* (11), 6199–6207. https://doi.org/10.1021/acs.cgd.6b00536.

(48) Offeddu, F. G.; Cama, J.; Soler, J. M.; Putnis, C. V. Direct Nanoscale Observations of the Coupled Dissolution of Calcite and Dolomite and the Precipitation of Gypsum. *Beilstein J. Nanotechnol.* **2014**, *5* (1), 1245–1253. https://doi.org/10.3762/bjnano.5.138.

(49) Nardi, A.; Idiart, A.; Trinchero, P.; Vries, L.; Molinero, J. Interface COMSOL-PHREEQC (ICP), an Efficient Numerical Framework for the Solution of Coupled Multiphysics and Geochemistry. *Comput. Geosci.* **2014**, *69*. https://doi.org/10.1016/j.cageo.2014.04.011.

(50) Du, H.; Amstad, E. Water: How Does It Influence the $CaCO_3$ Formation? *Angew. Chem. Int. Ed.* **2020**, *59* (5), 1798–1816. https://doi.org/10.1002/anie.201903662.

4.1.6 METHODS

Materials. Calcite (98%, Socal 31, Solvay), sodium bisulfate (anhydrous 95%, Honeywell Fluka), calcium carbonate-^{13}C (99 atom % ^{13}C, isotec), calcium sulfate dihydrate (99%,Sigma Aldrich), calcium sulfate hemihydrate (98%,Sigma Aldrich), cyclohexane (Analytical reagent grade, Fisher Chemicals), ethanol (absolute 99.8+%, Fisher Chemicals), acetonitrile (for HPLC, gradient grade, 99.9 %, Honeywell Riedel-de Haën) and milliQ deionized water.

Synthesis of amorphous calcium carbonate sodium hydrogen sulfate. Sodium hydrogen sulfate (0.120 g, 1 mmol) was treated with calcium carbonate (0.100 g, 1 mmol) in a planetary ball mill (Pulverisette 7 Classic, Fritsch). The starting materials and 10 mL of cyclohexane were transferred together with 3.65 grams of grinding balls (about 1100 balls, 1 mm diameter, ZrO_2) into ZrO_2 grinding jars. The mixture was milled for 12 h at 720 rpm. To avoid overheating, alternate 10 minutes of grinding and then a 10 minute rest phase was used. Therefore, 720 minutes of ball milling results in 1430 minutes of reaction time. Afterward, the cyclohexane was removed with a pipette. The product was dispersed in ethanol and separated from the grinding balls by decanting. The product was isolated by centrifugation and dried in vacuo.

Crystallization experiments. The crystallization experiments were carried out by adding aCCSHS to a solution of acetonitrile and water resulting in a concentration of 3 mg/mL. To monitor the crystallization *ex situ* at a given time 1 ml of the dispersion was transferred to a microreaction vessel containing 0.5 ml acetone. After centrifugation, the liquid phase was decanted, washed with acetone again and dried in vacuo.

Characterization

X-ray Powder Diffraction. X-ray diffractograms were recorded with a STOE Stadi P equipped with a Mythen 1k detector using Mo Kα_1 radiation (λ=0.7093 Å). The dry samples were prepared between polyvinyl acetate foils in perfluoroether (Fomblin Y, Aldrich). The measurements were performed in the 2θ range from 2° to 45° with a step size of 0.015° (continuous scan, 150 s/deg). Crystalline phases were identified according to the PDF-2 database using Bruker AXS.

ATR-FTIR Spectroscopy. The attenuated total reflection (ATR) FTIR spectra were recorded on a Nicolet iS10 spectrometer (Thermo scientific) using a frequency range from 550 to 4000 cm^{-1} with a resolution of 1.4 cm^{-1} per data point.

Raman Spectroscopy. Raman spectra were measured on a Nicolet 5700 FT-IR spectrometer combined with NXR 9650 FT-Raman Module equipped with a 1064 nm laser, a Microstage Microscope, and a NXR Genie Ge-detector using single crystals in glass capillaries under inert gas.

Solid-State NMR Spectroscopy. All solid state NMR spectra were recorded on a Bruker Advance 400 DSX NMR spectrometer (Bruker BioSpin GmbH, Rheinstteten, Germany operated by Topspin 1.3, 2007, patchlevel 8) at a ^{1}H frequency of 399.87 MHz, ^{13}C frequency of 100.55 MHz and ^{31}P frequency of 161.87 MHz. A commercial 3 channel 4 mm Bruker probe head at 10 kHz magic angle spinning (MAS) was used for all experiments. The ^{1}H NMR spectra and ^{1}H background corrected spectra were recorded averaging 32 transients with 8 s recycle delay. For all solid-state ^{13}C cross-polarization (CP) magic angle spinning (MAS) NMR experiments, an initial 90° pulse with 4.0 μs length and 5 s recycle delay were used. A ramped CP pulse (from 64 to 100%) with duration of 20 μs, 50 μs, 100 μs, 200 μs, 500 μs, 1 ms, 2 ms, 3 ms, 5 ms and 7 ms was used for recording the CP build-up curves. Two pulse phase modulation (TPPM) ^{1}H decoupling scheme was used while acquiring the ^{13}C signal. 512 transients were averaged for the CP experiments. The spectra were baseline-corrected and a broadening of 30 Hz was applied. Quantitative ^{13}C single pulse excitation experiments allowing full relaxation have been recorded averaging 16 transients with a recycle delay of 2200 s and TPPM heteronuclear decoupling. The spectrum was background corrected and a broadening of 30 Hz was applied. The ^{1}H-^{13}C heteronuclear correlation (HETCOR) 2D NMR spectra were acquired using ^{1}H-^{13}C magnetization transfer with contact times of 50 and 2000 μs and 256 transients/t1. The data points recorded were 1 k (t1) and 96 or 128 (t2) and zero-filled to 4 k (t1) and 256 (t2) before the 2D Fourier transformation. The other parameters were identical to those for the 1D CP NMR experiments. Spectral deconvolution were performed using self-written Matlab scripts (version 2017b).

Thermal Analysis. Coupled thermogravimetry-differential thermal analysis (TG-DTA) was carried out at a Netzsch STA 449 F3 Jupiter device. About 10 mg of the sample was heated in an alumina cup in argon atmosphere from 50 to 900 °C at a heating rate of 10 K/min.

Transmission Electron Microscopy (TEM). TEM samples were prepared by dispersing the dry powder mixture in ethanol and spraying it on a carbon-coated copper grid with a UIS250v Hielscher sonifier. A FEI Tecnai F30 S-TWIN TEM equipped with a field emission gun and operated at 300 kV was used for their inspection. The fast and automated diffraction tomography (Fast-ADT) routine in STEM mode, which is implemented as a Digital Micrograph plug-in, was employed for the acquisition of 3D electron diffraction (3D ED) datasets [1]. During these diffraction collections, a quasi-parallel beam of 150-nm in size was set to acquire the patterns by means of a 10-µm condenser aperture, spot size 6 and gun lens 8 [2]. The energy dispersive X-ray spectroscopy (EDS) measurements were conducted with a 50-µm condenser aperture, spot size 6 and gun lens 1 to increase the electron dose and have a reliable number of counts on the EDS detector (EDAX EDAM III). STEM images were collected using a Fischione high-angle annular dark field (HAADF) detector, while electron diffraction patterns were acquired with an UltraScan4000 CCD-based detector (Gatan, 16-bit, 4096 x 4096 pixels). Hardware binning 2 and exposure time of 1 second were used to acquire non-saturated reflections. Precession electron diffraction (PED) was coupled to the Fast-ADT routine to minimize the dynamical effects of the diffraction data and improve the reflection intensity integration quality [3–5]. PED was applied from the DigiStar signal generator unit developed by NanoMegas SPRL and it was kept to 1° for all 3D ED datasets.

A FEI single-tilt holder as well as a Fischione tomography holder were used to acquire seven 3D ED datasets with a maximum angular range between -60° and 60°. The processing of the obtained diffraction data for unit cell determination, space group identification and reflection intensity extraction was carried out by eADT and PETS2 programs [6,7]. Ab initio crystal structure determination was performed with Sir2014 and Jana2006 using direct methods and the charge-flipping algorithm, respectively [8,9]. EDS peak identification was done via the ES Vision software.

In order to increase the crystallographic completeness of the 3D electron diffraction data, three datasets were merged as one and reconstructed with PETS2.06 [7]. It was necessary to carefully refine the orientation of each single frame. The data integration with the subunit cell resulted in R_{int}(all) of 11.76% for Laue class *mmm*. Ab initio structure solution was performed ($R_F = 15.9\%$) assuming the kinematic approximation $I \sim |F_{hkl}|^2$ by Direct Methods implemented in the program SIR2014 [8]. The atomic coordinates sorted by scattering density are listed Table S2. The atom types of S2 was changed into calcium and

Ca1 and C1 were changed into sulfur. Atomic sites referenced to sodium are O1, O2 and S1, S3, Na1, Na2, Na3, C3 belongs to oxygen. The atom type of O1 was changed into carbon, whereas O10, C2, C4, C5, C6 and C7 have been deleted. The isotropic atomic displacement parameters of Ca, S, Na and O, C atoms were set to 0.015 Å² and 0.003 Å², respectively. After the structure refinement (Table S1 and S2) with Shelxle/SHELXL [10] high residuals (78 e–m-3:Q1-C2 = 0.598 Å; 54 e–m-3:Q2-S3 = 0.625 Å and 31 e–m-3:Q1-Q5 = 1.515 Å) could be attributed to an overlay of sulfate with carbonate (displacement factors fixed to 0.01 for S3, C1, S4, C2). In addition, two water positions were detected. The refinement assuming 1:1 ratio of sulfate to carbonate and water converged to a residual of R1=17.1% (highest residual 0.24 e–m-3@ Na). Due to preferred crystal orientation the intensity data complete-ness (coverage of independent reflections) reached only 80% after merging thus, the structure model was not refined on the basis of the detected supercell.

Synchrotron X-ray powder diffraction data. High resolution synchrotron powder diffraction data were collected using beamline 11-BM at the Advanced Photon Source (APS), Argonne National Laboratory using an average wavelength of 0.458104 Å. Discrete detectors covering an angular range from -6 to 16 º 2θ are scanned over a 34º 2θ range, with data points collected every 0.001º 2 θ and scan speed of 0.01º/s.

Total Scattering. Total scattering measurement of the amorphous calcium carbonate sodium hydrogen sulfate were performed at beamline I15-1 at the Diamond Light Source, UK, using an X-ray energy of 76.69 keV ($\lambda = 0.161669$ Å). A Perkin Elmer XRD 4343 CT and a PerkinElmer XRD 16611 CP 3 was used as a primary and secondary detector. The resulted 2D images were integrated by using the software *DAWNscience*.[11] The analysis of the atomic pair distribution function (PDF) was performed utilizing the *GudrunX* software with Qmax = 25 $Å^{-1}$. We used TOPAS AcademicV6 for modelling and simulating the PDFs. Structural models were derived for a set of 42 calcium 42 sodium 42 hydrogen, 42 carbonate and 42 sulfate ions inside a cubic box of space group symmetry P1. We treated carbonate, hydrogen carbonate, sulfate, and hydrogen sulfate ions as rigid bodies. Furthermore, for electrostatic interactions the Lennard-Jones Potential was utilized as a light penalty via the General Real Space (GRS) interaction by TOPAS [12]. Also, we applied minimum distance restraints for all atom pairs to avoid chemical unreasonable solutions. All fractional and rigid body coordinates have been set initially to the origin. Simulated Annealing with a high starting "temperature" allow probing the entire real space in the beginning of a run."

4.1.7 SUPPORTING INFORMATION

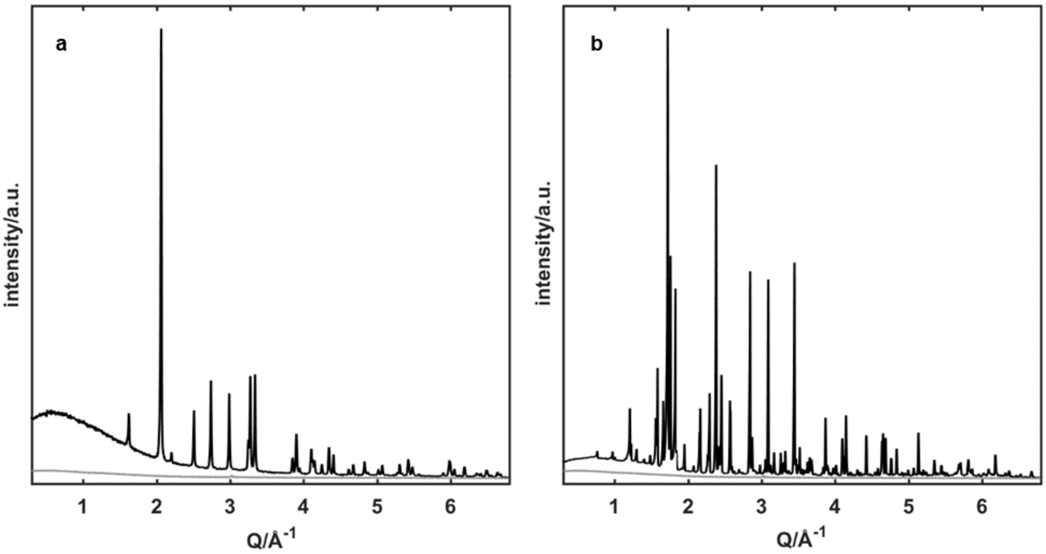

Fig S26. X-ray powder diffractograms of the starting materials (a) calcite and (b) $NaHSO_4$. $NaHSO_4$ is a mixture of $NaHSO_4$, $NaHSO_4 \cdot H_2O$ and $Na_3H(SO_4)_2$.

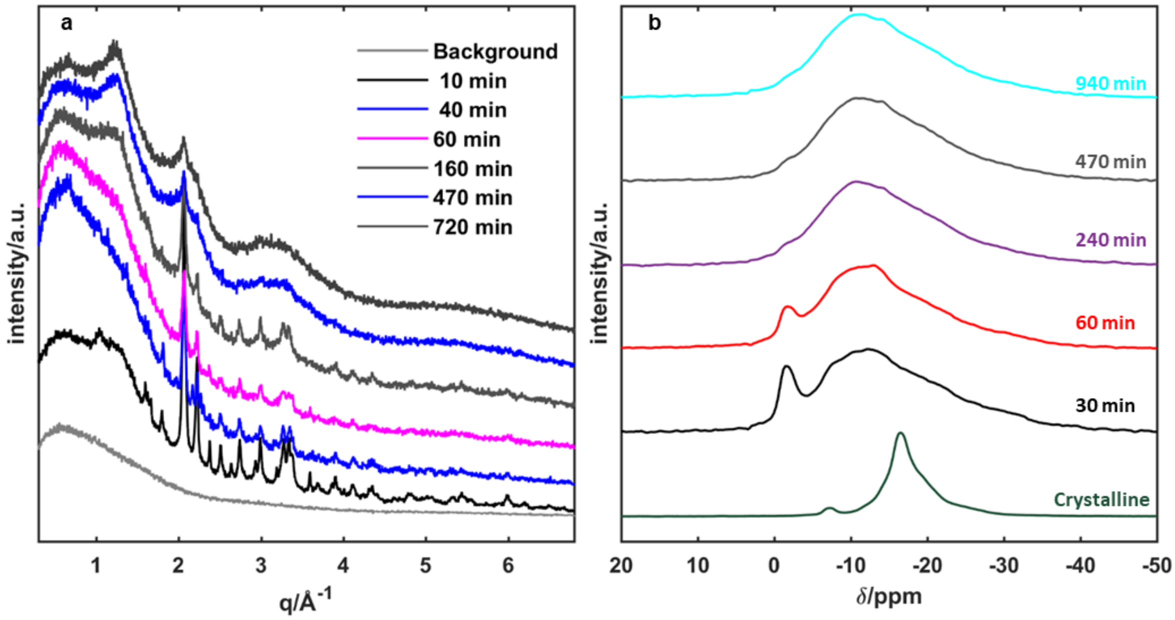

Fig S27. (a) X-ray powder diffractograms of the amorphization process monitored ex situ. The broadening and loss of reflections as a function of time displays the process of amorphization. **(b)** ^{23}Na-MAS-NMR spectra of the ball mill reaction before starting the grinding process (green line) and after different times of grinding indicates the formation of the amorphous phase.

The course of the ball milling reaction between $CaCO_3$ and $NaHSO_4$ could be monitored by ^{23}Na magic angle spinning nuclear magnetic resonance (^{23}Na-MAS-NMR) spectroscopy. The ^{23}Na-MAS NMR spectrum of crystalline $NaHSO_4$ shows one slightly asymmetric intense signal at ~-18.4 ppm and a second weak signal at ~-8.1 ppm corresponding to the non-symmetric (6+1) Na^+ coordination in the γ-$NaHSO_4$ structure (fig S2b), while each Na^+ cation is coordinated octahedrally by six HSO_4^- units in α-$NaHSO_4$.[13] After a milling time of 30 min the signals had shifted and split, corresponding to the presence of two possible bonding geometries (8- and 9 coordinated) of Na+ in the omongwaite struc-ture (Figure 2B). These signals further broadened, and after 240 min only a single broad ^{23}Na signal centered at ~-12 ppm was observed.

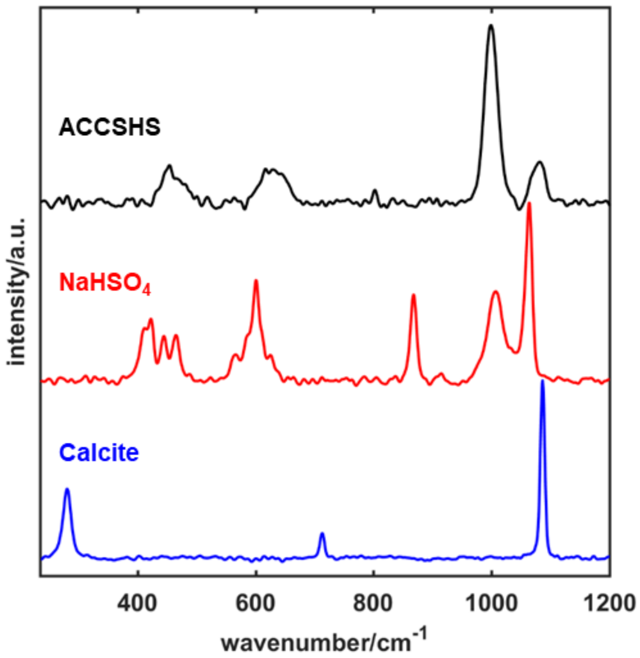

Fig S28. Raman spectra of aCCSHS (black line) with the corresponding starting materials calcite (blue line) and sodium hydrogen sulfate (red line).

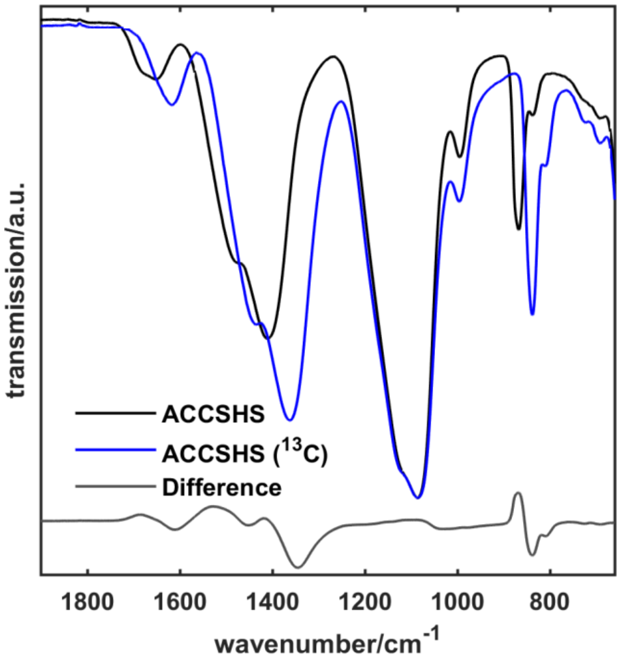

Fig S29. FTIR spectra of aCCSS (black line) and ^{13}C-enriched aCCSS (blue line) allows to distinguish between carbonate and sulfate vibration modes (difference curve, grey line).

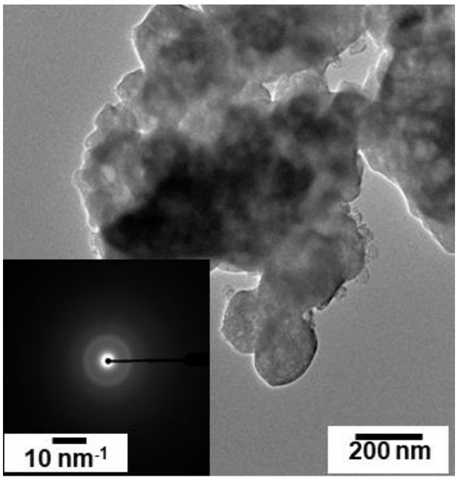

Fig S30. TEM image of aCCSHS and the associated diffraction pattern after 470 min of milling show complete amorphization.

The morphology of the particles is very different compared to amorphous carbonates precipitated from solution, and the particles have much larger diameters (up to 1 μm).[14]

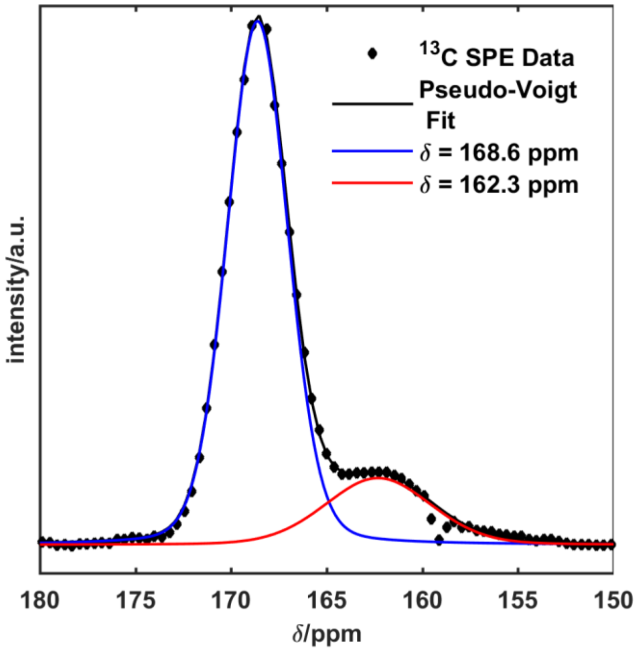

Fig S31. Best Pseudo-Voigt Fit of the ^{13}C MAS SPE NMR spectrum of aCCSS recorded with 2400 s recycle delay to ensure complete relaxation showing a ratio of 4.5:1 carbonate to hydrogen carbonate.

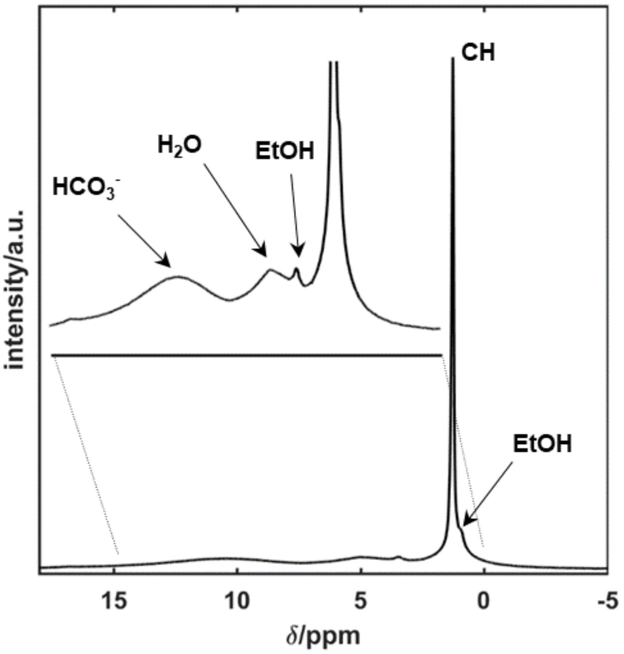

Fig S32. ^{1}H-MAS-NMR single pulse excitation (SPE) spectrum of aCCSHS.

The signals of the ^{1}H-SPE-MAS-NMR spectrum appear at 1.43 ppm (cyclohexane, dispersant), 5 ppm (water), 11 ppm (bicarbonate). Additionally, signals at ~1.3 and ~3 ppm due to the CH_3 and CH_2 groups of ethanol used to wash the amorphous material are detected while the resonance of the OH protons overlaps with the water signal. Despite washing the amorphous material with ethanol, cyclohexane is still present in the product (probably located within the grain boundaries of the amorphous material). However, cyclohexane does not show up in the HETCOR experiments. Therefore, the dispersant retains high mobility which leads to significantly reducing the dipole-dipole couplings and resp. to failure to detect in the cross-polarization experiment. Another confirmation is the sharp ^{1}H resonance signal of cyclohexane which correlates well with high mobility.

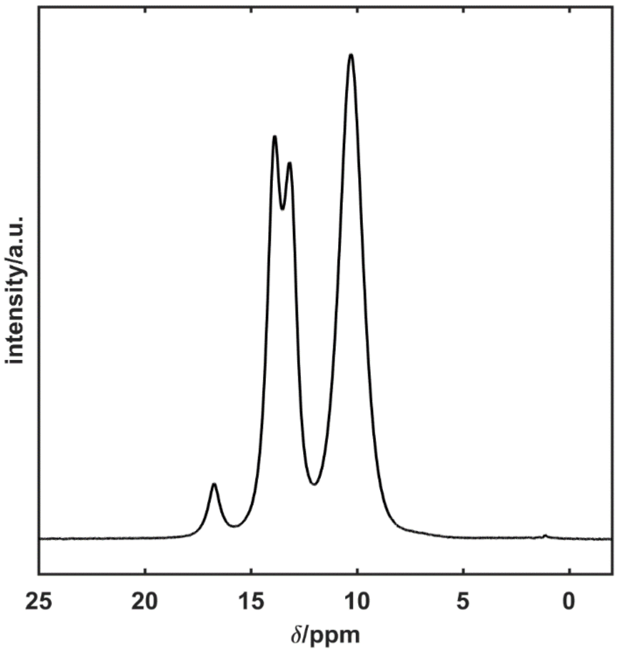

Fig S33. ^{1}H-MAS-NMR single pulse excitation (SPE) spectrum of $NaHSO_4$.

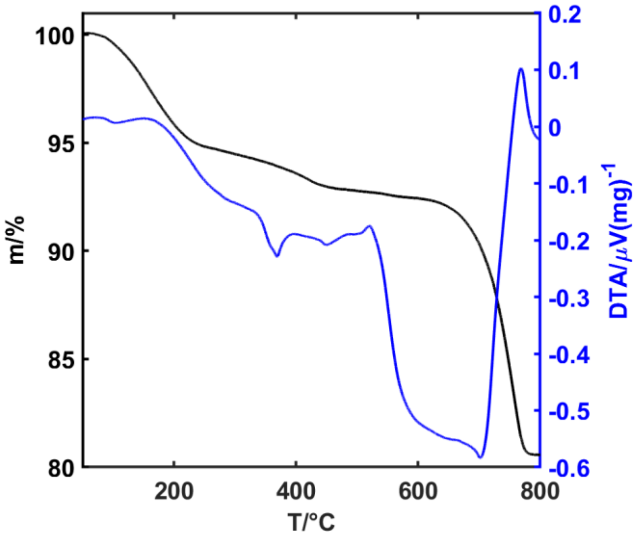

Fig S34. Thermogravimetric (black line) and differential thermal analysis (blue line) of aCCSHS.

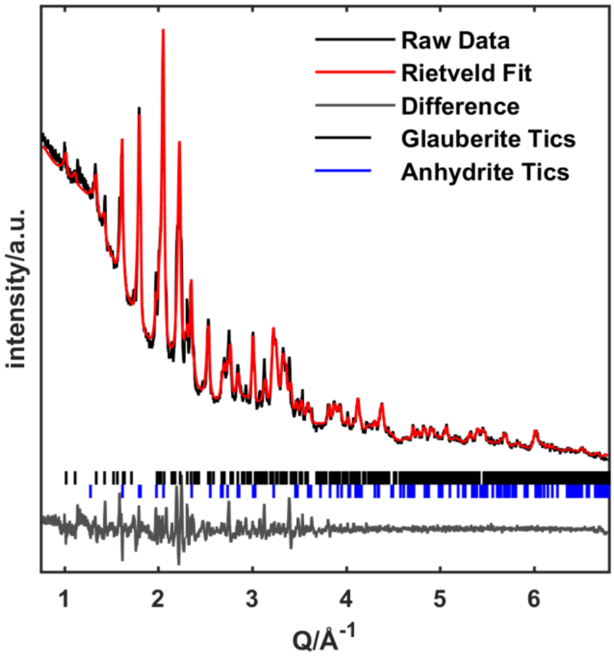

Fig S35. X-ray powder diffractorgram of aCCSS annealed at 450 °C. The Rietveld fit reveals the formation of glauberite ($Na_2Ca(SO_4)_2$).

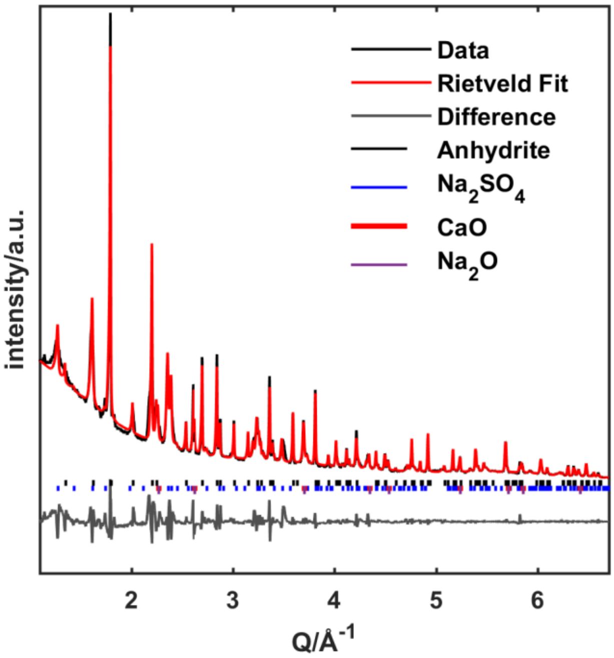

Fig S36. X-ray powder diffractogram of aCCSHS after annealing at 750 °C. The Rietveld fit reveals the formation of glauberite ($Na_2Ca(SO_4)_2$).

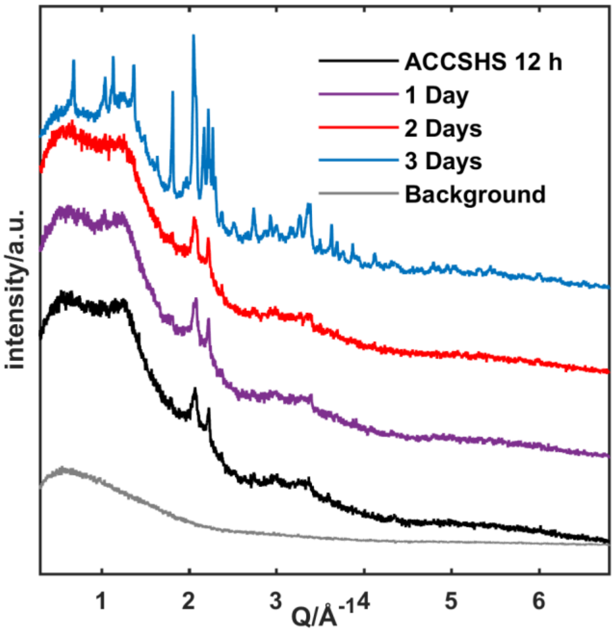

Fig S37. X-ray powder diffractogram of aCCSHS in paraffin oil. Slow crystallization occurs within several days.

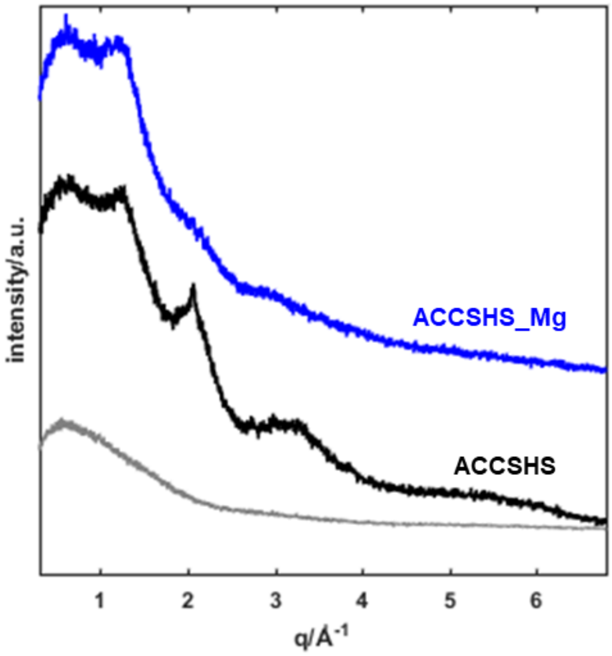

Fig S38. X-ray powder diffractograms of aCCSHS (black line) and aCCSHS synthesiszed with basic magnesium carbonate (ratio of Ca^{2+} to Mg $^{2+}$ is 1:1). The grey line is the background.

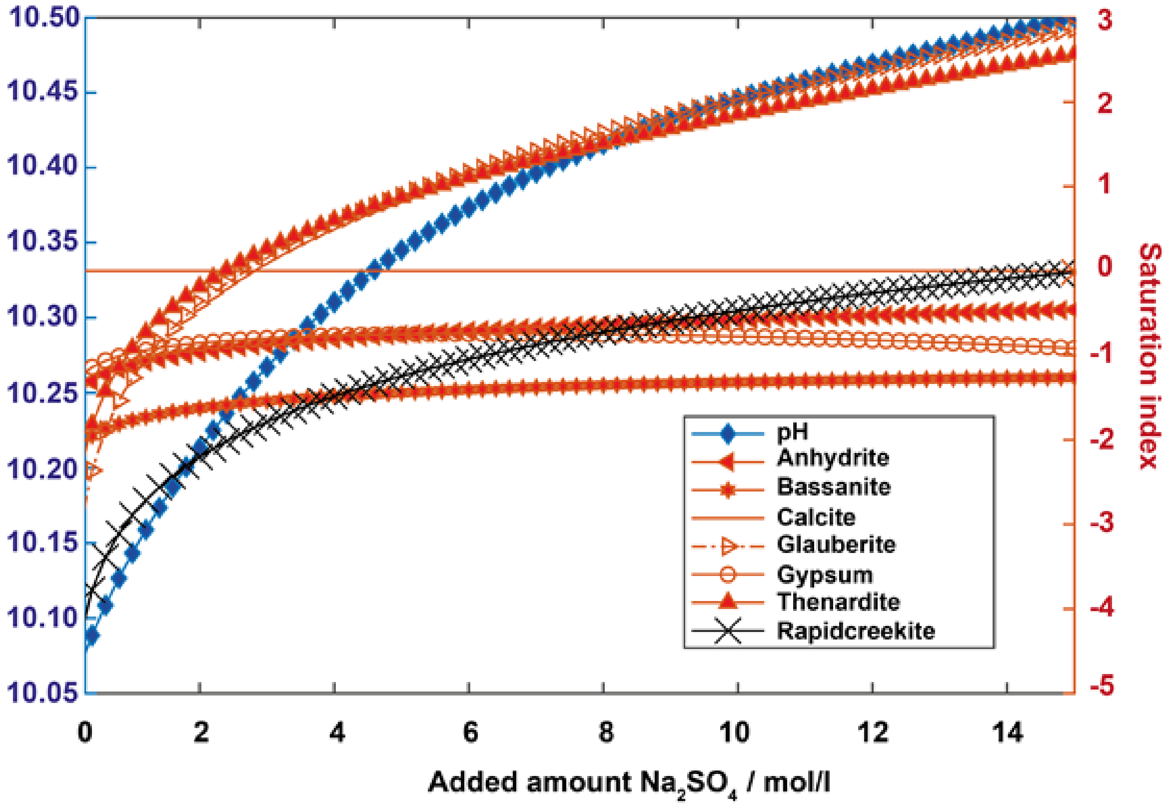

Fig S39. Approximated solubility window of various sulfate phases. $Ca_2(SO_4)(CO_3)\cdot4H_2O$ (rapidcreekite), glauberite and thenardite are expected to be precipitated. Remarkably, glauberite can be detected as a secondary phase in the SXRPD.

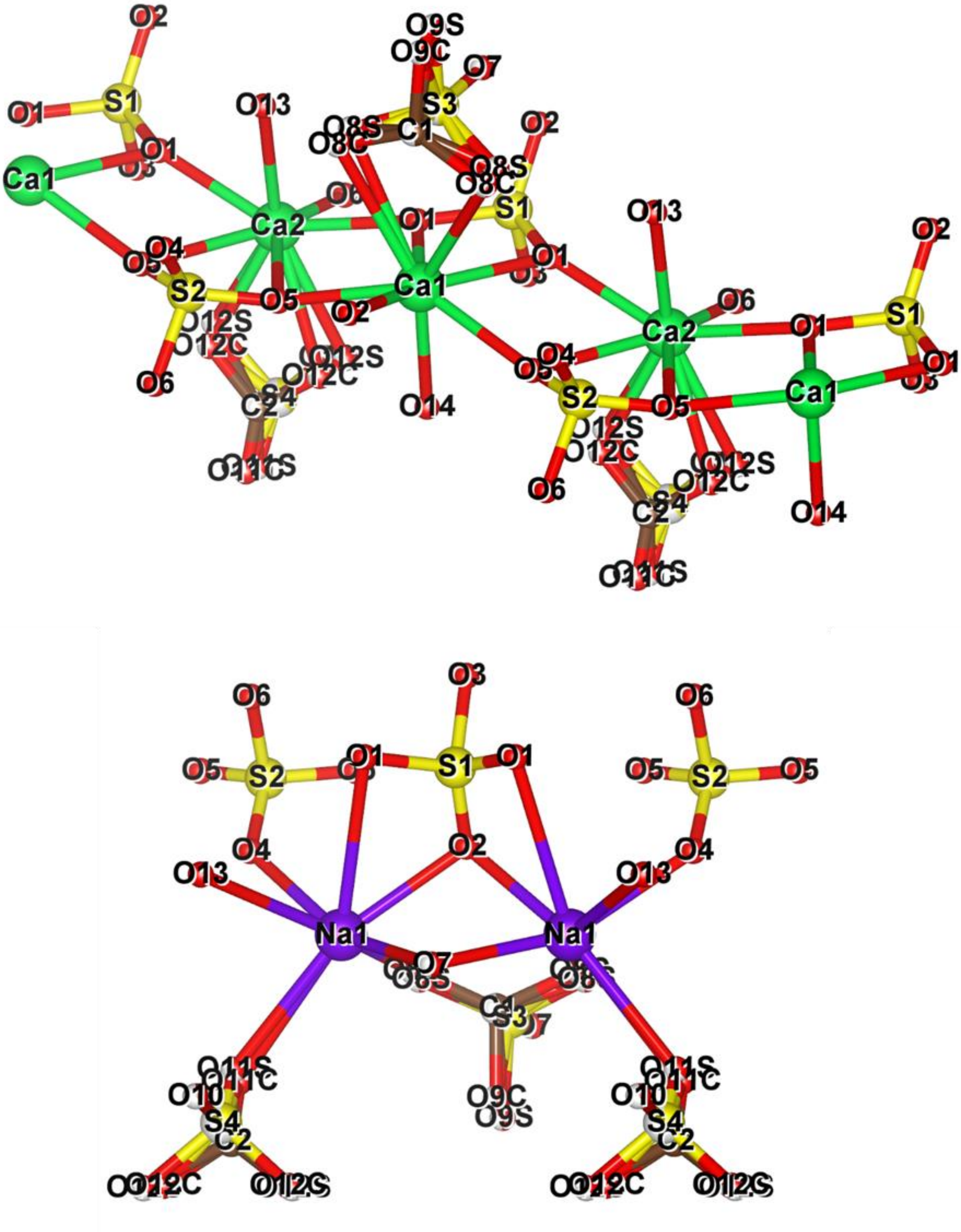

Fig S40. Sketch of Ca coordination in Mainzite. Calcium atoms green sphere, sulfur atoms yellow sphere, oxygen atoms red sphere. Atom names according to Tables S2, S3, S4.

Table S5. 3D ED parameters, structure solution and residuals.

	Mainzite
Crystal data	
Crystal system, space group	orthorhombic, $Pcm2_1$ (No. 26)
a (Å), b (Å), c (Å), V (Å^3)	6.431(1), 6.906(1), 18.321(5), 813.6(3)
Z	2
Unit cell content	Ca4Na8S6C2O35
Data collection	
Radiation type	electrons, 300 kV
Wavelength (Å)	0.01970
Temperature (K)	293
Precession angle (deg.)	0.94
Resolution (Å^{-1})	0.83
Tilt step	Three combined datasets, each with 1° tilt step
No of frames	213
Completeness	80%
Structure solution	
R_F (%)	17.13
Kinematical structure refinement (with fixed coordinates)	
Calculated density (g.cm^{-3})	2.402 (without hydrogen atoms)
No. of used reflections (obs/all)	1172/1203
R1(obs)/R1(all), wR1(obs) (%)	21.6/21.9, 53.5
goodness of fit (obs/all)	3.09/3.9
No. of refined parameters/restraints	84/41
Fixed geometry (S-O, C-O, CO3,O-O$_{tetra}$)	(1.5, 1.3, flat, 2.4)
Fixed U_{iso} and occupancy for	sulfur, carbonate and water groups

Table S6. Atomic positions of mainzite.

Atom	Label	x	y	z	Occ.	U_{iso} (Å^2)
Ca	Ca1	0.3851(18)	0.50000	0.6421(9)	1.000	0.038(3)
Ca	Ca2	0.108(3)	0.00000	0.6874(14)	1.000	0.068(5)
Na	Na1	-0.163(3)	0.242(3)	0.5202(15)	1.000	0.054(5)
Na	Na2	-0.253(4)	0.265(4)	0.817(2)	1.000	0.070(6)
S	S1	-0.103(3)	0.50000	0.657(2)	1.000	0.063(6)
O	O1	0.049(3)	0.330(3)	0.6577(16)	1.000	0.049(5)
O	O2	-0.243(8)	0.50000	0.598(3)	1.000	0.093(15)
O	O3	-0.184(3)	0.50000	0.7376(15)	1.000	0.026(5)
S	S2	-0.4203(14)	0.00000	0.6643(8)	1.000	0.013(2)
O	O4	-0.295(6)	0.00000	0.597(2)	1.000	0.063(10)
O	O5	-0.538(3)	0.175(3)	0.6765(14)	1.000	0.047(5)
O	O6	-0.249(3)	0.00000	0.7236(16)	1.000	0.030(5)
S	S3	0.287(4)	0.50000	0.4788(18)	0.51(5)	0.024(5)
O	O7	0.060(6)	0.50000	0.484(3)	0.51(5)	0.024(5)
O	O8S	0.366(5)	0.313(5)	0.507(2)	0.51(5)	0.024(5)
O	O9S	0.316(7)	0.50000	0.394(3)	0.51(5)	0.024(5)
C	C1	0.417(7)	0.50000	0.480(5)	0.49(5)	0.047(6)
O	O8C	0.432(6)	0.312(7)	0.511(3)	0.49(5)	0.047(6)
O	O9C	0.386(10)	0.50000	0.407(5)	0.49(5)	0.047(6)
S	S4	0.102(5)	0.00000	0.860(2)	0.38(4)	0.024(5)
O	O10	-0.156(7)	0.00000	0.869(4)	0.38(4)	0.024(5)
O	O11S	0.206(8)	0.00000	0.910(4)	0.38(4)	0.024(5)
O	O12S	0.092(7)	-0.168(6)	0.805(3)	0.38(4)	0.024(5)
C	C2	0.207(7)	0.00000	0.850(4)	0.62(4)	0.047(6)
O	O11C	0.268(8)	0.00000	0.903(4)	0.62(4)	0.047(6)
O	O12C	0.170(6)	-0.141(6)	0.811(3)	0.62(4)	0.047(6)
O	O13	0.180(8)	0.00000	0.553(4)	1.0000	0.089(8)
O	O14	0.346(8)	0.50000	0.770(4)	1.0000	0.089(8)
O	O15	-0.398(8)	0.00000	0.966(4)	1.0000	0.089(8)

Table S7. Atomic distances.

Atom 1	Multiplicity x Atom 2	Distance/Å
Metal-oxygen Distances		
Na1	1 x O2@S1	2.34(5)
Na1	1 x O4@S2	2.34(4)
Na1	1 x O7	2.38(4)
Na1	1 x O11@S4/C2	2.80(7)
Na1	1 x O13	2.83(5)
Na1	1 x O1@S1	2.93(4)
Na1	1 x O8@S3/C1	3.08(4)
Na2	1 x O10@S4/C2	2.15(4)
Na2	1 x O9@S3/C1	2.18(3)
Na2	1 x O3@S1	2.22(4)
Na2	1 x O12@S4/C2	2.32(1)
Na2	1 x O6@S2	2.51(4)
Na2	1 x O15	3.42(7)
Ca1	2 x O1@S1	2.48(3)
Ca1	1 x O14	2.36(8)
Ca1	2 x O5@S2	2.38(3)
Ca1	1 x O2@S1	2.52(2)
Ca1	2 x O8@S3/C1	2.79 (4)
Ca2	2 x O1@S1	2.37(3)
Ca2	2 x O5@S2	2.59(3)
Ca2	1 x O6@S2	2.39(3)
Ca2	1 x O13	2.51(8)
Ca2	2 x O12@S4/C2	2.45(6)
Carbon-oxygen Distances		
C1	O8	1.42(7)
C1	O9	1.35(1)
C2	O11	1.05(1)
C2	O12	1.23(7)
Sulphur-oxygen Distances		
S1	O1	1.57(3)
S1	O2	1.41(7)
S1	O3	1.49(5)
S2	O4	1.47(4)
S2	O5	1.44(3)
S2	O6	1.55(3)
S3	O7	1.46(5)
S3	O8	1.48(4)
S3	O9	1.56(7)
S4	O10	1.67(6)
S4	O11	1.46(6)
S4	O12	1.54(6)

Table S8. Atomic oxygen-oxygen distances.

Atom 1	Atom 2	distance/Å
Ca-O polyhedron (distorted square antiprismatic)		
O1	O1	2.35(5)
O1	O5	2.88(3)
O2	O5	3.27(5)
O1	O6	3.21(3)
O1	O8	3.43(5)
O2	O8	2.93(7)
O1	O12	2.98(7)
O1	O13	3.10(6)
O1	O14	3.04(6)
Na-O polyhedron (heptagon)		
O1	O2	2.47(6)
O1	O4	3.37(4)
O1	O7	3.39(6)
O1	O13	3.10(6)
O4	O13	3.16(7)
O7	O11	4.09(5)
O8	O11	3.50(7)
O11	O13	3.61(1)
C-O polyhedron (trigonal planar)		
O8	O8	2.60(1)
O8	O9	2.32(1)
O11	O12	2.05(9)
O12	O12	1.95(9)
S-O polyhedron (tetrahedral)		
O1	O1	2.35(5)
O1	O2	2.47(6)
O1	O3	2.40(4)
O4	O5	2.45(4)
O4	O6	2.34(5)
O5	O5	2.42(5)
O5	O6	2.38(3)
O7	O8	2.39(5)
O8	O8	2.58(7)
O10	O11	2.45(8)
O11	O12	2.36(9)
O12	O12	2.32(9)

References

(1) Plana-Ruiz, S.; Krysiak, Y.; Portillo, J.; Alig, E.; Estradé, S.; Peiró, F.; Kolb, U. Fast-ADT: A Fast and Automated Electron Diffraction Tomography Setup for Structure Determination and Refinement. *Ultramicroscopy* **2020**, *211*, 112951. https://doi.org/10.1016/j.ultramic.2020.112951.

(2) Plana-Ruiz, S.; Portillo, J.; Estradé, S.; Peiró, F.; Kolb, U.; Nicolopoulos, S. Quasi-Parallel Precession Diffraction: Alignment Method for Scanning Transmission Electron Microscopes. *Ultramicroscopy* **2018**, *193*, 39–51. https://doi.org/10.1016/j.ultramic.2018.06.005.

(3) Vincent, R.; Midgley, P. A. Double Conical Beam-Rocking System for Measurement of Integrated Electron Diffraction Intensities. *Ultramicroscopy* **1994**, *53* (3), 271–282. https://doi.org/10.1016/0304-3991(94)90039-6.

(4) Mugnaioli, E.; Gorelik, T.; Kolb, U. “Ab Initio” Structure Solution from Electron Diffraction Data Obtained by a Combination of Automated Diffraction Tomography and Precession Technique. *Ultramicroscopy* **2009**, *109* (6), 758–765. https://doi.org/10.1016/j.ultramic.2009.01.011.

(5) Palatinus, L.; Jacob, D.; Cuvillier, P.; Klementová, M.; Sinkler, W.; Marks, L. D. Structure Refinement from Precession Electron Diffraction Data. *Acta Crystallogr. A* **2013**, *69* (2), 171–188. https://doi.org/10.1107/S010876731204946X.

(6) Kolb, U.; Krysiak, Y.; Plana-Ruiz, S. Automated Electron Diffraction Tomography – Development and Applications. *Acta Crystallogr. Sect. B Struct. Sci. Cryst. Eng. Mater.* **2019**, *75* (4), 463–474. https://doi.org/10.1107/S2052520619006711.

(7) Palatinus, L.; Brázda, P.; Jelínek, M.; Hrdá, J.; Steciuk, G.; Klementová, M. Specifics of the Data Processing of Precession Electron Diffraction Tomography Data and Their Implementation in the Program *PETS2.0*. *Acta Crystallogr. Sect. B Struct. Sci. Cryst. Eng. Mater.* **2019**, *75* (4), 512–522. https://doi.org/10.1107/S2052520619007534.

(8) Burla, M. C.; Caliandro, R.; Carrozzini, B.; Cascarano, G. L.; Cuocci, C.; Giacovazzo, C.; Mallamo, M.; Mazzone, A.; Polidori, G. Crystal Structure Determination and Refinement *via SIR2014*. *J. Appl. Crystallogr.* **2015**, *48* (1), 306–309. https://doi.org/10.1107/S1600576715001132.

(9) Petříček, V.; Dušek, M.; Palatinus, L. Crystallographic Computing System JANA2006: General Features. *Z. Für Krist. - Cryst. Mater.* **2014**, *229* (5), 345–352. https://doi.org/10.1515/zkri-2014-1737.

(10) Hübschle, C. B.; Sheldrick, G. M.; Dittrich, B. *ShelXle* : A Qt Graphical User Interface for *SHELXL*. *J. Appl. Crystallogr.* **2011**, *44* (6), 1281–1284. https://doi.org/10.1107/S0021889811043202.

(11) Filik, J.; Ashton, A. W.; Chang, P. C. Y.; Chater, P. A.; Day, S. J.; Drakopoulos, M.; Gerring, M. W.; Hart, M. L.; Magdysyuk, O. V.; Michalik, S.; Smith, A.; Tang, C. C.; Terrill, N. J.; Wharmby, M. T.; Wilhelm, H. Processing Two-Dimensional X-Ray Diffraction and Small-Angle Scattering Data in *DAWN 2*. *J. Appl. Crystallogr.* **2017**, *50* (3), 959–966. https://doi.org/10.1107/S1600576717004708.

(12) Coelho, A. A. *TOPAS* and *TOPAS-Academic* : An Optimization Program Integrating Computer Algebra and Crystallographic Objects Written in C++. *J. Appl. Crystallogr.* **2018**, *51* (1), 210–218. https://doi.org/10.1107/S1600576718000183.

(13) Sonneveld, E. J.; Visser, J. W. Structure and Hydrogen Bonding of α-NaHSO4. *Acta Crystallogr. B* **1979**, *35* (9), 1975–1977. https://doi.org/10.1107/S0567740879008281.

(14) Leukel, S.; Panthöfer, M.; Mondeshki, M.; Kieslich, G.; Wu, Y.; Krautwurst, N.; Tremel, W. Mechanochemical Access to Defect-Stabilized Amorphous Calcium Carbonate. *Chem. Mater.* **2018**, *30* (17), 6040–6052. https://doi.org/10.1021/acs.chemmater.8b02339.

5 Conclusion

In this dissertation, new amorphous calcium carbonate phases were mechanochemically synthesized by introducing “impurities”, in particular $CaHPO_4$, $NaHSO_4$ and basic $MgCO_3$. These impurities allowed a new class of amorphous mixtures to be stabilized. The amorphization path was monitored *ex situ* by a whole series of analytic methods. Therefore, these findings, shed light on mechanistic processes during ball-milling reactions.

Calcium carbonate represents a model system to investigate crystallization and polymorphism. Amorphous intermediates provide a possibility to control and influence crystallization processes. This new solid solutions of calcium carbonate and $CaHPO_4$/$NaHSO_4$/basic $MgCO_3$ allowed to obtain crystallization paths that lead to unique compounds. The ions in the solid solutions are spatially trapped next to each other, thus different crystallization conditions allow to obtain materials which are the kinetic or thermodynamic product, *i.e.* slow crystallization of the solid solution prevents phase separation, leading to thermodynamically less stable phases.

Each individual impurity provides a whole range of possible chemical compounds to be formed and therefore introduces new synthetic and analytical challenges. Therefore, this work is structured in the different impurities applied for the mechanochemical amorphization of calcium carbonate: i) amorphous amorphous calcium carbonate/calcium hydrogen phosphate (aCCP), ii) amorphous magnesium calcium carbonate (aMCC) and iii) amorphous calcium carbonate sodium hydrogen sulfate (aCCSHS).

In the first part of this dissertation, the formation of amorphous anhydrous alkaline earth carbonates in a planetary ball mill was explored. The amorphization is not only caused by the mechanical impact on the material and thus a simple substitution of the carbonate and phosphate anions. However, the primary driving force of the amorphization involves an acid-base reaction of hydrogen phosphate and carbonate. Furthermore, extended reaction times in the ball mill result in a condensation reaction of $CaHPO_4$ to $Ca_2P_2O_7$. The analysis of amorphous systems is challenging because standard powder diffraction methods are unsuitable for these systems. Therefore, the transient amorphous phases were investigated with local probes including vibrational spectroscopy, double resonance ^1H-^{31}P TEDOR , ^1H-^{13}C HETCOR and ^{31}P static spin echo spectroscopy. These methods are highly sensitive in the local environment and thus were able to reveal the formation of hydrogen phopshates and pyro phosphates in the amorphous solid. Further, crystallization of this metastable amorphous product aCCP faces kinetic hindrance because of the high-strain amorphous calcium phosphate network formation. XPCS spectroscopy revealed these dynamics, and coupled with FTIR spectroscopy, this could be partially attributed to a rigid hydrogen network.

Amorphization of calcite in the ball mill without impurities is not possible. Therefore, magnesium ions are crucial for the synthesis of amorphous calcium (magnesium) carbonate via a mechanochemical route. The aim of the second project was to find a promising alternative for the use of biodegradable materials with potential bone targeting capability. The recrystallization rate of aMCC is of high importance for its application. Amorphous calcium carbonate should be labile to guarantee the presence of an "ion buffer" for bone regeneration, however, at the same time it requires sufficient reactivity to form hydroxycarbonate apatite. By tuning the magnesium content of aMCC, the crystallization rate was controlled and different crystallization paths could be induced: i) The crystallization rate was reduced with increasing magnesium ion content, ii) Magnesium-rich calcite was formed at Mg^{2+} content up to 30%, iii) Mg^{2+} content >30% the crystallization path occurred via monohydrocalcite to aragonite. *Ex situ* FTIR investigations allowed to quantitatively follow this crystallization process and to detect the formation of the different phases These observations were explained in a chemically comprehensible way using PDF analysis as a local probe. The data indicated that higher magnesium content leads to stronger metal-oxygen bonding, which results in a higher hydration barrier of the material. In conclusion, the optimal mixture (aMCC 30%) formed in the presence of phosphate ions bone-like hydroxycarbonate apatite (HCA, dahllite). Additionally, BM-aMCC is biodegradable and exhibit no inflammatory potential.

The potential of carbonate ions to act as a base in ball mill reactions was utilized for the synthesis of aCCSHS in the third project. For this purpose, $NaHSO_4$ and calcium carbonate were treated mechanochemically, resulting in an acid-base ball mill reaction. Transient amorphous phases were obtained which recrystallized already at atmospheric humidity, since calcium sulfate compounds exhibit a lower hydration barrier than the analogous calcium phosphate compounds. This characteristic leads to the fact that a larger energetic barrier needs to be passed in order to achieve full amorphization. Thus, intermediate occur during the amorphization process, which were identified by *ex situ* powder diffraction measurements. Based on this, the amorphization process can be described by the following:

i) in the first step, an acid-base reaction takes place, resulting in $NaSO_4$, ii) in the following, a phase called omongwaite ($Na_2Ca_5(SO_4)_6 \cdot 3H_2O$) is obtained by the repeating local mechanical impact on the material *i.e.* substitution reactions take place, iii) Finally, the substitution reactions lead to the formation of a completely solid solution, the amorphous material. The latter could be verified by modelling the total scattering data. It was possible to control the recrystallization rate by acetonitrile-water mixtures, since the material is very hygroscopic and transient. Thus, the crystallization path could be specifically manipulated. Crystallization via bassanite to gypsum was detected in water according to the typical Ostwald step ripening. In acetonitrile-water mixtures, a new mineral, $Ca_2Na_4(SO_4)_3(CO_3) \cdot 3H_2O$ (*mainzite*) was discovered.

In summary, this thesis illuminates fundamental mechanochemical and crystallization processes. The acid-base ball mill reaction shows a novel way to obtain new materials with interesting properties and may not only be valuable in fundamental research but also have great potential for applications in the pharmaceutical and chemical industries. Furthermore, it could be demonstrated that it is possible to manipulate the crystallization rate and paths of amorphous materials in an elegant way. These findings enhance our current understanding of amorphous solids and their structures, crystallization, and mechanochemical reactions."

6 List of Figures

7 CURRICULUM VITAE

Publikationsliste

P. Opitz, S.-P. Ruiz, Y. Krysiak, G. Matveeva, P. Nocon, M. Maslyk, M. Mondeshki, U. Kolb and W. Tremel, Arrested precipitation from amorphous precursors as a tool to explore pathways of mineral precipitation. Adv. Mat. **2021,** submitted.

P. Opitz, O. Jegel, J. Nasir, T. Rios-Studer, D. H. Pham, J. Schmedt auf der Günne and W. Tremel, Defect-Controlled Halogenating Properties of Lanthanide-Doped Ceria-Nanozymes. Nanoscale **2021**, submitted.

M. Maslyk, T. Gäb, G. Matveeva, **P. Opitz**, M. Mondeshki, Y. Krysiak, U. Kolb and W. Tremel, Multistep crystallization pathways in the ambient-temperature synthesis of a new alkali-activated binder. Adv. Funct. Mater. **2021**, accepted.

D.-H. Quak, M. Sarif, **P. Opitz**, M. Lange, O. Jegel,D. H. Pham,L. Prädel,M. Mondeshki, M. N. Tahir, W. Tremel, Generalized synthesis of NaCrO2 particles for high-rate sodium ion batteries prepared by microfluidic synthesis in segmented flow. Dalton Trans. **2021**, accepted.

M. Lange, I. Khan, **P. Opitz**, J. Hartmann, M. Ashraf, A. Qurashi, L. Prädel, M. Panthöfer, A. Cossmer, J. Pfeiffer, F. Simon, M. von der Au, M. Mondeshki, M. N. Tahir and W. Tremel, A Generalized Method for High-Speed Fluorination of Metal Oxides by Spark Plasma Sintering Yields Ta3O7F and TaO2F with High Photocatalytic Activity for Oxygen Evolution from Water. Adv. Mat. **2021**, 33 (20), 2007434. https://doi.org/10.1002/adma.202007434

P. Opitz, L. Besch, M. Panthöfer, A. Kabelitz, R. E. Unger, F. Emmerling, M. Mondeshki and W. Tremel, Insights into the In Vitro Formation of Apatite from Mg-Stabilized Amorphous Calcium Carbonate. Adv. Funct. Mater. **2021**, 31, 2007830. https://doi.org/10.1002/adfm.202007830

P. Opitz, M. P. Asta, A. F.-Martinez, M. Panthöfer, A. Kabelitz, F. Emmerling, M. Mondeshki and W. Tremel, Monitoring a Mechanochemical Reaction Reveals the Formation of a New ACC Defect Variant Containing the HCO3– Anion Encapsulated by an Amorphous Matrix. Cryst. Growth Des. **2020**, 20, 10, 6831–6846. https://doi.org/10.1021/acs.cgd.0c00912